NASA/CR—2020-220488

NASA N+2 Advanced Low NOx Combustor Technology

Stephen Kramer
Pratt & Whitney, East Hartford, Connecticut

March 2020

NASA STI Program . . . in Profile

Since its founding, NASA has been dedicated to the advancement of aeronautics and space science. The NASA Scientific and Technical Information (STI) Program plays a key part in helping NASA maintain this important role.

The NASA STI Program operates under the auspices of the Agency Chief Information Officer. It collects, organizes, provides for archiving, and disseminates NASA's STI. The NASA STI Program provides access to the NASA Technical Report Server—Registered (NTRS Reg) and NASA Technical Report Server—Public (NTRS) thus providing one of the largest collections of aeronautical and space science STI in the world. Results are published in both non-NASA channels and by NASA in the NASA STI Report Series, which includes the following report types:

- TECHNICAL PUBLICATION. Reports of completed research or a major significant phase of research that present the results of NASA programs and include extensive data or theoretical analysis. Includes compilations of significant scientific and technical data and information deemed to be of continuing reference value. NASA counter-part of peer-reviewed formal professional papers, but has less stringent limitations on manuscript length and extent of graphic presentations.

- TECHNICAL MEMORANDUM. Scientific and technical findings that are preliminary or of specialized interest, e.g., "quick-release" reports, working papers, and bibliographies that contain minimal annotation. Does not contain extensive analysis.

- CONTRACTOR REPORT. Scientific and technical findings by NASA-sponsored contractors and grantees.

- CONFERENCE PUBLICATION. Collected papers from scientific and technical conferences, symposia, seminars, or other meetings sponsored or co-sponsored by NASA.

- SPECIAL PUBLICATION. Scientific, technical, or historical information from NASA programs, projects, and missions, often concerned with subjects having substantial public interest.

- TECHNICAL TRANSLATION. English-language translations of foreign scientific and technical material pertinent to NASA's mission.

For more information about the NASA STI program, see the following:

- Access the NASA STI program home page at http://www.sti.nasa.gov

- E-mail your question to help@sti.nasa.gov

- Fax your question to the NASA STI Information Desk at 757-864-6500

- Telephone the NASA STI Information Desk at 757-864-9658

- Write to:
  NASA STI Program
  Mail Stop 148
  NASA Langley Research Center
  Hampton, VA 23681-2199

NASA/CR—2020-220488

NASA N+2 Advanced Low NOx Combustor Technology

Stephen Kramer
Pratt & Whitney, East Hartford, Connecticut

Prepared under Contract NNC10CA11C

National Aeronautics and
Space Administration

Glenn Research Center
Cleveland, Ohio 44135

March 2020

Level of Review: This material has been technically reviewed by expert reviewer(s).

Available from

NASA STI Program
Mail Stop 148
NASA Langley Research Center
Hampton, VA 23681-2199

National Technical Information Service
5285 Port Royal Road
Springfield, VA 22161
703-605-6000

This report is available in electronic form at http://www.sti.nasa.gov/ and http://ntrs.nasa.gov/

CONTENTS

FIGURES

ACRONYMS

NUMERICS

1-D	One-Dimensional
2-D	Two-Dimensional
3-D	Three-Dimensional

A

AAC	Advanced Aeroengine Combustor ACd Flow Area
ACS	Axially Controlled Stoichiometry
ALF	Aft Looking Forward
ASCR	Advanced Subsonic Combustion Rig
ASR	Ambient Spray Rig
AST	Advanced Small Turbine
AtoMIST	Atomization Model Interfaced With Surface Tracking

B

BC	Boundary Condition
BH	Bulkhead
BPR	Bypass Ratio

C

CAD	Computer-Aided Design
CAEP	Committee on Aviation Environmental Protection
CASL	Cooling Analysis System for Liners
CCW	Counterclockwise
CEA	Chemical Equilibrium and Applications
CFD	Computational Fluid Dynamics
CLCS	Closed-Loop Cooling System
CO	Carbon Monoxide
CPU	Central Processing Unit
CR-ACS	Counterrotating Axially Controlled Stoichiometry
CRESS	Counterrotating External Staged Swirler
CRZ	Central Recirculation Zone
CW	Clockwise

D

DES	Detached Eddy Simulation
DPM	Discrete Phase Modeling

E

EBC	Environmental Barrier Coating
ED	Eddy Dissipation
EICO	Emissions Index Carbon Monoxide
EINOx	Emissions Index Nitrogen-Oxygen Compounds
EIS	Entry Into Service
EMI	Electromagnetic Interference
EMP	Electromagnetic Pulse
EPAP	Environmental Protection Agency Parameter
ERA	Environmentally Responsible Aviation

F

FADEC	Full-Authority Digital Engine Control
FAR	Fuel-Air Ratio
FETT	First Engine to Test
FFT	Fast Fourier Transform FLA Forward Looking Aft

H

HC	Hydrocarbon
HLES	Hybrid Large Eddy Simulations
HRIC	High-Resolution Interface Capture
HS	Hamilton Sundstrand
HTC	Heat-Transfer Coefficient

I

IBL	Inner Burner Liner
ID	Inner Diameter
IRZ	Inner Recirculation Zone

J

JBTS	Jet Burner Test Stand

L

L/D	Length/Diameter

LBO	Lean Blowout
LDI	Lean Direct Injection
LDV	Laser Doppler Velocimetry
LES	Large Eddy Simulation
LJIC	Liquid Jet in Crossflow
LRU	Line-Replaceable Unit
LSA	Linear Stability Analysis
LSF	Least Squares Fit
LTO	Landing and Takeoff
LVDT	Linear Variable Differential Transformer

M

MRJ	Mitsubishi Regional Jet
MTBO	Mean Time Between Overhauls

N

NERSC	National Energy Research Scientific Computing
NFFT	Number of Points in Fast Fourier Transform
NGPF	Next-Generation Product Family
NOx	Nitrogen-Oxygen Compounds
NRBC	Nonreflecting Boundary Conditions

O

OBL	Outer Burner Liner
OD	Outer Diameter
OPR	Overall Pressure Ratio
ORZ	Outer Recirculation Zone

P

P&W	Pratt & Whitney
PD	Positive Displacement
PDF	Probability Density Function
PDI	Phase Doppler Interferometry
PDPA	Phase Doppler Particle Analyzer
PF	Pattern Factor
PICS	Pilot-in-Can Swirler
PISO	Pressure Implicit With Splitting of Operations

PLIF	Planar Laser-Induced Fluorescence
PMT	Photomultiplier Tube
PRESTO	Pressure Staggering Option
PSL	Polystyrene Latex
PVC	Polyvinyl Chloride
PWM	Pulse Width Modulating

R

RANS	Reynolds-Averaged Navier-Stokes
RI	Rayleigh Integral
RMS	Root Mean Squared
RQL	Rich-Quench-Lean

S

SDVP	Split Discharge Vane Pump
SGTF	Study Geared Turbofan
SiC	Silicon Carbide
SLA	Stereolithography Apparatus
SLS	Selective Laser Sintering
SLTO	Sea-Level Takeoff
SMD	Sauter Mean Diameter
SOI	Silicon on Insulator
SOW	Statement of Work
SWD	Sum of Weighed Deviation

T

TAB	Taylor Analogy Breakup
TALON	Technology for Advanced Low Nitrogen-Oxygen Compounds
TCA	Turbine Cooling Air
TF	Transfer Function
TRL	Technology Readiness Level
TSFC	Thrust-Specific Fuel Consumption

U

UDF	User-Defined Function
UEET	Ultra-Efficient Engine Technology
UHR	Unsteady Heat Release

UTC	United Technologies Corporation
UTRC	United Technologies Research Center

V

VCP	Vapor Core Pump
VOF	Volume of Fluid

W

WALE	Wall-Adopting Local Eddy

INTRODUCTION

This contract was a 24-month effort to identify, design, and perform validation trials on combustor concepts that will meet NASA N+2 oxides of nitrogen (NOx) emissions goal of 75 percent below Committee on Aviation Environmental Protection (CAEP) 6. The combustor cycle conditions were based on a Pratt & Whitney (P&W) study engine cycle architecture and technology suite consistent with the 2025 Entry Into Service (EIS) N+2 timeframe. The program included system studies and engine cycle selection, conceptual combustor design and flame tube screening tests of fuel injectors and mixers, and development of enabling combustion system technologies. A multi-injector sector was designed and fabricated with initial screening tests conducted at P&W and United Technologies Research Center (UTRC) test facilities, followed by verification testing at the NASA Glenn Advanced Subsonic Combustor Rig (ASCR) facility at Glenn Research Center in Cleveland, OH. The NASA N+2 low NOx combustion technology program leveraged development and test rigs from the P&W's Next Generation Product Family (NGPF) TALON (Technology for Advanced Low NOx) programs and included significant cost share from P&W and UTRC.

1. TASK 3.1.1 — CYCLE SELECTION FOR COMBUSTOR REQUIREMENTS

Pratt & Whitney (P&W) had not initiated NASA N+2 application studies at the time the Contract started. An internal P&W study for a long range wide-body twin was selected as a representative N+2 engine cycle.

2. TASK 3.2.1 — COMPUTATIONAL FLUID DYNAMICS SPRAY EVALUATION

2.1 PRATT & WHITNEY TASK 3.2.1 — SWIRLER CFD INVESTIGATIONS

2.1.1 Objective

The objective of this study was to use Computational Fluid Dynamics (CFD) to better understand the flowfield of a high-shear swirler. As part of this effort, CFD results were validated against rig test data from the United Technologies Research Center (UTRC). Although test data and CFD results matched for many of the flow characteristics, CFD studies were also performed to investigate how the fidelity of the simulation could be improved.

2.1.2 Experimental Results and/or Analysis Details

The swirler of interest in this study is a high shear multi passage swirler. The swirler and nozzle are set up to flow from a plenum into ambient conditions, with a specified pressure drop. The rig data available for comparison was the spray patternation, Sauter mean diameter (SMD) distribution, and velocity profile downstream of the swirler. This data could then be compared to the CFD results to give quantative validation.

2.1.3 CFD Analysis

Initial CFD cases were performed, which simulated both the air-flow and fuel-flow through the swirler and fuel nozzle.

2.1.4 Subsequent Studies

A completely independent ambient rig at UTRC later performed LDV measurements of the swirler flowfield, but with airflow only. The CFD and test data showed much better agreement than the spray CFD and spray test data. Upon comparing the spray test/CFD results to the airflow only test/CFD results for axial velocity, it was observed that both the CFD and the data moved towards each other. The differences in the CFD results between this study and that study can be explained by using a different solver and a slightly modified configuration. The only difference between the tests was the inlet plenum size and the presence of the liquid spray.

Subsequent spray patternation tests were performed to investigate the impact of liquid flow on the air axial velocity. The spray test data recorded axial velocity profiles for three levels of liquid flow. These tests confirm that the difference in the air only and the spray test data is due to the level of liquid flow. As the level of liquid flow decreased, the spray test air axial velocity profile approached that of the air only axial velocity profile. This includes a decrease in the peak axial velocity, an outward radial movement of the peak, and a decrease in axial velocity at the centerline as liquid flow is decreased. The CFD cound not capture all of these effects.

2.1.5 Conclusions/Recommendations

Throughout the original CFD study, parameters of geometry, mesh element count, and boundary conditions, were varied in order to improve the match in axial velocity between CFD and rig data. Particularly, we saw what parameters alter the velocity profile at the measurement plane. In turn, we have also seen how these changes alter the spray patternation.

2.2 UTRC TASK 3.2.1 — CFD SPRAY EVALUATION

CFD spray calculations were performed for two swirler designs using Fluent. The objective of the modeling was to observe the swirler flowfield and fuel spray distribution and to compare them with the experimental observations. Large eddy simulation (LES) was used in Fluent with the Taylor Analogy Breakup (TAB) secondary breakup model. Two-way coupling was selected in Fluent to capture the proper particle dynamics. AtoMIST treats the primary breakup of liquid fuel (Jet A) including column breakup, surface stripping and film formation and breakup from a filming surface. Details of AtoMIST description can be found in Arienti et al. (2007). A brief description of the model is given in Section 2.2.5, *Brief Description of Spray Model Atomization Model Interfaced With Surface Tracking*. Constant mass flowrate inlet boundary conditions were used for the air and fuel. Detailed results and discussions for both swirlers are discussed below. The two swirlers evaluated are the counterrotating external staged swirler (CRESS) and the pilot-in-can swirler (PICS).

2.2.1 Counterrotating External Staged Swirler Evaluation

2.2.1.1 Geometry and Grid

The CRESS has multiple fuel and air passages arranged circumferentially. The full 360 degrees of geometry was modeled in CFD. The filmer wall used boundary layer; the grid includes the upstream plenum, swirler and downstream. Two droplet sampling planes were located downstream of the swirler exit. These conditions modeled matched the air velocity and fuel to air momentum flux ratio of the chosen cycle conditions.

2.2.1.2 Results and Discussions

Since CFD inlet condition was set as mass flow boundary condition, the calculated pressure drop may have some difference compared to the designed value potentially due to Acd measurement and the CFD value based on the geometry and grid. The difference here is insignificant. ***Figure 2-1*** shows film thickness at the swirler exit.

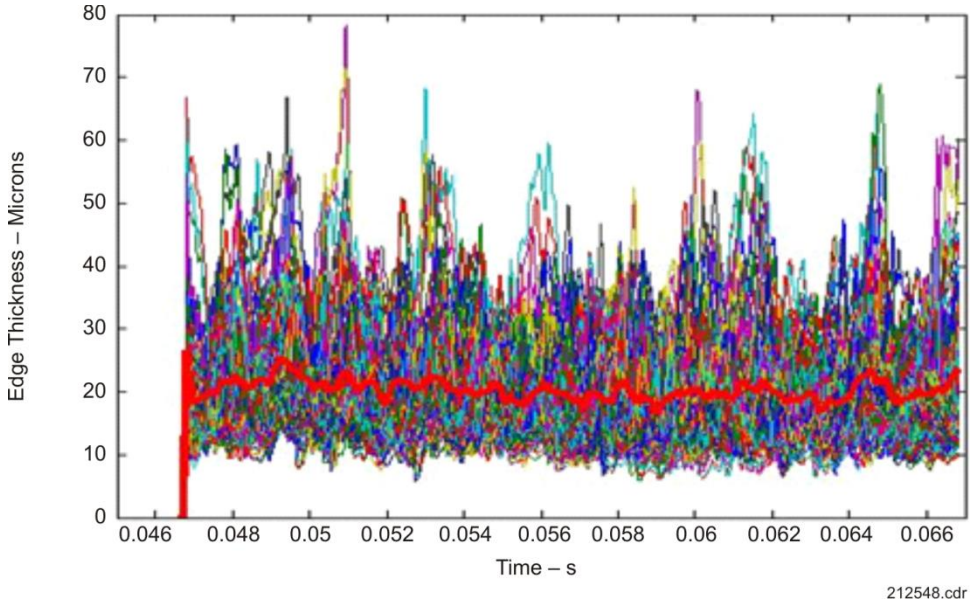

Figure 2-1. *Film Thickness*

CFD results were compared with experimental measurements. The fuel mass flux was compared to experimental fuel patternation. Velocity and particle SMD were compared to PDI measurements.

2.2.2 Pilot-in-Can Swirler Evaluation

2.2.2.1 Geometry and Grid

The PICS has several fuel orifices evenly distributed circumferentially. A total of 102.8 degrees of geometry was modeled in CFD. The filmer wall used boundary layer mesh and a starting grid of 10 μm. Snapshots of the grid are shown in ***Figure 2-2***. The grid includes the upstream plenum, the swirler, and the downstream region. The modeled conditions matched the air velocity and fuel to air momentum flux ratio of the chosen cycle condition.

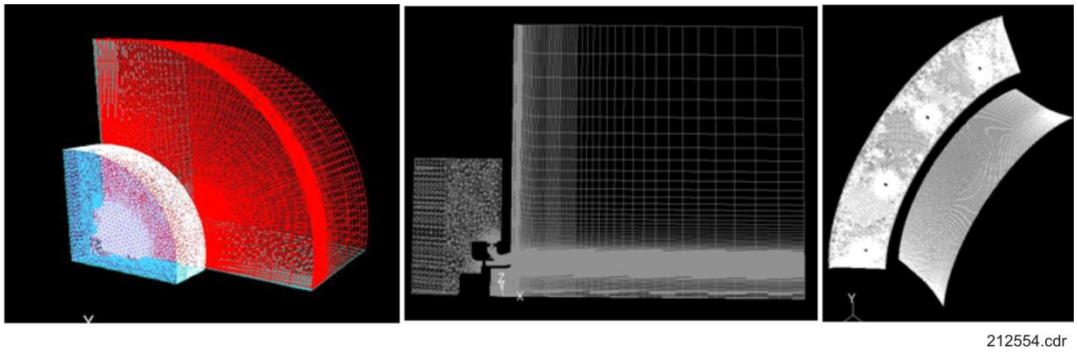

Figure 2-2. *Grid of PICS (Overall Grid, Center Cut Plane, and Filmer Wall)*

2.2.2.2 Results and Discussions

The modeled particle size from the film breakup was very small due to the thin film, as shown in ***Figure 2-3***.

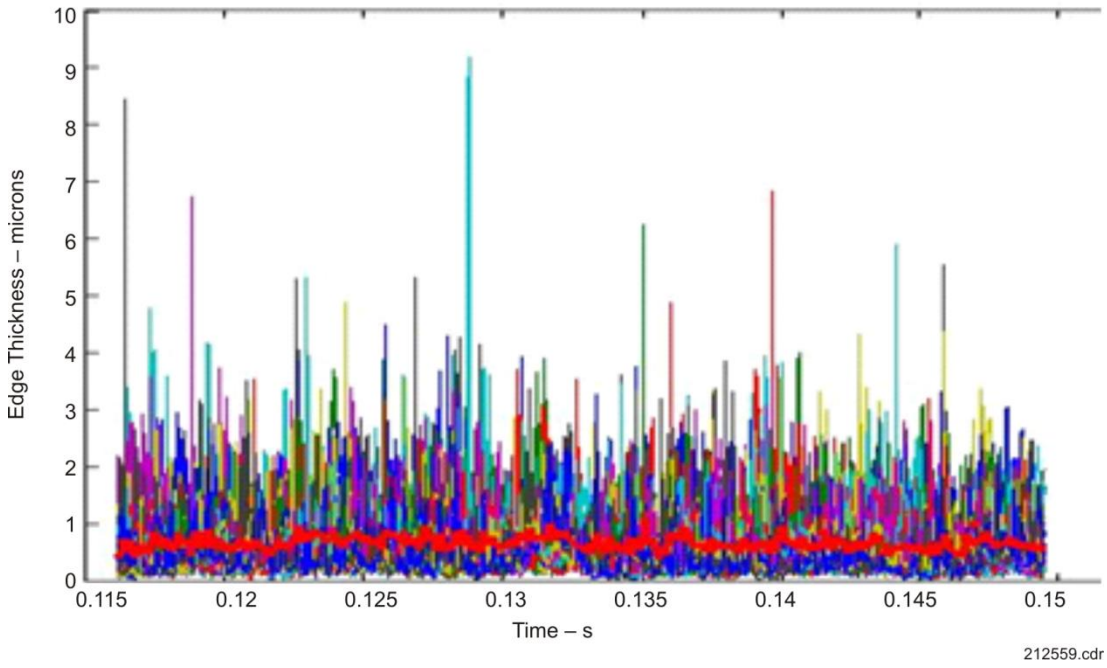

Figure 2-3*. Film Thickness at the Swirler Exit*

CFD results were compared with experiment measurements. The fuel mass flux was compared to the experimental fuel patternation results. The particle axial velocity and SMD are compared to PDI measurements at downstream of swirler.

2.2.3 Counterrotating Swirler Evaluation (Axially Controlled Stoichiometry Main Fuel Injector)

2.2.3.1 Geometry and Grid

The geometry of the counterrotating axially staged combustor (CR-ACS) includes a number of fuel orifices evenly distributed circumferentially. Note that for this case, the film was not modeled in CFD, so that there is no film breakup. Particles were generated from column breakup or column stripping. A total of 360 degrees of the geometry was modeled in CFD that captured all fuel orifices, with a resulting grid size much less than CRESS and PICS models due to the lack of boundary layer cells for the film. The grid includes the upstream plenum, swirler, and downstream volume that is open to ambient. Two droplet sampling planes were located downstream of the swirler exit. The modeled conditions matched the air velocity and fuel to air momentum flux ratio of the chosen cycle condition.

2.2.3.2 Results and Discussions

CFD results were compared with experiment measurements. The fuel mass flux was compared to the experimental fuel patternation results. The particle axial velocity and SMD were compared to PDI measurements downstream of the swirler.

2.2.4 CRESS

2.2.4.1 Geometry and Grid

The geometry of the CRESS is the same as in earlier discussion (see Section 2.2.1, *Counterrotating External Staged Swirler Evaluation*). The difference is that the film model was removed so that the grid does not include the boundary layer model to account for the film at the wall, thus resulting in a significantly reduced grid size. The run conditions are the same except that compressible ideal gas law was used for the mixture.

2.2.5 Brief Description of Spray Model Atomization Model Interfaced With Surface Tracking

AtoMIST was developed in-house as a user defined function for Fluent. It quantifies a liquid jet in crossflow (LJIC) primary breakup and film breakup.

More detailed information can be found in Arienti et al. (2007).

2.2.6 Summary

Ambient spray evaluation was performed using the UTRC in-house spray model AtoMIST for three swirlers: CRESS, PICS and CR-ACS. The run conditions for all swirlers were set such that the air velocity and fuel to air momentum flux ratio are matched for the chosen cycle conditions. The ACd of the three swirlers varied, representing a significant difference in swirler sizes. CFD results were compared to experimental fuel patternation and PDI measurements. Future work will focus on defining the required areas of improvement to enable the model to be applicable to a wider variety of fuel injectors.

2.2.7 Reference

Arienti, M. and Soteriou, M., *Dynamics of Pulsed Jet in Crossflow*, Proceedings of GT2007, GT2007-27816, Presented at the ASME Turbo Expo, May 14-17, 2007, Montreal, Canada.

3. TASK 3.2.2 — COMPUTATIONAL FLUID DYNAMICS INTERNAL MIXER EVALUATION

The objective of this effort is to study the impact of air turbulence on fuel/air mixing through numerical modeling. Several cases were simulated using a high fidelity HiMIST code, where liquid was injected in a gaseous crossflow at high Weber number and subjected to different turbulence levels. The results were compared with data obtained from parallel experiments (see Section 9, *Task 3.3.2 — Internal Mixer Testing*). Specific tasks accomplished include: initialization of air turbulence at application relevant parameters, investigation on decaying of single phase air turbulence in channel flow, two-phase simulation of liquid jet in crossflow at given Weber number and different turbulence levels, liquid jet breakup features, and statistical analysis of downstream droplets distribu- tion in terms of size and spatial location.

3.1 GENERATION OF AIR TURBULENCE

In this section, we first look at the generation of homogeneous isotropic air turbulence, which will be introduced into the flow domain of a channel as the inlet boundary. In the course of simulation, at each time step, a slice of velocity field is extracted from the combination of turbulence boxes and fed into channel flow as inlet boundary condition.

The homogeneous isotropic turbulence is generated using a pseudospectral method. The turbulence box is initialized with a random velocity field following the normal distribution with a standard deviation. The random velocity box is then modulated in the spectral space.

At each time step in the simulation, a two-dimensional (2-D) planar velocity field needs to be extracted from the turbulence box to feed the channel flow as inlet boundary. The location of the 2-D slice relative to the box is determined by summing up an arbitrary initial cut located at x_0 within the box and the distance traveled during elapsed time with mean velocity. The distance is then projected into the range of the lateral length of the box, consistent with the periodic boundary condition used when generating the box turbulence.

3.2 DECAYING OF SINGLE PHASE AIR TURBULENCE IN CHANNEL FLOW

The intensity of the air turbulence decays as the flow travels through the channel due to viscous dissipation, and the characteristic turbulent length scales increase accordingly. Since these characteristics have direct impact on the interaction between the liquid and gas phase, and consequently affect the liquid breakup and mixing process, it is necessary to quantify the single phase turbulence evolution along the channel.

3.3 TWO-PHASE SIMULATION OF LIQUID JET IN CROSSFLOW AT HIGH WEBER NUMBER AND DIFFERENT TURBULENCE LEVELS

After quantification of the decay of single phase air turbulence in the channel flow, several two-phase simulations of liquid jet in gaseous crossflow were completed. The high-fidelity HiMIST code is ideal for this type of two-phase simulation. It features the coupling of the level set method and the VOF method, which retains the sharp interface between liquid and gas phase while accurately preserving the liquid mass. In addition, the HiMIST code uses the block-structured adaptive mesh refinement. In this way, the interface region, where the large density and viscosity ratio occurs, can be well resolved with fine grid resolution, and the rest of the domain where the fluid properties are stable, can be computed with coarser grid resolution, so that the total grid count and computational cost can be significantly reduced.

From the instantaneous flowfield, the difference in velocity fluctuations are quite clear, though the difference between the liquid jets for the two cases is barely noticeable. Also note that the simulations require very large amount of computational resources, and had to be performed on supercomputers at National Energy Research Scientific Computing (NERSC) center.

However, it was concluded that completion of these calculations was too expensive even with these supercomputers.

Figure 3-1 demonstrates the estimation of the grid counts based on a base resolution of 160 μm per grid spacing together with four levels of refinement. Under this configuration, there are about 35 million cells when

the jet reaches half the full penetration height, as shown by the green line in ***Figure 3-1***. As the liquid jet keeps being injected into the gaseous flow domain, the interface area would keep increas- ing till the jet reaches full penetration height and becomes statistically steady. Accordingly, the total grid counts would increase to 80 to 100 million if linearly projected to the steady state with current growth rate. In addition, the computational time per time step would also increase as the total grid counts increase. A rough estimation predicts that even with 512 cores on NERSC machines, it would take more than 100 days to finish running the simulations until steady state, which would not be economically feasible.

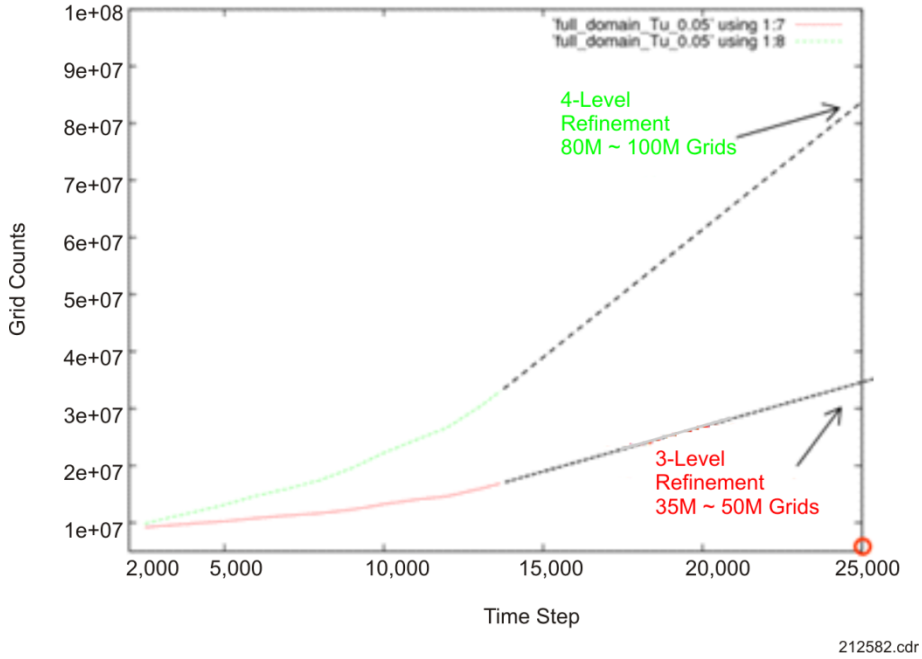

Figure 3-1. *Estimation for Grid Counts*

To increase the speed of the. simulation, a split domain approach was developed. The idea is based on the observation that at high Weber numbers, the liquid jet breakup is contained in a relatively small region compared to the whole domain. In a short distance downstream to the jet location, the breakup process is completed and the liquid column is transformed into small droplets. Since these droplets are small, their surface features do not need to be resolved. In other words, only the near field of the liquid jet requires high resolution and correspondingly fine time steps to capture the breakup process. The spatial and temporal resolution can be significantly relaxed for the rest of the domain. In this way, the computational cost can be greatly reduced.

Care is also taken to ensure the droplet and flowfield information at the exit plane are saved for time interval long enough, so that the fully representative statistical information is collected. A reasonable time scale can be approximated as the time needed for the jet to travel from the injector exit to the position of its breakup.

3.4 LIQUID JET BREAKUP FEATURES AND STATISTICAL ANALYSIS OF DOWNSTREAM DROPLETS DISTRIBUTION

Two measurement planes, downstream from the liquid jet, are set in the large domain to collect the droplet statistical data. First the jet injection in the reduced domain is computed until the liquid jet reaches its equilibrium status. The flowfield data and droplet information are then stored to be used as inlet boundary conditions to the large domain at each time step. Data mapping and interpolation are carried out in the manner described in the previous section. The large domain simulation continues until the droplet statistical data collected at the two measure planes reaches steady state.

Figure 3-2 (a) and (b) show the results from the reduced domain simulation for 2 turbulent. Snapshots are taken from different perspectives for the liquid jet when it reaches equilibrium state. Some observations can be

made from the side by side comparison of the two cases. First, from the front view ***Figure 3-2*** (a) and (b), it is clearly demonstrated that the upwind surface of the liquid jet column is smoother at lower turbulent intensity, while it is more severely disrupted by higher turbulence. Second, the two cases are similar to each other in terms of penetration height, as seen from the side view ***Figure 3-2*** (c) and (d). Specifically, compared with the correlation in [6, 7], current simulations underestimate the jet penetration height for both cases. This difference can be attributed to the fact that current simulations focus on higher Weber numbers than previously investigated. It is also observed that the near field liquid droplets have slight broader distribution in spanwise direction at more intense turbulence, as manifested from top view ***Figure 3-2*** (e) and (f).

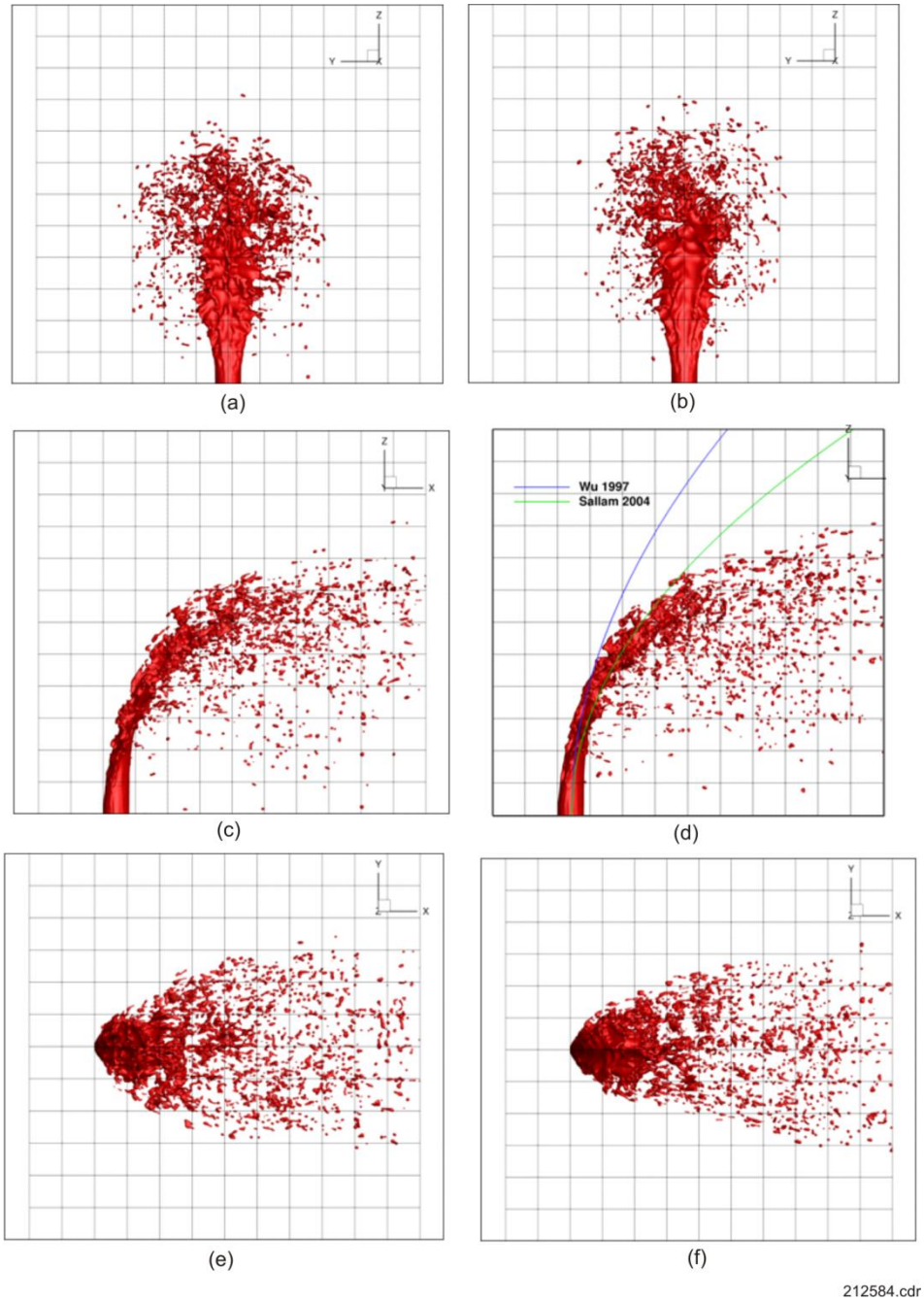

Figure 3-2*. Snapshots From Different Perspectives for Liquid Jet*

In conclusion, the split domain approach that couples a reduced domain and an adjacent large domain has been successfully demonstrated. This multidomain, multiresolution coupling approach significantly reduces the computational cost for the study of gas turbulence effects on liquid jet in gaseous crossflows. Simulations at high Weber number and two turbulence levels show qualitatively reasonable results, although quantitatively better results in terms of liquid jet penetration height and droplet size distribution can be achieved by employing denser grid in the reduced domain simulation near by the liquid jet.

3.5 REFERENCES

1. Baines, W.D. and Peterson, E.G., "An investigation of flow through screens", Trans. of the ASME, July 1951.
2. Roach, P.E., "The Generation of nearly isotropic turbulence by means of grids", Heat and Fluid Flow, vol.8 (2), 1987.
3. Pope, S.B, "Turbulent Flows", Cambridge University Press, 2000.
4. Comte-Bellot, G. and Corrsin S., "Simple Eulerian time correlation of full and narrow-band velocity signals in grid-generated 'isotropic' turbulence", J. of Fluid Mech., vol. 48 (2), 1971.
5. Marshall, A., Venkateswaran, P., Noble, D., Seitzman, J., and Lieuwen T., "Development and characterization of a variable turbulence generation system", Exp. Fluids 51, 2011.
6. Wu, P.-K., Kirkendall, A., Fuller, P. and Nejad, A., "Breakup process of liquid jets in subsonic crossflows", J. of Propulsion and Power, vol. 13 (1), 1997.
7. Sallam, K.A., Aalburg, C., and Faeth, G.M., "Breakup of round nonturbulent liquid jets in gaseous cross-flow", AIAA Journal, vol. 42 (12), 2004.

4. TASK 3.2.4 — COMPUTATIONAL FLUID DYNAMICS PERIODIC-SECTOR EVALUATION

4.1 COMPUTATIONAL FLUID DYNAMICS SIMULATIONS OF THE AAC ACS RIG

UTRC performed numerous experimental studies in the advanced aeroengine combustor (AAC) rig over the NASA contract time period. A large number of these tests focused on investigating the performance of an axially controlled stoichiometry (ACS) configuration. The initial version of these tests intro- duced lean, premixed gaseous propane jets into a lean vitiated flow (jet in crossflow). The emissions were measured at various downstream locations in the planar rig. A more detailed description of the full set of tests is listed in Section 10, *Task 3.3.3 — Single-Sector Reacting Testing*.

To validate the CFD model for future simulations, this AAC ACS test was simulated. The original three-dimensional grid was structured and used hexahedral elements.

4.2 CFD OF UTRC THREE-SECTOR AND SINGLE-SECTOR SLA COLD FLOW RIGS

4.2.1 Objective

A three-sector SLA cold airflow rig with high-shear swirlers was tested at UTRC. Detailed LDV measurements were taken. This data was then analyzed and compared with CFD simulations in order to anchor current CFD modeling approaches. Single-swirler, unconfined ambient tests were also run and compared with corresponding CFD simulations.

4.2.2 Summary

The three-sector confined rig and single-sector unconfined rigs were successfully run at UTRC and parametric CFD analysis was executed for each geometry to understand the characteristics of the flowfield, as well as identify modeling approaches to be used for future analysis of noncombusting swirling flowfields in combustor geometries. As would be expected, the rig results indicated differences in swirler velocity characteristics for the confined rig versus the unconfined rig. Unconfined flows tended to penetrate farther and were less diffusive than the confined swirler, likely due to the entrainment characteristics of the ambient unconfined flow. The CFD results generally matched the test results well, predicting radial profiles of both axial and tangential velocity. The parametric study of different modeling approaches illustrated some improvements to the analysis process that can be made. Using an advancing front gridding technique combined with the conversion to polyhedral elements yielded accuracy benefits for the unconfined rig results, as well as a 50 percent reduction in overall analysis time. Grid refinement and convergence studies were also performed with results showing no net benefit to the accuracy of the solution. However, all current and proposed modeling approaches indicate that there is significant room for improvement in modeling the central recirculation zone, especially near the swirler exit. The negative centerline axial velocity was underpredicted for the three-sector cases, but was over-predicted for the single-sector unconfined cases. The swirler ACd was also underpredicted.

4.2.3 Experimental Setup and Analysis Approach

4.2.3.1 Three-Sector Geometry

The three-sector rig was designed using a Rich-Quench-Lean (RQL) combustor geometry as its baseline with three sectors, each with a three passage high-shear swirler. The geometry was created using stereolithography (SLS), so no cooling holes are drilled into the outer diameter (OD) and inner diameter (ID) liners. Five individual passages are used to direct the airflow. The airflow from the individual upstream passages moves through the swirler and exits into the burner where it is no longer divided. This allows for analysis of possible swirler-to-swirler interaction and other three-dimensional (3-D) flow-fields. The flow then mixes with the OD and ID shroud flow through the dilution holes and exits out into the ambient environment. All of the corresponding cold-flow tests and CFD simulations are near ambient pressure.

4.2.3.2 Three-Sector Grid Generation

Because one of the primary focuses of this study was to investigate our ability to model the swirling flows in a three-passage high-shear swirler and burner, various grid generation approaches were used to generate grids to

understand the effect of grid topology on the solution. Two primary grid generation methodologies were used in this study. The first approach is the Octree approach. The second approach is the advancing front methodology.

The Octree approach essentially builds boxes inside of the geometry, then divides up the box based on the specified length scale into smaller boxes. Each small box is then divided into 12 tetrahedrons. Finally, the voids between the surface grid on the domain boundaries and the original boxes are filled using tetrahedrons to connect them. Some benefits and drawbacks of the Octree method include:

Benefits

- Robust grid generation methodology. Usually can make a grid on anything no matter how dirty the computer-aided design (CAD) geometry is with minimal cleanup.
- Strong control of volumetric length scale.

Drawbacks

- Tetrahedrons are anisotropic and have a wider variance in face angle. This usually leads to higher cell counts due to smaller volumes per cell and lower quality elements when compared to equilateral tetrahedrons. Additionally, depending on the solver, they can lead to less accurate numerical solutions.
- Poor near-wall treatment. Because the voids between the volume box and the walls are filled in last, the cells in the region tend to be more ad hoc and of lower quality. This can be especially problematic when growing boundary layer cells.
- Changing volumetric length scales causes an instantaneous jump in cell size which leads to poorer quality elements and potential numerical issues. The jump in cell length scale is by a factor of two.

The advancing front methodology essentially performs the exact opposite operational steps as the Octree approach. A surface mesh of triangles is created on each surface of the domain using surface lengths scales specified in the setup. The surface mesh is then extruded into the domain to create tetrahedral cells. The grid is finally merged in the center of the domain where volume meshes grown off the domain boundaries meet. Some benefits and drawbacks of the advancing front method include:

Benefits

- Higher quality cells. Equilateral cells have equal face angles, making them the highest quality tetrahedral cell shapes.
- Lower cell count. Tetrahedral cells have the maximum volume per length scale to optimize overall cell count.
- Better near-wall treatment. Since cells are grown from the wall, the first cell off the wall is typically of optimum quality given an appropriate surface mesh.
- Smoother length scale transitions. Advancing front grids do not jump length scales suddenly, but rather smooth grid from coarse to fine and vice versa.

Drawbacks

- Methodology is less robust than Octree approaches. More work may need to be done on the front end of the process to ensure a clear geometry and a close grid.
- Less control of volumetric length scale. Since grids are developed with smooth transitions in mind, downstream or upstream coarsening can affect desired length scale due to blending.

Since both methodologies have potential benefits, it was decided to generate grids with both and compare the solutions to rig data for accuracy. The Octree grid came out to be 28 million cells while the advancing front grid came out to be 20 million cells, which is a 28 percent reduction in total cell count.

An additional grid topology was investigated later in the analysis, the polyhedral mesh. A polyhedral mesh basically uses n-sided elements in the volume instead of triangular or quadrilateral fixed face elements. When compared to standard tetrahedral meshes, the polyhedral mesh has some significant benefits, but is also not without its own drawbacks, which include:

Benefits

- A potentially more accurate solution. This is most applicable in the flux terms through the face on a cell. Typical numerical solvers are most accurate when the convective term vector is normal to the face of the cell. A polyhedral cell has many sides, so the high magnitude convective term vectors will likely be more normal to the surface than in a tetrahedral cell.
- Dramatically reduced cell count with constant length scale. Polyhedral meshes typically have significantly lower cell counts because the volume of a cell is larger with constant edge lengths but with more edges.

Drawbacks

- Numerical methods are tougher to implement into solver. Typically only commercial solvers currently have this capability.
- Cell volume control is difficult. For equations that are heavily influenced by cell volume like some turbulence and combustion models, potential drawbacks may exist depending on model formulation.

The polyhedral grid was approximately 5 million cells, which is 75 percent smaller in cell count than the tetrahedral grid.

4.2.3.3 Single-Sector Geometry

Upon completion of the three-sector analysis, a decision was made to do some testing with a swirler that was not confined by the burner. One of the primary drivers behind the need to perform the single sector unconfined rig study was due to analysis observations from the ASR test of the three passage swirler with liquid injection. The three passage swirler was tested in the ASR with liquid injection at the higher pressure drop and was modeled using CFD (see Section 2.1, *Pratt & Whitney Task 3.2.1 — Swirler CFD Investigations*). However, code predictions, when compared to the rig data axial velocity results, were somewhat poor (the prediction of other flow characteristics was much better). Several changes were made to the code process (alternate gridding, additional ambient air mass entrainment, upstream plenum changes) all with only slight improvement in the results of the code. The CFD prediction of the strength of the swirler flowfield was considerably less than the rig data results.

Upon completion of the current airflow-only three-sector confined rig results, which showed considerably better data matching, it was then decided to rerun the rig with just a single sector unconfined and try to anchor the CFD process executed in the three-sector confined rig analysis, as will be described in the following sections. For the unconfined solutions, only a single sector of the three-sector rig was used. The corresponding swirler for these unconfined studies is metal, as opposed to the SLA swirlers used for the three-sector studies. The single-sector passage was mounted to a bulkhead (BH) plate and flowed into ambient conditions.

4.2.3.4 Single-Sector Grid Generation

The grid generated for the single-sector geometry followed the same rules as the three-sector rig. The grid was also converted to polyhedral cells. Due to the large length scale desired in the far field, an embedded surface algorithm was used to control the near field length scale of the plenum just downstream of the swirler exits. The grid was then significantly stretched to the far field to reduce overall cell count. The baseline tetrahedral grid was 12.6 million cells, while the polyhedral grid was 3.1 million cells. Note that for the single-sector CFD, two levels of pressure drop were applied, with high and low levels.

4.2.3.5 Rig Setup and Data Measurements

The test rig was setup to measure the velocity of the flow exiting the swirler using LDV, which uses the Doppler shift in a laser to measure the velocity of small particles moving through the flow field. These particles are mixed with the air upstream of the swirler and are small and light enough to generally follow the flow streamlines of the air passing through the swirler. The velocity field was measured at five axial locations downstream of the swirler along the swirler centerline.

4.2.4 Experimental Results and Analysis Details

4.2.4.1 Three-Sector Rig Results

The LDV results from the three-sector rig defined the axial velocity of the flow field exiting the swirler at the five axial locations.

4.2.4.2 Three-Sector Grid Generator Comparison

The first set of cases to be run used the Octree tetrahedral grid and the advancing front tetrahedral grid. The two grid types have similar flowfield predictions. Both grid types under predict the width of the swirler flowfield in the near field region, which likely contributes to the weaker central recirculation zone as observed in the CFD as compared to the test data. However, as the probe moves downstream, the advancing front grid solution falls on to the rig data curve in terms of both swirler flow field width and strength. This is likely due to a better prediction of the outer recirculation zone in the near field region by the advancing front grid. The impact of this is a faster diffusion of the swirler flowfield strength and an eventual widening of the main outer swirler flow.

While overall the results of the two grid types did not overly distinguish one grid type over the other, performance statistics did. The advancing front tetrahedral grid finished its calculation in approximately 4.5 days, while the Octree tetrahedral grid finished its calculation in approximately 5.5 days. The advancing front topology yielded a grid that produced slightly better results when compared to rig data with a 20 percent reduction in run time. Coupled with that, the Octree grid took over twice as long as the advancing front grid to build. With this significant reduction in total analysis time, coupled with the potential accuracy gains, the advancing front grid was chosen as the grid development methodology used in the remainder of the analysis.

4.2.4.3 Three-Sector Grid Cell Type Comparison

The next set of cases to be run used an advancing front tetrahedral grid and the same grid converted to polyhedral cells. The results of the polyhedral mesh and the tetrahedral mesh are nearly identical. Both centerline and radial profile plots of axial velocity lay on top of each other. However, while the tetrahedral grid solution time was approximately 4.5 days, the polyhedral grid solution time was approximately 2.25 days, which is a 50 percent reduction in solution time. With no discernible change in the solution and a significant reduction in solution run time, the polyhedral mesh was chosen for future analysis.

4.2.4.4 Three-Sector Floating Point Precision Comparison

The final set of cases to be run used the advancing front tetrahedral grid converted to polyhedral cells using both the single precision solver and the double precision solver. The desire to analyze potential differences in the precision of the solver stems from previous experience in the development of combustion models that the single precision solver does not adequately predict the flowfield. The decision was made to run both the single and the double precision solver in this study to ensure that the velocity field can be predicted appropriately with the single precision solver, which will save runtime memory requirements and disk storage space. The results indicate that the single and double precision solver have essentially identical velocity fields with a small amount of variation. With equal velocity field predictions indicating no net benefit of using the double precision solver, it was decided that the single precision solver would be used for further analysis.

4.2.4.5 Single-Sector Rig Results

For the outer peaks, the single sector rig has similar peak magnitude to the three-sector rig. However, the three-sector rig swirler strength dissipated out and became axial faster than the single sector unconfined rig. This is likely due to the confined rig forcing the flow axial and not allowing the swirling flow to persist where the

unconfined rig does not have any forced movement to the flowfield. Additionally, the single sector unconfined results show that the width of the forward moving swirler flow is less than that of the three-sector unconfined flow, as expected. The ORZ is nearly nonexistent in the unconfined rig due to a lack of an outer wall. Additionally, entrainment of outer air will help keep the unconfined flow moving forward and reduce overall diffusion.

The centerline axial velocity profile and the strength of the CRZ, however, are significantly different between the three-sector confined rig and the single-sector unconfined rig. The primary difference between the rigs is the near field centerline axial velocity profile within the first swirler diameter downstream of the swirler. The strength of the CRZ as measured in the three-sector confined rig is significantly stronger than that of the unconfined rig. Additionally, the single sector unconfined rig had a bump in its profile where the CRZ got weaker, then got stronger. This bump was actually present in both the low and high pressure drop cases, likely making it nonanomalous. This will become a significant part of the discussion for anchoring CFD analysis and could play a key role in the development of the CRZ in the ambient spray rig (ASR), which is used as a comparison in the final section.

4.2.4.6 Single-Sector Grid Cell Type Comparison

The first set of cases for the single sector unconfined rig used an advancing front tetrahedral grid and the same grid converted to polyhedral cells. While the three-sector rig results showed little difference between using a tetrahedral grid and a polyhedral grid, the results for the single sector unconfined rig have some addi tional differences. While the radial profiles of axial velocity show that the width and strength of the main swirler flow is approximately the same using the two cell type geometries, the CRZ prediction is considerably different. Similar to the three-sector rig results, the near field predictions of axial velocity along the centerline at axial distances less than one swirler diameter downstream of the swirler exit do not match up particularly well for both grid types. However, it is the far-field downstream behavior, greater than one swirler diameter downstream of the swirler, that differs considerably between the grid types. The polyhedral mesh predicts the CRZ to collapse and move axially at the same location and velocity as the rig data while the tetrahedral mesh predicted the collapse much farther downstream and with considerably less velocity.

The fact that the polyhedral and tetrahedral meshes had relatively identical results in the three-sector rig analysis and differed considerably along the centerline for the single sector unconfined rig is quite interesting. The likely cause of this is that the confined rig essentially forces the flow to move axially as there is nowhere else to go, but the unconfined single sector rig does not numerically force the flow to move axial, so it is up to the accuracy of the code to predict this without allowing the flow field to diffuse out. The fact that the polyhedral mesh correctly predicted the far-field behavior shows the potential benefits of using the polyhedral elements from an accuracy perspective. All studies performed for the rest of the single sector unconfined analysis used the polyhedral elements.

4.2.4.7 Single-Sector Grid Refinement Study

The next set of cases to be run used an advancing front tetrahedral grid converted to polyhedral cells and a refined grid with half the length scale in the swirler also using polyhedral cells. The grid refinement study reduced the length scale in the swirler by 50 percent as an attempt to better capture the swirling flow along the centerline. Previous studies have indicated that the polyhedral elements better capture the unconfined flowfield profile and reduced the cell count of the grid to a manageable number. The grid refinement study was then performed using the polyhedral grid due to both of these benefits. After reviewing the profiles of both the standard and the refined grid, there is very little difference in the swirler profiles. The strength of the outer swirler peaks are slightly stronger with the fine grid, which matches the data better. This makes sense as the fine grid will be less diffusive and will likely better capture these peaks. However, the toughest physical observation to capture, the near field centerline velocity profile, was still not captured well using the refined grid. It could potentially be that the turbulence model is not capable of capturing the kind of reversed flow and entrainment characteristics we are seeing with the unconfined flow. The fact that the boundary layer along the swirler wall is not fully resolved could also be a factor.

4.2.4.8 Single Sector-Subiteration Convergence Study

The next set of cases to be run used an advancing front tetrahedral grid converted to polyhedral cells using the same grid with twice as many subiterations per time step instead of the standard number during the time averaging phase. A hypothesis during the analysis was that the reason behind poor matching of the swirler centerline velocity profile was possibly due to not converging properly at each time step. To check this hypothesis, the case was restarted from the final solution and rerun using twice the number of subiterations per time step instead of the normal six and then time averaged over a certain number of time steps. However, line plots show that the solution is independent of the number of sub-iterations per time step. Therefore, for a noncombusting, swirling flowfield with similar characteristics, the lower number of subiterations is likely sufficient.

4.2.4.9 Single Sector Comparison to Ambient Spray Rig Results

For the unconfined, higher level pressure drop results, two different inlet boundary conditions were used. One boundary condition is to set a pressure inlet and a pressure outlet to create an elliptical well posed a problem. However, since the mass flowrate in the rig is known and CFD has the capability to explicitly set mass flow at the inlet, the mass flow inlet boundary condition was used in the single-sector analysis as well as the pressure inlet. The first observation that is made is that the mass flow inlet boundary condition better matches the axial velocity profile than the pressure inlet. This, along with statistics tracked in CFD, showed that the overall mass flow through the system using the pressure drop boundary condition is underpredicted.

Regardless of the inlet boundary condition used, the CFD analysis compared very favorably to the single sector unconfined results, and were much more favorable than the ASR CFD results compared to the rig. The first observation is that the ASR test results have much higher velocities than the single-sector results. Additionally, while strong CRZs were predicted in both the three-sector confined rig and the single-sector unconfined rig, the ASR does not show a strong CRZ. This was thought to be due to the blockage or drag effect of the liquid flow on the airflow. Since the spray model that was used accounts for only one-way coupling (the fuel is affected by the air but the air is not affected by the fuel), this effect would be completely neglected. A UTRC CFD study with a two-way coupled spray model supported that this could have an impact on the centerline flow. Later spray data also showed that the peak velocity magnitude and location were also affected for a three-passage high-shear swirler.

The second observation is that while the spray CFD solution is not too far off of the new single sector rig and CFD results, it still has a lower velocity prediction. The CFD plot used is the pressure inlet boundary condition case, which also predicted lower velocities than the rig and yet still has higher velocities than the spray CFD results. Besides the presence of liquid fuel in the spray CFD case and the code differences, the grid is also different between these analyses. The spray CFD case was run using the octree tetrahedron grid while the other CFD case was run using the advancing front tetrahedron grid converted to polyhedral cells. In previous cases in the document, it was shown that the results from the advancing front grid and poly mesh matched data better than the standard octree grid using the same grid length scales.

The final physical parameter reviewed was the tangential velocity of the swirl flowfield. While the axial velocity field did not match well with data for the ASR tests, the tangential velocity field did in fact match well, as does the single sector unconfined rig results. This indicates that the CFD can match the swirling nature of the flowfield well, but the axial component of the velocity vector is tougher for the CFD to resolve.

4.2.5 Conclusions and Recommendations

The analysis of the three-sector confined rig and the single sector-unconfined rig provided good insight into our current capabilities to model noncombusting, swirling flowfields, as well as swirler performance in both confined and unconfined environments. The CFD results generally matched the LDV test data well, often showing good agreement in radial profiles of axial and tangential velocity. However, the CFD results indicate that there is room for improvement in modeling the central recirculation zone, especially near the swirler exit. It is interesting to note that the negative centerline axial velocity was underpredicted for the three-sector cases, but was overpredicted for the single-sector unconfined cases. This may be due to the fact that an SLS swirler was used for

the confined studies and a metal swirler was used for the unconfined studies. The metal swirler would provide a better match to what would be run in an engine. The swirler ACd was also underpredicted.

Regarding the numerous CFD studies that were executed, ***Table 4-1*** identifies the different trades performed, with recommended configurations highlighted. Characterization of a confined, swirling flowfield is best performed using an advancing front type grid converted to polyhedral elements. The advancing front grid provides better characterization of the CRZ and the ORZ, which establishes the strength of the swirl and its persistence into the burner. The polyhedral mesh provides the same level of accuracy with an additional speed-up that, coupled with the advancing front methodology, reduces the total analysis central processing unit (CPU) time by 50 percent over the baseline octree tetrahedral meshing approach. For noncombusting flows, the double precision solver does not provide any additional accuracy to the solution; therefore, it is recommended that the single precision solver be used to reduce file size and storage footprint.

Table 4-1. *Comparison Summary*

Geometry	*Comparison Title*	*Comparison Case 1*	*Comparison Case 2*
3 Sector Confined Rig	Grid Generation Technique	Octree	Advancing Front
3 Sector Confined Rig	Grid Cell Topology	Tetrahedral	Polyhedral
3 Sector Confined Rig	Floating Point Precision	Single Precision	Double Precision
Single Sector Unconfined Rig	Grid Cell Topology	Tetrahedral	Polyhedral
Single Sector Unconfined Rig	Grid Refinement Study	Baseline Grid	Refined Grid
Single Sector Unconfined Rig	Subiteration Convergence	Baseline Subiterations	Double Subiterations
Recommended Configurations			

The unconfined results illustrated the potential accuracy gains a polyhedral mesh can achieve. Unconfined flows are not nearly as controlled using geometric surfaces, so the code is allowed to more freely solve the solution, meaning code accuracy becomes paramount. The polyhedral mesh proved to be significantly more accurate than the tetrahedral mesh when compared to rig data, although both struggled with the near field swirler flow, especially in the CRZ, indicating more work will need to be done in this area. Both a grid refinement study and a convergence study were initiated, with both indicating that further generic swirler grid refinement provided little accuracy benefits and acceptable convergence levels using current time stepping. However, the one area that was not explored in detail was the characterization of the near wall region within the swirler. External airfoil studies have shown that proper characterization of the near wall region with prism layers greatly enhances the accuracy of the viscous solution. Prism layer refinement coupled with a turbulence model study could provide a path to better capturing the shear layer which drives the strength of the CRZ.

4.3 LEAN FRONT END PILOT COMPUTATIONAL FLUID DYNAMICS STUDY OF RQL GEOMETRY

4.3.1 Objective

Analyze the performance of current two passage high-shear swirlers when running fuel lean in the front end of the burner. Use existing CFD geometry from the NGPF program to perform the initial assessment.

4.3.2 Summary

A study was performed to investigate high-shear two passage swirlers in a fuel lean front end configuration. Front end equivalence ratios of 0.5, 0.6, and 0.7 were investigated and compared to the RQL baseline case. The CFD code could not properly sustain combustion for the φ_{sw} = 0.5 and 0.6 cases. As the combustion model has typically been operated in the fuel rich or stoichiometric regimes, further model development is warranted for excessively fuel lean systems. For the φ_{sw} = 0.7 case, results were quite promising. NOx levels were greatly reduced in the front end due to the dramatic decrease in combustion temperature. Temperature profiles just upstream of the quench jets indicate that the current configuration has more than adequate length to mix the combustion products. Reductions in cooling air will only continue to help the temperature uniformity at this

location. A possible concern is the slight rise in carbon monoxide (CO) due to the cooling air quenching some of the reaction before it can complete. Reduction of front end cooling, now allowable due to the decrease in combustion temperature, will help offset this. Additionally, a reduction in the front end length may be considered as an option depending on further investigation into cooling air reductions and temperature uniformity leading into the quench jets.

4.3.3 Analysis Approach

A goal of the NASA N+2 program is to investigate alternative ways to burn fuel in a gas turbine combustor to further reduce NOx, CO, and particulate emissions by employing fuel lean combustion through all stages of the burner. Traditional RQL burners use fuel rich combustion at the front end with dilution air introduced to make the entire combustor system fuel lean. This study was initiated to study how current CFD methods can be employed on a two-passage high-shear swirler operated at fuel lean conditions in the front end. The investigation applied the current CFD methodology used in RQL systems to a fuel lean system by simply reducing the fuel flowrate in the front end swirler. Existing geometry and codes were used to perform the analysis with quick turnaround and to provide a one-to-one comparison. Previous RQL geometry was used as a baseline for this effort. The fuel flow rate at the front end was decreased considerably to create a fuel equivalence ratio in the swirler (φ_{sw}) of 0.5, 0.6, and 0.7. Airflow conditions were set to the sea-level takeoff (SLTO) run conditions in the rig.

4.3.4 Analysis Details

The analysis focused on three areas: the ability of the code to ignite the fuel-air mixture and maintain combustion; the performance of the combustion process if it is maintained; and the emissions characteristics of the lean front end burn. Each of the following sections details this analysis.

4.3.4.1 Combustion Ignition

The first part of this study was to analyze the ability of the CFD code to initiate and sustain combustion at these fuel lean conditions in the front end swirler using an RQL baseline. Results indicate that the $\varphi_{sw} = 0.7$ case was able to ignite and sustain combustion, while the $\varphi_{sw} = 0.6$ and 0.5 cases did not. There is considerably less heat release in the fuel lean case as compared to the baseline case, as less fuel in the system causes total energy output to decrease for an overall lean system with approximately complete combustion.

While combustion was not sustained in the $\varphi_{sw} = 0.6$ and 0.5 cases, that does not mean that ignition did not occur followed by lean blowout (LBO). No intermediate solutions were saved, so we cannot see pictures of earlier time steps. However, several solution monitors were in place for the entire solution that were post-processed to give some visibility to the ignition process. ***Figure 4-1*** shows the burner exit monitor for CO. With CO being a radical, it will indicate if the reaction process starts but is potentially incomplete. For the $\varphi_{sw} = 0.7$ case, we can see that CO is being produced at a relatively consistent rate over the course of the solution time, indicating that the combustion process has reached a quasi-steady state. However, for the $\varphi_{sw} = 0.6$ case, there is an initial spike in the CO levels at the exit which eventually falls off to 0 by the end of the solution. This indicates that the combustion process was started but was incomplete, producing a lot of CO at the onset and reducing to zero as the combustion process is unable to sustain itself. The $\varphi_{sw} = 0.5$ case does this to a much lesser extent, indicating the likelihood that the $\varphi_{sw} = 0.5$ barely initiated combustion at all.

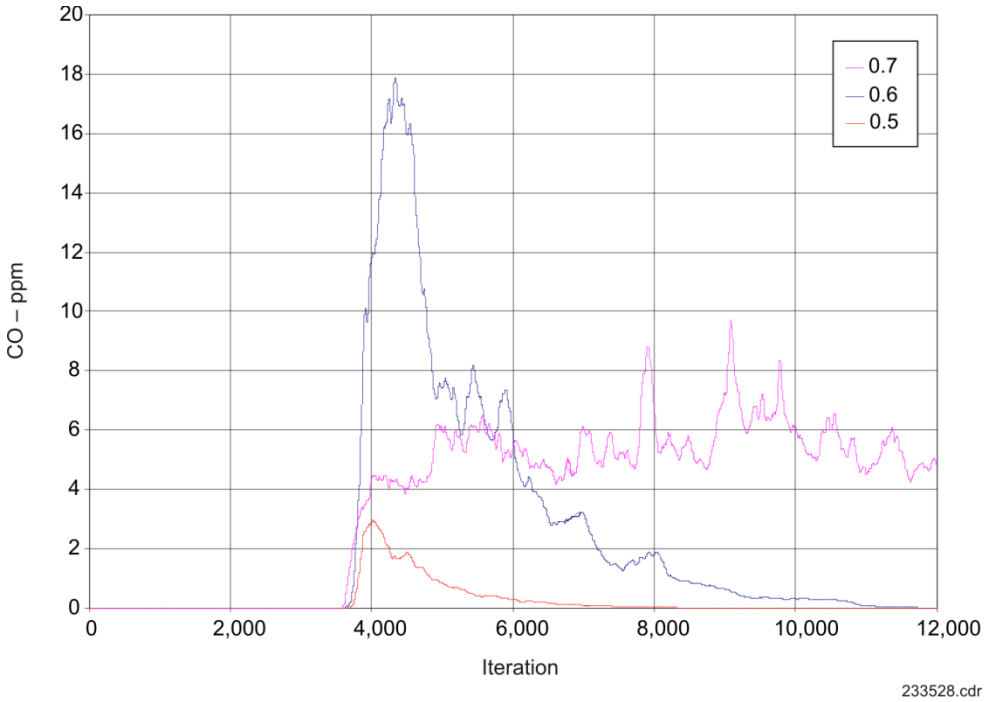

Figure 4-1. *Time History of CO at Burner Exit for Three Equivalence Ratios*

4.3.4.2 Combustion Performance

Since the φ_{sw} = 0.7 case was the only fueled case that sustained combustion, this section will only cover the combustion performance of the φ_{sw} = 0.7 case as it compares to the baseline RQL case. Several characteristics of the performance need to be evaluated: The heat release profile, fuel conservation, temperature variation just upstream of the quench holes, and exit total temperature.

The pattern of the heat release profile is interesting. The first trait observed is how the baseline case begins reacting soon after exiting the swirler and into the burner, while the φ_{sw} = 0.7 case takes longer to react. This delay in fuel ignition is likely caused by the reduced temperature of the combustion products. With a reduction in the temperature of the combustion products, it takes longer for the fuel air mixture to heat up before it ignites. Design considerations would need to be made in a fuel lean swirler redesign to account for this and to ensure proper flameholding. Additionally, in the φ_{sw} = 0.7 case, no heat release is observed as the hot front end flow is mixed with dilution air, while the baseline case has significant heat release at this point. The baseline case, being fuel rich in the front end, has excess fuel after the combustion is complete and therefore reacts with the quench flow to complete the combustion process. However, the φ_{sw} = 0.7 is fuel lean in the front end, and ideally should not have any excess fuel available at the point of impact with the quench holes. The fact that no heat release occurs when the front end flow is impacted by the dilution jets indicates the likelihood that the φ_{sw} = 0.7 completes its combustion before it reaches the quench holes.

A second measure of the combustion performance is to look at the burner exit total temperature and compare it to the expected adiabatic flame temperature at the current inlet temperature and pressure conditions and the fuel air ratio of the burner. Using the baseline case as an example, the Chemical Equilibrium and Applications (CEA) code from NASA-Glenn Research Center predicts the adiabatic flame temperature for a constant pressure combustor. ***Figure 4-2***, which shows the exit total temperature by the CFD in degrees Rankine, indicates that the CFD calculates an exit total temperature of 3,052°R, which is 99.3 percent efficiency. For the φ_{sw} = 0.7 case, CEA predicts an adiabatic flame temperature of 1,958°R while the CFD calculates an exit total temperature of 1,962°R, (this greater than 100 percent efficiency is due to numerical error of the CFD). The fact that both solutions show high combustion efficiency indicates that even in a fuel lean environment, the current swirler design completes

combustion in an acceptable length. Further modifications can be made to the swirler to continue to shorten the length of the burner front end.

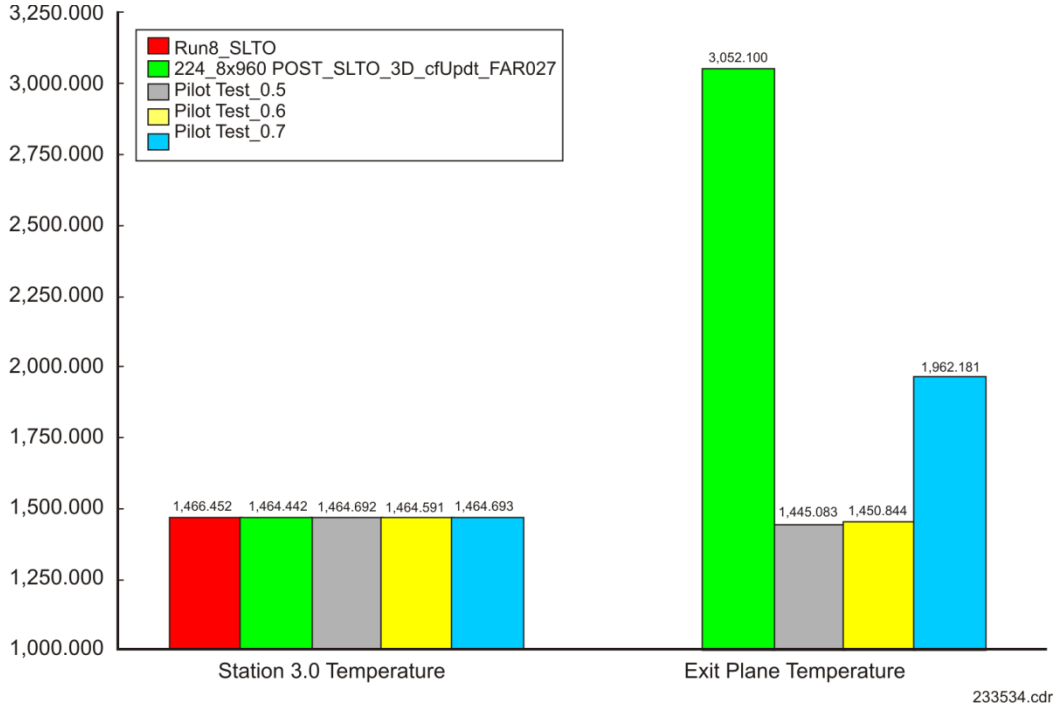

Figure 4-2. *Exit Total Temperature*

The final consideration related to combustion performance is the temperature profile in the front end of the combustor. The baseline results show a relatively hot BH wall region and a quick increase in temperature along the centerline of the swirler. The φ_{sw} = 0.7 case shows a significant decrease in BH temperature and a delay in the rise of temperature along the centerline. The delay is also indicated in the heat release profile and is expected for this current design. The decrease in BH temperature is the result of the lean burning and the combustor being overcooled for this fuel schedule. The hot combustion products mix with the panel cooling air as they recirculate back to the BH along with the BH injection. Because the φ_{sw} = 0.7 combustion products are significantly cooler due to the reduced FAR, and because the combustion products are lean instead of rich, the addition of the cooling air dramatically reduces the temperature along the walls and the BH, without causing any significant increase in combustion. Significant reductions in the cooling schedule should be considered in future designs due to the dramatic decrease in combustion product temperature.

It is also important to look at the temperature profile just upstream of the quench holes. The optimal result would be a uniform temperature profile upstream of the quench jets. Interrogation of the results shows that for the φ_{sw} = 0.7 case the temperature profile just upstream of the jets is relatively uniform. However, while the hot gas section is fairly uniform, the panel cooling air causes a significant gradient near the wall. This indicates that the reduction in cooling should help reduce this nonuniformity. Since the panel walls are likely much cooler than they need to be per the material requirements, removing cooling to enhance the temperature uniformity should be considered.

4.3.4.3 Emissions Characteristics

One of the primary goals of the fuel lean combustion system is to reduce emissions, particularly NOx and soot particulates. Because the fuel is effectively reacted in the φ_{sw} = 0.7 case, we can assume that soot levels are low. NOx and CO production are shown in ***Figures 4-7*** and ***4-8***, respectively. NOx production is greatly reduced for this fuel lean pilot swirler as compared to the baseline. This is expected as the combustion temperatures have been greatly reduced.

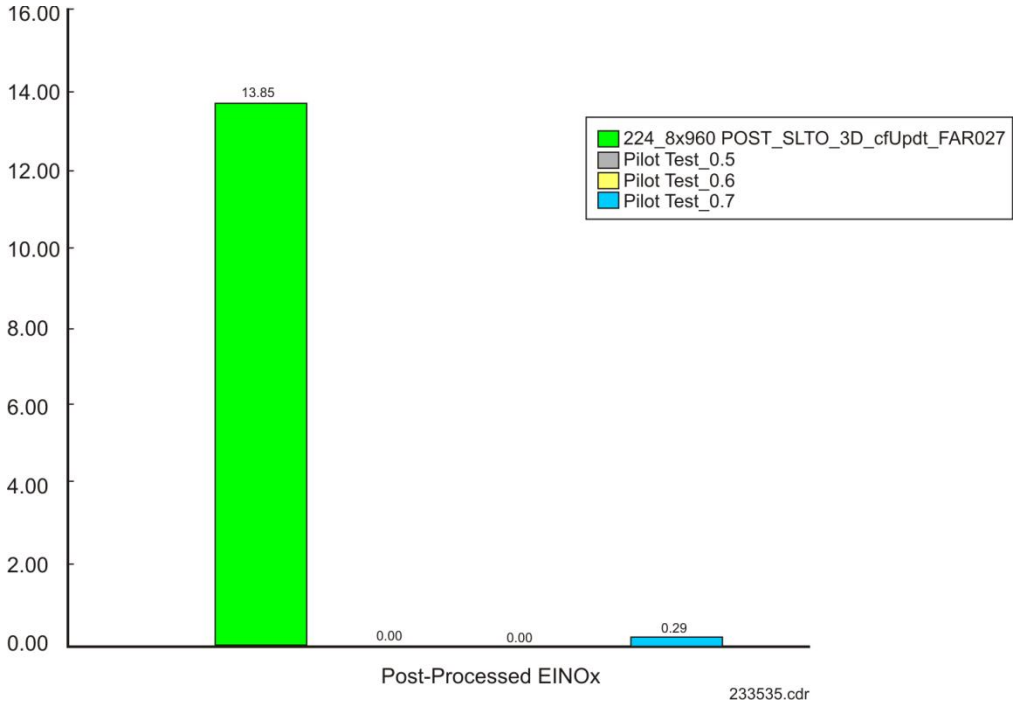

Figure 4-3. *Post-Process EINOx at Burner Exit*

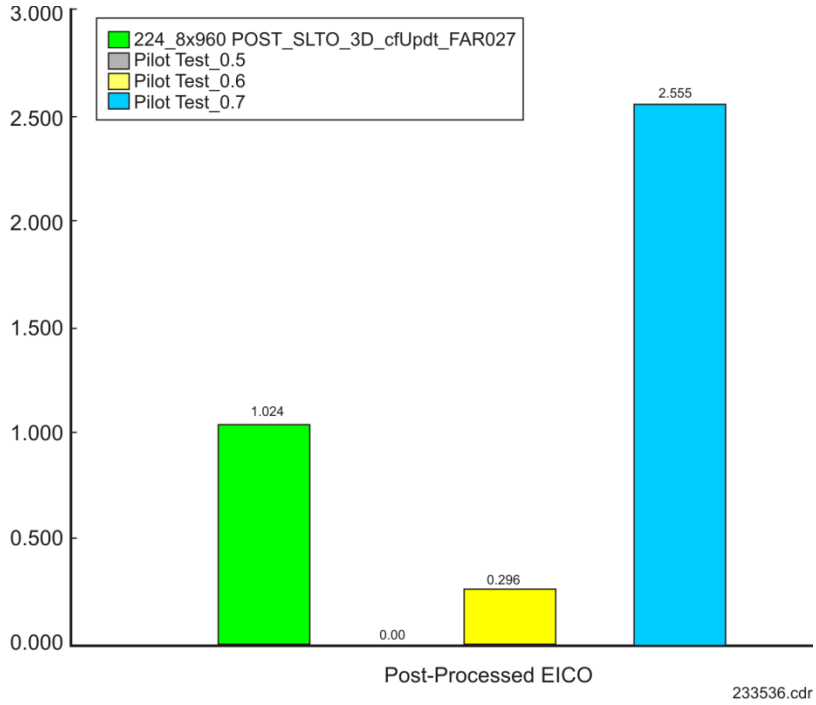

Figure 4-4. *Post-Process CO at Burner Exit*

One concern is the increase in CO levels. CO levels in the φ_{sw} = 0.7 case are 150 percent greater than the baseline case. This is likely caused by the overabundance of cooling air, which is quenching some of the reaction before it can complete. A reduction in the cooling air could likely mitigate this and allow the combustion process to complete before being quenched.

4.3.5 Conclusions/Recommendations

This study focused on the performance of the current two passage swirler when used in a locally fuel lean environment. The analysis indicates that the current design of the swirler can effectively burn the fuel air mixture at $\varphi_{sw} = 0.7$. Fuel air mixtures below $\varphi_{sw} = 0.6$ could potentially cause a decrease in combustion efficiency. The combustion efficiency with $\varphi_{sw} = 0.7$ is essentially 1.0, within the error of the code. The temperature profile just upstream of the quench holes is adequately uniform. The burner design as a whole will need reductions in cooling air and length to reach an optimum design. It is recommended that cooling be reduced first to understand mixing length requirements and the burner front end length adjusted accordingly. NOx emissions are at a low level, which is the goal of the fuel lean pilot, but CO emissions have increased. The reduction of cooling air could help to reduce the CO emissions.

4.4 MIXER DEVICE DESIGN AND PERFORMANCE FOR AXIALLY CONTROLLED STOICHIOMETRY COMBUSTORS

4.4.1 Summary

Because an axially controlled stoichiometry (ACS) combustor separates the pilot and main zones spatially, the conventional pilot can sustain combustion using traditional swirling recirculation zones, without interference from the main zone. By providing hot products to the downstream main zone, the pilot can also theoretically sustain the downstream main zone. Four small-scale fuel air mixing devices were designed, analyzed, optimized, and evaluated using cold-flow CFD. The objective was to mix the fuel and air as much as possible before the flow exits the device, or, in other words, before the flow is introduced to the hot products of the main combustion chamber. The intent of this premixing is to decrease the NOx emissions to low levels.

Each of the analyzed devices had its potential benefits and disadvantages. The first design, or the Turbulator design, proved to be highly dependent on the diameter of the fuel droplets. When the size of the fuel droplets was large, the mixing was good (due to good penetration of the fuel to the outer portion of the device). However, the fuel vaporization was poor. When the size of the fuel droplets was small, the vaporization was good but the penetration of the droplets was poor, as most of the fuel remained in the center of the device. Good mixing and fuel vaporization was only achieved when the exit velocity of the fuel (and pressure drop) was large. The second design, or the Lobed Mixer design, produced adequate mixing and vaporization when eight lobes and eight fuel injection points were employed. However, at the current scale, having eight fuel injection points would likely lead to either a fuel pressure drop that is too small, or to plugging of holes. This design may work better if a larger scale device is employed. The third design, or the Jetta-Mixer design, was not able to produce the necessary effective flow area (ACd) for the design airflow. For the final design, or the Dual-Swirler Mixer design, only the aerodynamic characteristics were analyzed without fuel flow. This analysis indicated that for future designs, the swirl direction of one of the swirlers would need to be reversed to mitigate the effects of net swirl. Another difficulty with this design is that it will likely not scale well if a larger effective flow area is necessary. This is because as the effective flow area increases, the distance between fuel injection and the exit increases, leading to possible autoignition.

4.4.1.1 Design Requirements

The design of the mixing device needs to meet several requirements. The requirements are specific to two different rig designs, the AAC test rig and the ACS arc sector rig. For the mixer designs, there is a specified pressure drop, ACd, length from fuel injection to mixer exit, and exit diameter. The intention is to mix the fuel and air as much as possible by the exit of the device. Also, it is important to reduce the size of or avoid any recirculation zones after fuel has been introduced, to limit the ability of the device to hold flame should a flashback from the main combustion chamber occur.

4.4.2 Turbulator Design

The intent of the Turbulator design was to create a design that not only mixed the fuel properly with the air, but to create a very robust design that could easily be implemented into an engine configuration. The design implemented the use of vortex generating tabs that use large eddy structures to mix the fuel and the air. The

design of the device is compact and should fit into any engine configuration along the outer diameter of the burner. The fuel injection system is also simplified into a single injector element for each device. This injector element can be sized to fit the fuel penetration needs and the turndown ratio requirements of the engine configuration.

Originally, the design was derived from the need for a low-pressure drop device. It has a high Cd while still providing good fuel-air mixing. However, the design proved hard to implement for two reasons. The exit diameter of the device was too large for the final exit diameter requirement, which had changed during the design cycle. Additionally, the large entrance diameter caused device-to-device interaction which could not be implemented into the rig. The device was resized to fit the new requirements. It is important to note that these designs are, in fact, very different from each other. The inlet is considerably smaller than the original, providing the additional drag needed to meet the ACd requirement. As further analysis would show, this actually helped out the mixing characteristics of the design.

The Turbulator concept was also designed with the intent to tune the design to specific requirements, making it scalable to different geometries in a simple way. The angle of the tabs can be adjusted to size the vertical structures to increase mixing. This feature needs to be properly balanced with designed ACd requirements and manufacturability. Additionally, the radial positioning of the tabs can be adjusted. Finally, and perhaps most importantly, the fuel injector design can be altered to deliver fuel at the best angle to enforce mixing with the large vertical structures generated by the tabs.

4.4.2.1 Turbulator Performance Analysis

The CFD analysis of the Turbulator showed that it was an adequate performer from a fuel-air mixing perspective. However, to understand its intent, it is important todiscuss the physics at play within the design. The Turbulator relies on vertical structures being generated from the tabs to mix the fuel. The design not only generates large eddy mixing, the most important feature given the short mixing length stipulated by the requirements, but small scale mixing will occur that may not be captured by the CFD analysis.

The first thing that was observed was the dependence of droplet size on the mixing characteristics of the device. There is a dramatic difference in fuel droplet penetration with just changing droplet injection size. The two droplet sizes bound the problem, but each of them has positive and negative characteristics. The larger droplet size has good penetration characteristics; however, the vaporization is poor due to the size of the droplets.

Without any secondary droplet breakup, mixing is good, but vaporization is poor because the heat required to vaporize the droplets is not present in the working fluid. As the secondary breakup model was turned on however, fuel penetration decreased dramatically, causing poor mixing performance, although 100 percent vaporization was achieved. All further analysis was performed using the secondary breakup model.

As the requirements of the rig were modified, the device had to be resized. This actually helped the mixing performance of the design due to the higher drag associated with the constrained flow environment. It soon became apparent that the injection velocity of the fuel was paramount to the performance of the devices due to the required fuel penetration. A study was initiated to determine the effect of fuel injection velocity. The minimum velocity, which was set by the initial injector design, could be increased to meet performance requirements by reducing the exit diameter of the fuel injector orifice. For the AAC rig, low, medium, and high velocities were selected for analysis. It became apparent that the fuel injection velocity plays a critical role in the mixing characteristics of the device. The effect of fuel injection velocity is less pronounced for the ACS arc sector rig condition. This is due to the much higher air velocities around the fuel injection location of the device. The high velocities cause the droplets to shear and breakup, limiting overall fuel penetration. Larger droplets would likely penetrate more, but the vaporization performance may be adversely affected. Future designs using these geometry features should optimize using fuel penetration and droplet size as two primary variables.

4.4.2.2 Turbulator Testing Analysis

While this document does not plan to go into full detail regarding the test results from the rig test series, initial rig tests were run. The Turbulator design exceeded the desired NOx emission level. This is important

because the final, as manufactured device was not able to meet the recommendations in this document. An off-the-shelf fuel injector element was not available, so a nonoptimized injector design was implemented into the rig.

4.4.3 Lobed Mixer Design

The intent of the lobed mixer design is similar to that of the Turbulator. A lobed body is placed in the center of the mixing device to produce vertical structures which induces fuel-air mixing. One important feature that is different from that of the Turbulator design is the fuel delivery system. While the Turbulator employed the use of a single simplex fuel injector element, the lobed mixer design was constrained by its diameter and could not fit such an element. Instead, a needle-like fuel injector was employed with discrete holes drilled circumferentially. Due to the fuel flow rate and desired injection velocity, rather small holes needed to be drilled (four approximately 0.015-in. injection holes). Conceptually and practically, this can be done, but there is a concern that the small hole size could lead to fuel injection problems, such as coking, which could plug the injection passage and decrease performance.

Initially, a lobed mixer with a low amount of lobes was designed. However, it soon became apparent that more lobes would be required, and a mixer with more lobes was designed. In each design case, the number of drilled holes for fuel injection coincided with the number of lobes, with the holes in line with the lobed passage. The total fuel injection area was held constant, so the injection holes for the eight-lobed mixer design needed to be reduced, which is just on the edge of manufacturability but makes fuel passage blockage by coking a higher probability.

4.4.3.1 Lobed Mixer Analysis

Like the Turbulator design, the primary mixing mechanism employed in the lobed mixer is large vertical structures that provide both large scale and small scale mixing. There are two primary differences when compared to the Turbulator: the orientation of the vortices and the relative strength of the vortex structures. While the Turbulator vertical structures have equal and opposite orientation, the lobed mixer structures are equal, but do not have opposite orientation. While not inherently bad from a mixing perspective, the result of this vortical orientation causes the structure to break down much more quickly. This can be seen at the exit of the device with the relative strength of the Turbulator being larger than that of the lobed mixer.

The design of the fuel injector allows for a much finer spray than the simplex injector element in the Turbulator design due to the smaller holes. Additionally, the fuel is injected into the cross flow, better facilitating primary and secondary break-up. Due to these injector design features, vaporization with the lobed mixer was not much of an issue. However, with the discrete injection locations, circumferential fuel air mixing becomes a point of concern. The mixer with less lobes has severe issues with overpenetration and circumferential mixing. The overpenetration was, in fact, not a product of fuel injection, but rather the lobes effectively flinging the fuel directly to the outer wall. While a reduction in the fuel injector penetration would limit this, it would not be eliminated due to the design intent of the device. It is desired that the lobed structure not produce such dramatic outward movement to the wall by reducing the angle of the lobe. Additionally, the circumferential mixing of the device was poor. To combat this, a decrease in the lobe deflection angle, an increase in the number of lobes, and coincidentally the number of fuel injection locations, was implemented into the design. This dramatically improved mixing performance, both in the radial and circumferential directions. While attractive, this design was ultimately eliminated from consideration due to concerns with the fuel orifice injection size on the center body. This design could potentially be applicable for a larger scale, where more air and fuel flow are applied. This would allow the number of fuel injection points to remain constant, while increasing the fuel orifice size and the pressure drop.

4.4.4 Jetta Mixer Design

While the Turbulator and lobed mixer designs focused on large scale vortex generation to mix the fuel air mixture, the Jetta mixer design employs the use of small-scale turbulent mixing by having high velocity airjets impinge on each other to create a turbulent flowfield. The fuel is then injected and mixed using the small-scale mixing. The fuel injector is a simplex type element that is placed along the centerline of the device.

4.4.4.1 Jetta Mixer Analysis

Inspection of the CFD results shows that the jets do collide with each other, which generates the turbulence. However, the most glaring weakness in the current design is the size of the recirculation zones, most notable along the centerline. The recirculation zones along the outer wall can be eliminated with a redesign of the cup and are not a specific concern. However, the centerline recirculation zone brings potential flameholding into play inside of the cup. While the injector used is the same size as the Turbulator design, the Jetta mixer has airflow velocities that are much higher than the Turbulator, which makes the recirculation zone around the injector tip considerably larger. Also, with the current restrictions, it was not possible to create a device with sufficiently large ACd (the ACd was below the design requirement by roughly 20 percent). This deficit in ACd, along with the increased potential for flameholding, ultimately led to the design no longer being considered for rig testing. The higher velocities had an additional adverse effect on the flowfield. The high crossflow velocities induced by the jets limited fuel penetration significantly. The fuel is not able to penetrate into the main jets and mix properly, resulting in the poor mixing characteristics.

4.4.5 Dual Swirler Design

The dual swirler design employed the use of two opposing swirl vortex generators that collide with each other and dump into the burner. The purpose is to use large-scale mixing, by using the swirl generators, and small-scale mixing, by colliding the two paths together. CFD analysis of the design was performed without fuel injection to understand the nature of the flow.

4.4.5.1 Dual Swirler Analysis

The flow enters through each swirler passage, meets in the middle, and then flows at a high velocity into the burner. The device yielded an ACd within 5 percent of the design requirement. This device has a swirl number of 0.7 at the exit of each swirler.

One of the main intents of the device was to have the two swirl devices cancel each other out, which would actually increase the drag. However, the orientation of the swirling flow from each side actually fed into each other, creating a strong swirl which dumps into the domain. The intent of the design is to have no velocity through the plane at the point of burner injection, but the swirling flow builds upon itself. If future design iterations are undergone with the same design intent, it is recommended that the orientation of one of the swirlers be flipped so that the swirling flows will cancel out and create linear flow into the burner. This should also increase the turbulence and mixing of the device. However, it is anticipated that difficulty in scaling and packaging the device may limit its implementation for future use. This is because as the effective flow area increases, the distance between fuel injection and the exit increases, leading to possible autoignition.

4.5 FIVE-SECTOR RIG PRELIMINARY COMPUTATIONAL FLUID DYNAMICS ANALYSIS

4.5.1 Objective

Study the predictive capability of the Fluent CFD code for the five-sector Talon X rig with the baseline three passage swirler. Explore the effects of changing modeling approaches, boundary conditions, grid topologies, overall fuel-air ratio, and NOx modeling processes.

4.5.2 Summary

All of the planned cases were successfully set up and executed. However, due to time and resource constraints, only the initial case was analyzed. Initial results indicate that a high-temperature central recirculation zone (CRZ) penetrates into the swirl. This has also been observed in other combustor CFD simulations with a three passage swirler. The strength of this recirculation zone is likely overpredicted as compared to the actual combustor. Also, two-passage high-shear swirler combustor CFD simulations have not observed this CRZ penetration. The velocity field of the current three passage swirler simulations is consistent with recently completed air cold-flow CFD studies of three passage swirlers with no front end cooling that were validated by LDV data collected in the rig. However, the thermal flow field has yet to be validated, so it is not yet known if the CFD predicted thermal field is accurate. An initial NOx production study was also executed on the initial case with mixed results. The model likely underpredicted the total NOx formation in the burner.

4.5.3 Analysis Approach

4.5.3.1 Geometry

The geometry setup for the five-sector rig CFD study is that of the Talon X burner with a three passage swirler. Although various swirler configurations with reduced ACd values will be tested with the five-sector combustor, only the baseline three passage swirler is currently being analyzed. The three-passage swirler is employed to enhance the mixing effectiveness of the swirler. With a more uniformly mixed front end, a richer FAR can be maintained to lower NOx production, while also producing acceptable levels of smoke.

4.5.3.2 Case Matrix, Boundary Conditions, and Analysis Execution

The baseline combustor has been tested in the UTRC jet burner test stand (JBTS). Although the actual SLTO condition cannot be achieved in this rig, the conditions were scaled using the flow parameter. These rig SLTO flow conditions were used for each of the analyses. The intent of the study was not only to quantify the emissions of the combustor at several burner FARs (three FAR conditions have been run so far), but also to explore different modeling techniques for the burner than could potentially increase accuracy and/or decrease execution time.

4.5.4 Analysis Details

4.5.4.1 Burner Results for Baseline Case

While many cases were run for use in the analysis, only the baseline case was analyzed in 2011 and will be discussed here. This section is only meant to be a preliminary analysis of the solution and not an in-depth discussion.The calculated flowfield of the baseline case was relatively consistent with results that have been observed previously, with one notable exception. The temperature contours show significant hot gases along the centerline of the swirler all the way in to the fuel tip. Initial tests of the rig did not indicate any thermal issues that normally result from the presence of hot gases inside of the swirler. To determine the cause of the presence of hot gases inside of the swirler, several solution variables were interrogated.

To verify that the presence of hot gases is physical in nature, the contour plot of FAR was generated. FAR is a measure of both the reactants and products, so a high FAR indicates the presence of fuel, whether as a reactant or as a post-reaction, hot product. These contours show a high FAR, near or above stoichiometric, along the swirler centerline and inside of the swirler, which indicates the presence of hot combustion products. Little heat release happens within the swirler, which suggests that the hot combustion products must be recirculated back into the swirler from the main burner as part of the central recirculation flameholding process.

Finally, the velocity field of the swirler was investigated. The CRZ is weaker than the main outer swirling zone. However, the strength of the CRZ is quite high in the near field region at the swirler exit. Velocity vectors indicate that a rather strong CRZ is present which pulls the hot combustion products into the swirler from the burner. This is consistent with the three-sector cold-flow SLA rig, which contained no panel or BH cooling.

To verify the performance of the burner, contour plots of combustor exit temperature and pattern factor were examined. There exists a hot spot at the exit of the burner that may require more in depth investigation. The final parameter to analyze was the combustion efficiency of the burner, which was calculated to be effectively 100 percent.

4.5.4.2 NOx Results for Baseline Case

A very low EINOx at the combustor exit was calculated. To understand how the CFD is operating, an investigation into the NOx flowfield was performed. Significant NOx is observed along the centerline of the swirler, which is also the highest temperature region of the flow. However, the most concerning observation is that a small portion of NOx appears outside of the burner region in the OD shroud. The NOx production contour plots do not show NOx produced in the OD shroud and none of the quench jet flows has any backward momentum. One of the causes of this could potentially be divergence of the NOx model. ***Figure 4-5*** shows the NOx residuals, and a sudden jump in residuals about 400 iterations into the NOx calculation indicates a potential model calculation error. However, at present, the presence of NOx outside of the burner is not physical.

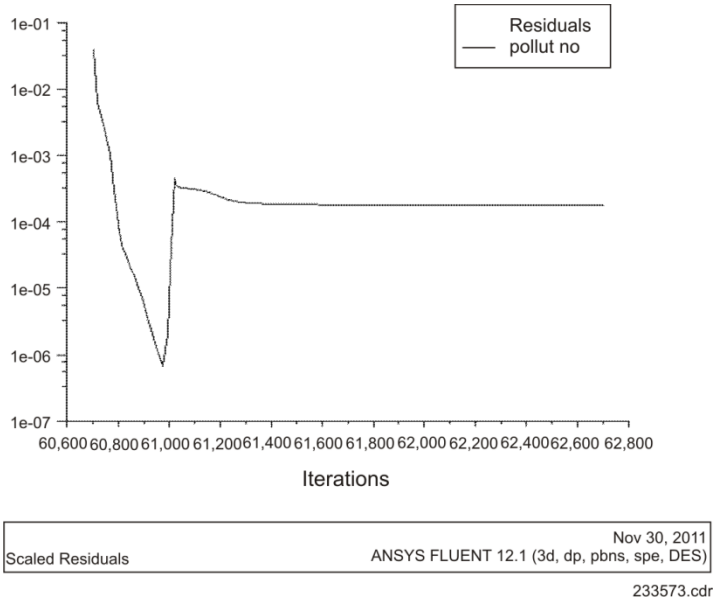

Figure 4-5. *NOx Calculation Residuals*

4.5.5 Conclusions/Recommendations

The five-sector rig Fluent CFD results indicated a similar near-swirler flowfield as previous CFD when a three passage swirler is applied. Although actual reaction in the swirler is not significant, hot combustion products are brought into the swirler by way of a stronger recirculation zone likely caused by the geometry of the three passage swirler. Although this effect may be physical in nature, the strength of the CRZ is likely overpredicted, as there are not strong signs in the engine or rig tests that hot products are impinging on the fuel nozzle tip. While the velocity field calculation is consistent with the three-sector rig CFD analysis and data, the reaction and temperature fields have yet to be validated. It is recommended that more investigative work be done to understand whether the calculated phenomenon is real and, if so, what can be done to mitigate the heat transfer effects. It is recommended that more investigation be done with respect to the NOx modeling.

5. TASK 3.2.5 — ADVANCED MATERIAL AND COOLING ENABLING TECHNOLOGY

The hot-day, takeoff engine condition of the cycle is a stringent scenario for the combustor due to high cooling air and gas temperatures. To develop a liner that is capable of withstanding this extreme environment, evaluation of a non-metallic liner (which has a higher temperature limit than the previously used metals) was completed for a fuel lean environment. Two-dimensional Cooling Analysis System for Liners (CASL) analysis was performed for the outer burner liner (OBL) and the BH.

Initial 2-D standard-work analysis was performed using the CASL, Version 2.2.16. The existing pure power engine OBL and BH models were adjusted based on a combination of pretest and data-matched boundary condition information.

Combustor fuel and airflow previously determined were used to develop the fuel-lean combustion environment used in the CASL model.

While the initial analysis goal was to keep the temperatures below material capability, a fuel lean analysis was performed to significantly reduce the air cooling necessary to maintain these material temperatures. The OBL results show that the air flow splits succeed in keeping material temperatures in the viable range. The maximum liner temperature seen is less than 15°F above the limit. This is believed to be within the error due to boundary condition uncertainties. Most importantly, at these temperatures the air cooling was reduced.

6. TASK 3.2.6 — FUEL SYSTEMS AND IMPLEMENTATION OF STAGING ENABLING TECHNOLOGY

6.1 ABSTRACT

The report presents the results and conclusions from a P&W-led N+2 staged combustor fuel system architecture study. Three contractors were supplied a statement of work (SOW) outlining the requirements for a hypothetical N+2 staged combustor. The contractors were requested to explore both system architectures and the requisite enabling technologies to make these architectures an implementable reality. The results from the study are summarized herein including a fuel systems architecture evaluation matrix and an enabling technology ranking. Architectural evaluation results show that nozzle level control systems are clearly the favorable system architecture for obtaining the stringent fuel metering accuracy and nozzle-to-nozzle variation requirements. Among the enabling technologies identified, those pertaining to high temperature electronics, distributed control systems and in-situ combustion sensors emerged as the most empowering for pursuance of the proposed architectures. The results from this study are intended to give direction to future pursuits of staged combustor architectures and research efforts into the enabling technologies required for system implementation.

6.2 STUDY OVERVIEW

The purpose of this study was to explore the spectrum of possible fuel system architecture changes and the requisite enabling technologies for an advanced staged combustion system to meet NASA N+2 engine performance goals. The objective was to seek the perspective of key suppliers within the aerospace fuel systems market on innovative ways to design a fuel system for a future combustor design that would meet N+2 program goals and to provide an evaluation of the necessary enabling technologies to make these systems possible. The P&W N+2 program goal is to demonstrate a 75 percent reduction in nitrogen-oxygen compound (NOx) emissions in a next-generation commercial geared turbo fan engine at Technology Readiness Level (TRL) 6 by 2020.

Three contractors participated in the study, individually addressing the staged engine cycle and performance metrics established in the subcontract SOW. In addition to the performance points and staging map the following system functional requirements were to be met:

- Fuel control variation capability
- Built-in test capability
- Typical commercial flow rate requirements
- Fuel types with densities specified in the subcontract SOW
- Possible pressurization pending architecture per typical commercial mission
- Fuel shut off as required
- Meet typical commercial aircraft fuel inlet pressurization requirements
- Meet typical commercial ecology requirements
- Be able to mitigate typical fuel contamination levels
- System reliability requirements — same or better than current systems
- Meet system safety requirements for fire, explosion-proofness, bladeout condition, failsafe and failsafe rate requirements
- Increased minimum bandwidth of transfer function of actual engine to requested fuel flow
- Increase overall fuel system accuracy

- Ability to control fuel flow at at each fuel
- Each manifold/stem shall be kept cooled under all conditions to avoid coking.

Overall system requirements were stipulated that the system be designed to typical commercial specifications for component life; physical envelope; vibration loading; electromagnetic interference (EMI)/electromagnetic pulse (EMP)/ lightning levels; and mean time between overhauls (MTBO) and line-replaceable unit (LRU) removal time.

The three participating contractors in the study were Hamilton Sundstrand (HS), Goodrich Engine Controls and Woodward, Inc. P&W has varying levels of engagement with each supplier and each brought a different set of expertise and experience to the program, which was manifest in their study outcomes.

6.3 STUDY RESULTS

The participating contractors proposed both zone and nozzle level (also referred to in some reports as sector level) control scenarios and identified the benefits, costs, and enabling technologies required for implementation. In general, fuel systems based around zone control architectures are more readily implementable (i.e., they require fewer enabling technologies or more near term achievable ones) while nozzle level control architectures offer lower weight increases with greater possibilities for performance improvements and novel closed loop adaptive control systems.

6.3.1 Proposed Fuel System Architectures

A schetch of a typical zone control fuel system was provided to the fuel system contractors. The key elements are the primary pump or pump system (in this case consisting of a boost pump and high-pressure vane pump), an individual zone controlling valve or other flow regulation device and distribution manifolds feeding the individual nozzles. The choice of components for each element varied by contractor but the architectural elements remained constant.

The primary benefit of this type of system is the reduced cost and complexity versus a nozzle level control system while still providing for staging capabilities and increased fuel metering accuracy over current systems. The anticipated reduced complexity is with respect to component count and does not, however, reflect the impact upon manifolds. Manifold packaging and manufacturing are significant considerations which should be taken into account when evaluating such a system. Reduced cost is presumed based upon component counts and the cost of miniaturizing pump and valve components as would be required with a nozzle level control system. Additionally, the proposed system components tended to be of higher TRL levels because the system is effectively only an incrementally more difficult system compared to the state of the art.

The negative impacts of this system are increased manifold mass and complexity (even if integrated into one body) and tighter manufacturing tolerances to ensure that the circuit flow requirements for nozzle-to-nozzle variation and overall fuel metering accuracy are met. The former of these is of greater concern due to cost implications. The ideal system would use smarter components, which may require calibration but do not require a level of high-precision manufacturing. The idea of smart components will become evident in the next system considered.

A characteristic nozzle-level control system configuration has the key elements of the primary pump module (here consisting of a boost pump and main pump), a single distribution manifold and an integrated local sector control system distributing fuel to each individual nozzle. The choice of components for each element varied by contractor but the architecture elements remained constant.

The primary benefit of this system is increased control. The ability to control individual nozzle flows opens the door for a multitude of possibilities in closed loop feedback control with the use of fuel flow measurements and combustion sensors. The latter category is a particularly empowering one and will be discussed further in Section 6.3.2, *Enabling Technologies*. Additional benefits include reduced manifold complexity and weight (with respect to zone control) and reduced wiring harness weight by locally controlling the combustor and feeding back minimal information to the full-authority digital engine control (FADEC). This local control enables what was

previously referred to as smart components. These components could be locally controlled and calibrated as a subunit to allow for lower precision (and consequently lower cost) manufacturing processes while maintaining accuracy over the life of the component due to local monitoring and adaptation.

The downside of this system is increased complexity and the challenge of miniaturization to prevent excessive weight gain and provide for feasible packaging solutions. With shrinking engine cores, particularly in the case of the geared turbofan, packaging and thermal management of the packaged solution is going to be an area requiring increased attention and research efforts.

A characteristic hybrid system architecture is made up of a main pump module, multiple distribution manifolds, complete zone flow regulation systems, and distributed localized flow regulation systems at the nozzle. The hybrid element of the system is that particular zones are selected to flow through zone-specific flow regulators to accommodate higher flow rates and the remaining zones which have lower flow requirements can flow through a common fuel line into smaller lower power flow regulating devices.

The hybrid concept attempts to marry the best of both worlds by reducing the manifold mass and complexity of a pure zone controlled system and reducing the part count of a pure nozzle level controlled system. Distributed control systems with calibrated individual models would decrease the required manufacturing tolerances for the nozzle level control elements thus decreasing manufacturing costs for those components.

The downside of this system is that it is a middle-of-the-road solution not providing either of the other system's full benefits. It is heavier than a nozzle level controlled system and more complex than a strictly zone controlled system. Additionally, all of the technological hurdles of a nozzle level control system must be overcome to implement such a solution. This means pursuing all enabling technologies for both systems. As will be demonstrated shortly, there is significant overlap in the required enabling technologies. This overlap, however, is not all encompassing over the breadth of identified enablers. Consequently a hybrid system would require the most technological development work to achieve the N+2 objectives.

6.3.2 Enabling Technologies

Implementation of the previously discussed N+2 fuel system architectures relies heavily upon the advancement of several enabling technologies. Many of these technologies were identified by multiple contractors and applied to differing system architectures. The technologies contained herein are discussed in order of significance based upon Pratt & Whitney's assessment of the technological needs for an N+2 staged combustor using feedback from the individual contractor studies.

High temperature electronics were identified as the single most important enabling technology. Specifically, electronic logic controllers and integrated circuits which can handle operating temperatures greater than 400°F are necessary for the implementation of distributed sensor and controls systems. These systems will be required to operate at areas directly surrounding the combustor. Given today's T3 temperatures this is a challenge which will only be exacerbated by the increasing T3's of the future, anticipated to be in the range of 1,300 to 1,400°F. High-temperature electronics are considered to be at TRL-2 with high potential for temperature growth on the horizon thanks to advancements in silicon on insulator (SOI) and silicon carbide (SiC) electronics. Economies of scale will be important in driving down the costs of such components but their breadth of potential applications inside and outside of the aerospace industry hold promise for significant price reductions.

Distributed controls will be integral for implementing closed loop feedback control systems, increasing sampling rates and decreasing overall wiring harness weight. Multiple contractors identified the need for local closed loop feedback control. This would allow for lower cost flow modulation devices and significantly larger manufacturing tolerances. Local control systems could also operate on a higher frequency than the FADEC itself thus improving control loop response times and a variety of trimming operations to provide for more optimal fuel control. Finally, the overall wiring harness weight could be reduced by locally concentrating both sensors and actuators and sending only a more general status report back to the FADEC. This technology is considered to be TRL-3, though it does rely on some TRL-2 technologies such as high temperature electronics or select feedback sensors.

The category of feedback sensors constitutes a key enabling technology suite. It is generalized as such because the type of feedback sensor may vary based upon the chosen system architecture or nuances of programmatic demands. Six specific types of feedback sensors were identified as having the highest potential system utility: combustion sensors (TRL-2); high bandwidth accurate flow meters (TRL-2); real-time densitometers (TRL-3); humidity sensors (TRL-3); real-time acoustic/dynamic pressure sensors (TRL-3). Combustion sensors are of interest because they would enable the most useful form of feedback, direct measurement of the combustion process or combustion results. While fuel flowrates were a frequent candidate for feedback control input within this study, the measurement of fuel-air ratio, pattern factor, temperature profiles or emissions components would be a much greater enabler. This would allow for manipulation of the fuel flow to produce actual targeted outputs instead of predicted outcomes based upon mapped fuel flow rates for given inlet conditions. This type of system was termed a *smart nozzle*. Additionally, low accuracy but high precision fuel control devices could be used thus reducing manufacturing costs. High bandwidth accurate flow meters were determined to be necessary for achieving the overall fuel metering requirements (1 percent of target flow) over the broad fuel flow range specified. Real-time densitometers were noted as key for enabling the use of alternative fuels. This would allow for calibration of volumetric fuel flow meters with changing fuel inputs which will be particularly important in the case of bio-fuels and bio-fuel derivatives due to widely varying feedstocks. Humidity sensors would allow for adjustments in the F/A to compensate for increased moisture content in the air thus improving overall engine performance in varying conditions. Real time acoustic/dynamic pressure sensors would allow for the in-situ monitoring of combustion instabilities and allow for real time instability mitigation through fuel flow shifting.

Electric main pumps were proposed for a number of the investigated system architectures. By switching to electrically driven main pumps the pump can be run at the optimal flow rate because it is decoupled from the engine speed. This provides for maximum efficiency thus allowing for minimum enthalpy gain in the fuel and minimization of temperature rises across the main pump. Additionally, the recirculation of excess pumped fuel would no longer be required thus reducing system complexity and weight. This technology is approximately at TRL-3.

Individually calibrated distributed metering modules are a subset of the *smart-nozzle* system. This technology would allow for nozzle and valve assemblies to be calibrated as a unit and controlled by a local controller (i.e., distributed controls). This in turn would provide for the lessening of manufacturing tolerances on the assembly and individual components while not compromising the system level accuracy and nozzle-to-nozzle variation. This technology is approximated to be at TRL-5.

The coking management systems presented fell into two categories: integral fuel flow paths and on-board de-oxygenation systems, both estimated to be at TRL-2. Integral fuel flowpaths include both compound manifolds and in-nozzle fuel cooling flow. On-board deoxygenation systems would reduce the fuel oxygen content to levels such that the fuel residence time and temperature path would not allow for an appreciable quantity of coke to form.

6.4 STUDY SUMMARY AND CONCLUSIONS

The P&W N+2 combustor study solicited industry feedback on the future of staged combustors from both architectural and enabling technologies standpoints. Three separate companies participated in the study bringing varying areas and degrees of expertise to the effort: Hamilton Sundstrand, Goodrich Engine Controls and Woodward, Inc. The theoretical staged combustor and a set of system constraints was presented to the contractors to work from. Each study yielded different architectural results but all provided a significant amount of overlap in the identified enabling technologies for their hypothetical systems.

Among the identified enabling technologies, the most significant of all enablers was high temperature electronics. This technology is key to distributed controls architectures, distributed measurement devices for feedback and combustion sensing technologies, all of which are also key enabling technologies. This suite of distributed controls, feedback sensors and specifically combustion sensors would allow for lower precision manufacturing methods and smart systems which self calibrate over time to ensure continued performance and

precision. Additionally, they would provide the ground work for more advanced on board diagnostics, fuel burn optimization and fleet wide learning all of which have implications well beyond the targeted fuel burn and emissions improvements typically associated with staged combustion.

Therefore, future studies on and investigations of staged combustion systems should focus on the identified key enabling technologies and their implementation into nozzle level controlled fuel systems. This will provide the highest accuracy, highest precision over life and most broadly impactful future combustor for N+2 engines, meeting the 75 percent NOx reduction goals while also improving combustor life, fuel burn, increasing overall system control and accelerating learning from in service engines. With the level of overlap between zone control and nozzle level control enabling technologies, the pursuance of the identified technologies will also enable better zone control systems, where they to emerge as a favorable architecture for a particular application.

7. TASK 3.2.7 — COMBUSTOR DYNAMICS ENABLING TECHNOLOGY

7.1 TASK 3.2.7: ENABLING TECHNOLOGIES: COMBUSTOR DYNAMICS

Under NASA's Environmentally Responsible Aviation (ERA) funding, P&W and UTRC are developing advanced combustor concepts to achieve very rapid uniform mixing of fuel and air to reduce LTO NOx emissions and meet or exceed the N+2 emissions goals. While these concepts will enable low NOx emissions, they may also have negative consequences for an engine. Lean, premixed combustion systems have historically encountered combustion instabilities, resulting in hardware damage and increased noise and vibration.

Classical modeling of combustion instabilities has focused on using a feedback based dynamic system to capture the interaction between the unsteady heat release (UHR) and acoustics. This approach has been widely used, since no single tool exists to simultaneously solve the coupled acoustics and heat release problem for a relevant sized combustor. With advances in CFD, this coupled capability will be realized in the future, but a dynamic system approach will be the most practical technique used in the near term. CFD in the form of LES can play a more immediate role in advancing the sophistication of UHR models. Recent application of LES codes with boundary condition forcing has been used to capture more complex unsteady flowfields.

The current effort is focused on using the best submodels available and exercising them in a system model construct recently developed for aeroengine combustors. The system model construct uses high-fidelity tools to calculate the acoustic modes and UHR field for use in a stability analysis. The acoustic modes are calculated using a proprietary 3-D finite element solver (AC3D).

An LES CFD solution is used to obtain the UHR. Over time, three different models (Gen 1, Gen 2, and Gen 3) have been developed to calculate an unsteady heat release from a resolved CFD solu-

Using the tools outlined above, the overall objective is to make a qualitative stability comparison of two low-emissions combustor designs being developed in the ERA program and compare these stability predictions with results from the AAC rig. The two designs being analyzed include the CRESS and ACS. Ultimately, the downselected design will be chosen based on more critical criteria such as performance, emissions, manufacturability, etc, but this exercise will provide a comparison of each design's propensity for combustion dynamics. Of course, many caveats must be recognized in such an analysis; most significantly, that the comparison of these designs will be based on a single operating point, and thus do not provide any insight into how stable these designs will be over a wide range of conditions.

As part of this effort various submodels will be verified. Through AAC rig testing the acoustic mode prediction from AC3D can be verified using and array of high-speed pressure transducers. Using the rig's optical access and high-speed imaging, qualitative comparisons can be made between the UHR calculated from CFD and imaged from the rig. Another important submodel is the AtoMIST spray model which is incorporated into the CFD using a user-defined function (UDF). Since the spray dynamics are important to the UHR, a significant effort was placed on verifying the dynamics of the spray. Ambient spray measurements were made and compared to forced CFD with AtoMIST to determine the quality of the spray model.

The remainder of the combustor dynamics section will focus on the details of sub-model verification and stability comparisons of the CRESS and CR-ACS designs. Section 7.2, *Forced Spray Experiments and Model Verification* discusses the verification of the AtoMIST spray model with ASR results as well as the physical interpretation of these results. Section 7.3, *Exercising of Combustion Dynamics System Model* will provide details on the various component models (UHR-Forced CFD, Acoustics-AC3D, Stability Analysis-LSA) used in generating the system stability analysis for the CRESS and ACS designs.

7.2 FORCED SPRAY EXPERIMENTS AND MODEL VERIFICATION

The primary objective of the forced spray measurements was to provide data for verifying the CFD-based spray submodel AtoMIST. Of equal importance was using the experiments and CFD to investigate the effects of air flow forcing on fuel spray characteristics for premixing swirlers. How the fuel and air interact in a forced environment can provide important information for understanding combustion dynamics.

7.2.1 Experimental Investigation

Experimental measurements were performed using phase-locked PDI on three different swirler/mixer designs, CRESS, PICS, and CR-ACS. Point wise PDI measurements provided droplet velocity and size information. Data taken at multiple spatial locations provided an overall spray velocity and droplet size distribution. With postprocessing of the basic data both fuel spray mass flow rate fluctuations and fuel/air ratio fluctuations were calculated.

The experiments were conducted at ambient temperature and pressure. This does not correspond to actual aeroengine operating conditions, but spray tests at actual operating conditions are very difficult to execute and have numerous safety implications due to the risk of autoignition.

7.2.2 Development of Experimental Setup and Postprocessing Procedure

The PDI measurements were carried out by a two-channel laser (532 nm and 660 nm), receiver, and processing system (Artium). This instrument was used to measure droplet size, axial droplet velocity, and tangential droplet velocity. It was assumed that the smallest droplets, less than 15 µm, seamlessly tracked the gas-phase velocity. The spatial scanning of the PDI measurement was achieved by moving the plenum using a three-axis stepper motor. A large number of realizations (droplets) were measured at each spatial location to ensure that the statistics of phase-averaged measurements were adequate. The droplet size and velocity information collected by the PDI system was post-processed by an in-house Matlab code.

Figure 7-1 briefly depicts the post-processing required for calculating the phase-averaged fuel mass flow and FAR fluctuations from the PDI size and velocity data.

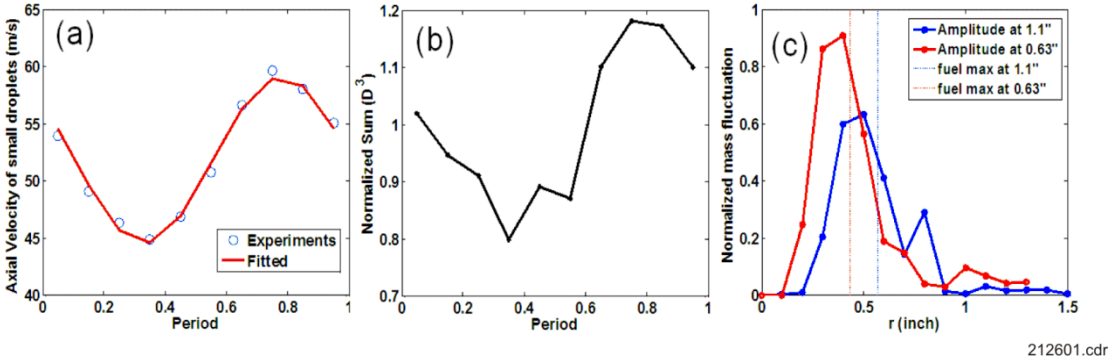

Figure 7-1. *Postprocessing Required for Calculating Phase-Averaged Fuel Mass Flow and FAR Fluctuations*

The result was then mean-scaled, eliminating an intrinsic disadvantage of PDI-based volume flux measurement, the rejection of nonspherical and/or concomitantly captured droplets, by replacing the mean mass flow from PDI with that of the more robust patternation measurement. It should be noted, though, that the fluctuating component of the mass flowrate still relies on the phase averaged PDI measurement.

As a final step, the dimensional mass flow rate is renormalized such that one can make a fair comparison between two injector designs with differing flow rates. Each set of the phase-locked data at specific locations was then fitted with a sinusoid to determine the phase and amplitude of the fluctuation. The resulting amplitude was then plotted as a function of radius at a specific axial plane (See ***Figure 7-1c***).

A similar procedure was applied to investigate FAR fluctuations.

7.2.3 Results

In this section, the experimental comparison of CRESS and PICS results will be described, followed by CR-ACS results.

Figure 7-2 shows the radial profile of mean axial air velocity and fuel mass flux for both designs while the fluctuating component of the air velocity is shown by the blue bars. These plots show closer alignment of the fuel

and air flux profiles for the CRESS (left) than for the PICS (right). The close alignment is normally beneficial for low emissions since it indicates better fuel/air mixing at this plane. It is also worthwhile to note that the maximum air velocity fluctuations occurred at or near the peak of the mean velocity profile.

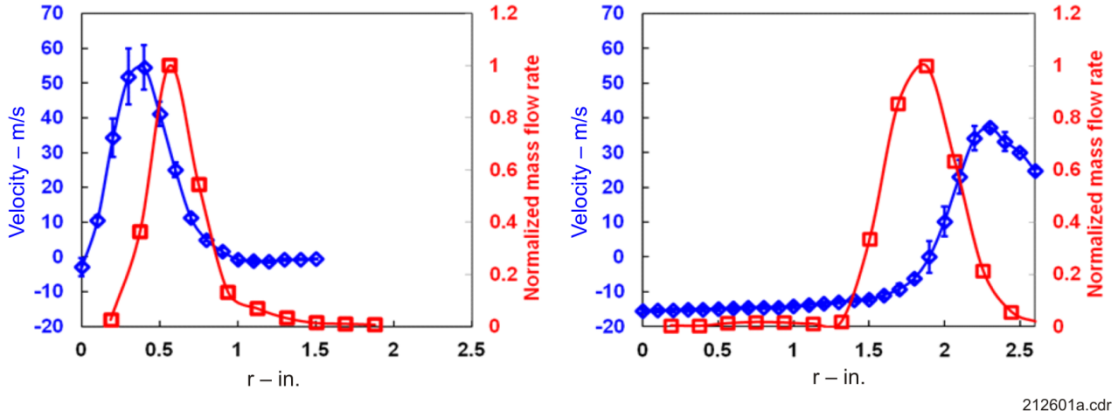

Figure 7-2. *Air Velocity Profiles and Normalized Fuel Mass Flowrate*

There are two main fuel preparation mechanisms that can lead to thermoacoustic coupling in these types mixers. Acoustic forcing can lead to a time-varying delivery of fuel to the flame zone, thus modulating the FAR. This can occur either as a result of varying droplet size and/or varying droplet velocity, which is out of phase with the air fluctuations. Alternately, if the air and fuel fluctuate nearly in phase, the FAR will remain relatively steady, but the overall mass flowrate will fluctuate. In this context, analysis of the droplet size distributions followed by mass and FAR fluctuations will be discussed in the following sections.

Figure 7-3 shows the mean droplet diameter profiles along a radius for steady-flow (red) and forced-flow (blue) for both swirlers. The location of the peak fuel mass flux is also indicated (black dotted lines) on the plot. The unsteady (phase-averaged) variation in droplet size is shown by the blue bars. For both designs, the droplet size difference between the steady and the forced cases is minimal and the fluctuating component of the droplet size was small compared to the mean value. This result indicates that acoustic air forcing does not significantly change the primary atomization process, thus droplet size fluctuations is not likely a key contributor to combustion dynamics. It may be noteworthy that the steady droplet size produced by the PICS near the peak fuel mass flux location was significantly larger than that for the CRESS.

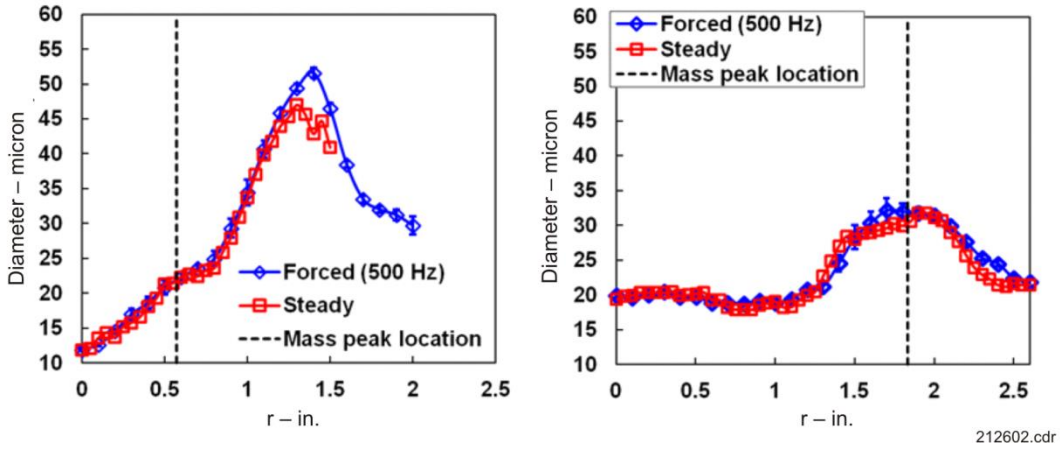

Figure 7-3. *Mean Droplet Diameter Profiles Along a Radius of CRESS and PICS*

Figure 7-4 shows the fluctuation amplitudes of normalized fuel mass flowrate and FAR of CRESS and PICS. Again, the dotted vertical line represents the location of the peak in steady fuel mass flow. The most interesting

observation from the figure is the fact that the fluctuation amplitudes of both fuel mass flowrate and FAR were higher in CRESS than those of PICS. However, the relative location between the peak in steady fuel mass flowrate and these peaks should be considered to correctly quantify the overall dynamic characteristics. For example, the high FAR peak for the CRESS may not cause a significant level of FAR induced acoustic coupling because it is so far away from the peak in fuel mass flow rate that only a small amount of fuel flow passes through that region. On the other hand, the location of high fuel mass flowrate fluctuation in the CRESS could have a significant impact on combustion dynamics since it peaks close to the fuel mass peak.

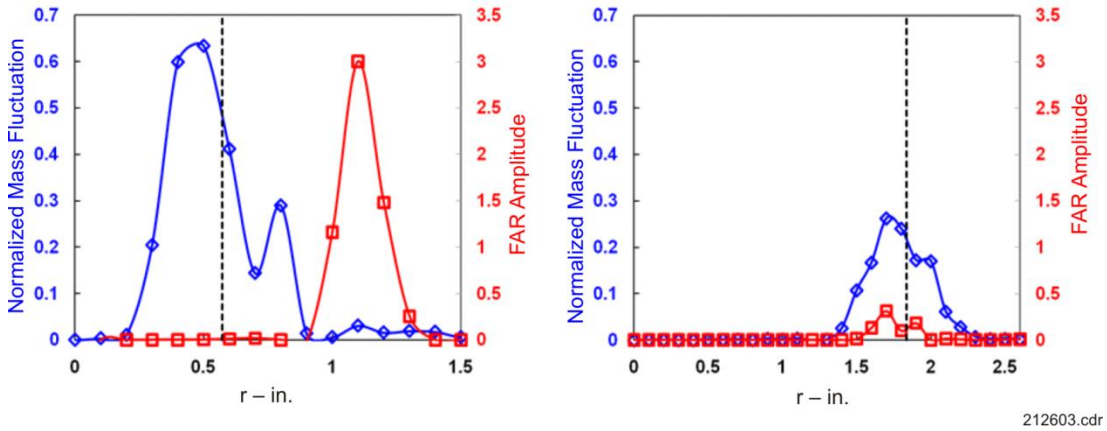

Figure 7-4. *Normalized Fuel Mass Fluctuation Amplitude and FAR Fluctuation Amplitude Profiles*

In summary, the close alignment of the fuel and air flux profiles in the CRESS, along with the smaller droplets created by that device, led to a strong fuel mass flow response to the acoustic forcing. In the PICS, where the droplets were larger and the profiles exhibited poorer mixing, there was a stronger tendency for FAR variations in response to the acoustic forcing.

To generalize the previous observation, it was hypothesized that a swirler whose fuel flux and air flux profiles are closely aligned, and whose fuel droplet diameter is small, will have the propensity for high mass flowrate fluctuations. It should be expected that, if either of these conditions is not met (i.e., the droplets are too large to track the air velocity oscillations or the fuel flux and air flux profiles are not well aligned), then the flow will exhibit larger FAR fluctuations and smaller fuel mass flowrate fluctuations.

To be more quantitative, a brief analysis was carried out to compare the droplet behavior in oscillating air flows for conditions representative of the CRESS and PICS designs. In this particular analysis, the droplet and fluid velocities and the corresponding droplet diameter distributions have been collected at a spatial location which corresponds to the peak mass flow in ***Figure 7-2***; and in a specific temporal phase which gives the maximum phase averaged air velocity in the specific spatial locations.

Figure 7-5 shows a histogram of diameter, d_i, (blue) and average velocity ($U_{o,i}$) of the diameter bin i (green) for CRESS (left) and PICS (right) at the specific spatial location and the phase described above. Regardless of droplet class, it is clear that the U_p is not a profile of real droplets, but it may practically represent the behavior of a collection of droplets.

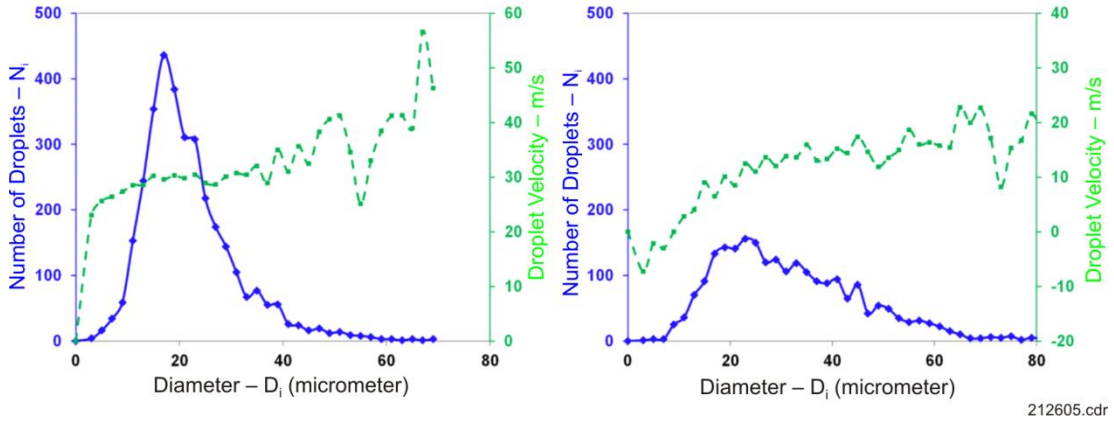

Figure 7-5. *Histogram of Droplet Size and Corresponding Averaged Droplet Velocity of CRESS and PICS*

In ***Figure 7-6***, the time series of U_p (black) and air velocity are compared for CRESS (left) and PICS (right). As expected from the larger droplet sizes of PICS, the amplitude ratio of droplet velocity to the air velocity in the case of PICS was significantly smaller than that of CRESS. Also, the characteristic time required for the droplets to track the airflow is much longer for the PICS compared to the CRESS. The practical result of this is that the droplets from the CRESS were smaller, and therefore responded more quickly to air velocity oscillation. Conversely, the larger PICS droplets responded slower to air oscillations.

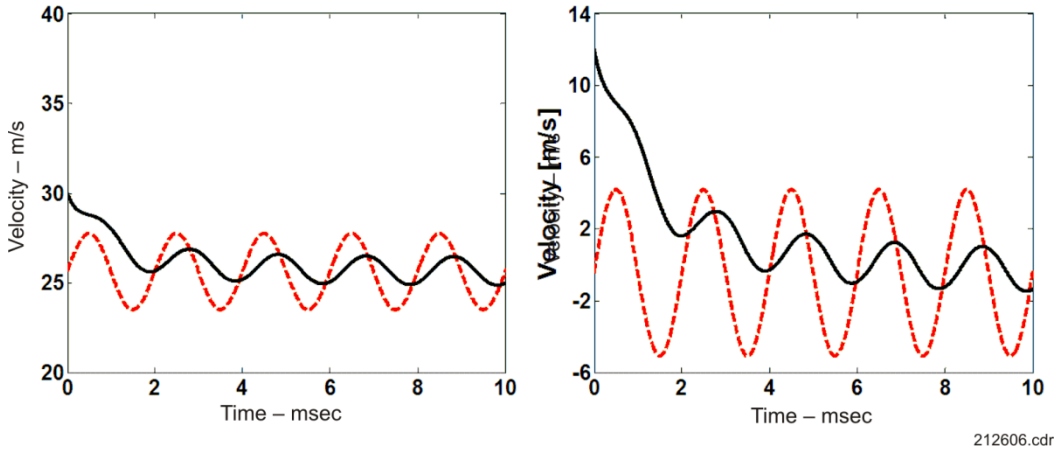

Figure 7-6. *Droplet Velocity Profiles in Oscillating Airflows of CRESS and PICS*

This simplified analysis does not capture the complexity of the swirler geometry or two-way momentum coupling between the fuel and airflow. The numerical investigation to follow will provide some insight into some of these complexities.

Identical measurements and postprocessing were carried out for the CR-ACS swirler design, with results summarized in ***Figure 7-7***. In the top row, velocities and their amplitudes for different droplet size classes are shown. The peak velocities are higher than those of CRESS and PICS even though the pressure drop across the swirlers is identical. It is interesting that the velocity fluctuation level is lower than that of CRESS or PICS (see ***Figure 7-2***) despite the high velocity. The lower velocity fluctuation could be due to the smaller ACd, which reduces the amount of acoustic energy transmitted from the upstream plenum compared with the CRESS and PICS.

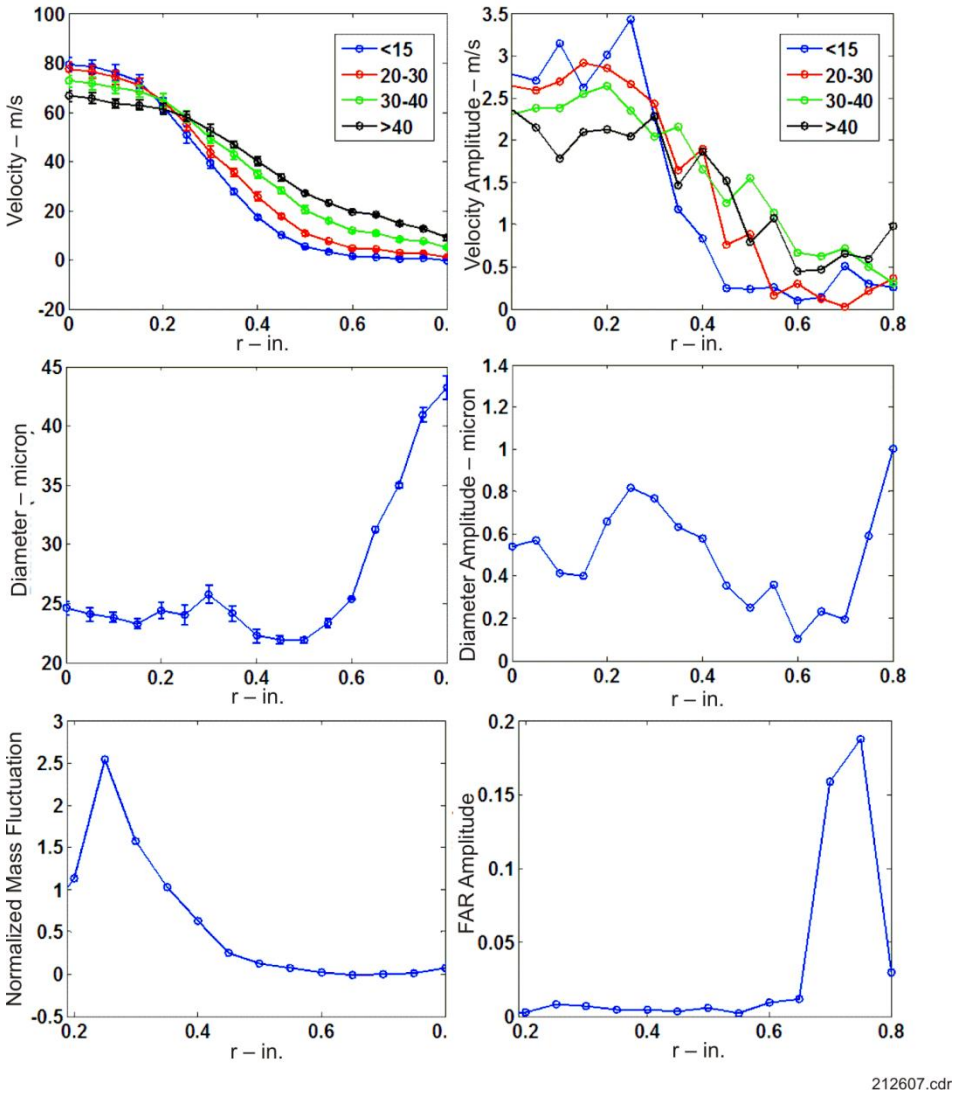

Figure 7-7. *Forced Spray Characteristics of CR-ACS Swirler*

Mean and fluctuating droplet diameter values are consistent with those observed for the CRESS and PICS, again implying that primary breakup of fuel is not significantly affected by the air forcing.

The peak normalized fuel mass fluctuation level is considerably higher than the CRESS, even though the droplet diameter of CR-ACS is larger than that of CRESS. This may seem inconsistent with the argument developed earlier that attempted to show that smaller droplets induce higher mass flowrate fluctuations. The inconsistency is explained as follows:

- Relative to CRESS and PICS, the flow from the CR-ACS swirler is quite localized due to the swirl design. Therefore, the total amount of fluctuation from the CR-ACS should be lower than the peak level of fluctuation. In other words, the ratio of peak values of CR-ACS to CRESS is very high, but the ratio of the total mass fluctuation is lower.
- Relative to the CRESS and PICS, there is less damping due to the limited amount of entrained air which is again a result of the swirl design.
- The integrated fuel flow rate of the CR-ACS swirler is significantly lower than those of the CRESS and PICS, thus amplifying any fluctuations in an absolute sense.

Therefore, the resulting *normalized* mass fluctuation level of CR-ACS plotted in ***Figure 7-7*** must be more exaggerated than those of CRESS and PICS. Meanwhile, the FAR amplitude shown in ***Figure 7-7***, bottom right, is lower than that of PICS and slightly higher than that of CRESS. This is consistent with the hypothesis.

In summary the experiments demonstrated the following:

- Acoustic air forcing did not significantly change the primary atomization process, but did influence the unsteady transport of fuel droplets within the swirler flowfield.
- The level of fuel mass flow fluctuation was approximately two times higher for CRESS than for PICS.
- The level of FAR fluctuations for CRESS was negligible while PICS had significant fluctuations.
- The CR-ACS swirler showed discrepant behavior due to its smaller size, lower fuel flow rate, and swirl design. The CR-ACS showed higher mean velocity, lower velocity fluctuation, higher mass flow fluctuation and lower FAR fluctuation compared to CRESS and PICS.

7.2.4 Numerical Investigation and Comparison

CFD simulations were performed using Fluent with the UTRC spray model AtoMIST as a UDF. The modeling objective was to understand how well AtoMIST captured the liquid fuel breakup and atomization process in a forced airflow. Due to the sequencing of development for various low emissions fuel injector designs, only the CRESS and PICS were evaluated in the forced CFD study. Given that the verification data was being generated from an ambient spray rig, only ambient conditions were considered in the CFD analysis. Conditions used for the CFD calculations were set to match the experimental tests discussed in the previous section. After using the ambient condition cases to verifying AtoMIST, the goal was to apply AtoMIST in calculations at engine relevant conditions.

7.2.5 Computational Fluid Dynamics Modeling Approach

LES was used in Fluent with the TAB secondary breakup model. Two-way coupling was selected in Fluent to interact with the particle dynamics. AtoMIST models the primary breakup of liquid fuel including column breakup, surface stripping, film formation, and breakup from a filming surface. A description of AtoMIST can be found in the document Arienti, M. and Soteriou, M., "Dynamics of Pulsed Jet In Crossflow," Proceedings of GT2007, GT2007-27816, Presented at the ASME Turbo Expo, May 14–17, 2007, Montreal, Canada. For the steady case, constant mass flowrate boundary conditions were used for both air and fuel. For the forced case, the air inlet was forced with a sinusoid function. The forcing magnitude and frequency were consistent with the ambient spray experiments. Fuel mass flowrate was kept constant.

Forced CFD results were compared with corresponding experiments in terms of air velocity, particle velocity, fuel mass as well as particle size distribution at fixed distances downstream of the swirler exit. For the CRESS, two sampling planes were chosen, downstream of the swirler exit. For the PICS, sampling was only done on a single downstream plane.

7.2.6 Postprocessing Tool Development

In this section, the fundamental analysis technique and methodologies will be discussed first. Representative CFD results and comparison with experimental data will then be discussed and interpreted with gaps identified.

There were 17 cycles of data saved for CRESS, and 25 cycles of data for PICS.

Monitors are internal Fluent calculations that show a real time record of various quantities during the CFD execution. They provide a way of checking intermediate results before the entire solution has been completed. ***Figure 7-8*** shows the times series and corresponding least squares fit (LSF) of mass flowrate and velocity at the inlet boundary and the swirler exit of the CRESS case. Given that the inlet mass flowrate is being forced, the time series is a smooth sinusoid, whereas noise is a component of the time series at other locations.

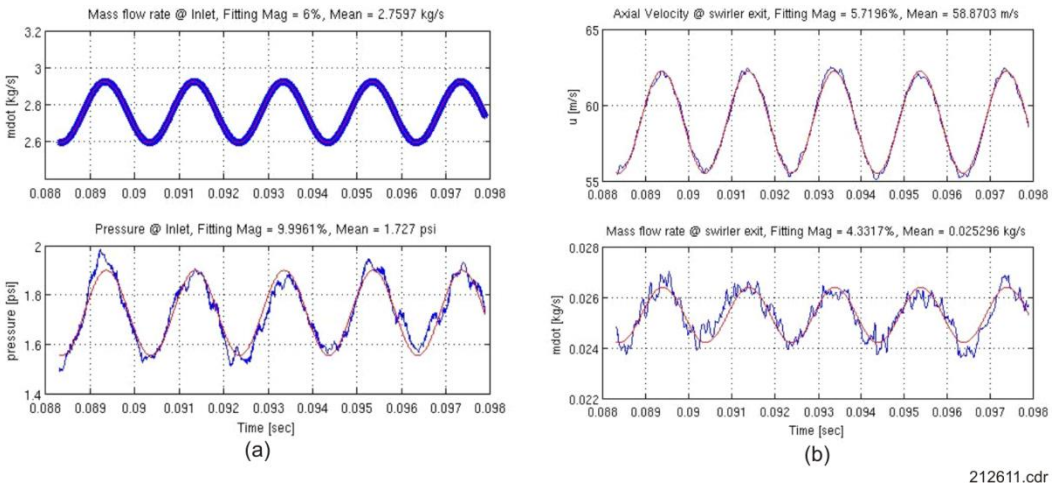

Figure 7-8. *Monitor Date With Sinusoidal LSF Fitting*

For extraction of gas phase information (i.e., air velocity) at various sampling planes, a Fortran program was written to read the saved files and calculate various quantities. An example of a calculated quantity would be the axial velocity profiles (radially or azimuthally distributed) as function of time on the sampling planes. Once axial velocity profiles were obtained, the response magnitude (i.e., fluctuating component) of the air velocity to the forcing frequency at different radial locations was determined by either an LSF or a fast Fourier transform (FFT). The LSF and FFT were calculated in Matlab. ***Figure 7-9*** shows the axial velocity at two radial locations as a function of time obtained from postprocessing files and then performed a sinusoidal LSF and an FFT. The result from FFT indicates a dominant forcing frequency at both radial locations. Expanding this postprocessing technique for all radial locations generates the same form of results as that extracted from the experiment (i.e., velocity as a function of radius). As an example, ***Figure 7-10*** shows the mean axial velocity and its response magnitude as a function of radius at the downstream planes.

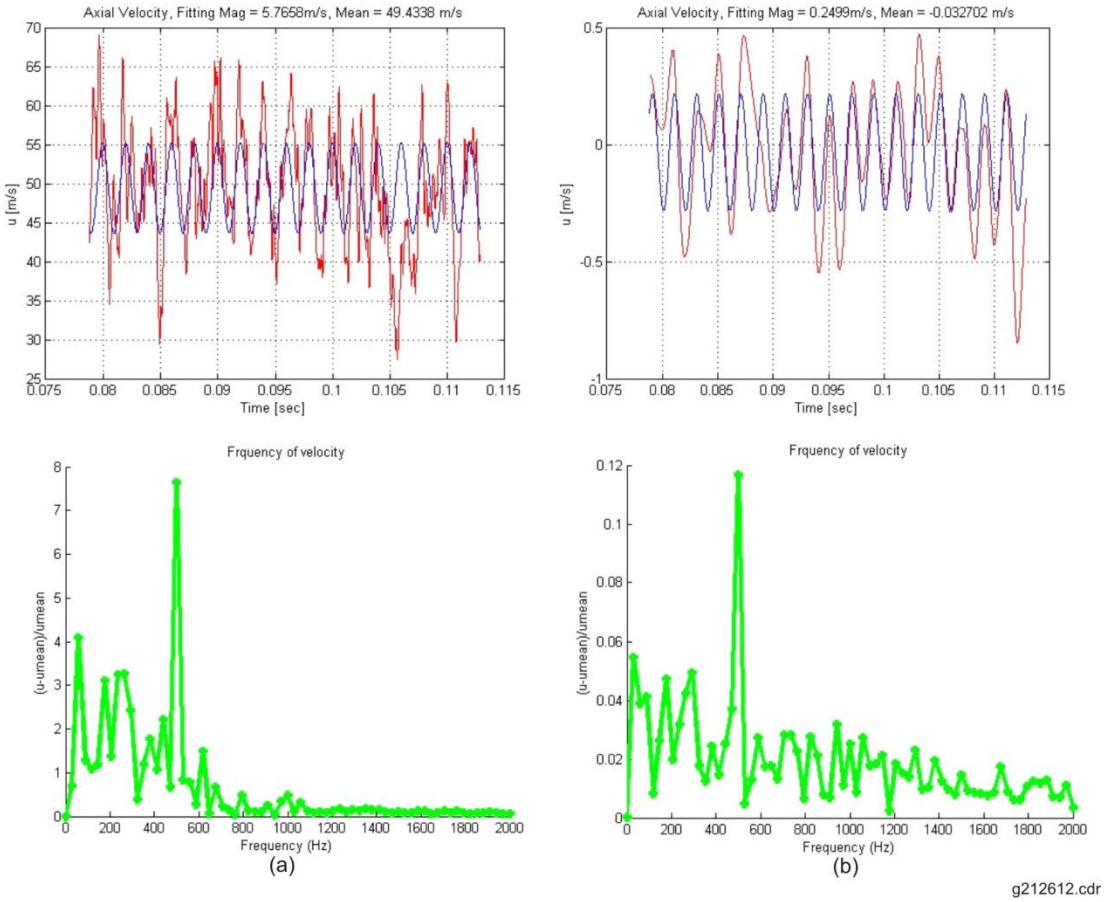

Figure 7-9. *Gas Phase Axial Velocity*

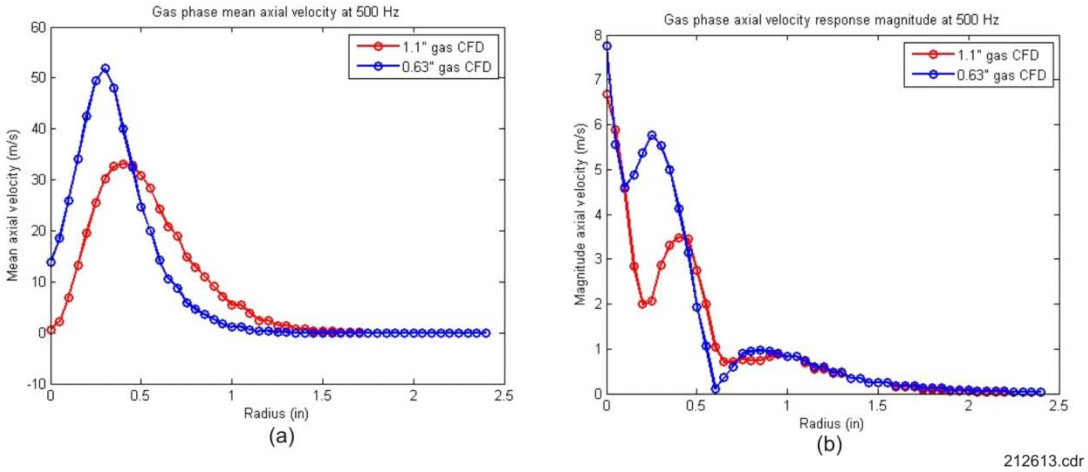

Figure 7-10. *Mean Axial Velocity and Response Magnitude as a Function of Radius Downstream Planes*

Similarly, for spray and particle postprocessing, a Matlab script was used to obtain the particle velocities, fuel mass, and particle diameter radial profiles as a function of time. Then, using the LSF or FFT techniques created for gas phase postprocessing, the spray and particle response (i.e., fluctuating component) to forcing could be calculated at different radial locations. ***Figure 7-11*** shows spray mass and its response magnitude forcing as a function of radius at both of the downstream sampling planes.

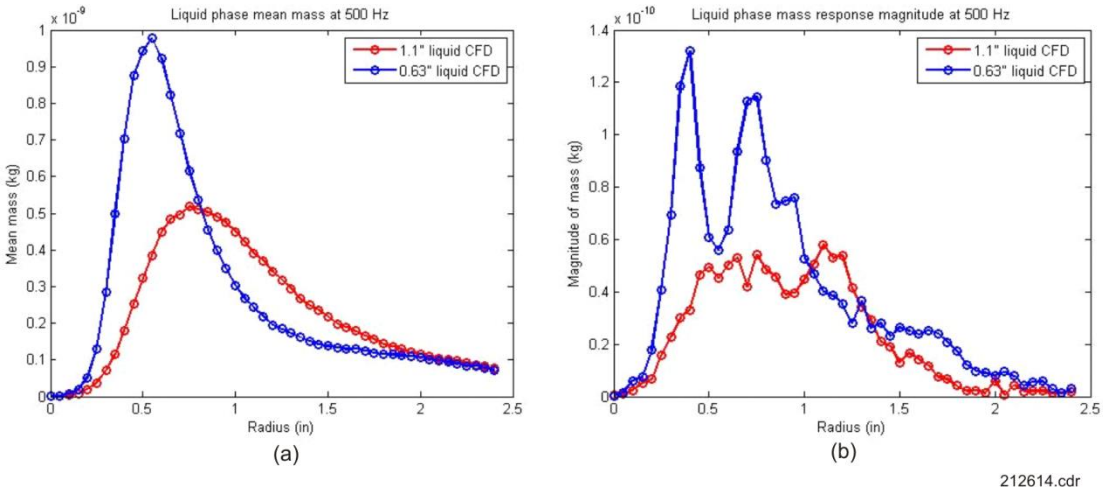

Figure 7-11. *Mean Spray Mass and Response Magnitude of Spray Mass Response Forcing*

Once the gas (air) velocity and spray mass were obtained as a function of time at different radial locations, the FAR could be calculated. To maintain consistency with the experiment, the FAR was defined as the fuel mass divided by the air velocity. The difference in the experiment is that the two quantities are calculated differently.

Figure 7-12 shows the FAR response to forcing at the downstream planes. When compared to the experimental data, the maximum response is normalized so that it matches the maximum response of the experiment. It should be noted that the peaks outside of the 1.5-in. radius are not meaningful because of the sparse amount of fuel in that region.

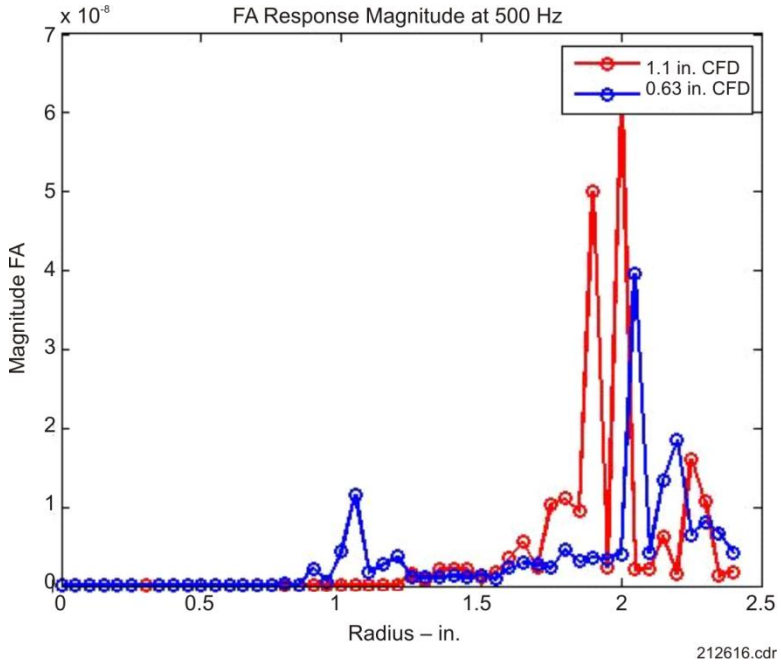

Figure 7-12. *Magnitude of FAR Response to Forcing at Downstream Planes of CRESS*

7.2.7 Comparison of Computational Fluid Dynamics With Experimental Data

Based on the postprocessing methodologies discussed above, ***Figures 7-13*** through ***7-19*** show comparisons between CFD and experimental results for the downstream planes of CRESS, and for PICS. Comparisons are made in terms of mean and fluctuating magnitude of gas phase (air) velocity, spray mass, and fuel-to-air ratio.

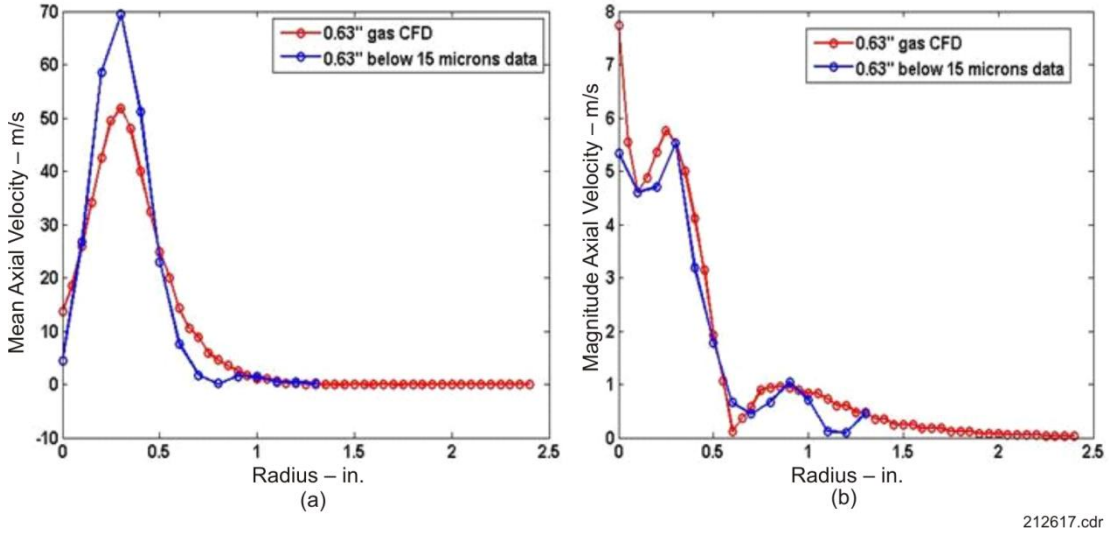

***Figure 7-13**. Mean Axial Velocity and Magnitude of Fluctuation as a Function of Radius, CRESS*

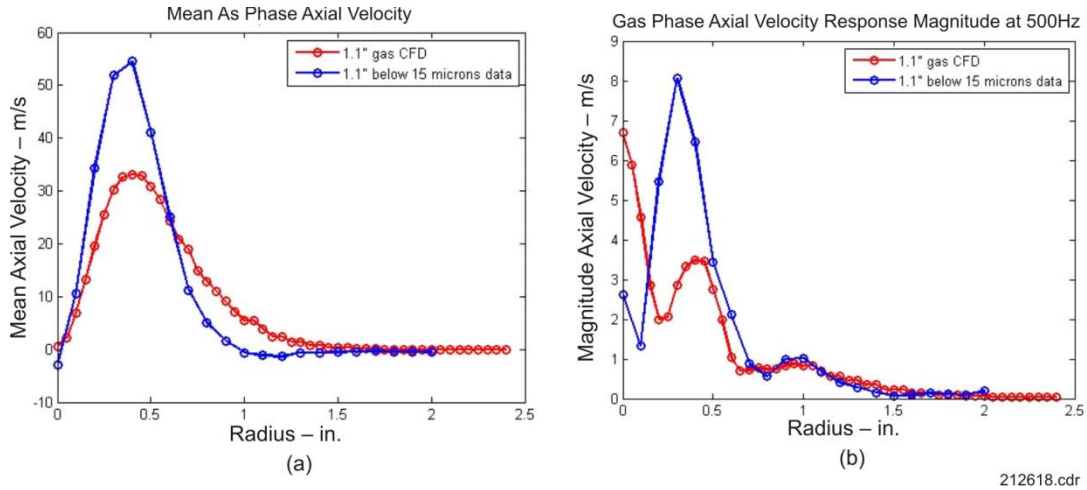

***Figure 7-14**. Mean Axial Velocity and Magnitude of Fluctuation as a Function of Radius, CRESS*

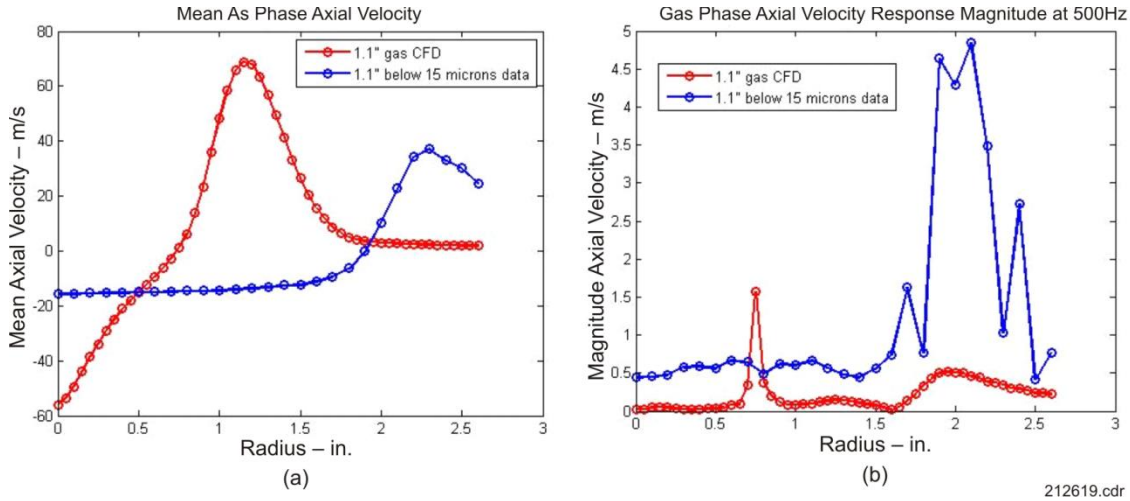

***Figure 7-15.** Mean Axial Velocity and Magnitude of Fluctuation, PICS*

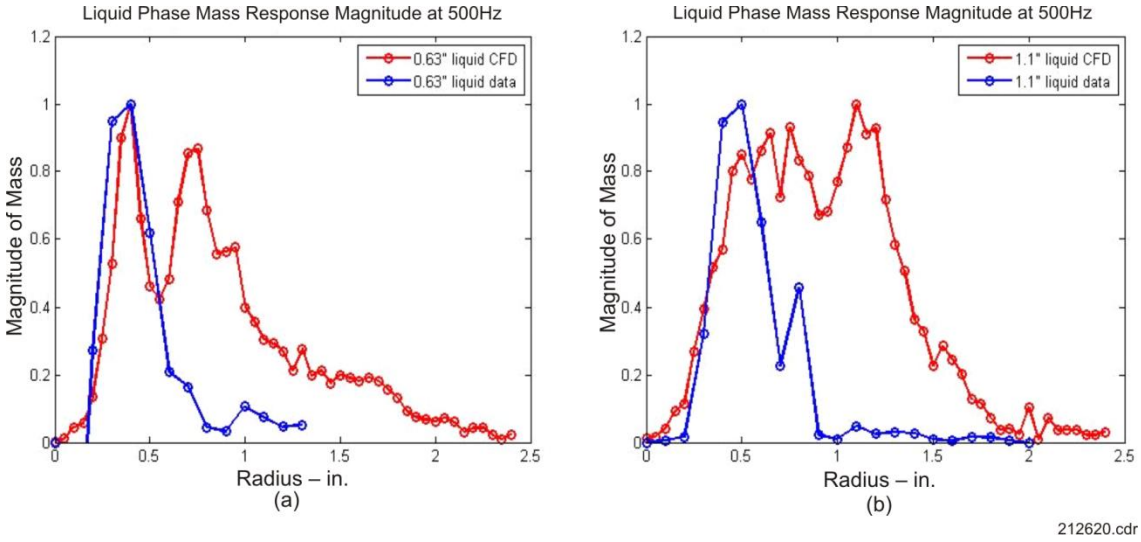

Figure 7-16. *Magnitude of Fluctuation of Fuel (Particle) Mass, CRESS*

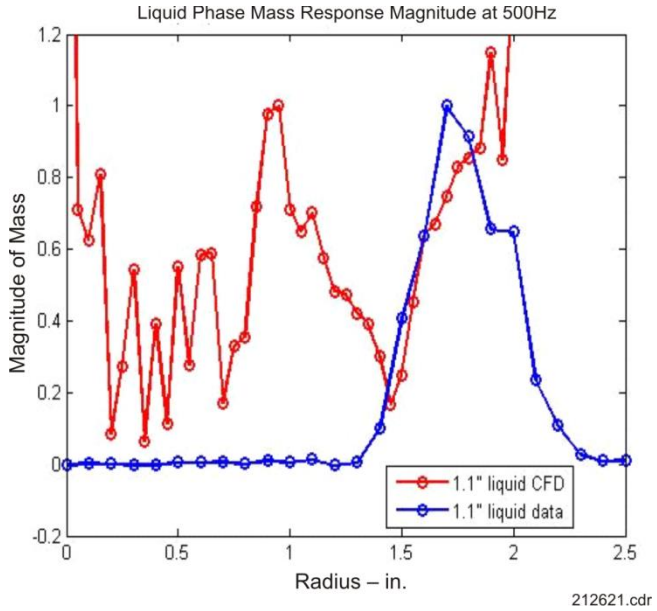

Figure 7-17. *Magnitude of Fluctuation of Fuel (Particle) Mass, Downstream From Swirler, PICS*

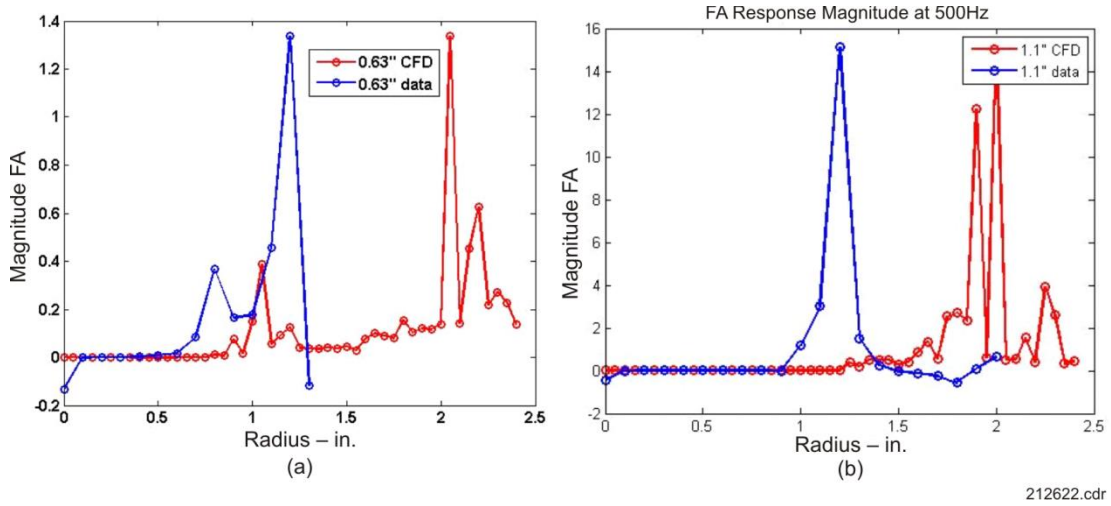

Figure 7-18. *Magnitude of Fluctuation of FAR, Downstream From Swirler Exit of CRESS*

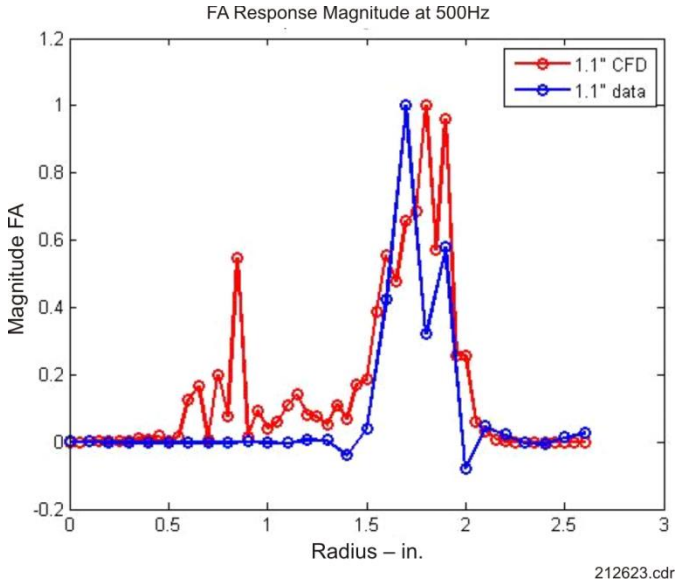

Figure 7-19. *Magnitude of Fluctuation of FAR of CFD and Data Downstream From Swirler Exit of PICS*

Figure 7-13 shows that both the mean (***Figure 7-13a***) and fluctuating component (***Figure 7-13b***) of axial air velocity agree very well with data at thedownstream plane for the CRESS. The model captured the peak location of the mean component, but missed the absolute value at the peak by approximately 25 percent. For the response magnitude, the peak location and value were matched. Note that, as mentioned in the experimental section, the experimental air velocity was indirectly represented by the velocity of the 15 µm of less droplet class. ***Figure 7-14*** shows the comparison at downstream plane for CRESS. Again, the peak location was well matched, but the peak absolute values differed. For response magnitude, CFD captured the trends, but the peak values differed.

Figure 7-15 shows the comparison at the downstream plane for the PICS. The CFD result differs significantly from data. Both show peaks just radially outboard of the wake region, but experimental data shows a large recirculation zone, whereas CFD shows a stronger recirculation zone that is less than smaller. This led to the difference of peak location and value. As one would expect after looking at the mean results, the response magnitude did not compare well between CFD and data.

Due to the fact that CFD and experiment have different total acquisition times (approximately 100 periods for experiment and approximately 17 periods for CFD), the fuel mass from CFD is only proportional. Therefore, for comparison purposes, the CFD and data were scaled by their respective peak values.

Figure 7-16 shows the comparison of response magnitude at downstream sampling planes for the CRESS. For the near plane, CFD agreed reasonably well with data in terms of primary peak location. The second peak in the CFD result occurs in a region with little fuel. Similarly, for the far plane, the peak response at r > 1 in. is not significant due to the sparse number of particles in that region.

For PICS, ***Figure 7-17*** shows the comparison of CFD and data at the downstream plane. Experimental data showed a single peak in response to the forcing at r = 1.75 in., which is located inboard of the peak in axial velocity at r = 2.25 in. The CFD has a peak response at r = 1 in. located near the peak in gas velocity, and another peak at r = 2.1 in. The r = 2.1 in. peak is not physically meaningful due to sparse number of particles in that region. The peak at r = 1 in. is aligned with the edge of the swirler where any film breakup would occur.

The comparison of fluctuating droplet diameter with data at the near plane of the CRESS was unfavorable (not shown) and was worse than the unforced results shown in Section 2.2, *UTRC Task 3.2.1 — CFD Spray Evaluation*. The droplet sizes ranged from 2 to 80 ?m in the CFD, whereas the experimental range was 10 to 70 µm. The droplets in the region of peak fuel mass (r < 0.8 in.) had diameters below 5 µm in the CFD and ranged from 10 to 30 µm in the experiment. Similar poor comparisons were also true at the 1.1-in. plane for the CRESS.

The comparison at the far plane for the PICS was even worse (See Section 2.2, *UTRC Task 3.2.1 — CFD Spray Evaluation*). The particle sizes were below 10 µm in the CFD and ranged from 20 to 50 µm in the experiment. This overall discrepancy was thought to be due to the film breakup model in AtoMIST where the film thickness correlation was validated using a high-shear swirler. If the film thickness is not captured correctly, the droplet size from the film breakup will also not be correct since the droplet size is directly related to film thickness. Further improvement and generalization of the model is required to accurately capture the spray characteristics for a wider range of swirlers.

The response magnitude of FAR to forcing at the sampling planes of CRESS is shown in ***Figure 7-18***. For the near plane, the largest peaks from both CFD and data were not physically meaningful because the particles were sparse with very low fuel mass locally. The peaks at 0.75 in. from data and 1 in. from CFD are both physically meaningful. For the far plane, the peaks at r > 1.5 in. were not meaningful from CFD for the same reason. Both CFD and data showed that the FAR response peaked at a larger radius than that of spray mass.

For PICS, ***Figure 7-19*** shows the magnitude of FAR response at the downstream plane. Coincidently, the CFD and data agreed well, but there was no physical meaning for peaks at r > 1.5 in. for the CFD because there were almost no particles in that region. The physically meaningful peak from the CFD resides near r = 1 in. and this was the location where 90 percent of the fuel mass was located due to film breakup.

7.2.8 Summary of AtoMIST Performance

The forced spray modeling results with AtoMIST and the comparison with experiment showed that AtoMIST reasonably predicts the spray behavior for the CRESS swirler, but not nearly as well for the PICS in terms of mean and fluctuating gas velocity and spray mass. For droplet size and distribution, AtoMIST produced poor results for both the CRESS and PICS (Section 2.2, *UTRC Task 3.2.1 — CFD Spray Evaluation*). Since 80 to 90 percent of droplets came from the film breakup model in both cases, it is believed that the discrepancy in droplet size is due to the film model. Based on this understanding, two specific areas should be examined:

- The correlation for film thickness may not be applicable for general types of swirlers since it was validated using a high-shear swirler. Therefore, the tuning parameters in the correlation should be revisited and generalized.
- The model also contains a free time constant which determines when column breakup occurs. This time impacts the percentage of fuel that gets stripped off the column versus the amount of fuel on the filmer

wall. Results tend to indicate that too much fuel ends up on the filmer wall, thus it may be important to determine if the time constant is applicable to fuel injectors such as the CRESS and PICS.

7.2.9 Transfer Function and Swirl Number Analysis

Since the CFD gas-phase results of CRESS were very encouraging, in that they closely replicated the experimental data, further analyses of the aerodynamic flowfield predicted by the CFD was performed. The goal was to gain a better understanding of what unsteady phenomena were acting to cause the unsteady droplet transport that was observed.

One technique used to analyze flow-field dynamics was to calculate a transfer function (TF) between the mass flowrate at the inlet and axial velocity at each sampling plane.

The results indicate that the forced swirling jet has preferential responses (high gains) for two locations separated by 180 degrees. Furthermore, this location was not the same for both planes, but a nearly 60-degree shift was observed for the far plane. Finally, the response to the forcing was much more complex inboard of the swirler diameter than outboard where the response was low.

It is interesting to investigate the response in term of phase. At specific radial locations, the phase between the input mass flow signal and the output axial velocity signal in both planes changed significantly in the circumferential direction. This can be highlighted with plots at distinct radii shown in ***Figure 7-20***.

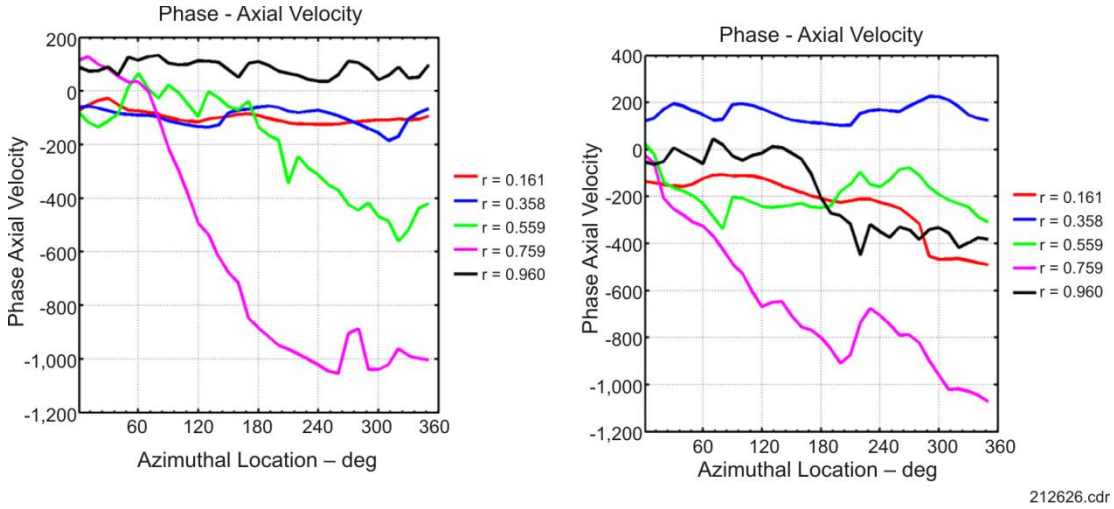

Figure 7-20. *Phase of TF at Various Radial Locations for Downstream Planes of CRESS*

In ***Figure 7-20***, the phase between the axial velocity signal and the mass flow signal is plotted for near (left) and far (right) at specific radii and as a function of azimuthal location (0 to 360 degrees). The curve at r = 0.759 in. recorded the maximum variation of phase along the circumferential direction. This may be induced by an asymmetric flow pattern. More resolved data (i.e., 3-D) beyond the planar data available in the current analysis is needed to understand the flow pattern more completely.

The swirl number calculation requires both the axial (u) and azimuthal (v) velocities on each sampling plane. As the velocity field is unsteady, the swirl number is computed as a function of time.

Given the planar velocity fields it is possible to perform the integration of this equation to get the evolution of the swirl number as a function of time.

Results in ***Figure 7-21*** indicate that the swirl number fluctuates due to the inlet forcing. An FFT analysis of these signals highlighted a peak at the forcing frequency for the signal in ***Figure 7-22a***, while the FFT of the swirl number signal in ***Figure 7-22b*** did not highlight the forcing frequency. As a function of time, the swirl number reached a maximum value close to 0.5 and a minimum value close to 0.25. This level of swirl number fluctuation almost guarantees that the recirculation zone would be altered by the air forcing.

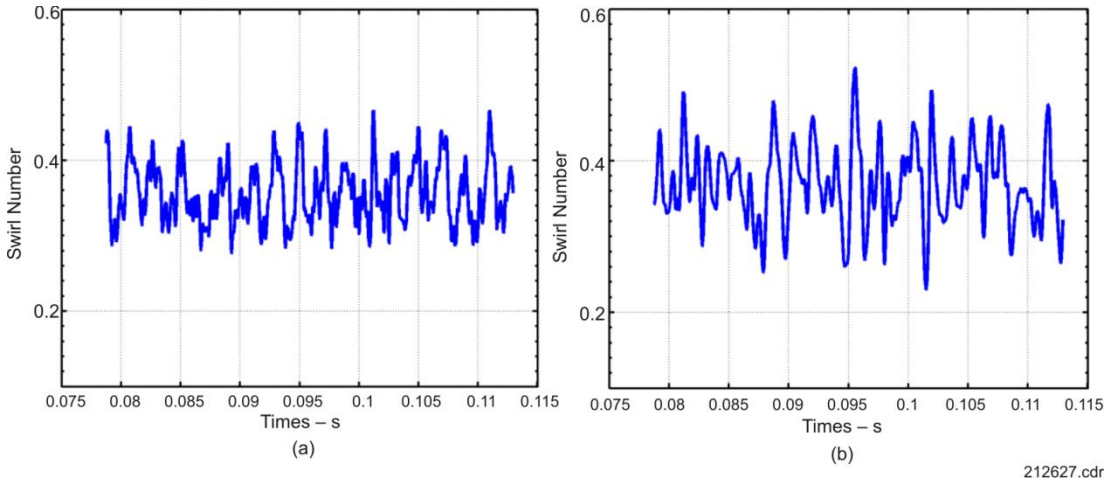

Figure 7-21. *Evaluation of Swirl Number as a Function of Time in Downstream Planes of CRESS*

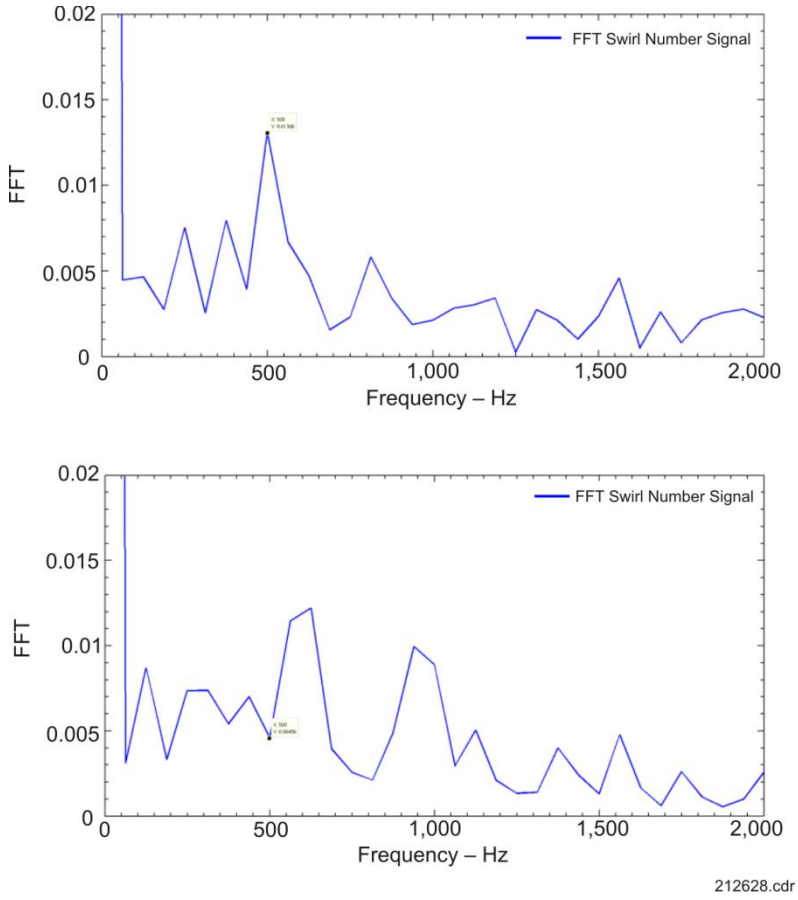

Figure 7-22*. FFT of Swirl Number at Downstream Planes of CRESS*

7.3 EXERCISING OF COMBUSTION DYNAMICS SYSTEM MODEL

7.3.1 Forced Computational Fluid Dynamics

The objective of the forced CFD component of this project is to use CFD flowfields under forced conditions to obtain UHR. The flowfield and UHR are used to calculate TFs defined by the 3rd-generation UHR model. The UHR is then coupled in the linear stability analysis tool with acoustic modes of the combustor to determine how

the mode's damping is shifted by the UHR, thus allowing for a stability comparison of various low NOx combustor designs.

The two most promising low NOx combustor designs being pursued are the ACS concept and the CRESS concept. The ACS concept features a front-end pilot flame to achieve low power stability and efficiency, and a main axial stage fuel injection downstream of the pilot flame to achieve good cruise and high power emission and efficiency. The CRESS design is an example of a multiple lean direct injection (LDI) concept with three radial stages for turndown and profile control. These two fuel injection designs are simulated in current study as designed for the single sector AAC rig. Therefore, the stability analysis will be conducted in the context of the AAC rig.

The response of the flow field and UHR to unsteady forcing conditions is simulated using the commercial CFD code Fluent. Unsteady forcing is realized by harmonically forcing the mass flowrate at the inlet boundary of the AAC rig computational domain.

Liquid fuel injection is resolved by using UTRC-proprietary spray model AtoMIST. AtoMIST is a reduced-order model that integrates a surface tracking method, VOF, for liquid fuel transport with a DPM for spray dynamics. It is implemented in Fluent using UDF. ***Figure 7-33*** gives a schematic of the major physics captured in AtoMIST.

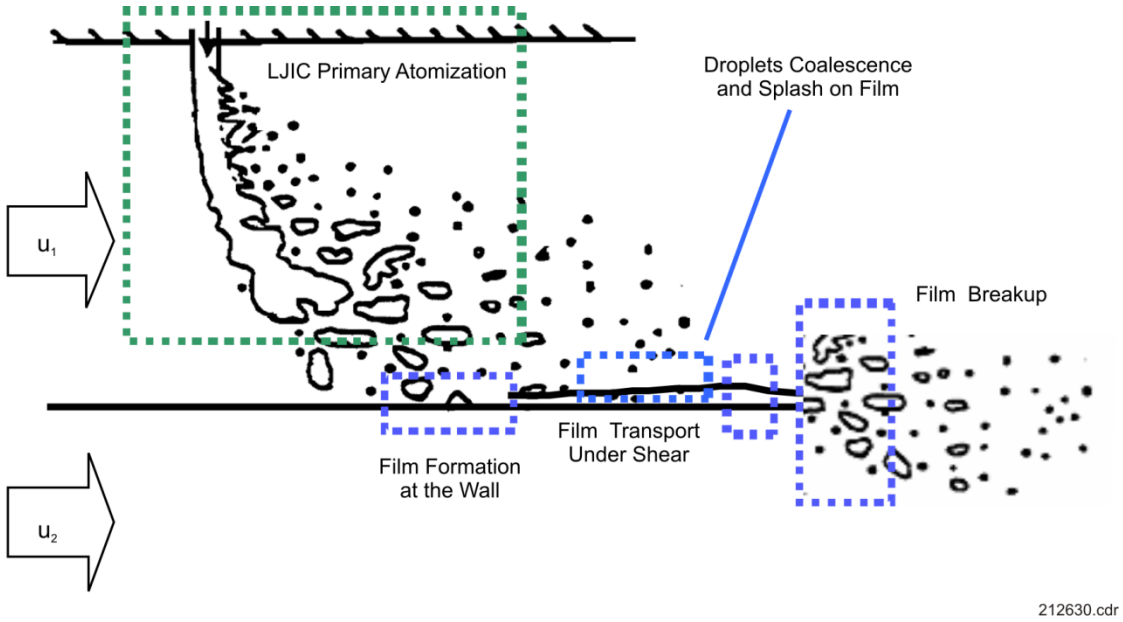

Figure 7-23. *Schematic of Major Physics of Fuel Injection in the Swirler/Injector Assembly*

One of the reasons for choosing AtoMIST is its ability, through its surface tracking-based methodology, to capture the blockage effect of the fuel jet column in swirling crossflows. In addition, AtoMIST is believed to be able to capture how forcing affects fuel jet breakup, droplet transport, and evaporation. However, this choice also leads to a comprise in turbulent combustion modeling.

The compromise is due to the VOF model used in AtoMIST. In Fluent, the relatively advanced combustion models that are based on mixture fractions or progress variables are not available when the VOF two-phase model is turned on in the simulation. Only the eddy dissipation (ED) model or its derivatives can be used. The plain ED combustion model was used in this simulation. The ED model is a fast chemistry model, and implies mixing controlled combustion, or mixed is burned. This model leads typically leads to a very compact flame. The shortcomings of the turbulent combustion model with respect to UHR need to be investigated in future studies.

This remainder of this section focuses on the procedure for carrying out the forced reacting flow simulations using Fluent with AtoMIST and the postprocessing of these results.

7.3.2 Numerical Damper Study

Due to a limitation in Fluent regarding nonreflecting boundary conditions (NRBC), and the complexity of implementing NRBCs in Fluent, a numerical damper was developed to eliminate reflections at the end of the computational domain.

The forcing of an acoustic wave was enforced at the plenum inlet upstream of the swirler through a fluctuation in mass flowrate. Both cases show a complete damping of the pressure wave in the damper downstream of the actual combustor exit. The case with artificial viscosity showed a smoother damping curve than the case without artificial viscosity.

7.3.3 Simulation of Counterrotating External Staged Swirler Advanced Aeroengine Combustor

7.3.3.1 Computation Domain and Mesh

The CRESS AAC rig encloses two CRESS swirlers in the front end BH, which are symmetric about the streamwise center plane of the rig. This symmetry is used in defining the computational domain and only half of AAC rig with one CRESS swirler is meshed for this CFD study. The streamwise center plane is treated as a symmetric boundary condition. The total mesh size is about 2 million grid count including the damper.

7.3.3.2 Mean Flowfield

Clearly seen from the velocity contours are three recirculation regions, two in the corners and one in the center. The one in the center appears to sit outside the swirler due to the purging flow from the center tube along the centerline of the swirler. The recirculation zones help to anchor and stabilize the flame, which appears to attach to the exit rim of the swirler. This flame attachment, however, seems to be questionable considering the distribution of the fuel vapor and the high velocity flow at the swirler exit. The combustion model's affect on flame location in the CRESS design needs to be investigated in the future studies.

Contours of instantaneous fields of temperature, axial velocity, fuel vapor mass fraction, and heat release rate confirm the observations made from the mean flowfields, such as the three recirculation zones, fuel vapor distribution, and short flame length. The large presence of fuel vapor inside the swirler confirms the prevaporized design intent of CRESS, as well as premixing in the swirler. This feature sets the CRESS design apart from the conventional high shear injectors that rely on film atomization to assist fuel vaporization and mixing. A rich fuel air mixture is usually formed from the high shear injector. CRESS, on the other hand, is intended for lean premixed low-emission combustors.

7.3.3.3 Forcing Response

The response of the flowfield and the UHR rate to the forcing of the combustor is the primary interest of this study. The forcing is realized by oscillating the air mass flowrate at the inlet of upstream plenum by 20 percent (0-peak). ***Figure 7-24*** shows the pressure signals and corresponding FFTs at three axial locations: swirler exit, plane downstream of the swirler exit, and combustor exit. The FFTs clearly show the response of the flowfield, an indication that the numerical damper is working properly. ***Figure 7-25*** shows specifically the response of the flow field at the swirler exit. The velocity amplitude fluctuation is about 10 percent of the mean.

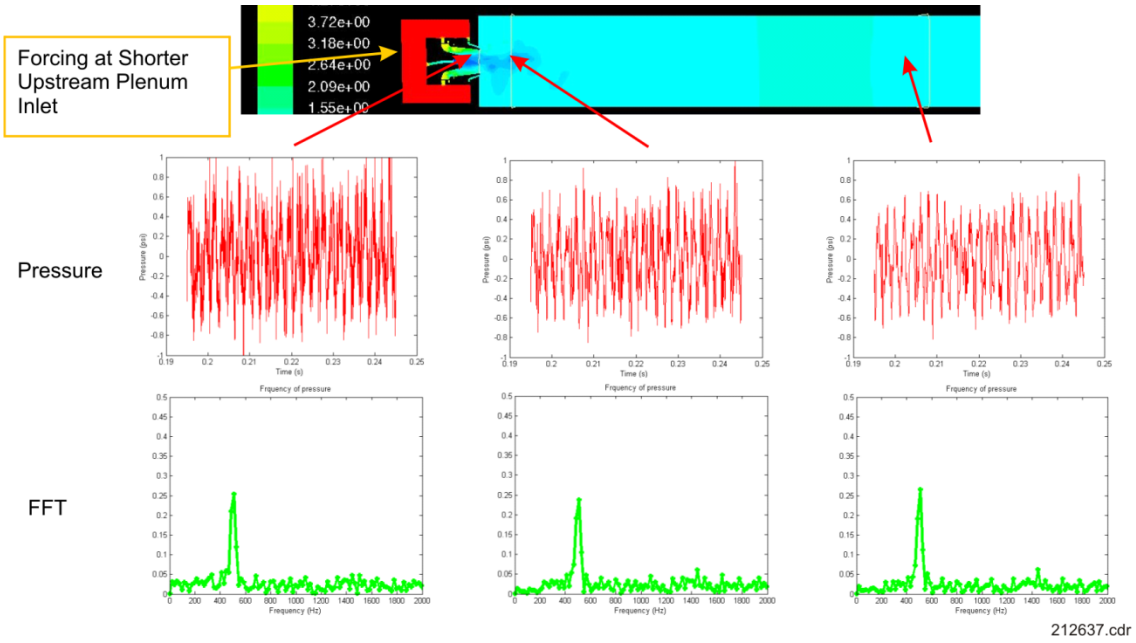

Figure 7-24. *Pressure Response at Different Axial Locations*

From Left to Right: Swirler Exit, Plane Downstream, and Combustor Exit

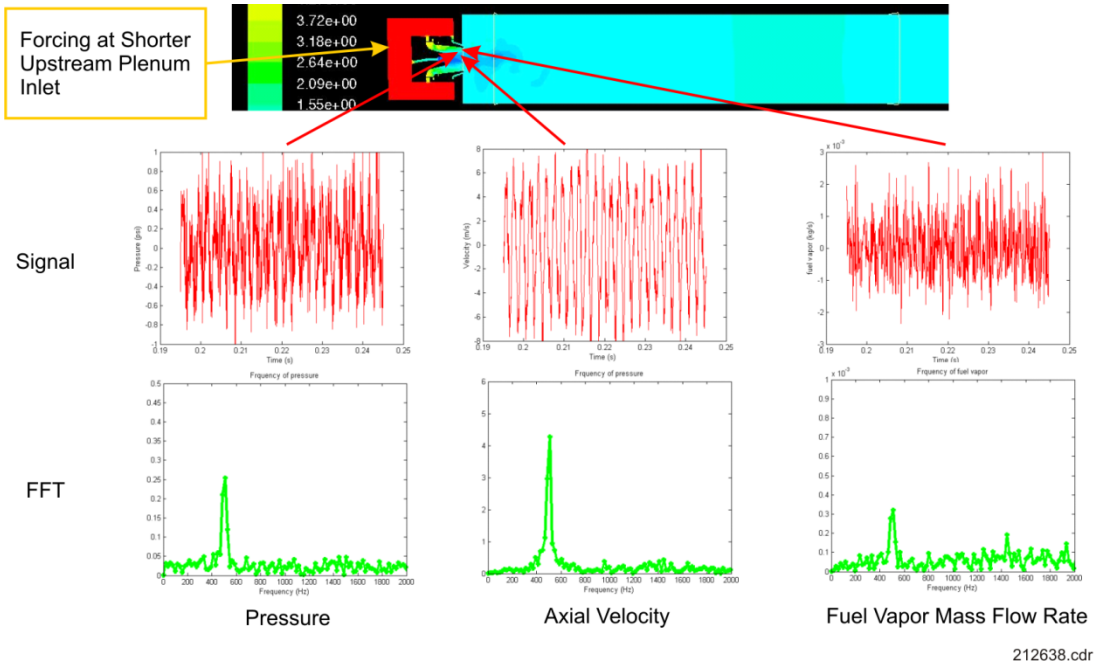

Figure 7-25. *Response of Pressure, Velocity and Fuel Vapor Mass Fraction at Swirler Exit*

Once a number of forcing cycles have been calculated, flowfield data is saved for postprocessing and stability analysis. Different sets of flow variables are saved in different domains. For example, heat release rate data is needed in the combustor part of the domain, but is unnecessary in the swirler and damper. Saving different sets in different domains is used in an attempt to reduce the amount of memory required for saving the data.

In total, 25 forcing cycles of data were saved. Each cycle has 25 data points, corresponding to 625 files for the swirler, combustor, and damper. The file sizes are 192 MB for each swirler, 140 MB for each combustor, and 82 MB for each damper.

7.3.4 Simulation of Axially Controlled Stoichiometry Aeroengine Combustor

The ACS concept features a front end pilot flame and a main stage fuel injection separated from the pilot flame. In the current study, the pilot flame is fueled with gaseous propane and the main stage with liquid Jet-A. Because the main stage is the most crucial part of the design, and because previous studies showed excellent mixing of the gaseous pilot fuel, the gaseous propane injection in the pilot stage is not modeled in the current CFD simulation. Instead, a mixture of premixed propane and air with specified fuel air ratio is applied at the inlet of the upstream plenum feeding the pilot tubes.

7.3.4.1 Computational Domain and Mesh

Although pilot fuel injection was not modeled in the simulation, the mesh resolution require by AtoMIST and for resolving the swirling flow of the main stage injectors was still high. Constrained by computation resources available at UTRC, it was decided to model only a portion of the AAC rig configured with the ACS design. The portion includes 1/5 of the pilot stage and 1/3 of the main stage. The side walls of the combustor were neglected, and instead periodic boundary conditions were used in the spanwise direction. It is assumed that this computational model of the ACS AAC rig is able to capture the main features of the ACS concept so that a realistic TF can be calculated for the linear stability analysis.

Because of the periodic boundary conditions, the combustor section becomes a 2-D channel with pilots at inlet and main injectors acting as jets in cross flow. The mesh for the computational domain is that of LES channel flow with refinements for pilot jets and main injector cross flow jets. In addition, finer mesh was placed outside fuel injection orifices in the main injector which were required for resolving the liquid fuel represented by VOF. The total mesh size is about 2.9 million, including the numerical damper which was constructed as defined in the CRESS AAC case.

7.3.4.2 Flow Features in the Main Stage Injectors

The flowfield inside the swirler is characterized by high-speed counterrotating swirling flows as shown by the Ux and Uy velocity contours. The counterrotating swirling flows are not able to cancel each other inside the swirler.

The ACS AAC features pilot flames in the front end that ignite the main stage fuel coming out of the main injector. The interaction of the pilot flame and main jets are an important feature of the ACS design. The propane mass fraction contour shows that the pilot fuel is consumed midway before reaching the main, a result of perfect mixing and the use of a fast chemistry combustion model. The temperature contours show that the pilot flames provide a burned gas mixture of a nearly uniform temperature distribution to ignite the main burners. This observation needs to be revisited when pilot fuel injection is considered and a more realistic turbulent combustion model is exercised.

The temperature contour also shows that the main flames bend in the flow, interact in the mid-stream of the combustor, and quickly complete combustion. The quick combustion of the main fuel, and the relatively large bending of the main flames, may be attributed to the fast chemistry combustion model. However, the bending of the main flames may also be influenced by the approaching pilot flames, as indicted by the velocity contours.

Pilot flames are generated by the pilot tubes. As such, the pilot fuel air mixture exits the tubes as a jet. The potential core of the jets is short compared to the velocity contours due to the fact that the combustion and subsequent thermal expansion of the pilot flames produce high velocities that reach all the way to the main. This leads to a strong influence by the pilots on the main in terms of flame shape and unsteadiness.

Forcing Response

The boundary condition forcing of the ACS AAC is different from the CRESS AAC since for the ACS configured AAC rig there are two air supplies, one for the pilots and one for the mains. Some acoustic modeling was required to determine the proper ratio of amplitude and phase to force each air inlet to account for the differing impedances of the pilot and main injectors. Another way to think of this is, if a wave is propagating in the combustor, what differing amplitude and phase would it have after propagating up the pilot tubes versus main

injectors. Figure 7-50 shows that the amplitude of a relevant acoustic mode upstream of the pilot is so low compared to the amplitude upstream of the main, that forcing the pilot can be neglected. Thus, only the main injector air mass flowrate was forced. The forcing frequency was based on acoustic analysis discussed in Section 7.4, *Acoustics*.

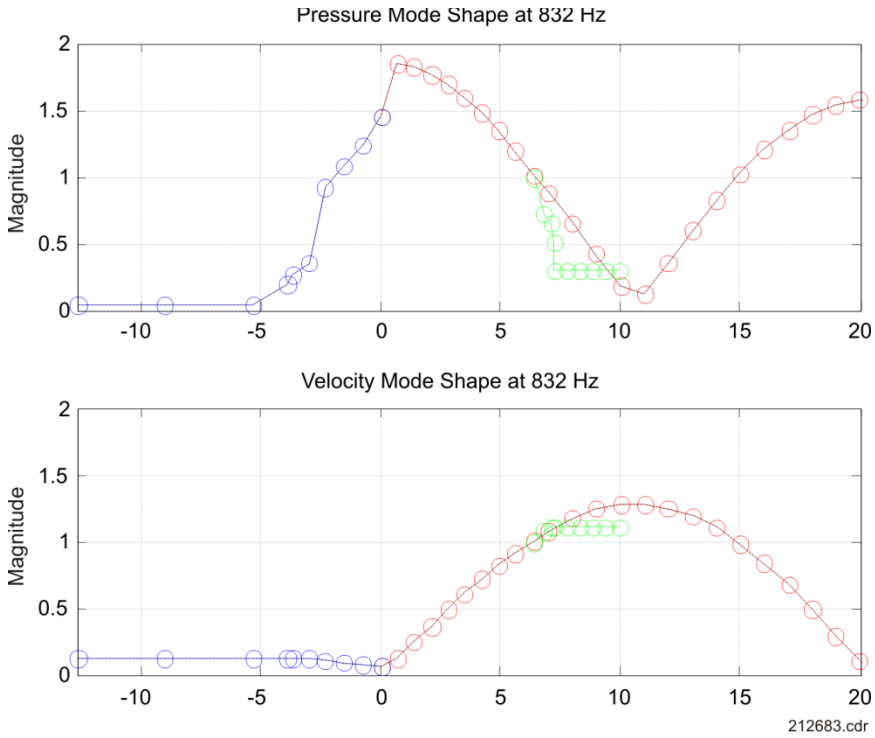

Figure 7-26. *Pressure and Velocity of 830 Hz Mode Shape for AAC Design in AAC Rig*

The saved data is similar to that for the CRESS case. For the ACS AAC case, 30 cycles of data were saved and there were 25 data points in each cycle, corresponding to 725 files for the top and bottom swirlers, upstream and downstream combustors, and the damper. The file sizes were 59 MB for each of the two swirlers, 95 MB for the each upstream combustor, 327 MB for each downstream combustor, and 26 MB for each damper.

7.3.4.3 Transfer Function Extraction

The transfer function of the flame is defined as the ratio between the UHR and the velocity fluctuation taken upstream of the flame.

The forced CFD calculations provide heat release fields for the entire combustor on a fine mesh (Fluent mesh). To be able to read the data extracted from the simulation with Matlab, an interpolation is carried out onto a coarser grid (AC3D mesh). This coarser grid is the grid used for the linear stability analysis. In addition, the TF is assumed to be well represented by a 1-D projection of the heat release, since the acoustic modes in the AAC rig are 1-D waves. The projection is accomplished by dividing the combustor into axial slices and then calculating the UHR for each slice. The velocity signal is taken at the outlet of the injector. Each signal is cell volume weighted. It is then possible to form the TF between the input velocity signal and the output heat release signal of each slice.

7.3.4.4 Counterrotating External Staged Swirler Combustor

For this configuration, the combustor was divided into 20 slices. The increment between slices was quadratic rather than linear in the axial direction to account for the concentrated heat release distribution at the swirler exit. The velocity signal taken at the outlet of the swirler is shown into ***Figure 7-27***. The blue line corresponds to the velocity signal on the fine grid (Fluent), the black line on the coarse grid (AC3D), which is the grid used for the linear stability analysis. The respective LSF of those signals are plotted in cyan and red. One can conclude from

this plot that the interpolation preserved the amplitude of the signal, even though the raw signal on the coarse grid has a significant amount of noise.

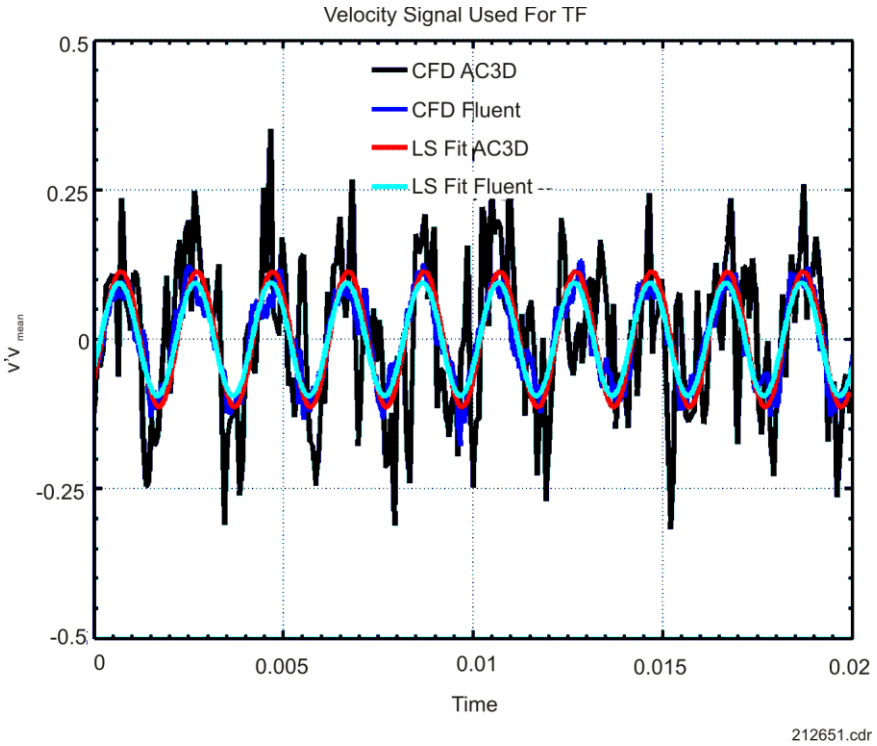

Figure 7-27. *Velocity Signals for Two Different Grids and LSF of Those Signals*

The heat release signals for the first six slices of the combustor are plotted in ***Figure 7-28***. The raw CFD signals (blue) and corresponding LSFs (red) are plotted. These results demonstrate that the forcing acts on the heat release signal, specifically in Sections 4, 5, and 6, where one can clearly distinguish forced content.

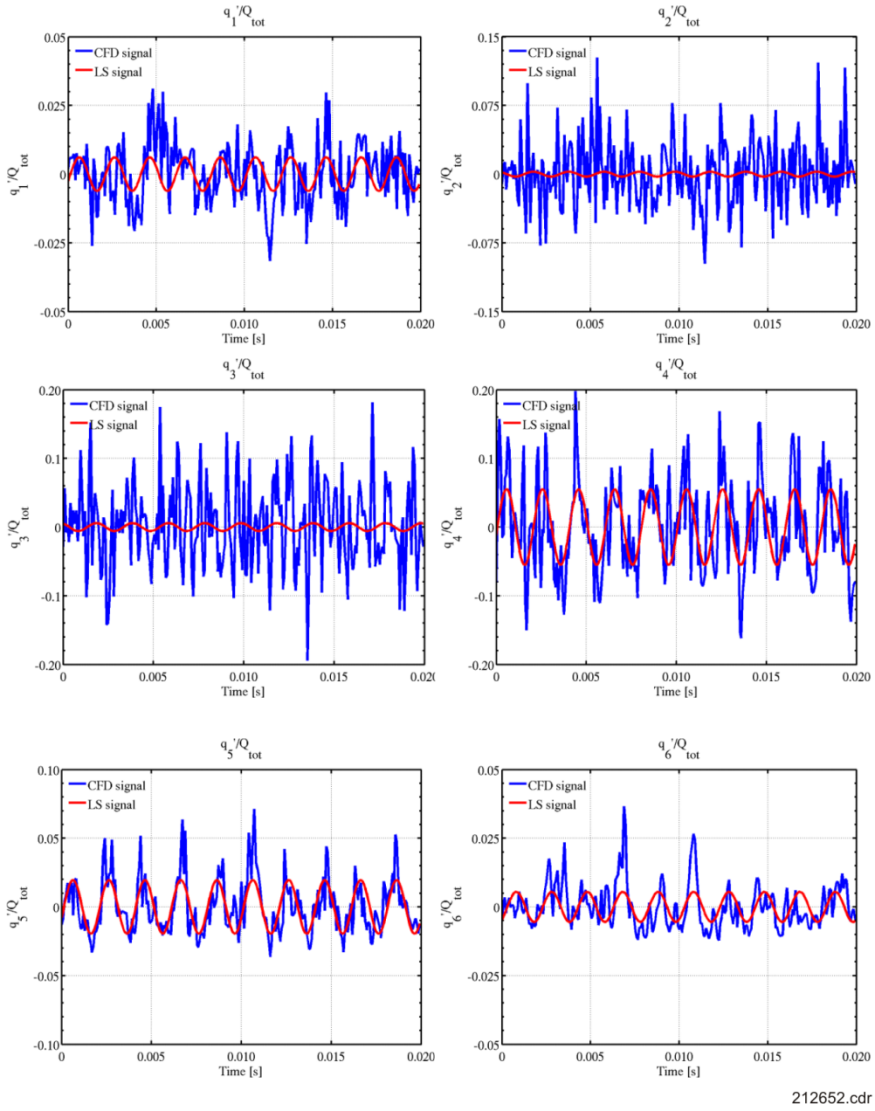

Figure 7-28. *Raw Heat Release Signals and Corresponding LSF for First Six Slices of Combustor*

It is now possible to form the transfer function with the built-in Matlab function (TFESTIMATE) and with the LSF of the input and output signals. TFESTIMATE is a frequency domain technique, whereas the LSF is a time domain technique that works well for extracting the amplitude ratio and phase difference between two signals at a single frequency. Both methods have been implemented because the LSF may be more appropriate when working with a very few cycles. The gain is plotted in ***Figure 7-29*** for both techniques. It should be noted that the flame response is concentrated near the swirler exit. Both techniques provide the same quantitative results with only small amplitudes differences. One can observe that the gain is zero after section number eight, highlighting the compactness of the flame. The phase of the transfer function is given in ***Figure 7-30*** using both techniques. Good agreement is obtained between both methods taking into account that the phase is wrapped, and that the phase has no meaning where the gain is at or near zero.

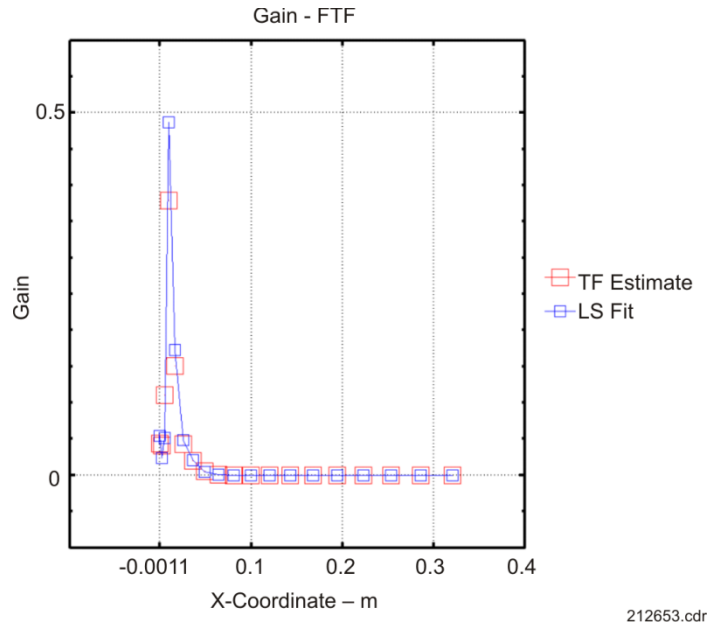

Figure 7-29. *Gain of the TF for CRESS*

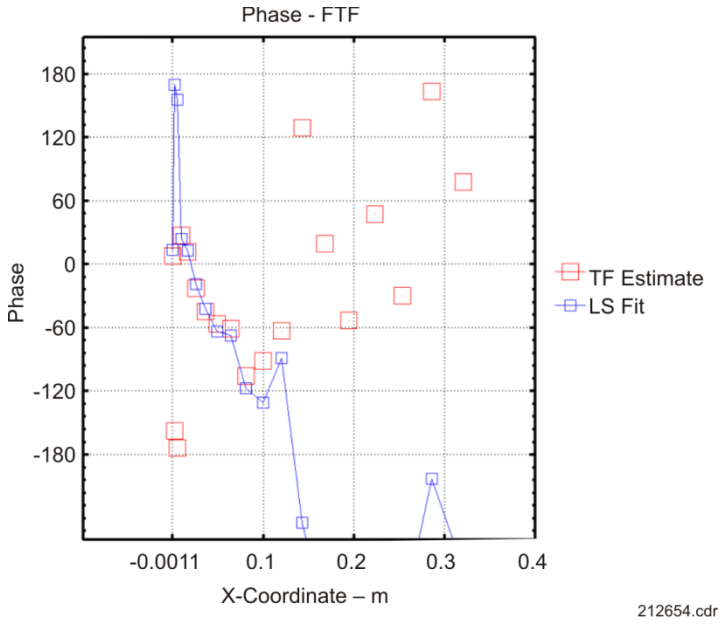

Figure 7-30. *Phase of the TF for CRESS*

Figure 7-31 shows the region where the CRESS flame transfer function is nonzero. The frequency domain TF technique (TFESTIMATE) allows for the calculation of not only gain and phase but also coherence. The gain presents a peak at the fourth slice where the maximum response is recorded. The phase of the fourth, fifth, and sixth points show convective behavior assuming a mean axial velocity near 100 m/s. It can be seen that the coherence is low for regions of low gain indicating poor signal to noise for those slices.

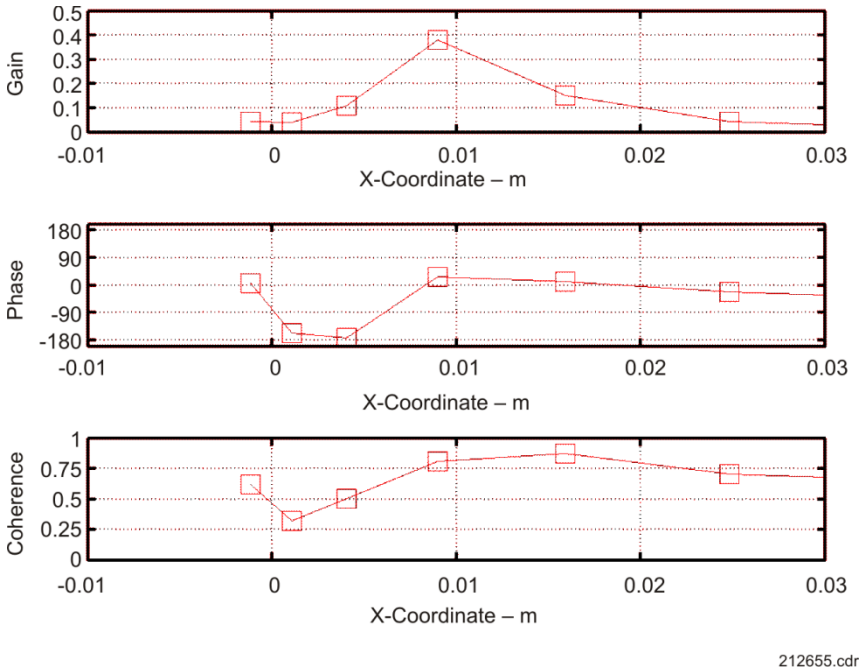

Figure 7-31. *Closeup View of the Flame TF for CRESS Using TFESTIMATE*

7.3.4.5 Axially Controlled Stoichiometry Combustor

The same postprocessing methodology is used for the ACS. Because the computational domain is made of two pieces, an upstream combustor with three pilot flames and a combustor with two main swirling flames, it is appropriate to treat each of these pieces separately. The results are first provided for the main combustor and then for the pilot.

The velocity signal at the main swirler exit is plotted in ***Figure 7-32*** for 30 cycles of modulation. Results of the transfer function are presented in ***Figure 7-33*** for a calculation done with 10 and 30 cycles to compare the effect of cycle number. Increasing the number of cycles results in more representative coherence values. This can be seen clearest in low gain regions where coherence is expected to be low. Even with increasing the number of cycles, only slight changes are seen in the gain and phase of the transfer function. It is interesting to note that the upstream section of the flame ($x < 0.0$ in.) has a higher response than the downstream section ($x > 0.0$ in.) indicating that the flame interaction with the flow is important.

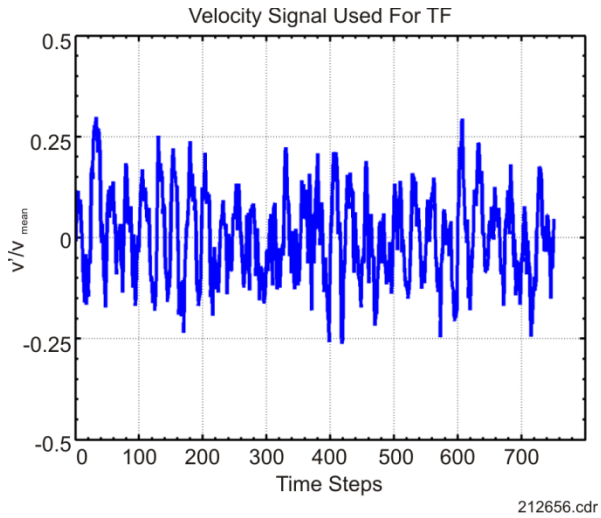

Figure 7-32. *Velocity Signal at Swirler Outlet for ACS With 30 Cycles*

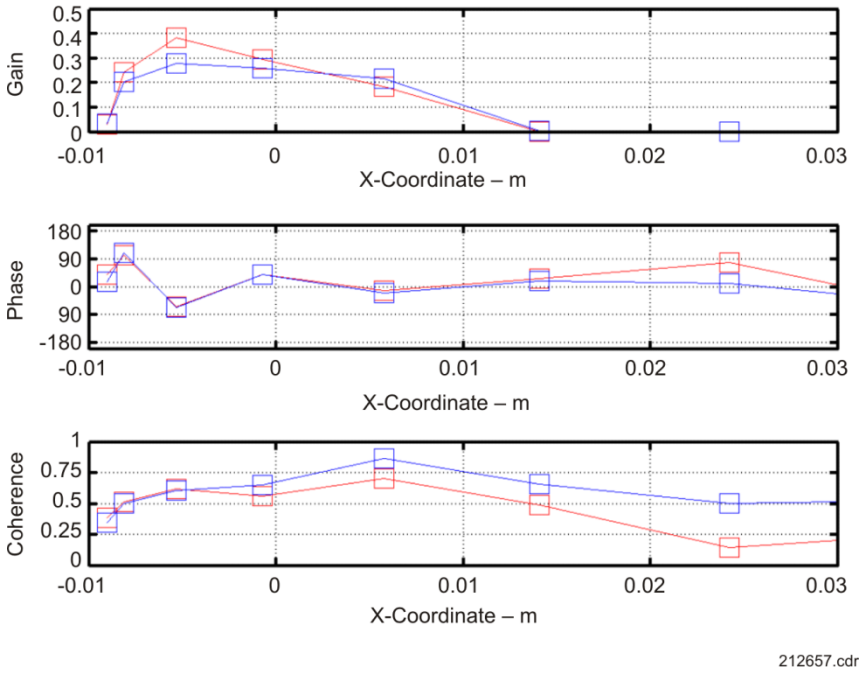

Figure 7-33. *Closeup View of Flame TF for ACS in Main Combustor Using TFESTIMATE*

The response of the pilot flames in the upstream combustor is presented in ***Figure 7-34***. The response shows a double peak response. The first peak is located very close to the pilot outlet while the second one is located midway between the pilot and main injectors. While the coherence between the signals is high for the first peak, the second peak has low coherence calling into question its significance.

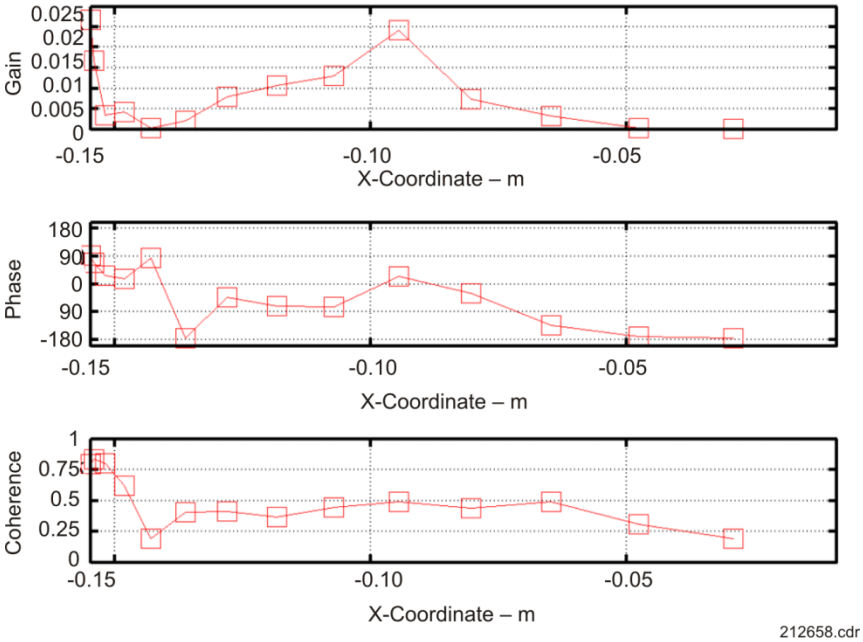

Figure 7-34. *Closeup View of Flame TF for ACS in Upstream Combustor Using 10 Cycles of Data*

7.3.4.6 General Conclusions

To conclude this subsection, a methodology has been developed and executed to extract the flame transfer function from two forced LES CFD calculations. The list below highlights some general conclusions applicable to both cases, plus specific conclusions regarding the CRESS and ACS designs.

- The time domain method (LSF) and the frequency domain method (TFESTIMATE in Matlab) for extracting the flame TF produce similar results assuming that the number of points in FFT (NFFT) is chosen so that a point exists at the forcing frequency.
- The increase in the number of cycles (10 to 30) used to form the TF shows a more representative coherence, but only slightly affects the TF, thus indicating that as few as 10 cycles of data captures the important magnitude and phase trends. This result is dependent on the amount of noise in the signals, more noise requires more cycles.
- The poor coherence calculated for some slices in the combustor could be improved by increasing the forcing amplitude, and thus increasing the signal to noise ratio.
- The TF was also calculated on the fine mesh (not shown) to compare with the corresponding coarse mesh TF. Calculating the TF on the fine mesh is challenging due to Matlab memory limitations, so only seven cycles of data were used to calculate the TF. Results indicate the same spatial distribution of gain and phase, but the absolute gain level decreased. This could be due to the interpolation of the data onto the coarse grid, but further investigation is required to confirm this result.

7.3.4.7 Counterrotating External Staged Swirler Conclusions

The CRESS TF is concentrated in the near field of the swirler exit. Nearly premixed, prevaporized flames are expected to be compact, but it is also believed that the Fluent combustion model used for these calculations also contributes to the compactness of the flame.

7.3.4.8 Axially Controlled Stoichiometry Combustor Conclusions

The TF result shows that the upstream section of the flame has a higher UHR when compared to the downstream section of flame indicating that the interaction with the cross flow is important.

The TF response of the pilot is significantly lower than the response in the main. This is mostly likely a result of the velocity mode shape in the combustor. Even though the pressure mode shape is near a maximum (antinode) at the pilot exit the velocity mode shape is near a minimum (node), thus resulting in a lower TF response (see ***Figure 7-26***).

7.3.4.9 Flame/Flow Dynamics

This section attempts to link the understanding of the TF with flame and flow visualization. The goal is to understand the physics which contribute to the flame TF response, as well as overall system stability. The visualization process is decomposed in three main steps. The first one is to form phase locked images with the available cycles of data, keeping in mind the memory limitations of Matlab. Once the phase locked images are formed, the second step consists of using Ensight to calculate fluctuating quantities like pressure, heat release and velocity. The final step focuses on estimating the RI by making use of the fluctuating pressure and heat release.

7.3.4.10 Counterrotating External Staged Swirler Combustor

The results for the CRESS design were visualized on the coarse grid because good qualitative agreement was obtained between the fine and coarse grid.

It was shown that the flame front of the swirling flame is symmetric with maximum heat release at the swirler outer diameter. The axial velocity field has a maximum around 107 m/s in the swirling jet region with a strong center recirculation zone. This velocity is in good agreement with the 100 m/s convective time delay observed in the transfer function phase. The pressure field is nearly uniform with a low pressure region at the center of the swirling flow due to the recirculation zone.

The fluctuating quantities of heat release and pressure, plus their product are used to calculate the RI. The fluctuating quantity is nondimensionalized by the maximum of the reaction rate in the cycle.

In general the pressure wave looks very one-dimensional away from significant area changes and the near flame region. Near the flame a more complex unsteady pressure field is observed.

7.3.4.11 Axially Controlled Stoichiometry Combustor

The results for the ACS design were visualized on the fine grid. Using the fine grid was required, because flow features looked too coarse using the AC3D (coarse) grid. Compared with the CRESS case, where the coarse AC3D grid was used for visualization, the ACS design has two main swirlers to grid, whereas the CRESS case had only one swirler. Given a fixed number of AC3D nodes, the ACS coarse AC3D grid has less resolution compared to the CRESS design. The mean flow has a higher level of turbulence up stream of the main injector and the low pressure region associated with the recirculation zone is smaller when compared to the CRESS. This is not surprising given the canceling affect of the counterrotating swirl.

To conclude this subsection, a methodology has been developed to postprocess data by forming phase locked images of forced LES CFD calculations. The spatial unsteady heat release and pressure have been computed. The product of pressure and heat release was then computed to form the RI. The computed flame surface area at each phase, not presented here, confirms that the forcing strongly affects the heat release response. These tools provide a starting point for understanding the physical mechanisms which could drive combustion instabilities. Obviously, greater analysis of the computational results could be done to further understand the dynamic response of the system, but this effort was primarily focused on setting up tools and procedures. As the downselected concept development progresses further more information will become available to refine the modeling capability and gain confidence in the submodels. Further development and parametric study will also provide more information on how design differences affect combustion dynamics.

From a technique point of view, this work highlighted some issues:

- Visualizations have been made with the coarse grid for CRESS while the fine mesh has been used for ACS. This is due to limitations in the size of the coarse AC3D grid. With a hard limit on the number of AC3D grid points, it can be seen that gridding two main swirlers for the ACS design will yield a coarser grid when compared to the single CRESS swirler.
- Matlab memory limits the analysis that can be completed on the fine mesh. Matlab is a desirable tool to perform frequency domain analysis, since its routines are robust and comprehensive, but future work could investigate Fortran-based analysis, which would alleviate some of the memory limitations.
- Visualizations of the pressure field near the injector exit indicate that the pressure field is not purely 1-D. As a consequence, it may be better to use a 2-D or 3-D representation of the transfer function. The RI captures the complex pressure field since the product of unsteady heat release and pressure are a per cell based calculation before the volume integral.
- The computation of quantities like swirl number or velocities over a tangential surface have not been completed. Further work using Ensight is required to form the tangential surface.

7.4 ACOUSTICS

The acoustics of a combustion system form the basis, or starting point, for most combustion dynamics analysis. Most instabilities occur near the natural, or resonate, frequencies of the combustion system. The role of UHR is to alter the damping of the natural acoustic mode. Therefore, all combustion dynamics tools require a model to predict the acoustic modes of the system. Typically, only one mode goes unstable at a given operating condition, but determining which mode can be challenging. In an exhaustive study the stability analysis would be done on all relevant modes and the least stable mode would be selected as the most likely to go unstable. Given the time intensive technique used for determining the UHR in the current system model, analysis can only be done on one mode (and frequency). Experimental information, if available, and experience were used to determine which mode to perform the complete stability analysis. The following section details how the acoustics were calculated for both the CRESS and ACS designs in the AAC rig.

The acoustic modeling tool used for this analysis is a United Technologies Corporation- (UTC-) developed finite element solver known as AC3D. AC3D can model complicated geometries and capture mean flow effects such as the effect of mean flow on wave speed, and the effect of mean flow gradients on acoustic mode damping.

The mean flow is imported from a CFD code, in this case the Fluent reacting mean flow calculated before forcing was turned on to obtain the UHR. Its only real limitation is the memory required for inverting large mass and stiffness matrices which are N × N in size (N = number of nodes). This limits the grid count of an AC3D mesh. The impact of this limitation was previously discussed in Section 7.3.1, *Forced Computational Fluid Dynamics*.

Modeling the acoustics of a single sector test rig such as the AAC rig is in general quite simple since the modes are typically only longitudinal in nature. The only complications are defining reasonable acoustic boundary conditions where long inlet and exhaust ducts exist, as well as obtaining the proper impedance for the fuel injector, which is the most complicated geometric component in the rig. To gain confidence that the injector is modeled properly, an impedance tube test was conducted on the injector geometry. Successful modeling of the impedance tube test provided confirmation that the model could capture the appropriate acoustic impedance.

Therefore, the acoustic section has four subsections, two sections which discuss the model to data agreement for the CRESS and ACS fuel injector impedance tests, and two sections showing the model predictions for modes of the CRESS and ACS designs in the AAC rig.

7.4.1 Impedance Measurement and Model for Counterrotating External Staged Swirler

Critical to any AC3D model is the ability to simplify the gridding of complex geometries. In this case the swirl nozzle geometry must be simplified so that enough memory exists to obtain a solution, while still maintaining sufficient resolution to capture the acoustics. To understand the gridding rules, a study was conducted using COMSOL to analyze the acoustic response without flow. Though a different acoustic solver (AC3D) will be used in the final analysis, COMSOL offered rapid turnaround to more quickly understand gridding tradeoffs.

At the top of ***Figure 7-35***, the final COMSOL grid is shown. The resolution in the vane passage is only one to two cells across the passages. The bottom of the figure shows the validation in terms of the impedance tube pressure ratio which shows remarkably good agreement. The gridding rules developed by this analysis were then implemented in the AC3D analysis.

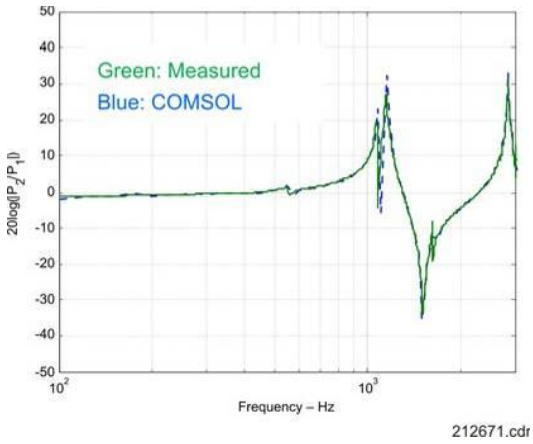

Figure 7-35. *Validation of Swirl Nozzle Geometric Simplification and Grid Resolution With COMSOL*

The COMSOL work provided basic gridding rules required for obtaining good results, but these rules required some additional fine tuning with the addition of flow gradients which are large in the injector region of the domain. The full annulus grid needed for the stability model requires a factor of 15 times more nodes.

Figure 7-36 shows the pressure ratio predictions for the two coarse grids. It is apparent that the first grid has more noise in the computation compared with the smooth response of the second grid. This is attributed to the improved resolution in the swirl vane region where resolving flow gradients is important.

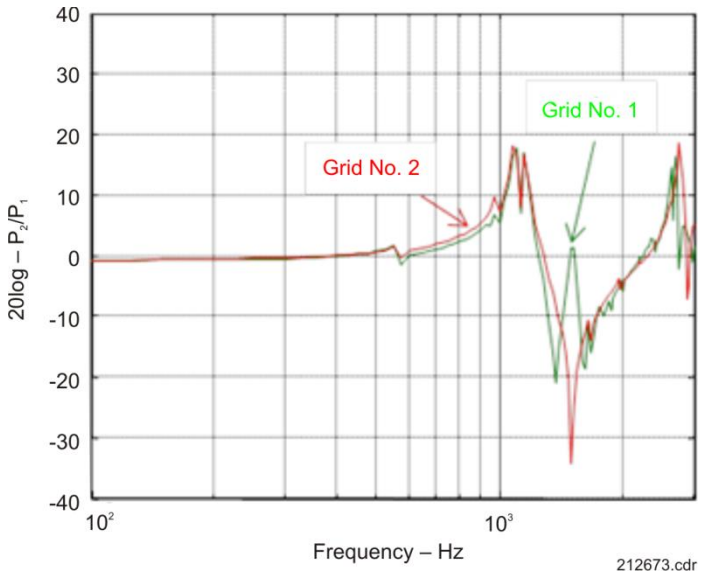

Figure 7-36. *Comparison of Pressure Ration Prediction for Two AC3D Grids*

Figure 7-78 shows the comparison of data with the AC3D computation for a range of pressure drops across the injector using the second grid. The AC3D solution is seen to capture the injector acoustic response quite well.

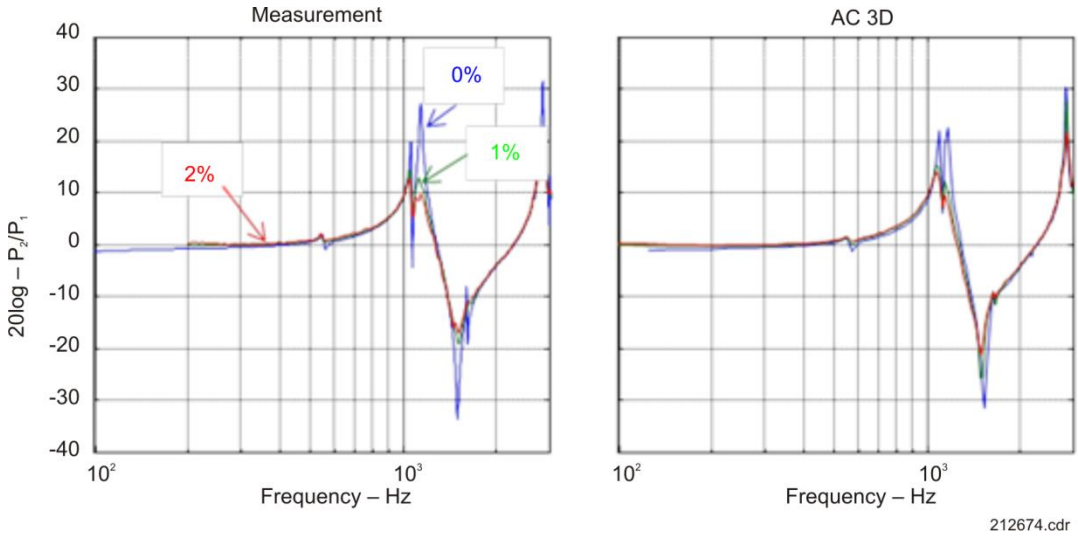

Figure 7-37. *Comparison of Impedance Tube Pressure Ration to Prediction by AC3D With Varying Flow*

With the confidence gained from modeling the CRESS injector in the impedance tube the next task was to obtain an AC3D model for the entire AAC rig. The important outcome of the impedance tube work was the development of AC3D gridding rules, which can be applied to the CRESS injector in the AAC rig.

7.4.2 Modeling of Counterrotating External Staged Swirler in AAC Rig

An AC3D model was developed for the AAC rig with a CRESS injector. The actual AAC rig is configured with two CRESS injectors, but only half of the domain (i.e., a single injector) was modeled in both the CFD and AC3D.

Since the model covers a relatively large volume including the plenum, the combustor, and a CRESS injector, the first AC3D grid contained 106,090 nodes, requiring 220 GB memory, which exceeded the largest-memory machine (64GB). Given that the CRESS injector mesh size had already been optimized in the CRESS impedance

tube tests, the mesh size of the plenum and combustor sections were adjusted to obtain a total number of nodes summing to 43,582. This node count required 38 GB of memory for no flow cases and 59 GB for cases with flow.

The mean flow was separately obtained from a Fluent CFD solution. This highly resolved flowfield is interpolated onto the coarse AC3D mesh, thus generating the AC3D geometry and flowfiles. Comparison between the AC3D and Fluent results shows that relevant velocity gradients and temperature distributions are still captured on the coarse grid which is important for capturing acoustic damping in the domain and the correct speed of sound distribution.

When studying combustion dynamics in rigs that do not have the same geometry as an actual engine, the goal is to configure the rig to have geometric features as similar as possible to an engine application. Historically this is achieved by installing a choked exit at the end of the combustion region to simulate the near choked condition of the turbine inlet. This provides a reasonable approximation of the longitudinal length, and thus a representative frequency band where combustion dynamics may occur in the actual engine. Obviously for annular combustors, one also needs to consider tangential modes, but longitudinal dynamics are the most that can be examined in a single sector rig such as the AAC rig.

It was anticipated that any dynamics testing in the AAC rig would require that a choked exit be installed. When design of a choked exit began, it quickly became apparent that the open area required for choking was 2.5 percent of the 3 in. × 5 in. test section area. This is due to the extremely low flowrate of the CRESS injectors. Given the difficulty in fabricating a choked exit to maintain such a small area, running the AAC rig with a choked exit for the CRESS configuration was abandoned. The implication of this decision is that the acoustic modes of the rig would be based on not only the length of the combustion region, but also the length of the exhaust piping, water spray, and back pressure valve.

From an acoustic modeling point of view it is very difficult to choose the appropriate exit boundary condition for such an exhaust system. Simple closed or open boundary conditions do not capture the complicated impedance of the exhaust duct, but modeling the complicated impedance is difficult as well. The most important issue in a combustion dynamics model is getting the acoustic mode shape correct in the region of the UHR. Away from that region the shape of the acoustic mode is not important. Using this knowledge, coupled with previous emissions testing in the AAC rig that indicated that the AAC rig with CRESS injector produced tonal behavior near 500 Hz, it was decided to use a simple open boundary condition and adjust the length of the AC3D domain to obtain a near 500 Hz mode.

With the mean flow interpolated onto the AC3D grid and a representative exit boundary condition selected, an eigenvalue search was executed to determine the modes of the AAC rig with CRESS injector. The upstream boundary condition was modeled as closed, and physically represented a perforated plate located in the upstream plenum. The mode shape indicates that at this frequency the upstream plenum does not participate. This is due to the fact that the effective area of the CRESS injector is small, thus the area ratio between the combustor and the injector is quite large. This area ratio makes the injector exit look acoustically closed to waves propagating in the combustor. This acoustically closed condition at the injector exit also results in a pressure antinode at the injector exit where the majority of the heat release occurs. This antinode would exist for any downstream boundary condition; therefore, the importance of the downstream boundary condition selection is not critical.

7.4.3 Impedance Measurement and Model for ACS Combustor Main and Pilot

As with the CRESS injector design, the most difficult piece of capturing the proper rig acoustic modes with the ACS design is modeling the injector. To gain confidence in the injector modeling, the ACS injector was tested in an impedance tube as well as modeled.

The impedance tube was modified slightly to adapt to the smaller ACS injector compared to the previous CRESS design. The reduced amount of hard wall area at the swirler exit plane (normal to sound wave propagation) produces better accuracy in the measurement. A standard 2-in. microphone spacing was used, along with a 2-in. distance from the downstream microphone to the impedance plane.

The AC3D model was developed and validated by the measurement. Grid simplifications were required for the ACS swirler to stay under the memory limitations of AC3D. This limitation requires a very coarse mesh, which initially produced poor results due to the high skewness factor around the ACS swirler vanes. To improve the skewness around the swirler vanes, the helical shape of vane passage was approximated by a straight passage of equivalent open area and length. This is similar to the meshing rules used for the CRESS AAC case.

With a reasonable grid which balances geometric complexity and memory limitations, a comparison can be made between the impedance tube tests and the AC3D solution. ***Figure 7-38*** shows the comparison of acoustic pressure ratios at varying levels of flow. The swirler impedance mode is observed at 2,000 Hz and the flow damping affect is well observed in both model and data. The mean flow for the impedance tube configuration was obtained using Fluent on the coarse AC3D grid. Some Fluent grid refinement was required to obtain reasonable results for the cases shown in ***Figure 7-38***.

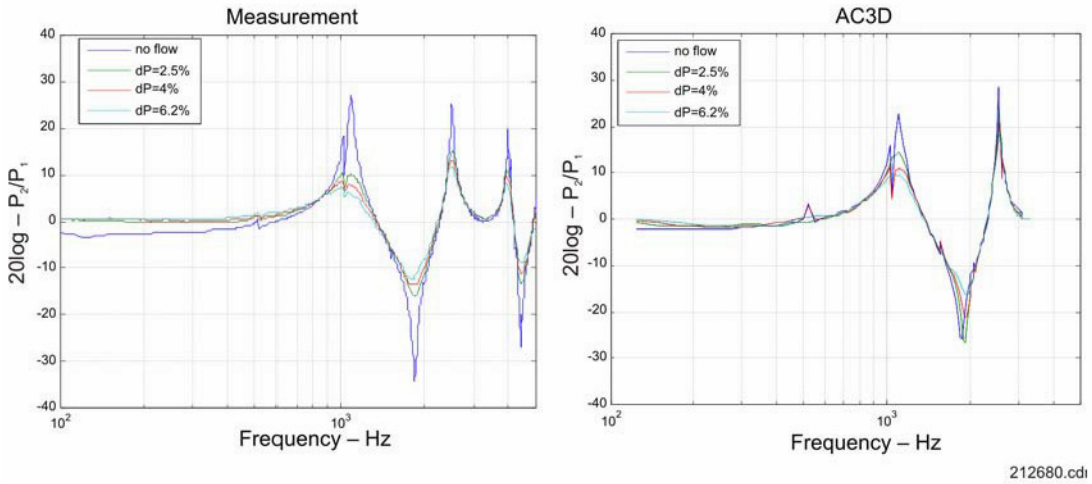

Figure 7-38. *Comparison of Data and Model for Counterrotating ACS Main With Varying Levels of Flow*

7.4.4 Modeling of Axially Controlled Stoichiometry Combustor Main and Pilot in AAC Rig

With the AC3D grid determined for the ACS main injector, a grid was generated for the ACS-configured AAC rig to obtain the rig acoustic modes. Again, the ultimate goal is to perform a stability analysis on the ACS configured AAC rig with a representative longitudinal combustor length. Unlike the CRESS-configured AAC rig, the flow rates for the ACS configuration are high enough for a choked exit to be practical. Due to the cost of resolving the entire domain, only one section was modeled, which consisted of three pilot tubes and two main injectors in the Fluent CFD as well as in AC3D.

The resulting AC3D analysis yielded two modes having mode shapes conducive to generating instabilities. These two modes are conducive to generating instabilities since they both have velocity antinodes near the main injector. This implies that the main injector fuel spray will see large amplitude velocity fluctuations if these modes get excited. Without additional analysis, it is difficult to determine which of the two modes is more likely to become excited. Without any experimental information, a decision was made to model the lowest frequency mode, since flames usually have a better response at lower frequencies. As with the CRESS case, the upstream plenum is effectively isolated from the modes in the combustor by the large area ratio between the combustor and the pilot.

Shown in ***Figure 7-39*** is a 1-D transmission line acoustic model. The result matches the AC3D analysis quite closely providing confidence that the modeling tools are capturing the right geometric and flow features of the rig.

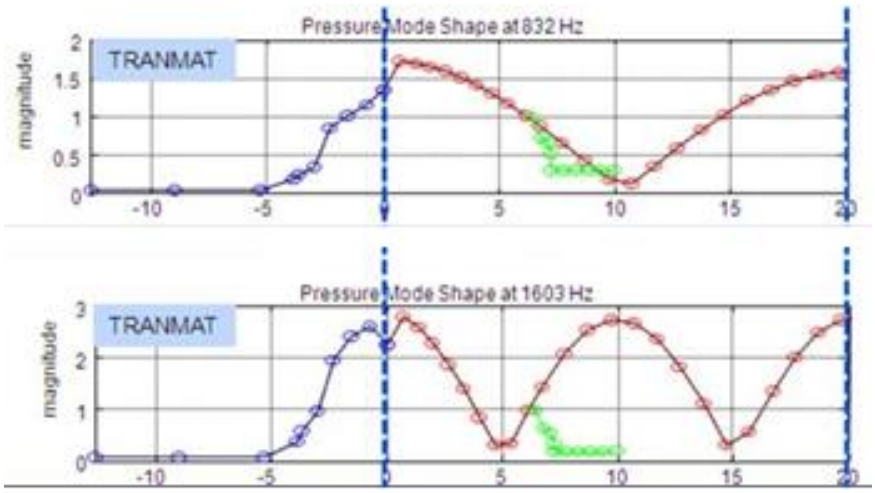

Figure 7-39. *AC3D Eigenvector for ACS in AAC Rig*

One additional acoustic modeling exercise was required for the system analysis. The boundary condition forced CFD requires the definition of a forcing level at the inlet boundary, but in the case of the ACS design there are two inlets, the pilot inlet and the main inlet. Using the 1-D model an analysis was completed to determine what the relative forcing amplitude and phase difference was between the two inlets. In an actual engine application, each inlet would be fed by a common plenum, but in the AAC rig they are fed by two separate air supply lines.

To construct a model both the pilot and main boundaries were set as nonreflecting (anechoic) boundaries, and a closed boundary was used for the choked exit of the combustor. ***Figure 7-26*** (shown in Section 7.3.4.3, *Flow Features in the Main Stage Injectors*) shows the pressure and velocity mode shapes for the acoustic mode. They indicate that the velocity amplitude in the upstream pilot plenum (blue) is much lower than the amplitude in the main injector (green). Because the Fluent calculation forces the mass flowrate at the boundary, the velocity is the parameter of importance. Given that the velocity ratio between main and pilot is quite large, there is no need to force both; rather only the main needs to be forced.

8. TASK 3.3.1 — SPRAY TESTING

8.1 SPRAY TESTING

8.1.1 8.1.1 Summary

The objectives of the ambient spray test were:

- To investigate the spray and mixing characteristics of several candidate fuel/air premixing fuel injectors
- To provide reference information to corresponding LES analysis.

The measurements were carried out on two different swirler/mixer designs, PICS and CRESS; and several enhanced Technology for Advanced Low NOx (TALON) X designs.

8.2 DESCRIPTION OF EXPERIMENTS

In the steady (unforced) spray testing, P&W used three techniques:

- PDI to concomitantly measure droplet size and velocity
- Mechanical patternation to investigate fuel distribution
- Line-of-sight droplet size measurement (Malvern).

Each of the fuel injection systems was mounted with its inlet inside a pressurized air plenum. A pressurized fuel line was connected to the fuel injector inside the plenum and the resulting fuel/air mixture issued into open atmosphere. A slight ventilating flow was present in this unconfined area to ensure the safety of the experiment. This facility has been described in detail in previous publications (McVey, J.B., Russell, S., and Kennedy, J.B., "High-Resolution Patternator for the Characterization of Fuel Sprays," AIAA Journal of Propulsion, Vol. 3, No. 3, May-June 1987, pp. 202–209). The measurements described below were made in this unconfined flow area. It should be noted that these results do not account for the effects of evaporation at higher temperature conditions, which may have an impact on their utility in predicting the reacting-flow performance of these devices.

The PDI measurements were carried out using a two-channel laser (532 nm and 660 nm), receiver, and processor system (Artium). Spatial survey along two orthogonal diametrical traverses (x and y with 0.05-in. resolution each) was achieved by moving the plenum using stepper motors in the cases of CRESS and CR-ACS. The two traverses yielded measurements of axial, tangential, and radial droplet velocities, as well as an assessment of droplet size uniformity as a function of spatial position within the spray. More detailed in-plane surveys were made by the traverses and the rotation of plenum for PICS.

The mechanical patternator (McVey, J.B., Russell, S., and Kennedy, J.B., "High-Resolution Patternator for the Characterization of Fuel Sprays," AIAA Journal of Propulsion, Vol. 3, No. 3, May-June 1987, pp. 202-209) has a circular array of 60 probing tubes, arranged along six radial arms, each of these having 10 individual probes with a probing area of 0.188 $in.^2$ each. The rotation of plenum by 10 degree step allowed sampling of total 360 in-plane points within a 2-in. radius.

The Malvern system was used for extracting representative droplet size information, averaged along the line of sight within the 0.5-in. laser beam diameter. While this measurement does not provide the spatial resolution of the PDI droplet size measurement, it does allow a quick assessment of atomization performance.

More detailed information was extracted from the patternation data, such as peak cone angle (spray incident angle corresponding to fuel peak), 90 percent cone angle (the angle which covers the 90 percent of fuel distribution) and eight-sector uniformity (a measure of circumferential uniformity of fuel distribution) by linearly extrapolating the fuel distribution measured from the patternation test. To track circumferential spray uniformity, the total flow collected by a virtual 45-degree sector, rotated through 36 azimuthal locations in the collection plane was calculated. The difference between the maximum and minimum values of this parameter was calculated and normalized by the average flow in a 45-degree sector to give a (maximum - minimum)/average ([max - min] / avg) value in the collection plane. This is a quantitative indicator of the circumferential uniformity of the spray (lower is better, higher is worse).

FAR was also computed as an indicator of fuel/air mixing. Again, it should be noted that all the fuel accounted for in this calculation was liquid fuel. Because the experiments were conducted at ambient temperature, there was little vaporization. For this calculation, air flux was extracted from PDI measurements assuming that small droplets (less than 10 to 15 μm) could represent gas velocity. Fuel flux was directly measured from the patternation experiment. The resulting FAR was normalized by the metered FAR, and then multiplied by the normalized (by its maximum) local fuel flux. These treatments eliminated misleadingly high FAR in regions with both low fuel and air fluxes (e.g., spray center) and they allow a fair comparison among swirlers which have different fuel and air flow conditions.

8.2.1 Pilot-in-Can Swirler Results

The air velocity and the fuel flowrate were set to the air velocity and the liquid to air momentum flux ratio at the 85 percent LTO condition. Only the main injection system was used in these tests to measure the ability of that circuit to achieve uniform fuel/air mixing. Later in this section, the results at the 7 percent LTO condition (pilot only) will also be presented.

Figure 8-1 gives photographs of the spray at the simulated 85 percent LTO condition (left). The right-hand image in ***Figure 8-1*** shows the spray at half the fuel flow of the 85 percent LTO condition (same airflow rate). Some remnants of the discrete fuel jets can be observed in the photograph on the left at these ambient pressure and temperature conditions. The fuel streak is less obvious in the half fuel case (photograph on the right).

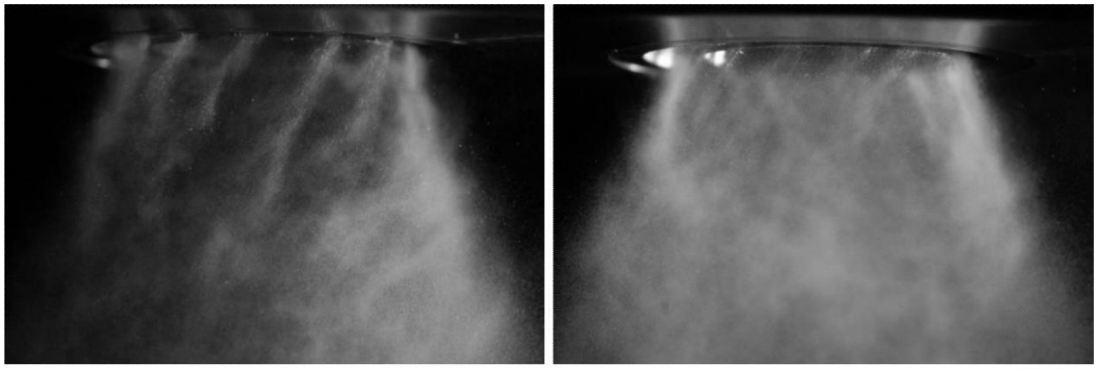

Figure 8-1. *PICS Main Spray at Simulated 85 Percent LTO Condition and Lower Fuel Flow Condition*

Figure 8-2 provides patternation results at two axial locations, 0.2 in. (left) and 1.1 in. (right), at the 85 percent LTO flow condition (top) and the half-fuel condition. A scaled fuel volume flux is plotted in these contours. The fuel jets are distinct at the 0.2-in. location. The jets have merged more by 1.1 in. For the lower fuel flow case, the jet characteristic significantly disappears at both axial positions. These results are consistent with the photographs in ***Figure 8-1***.

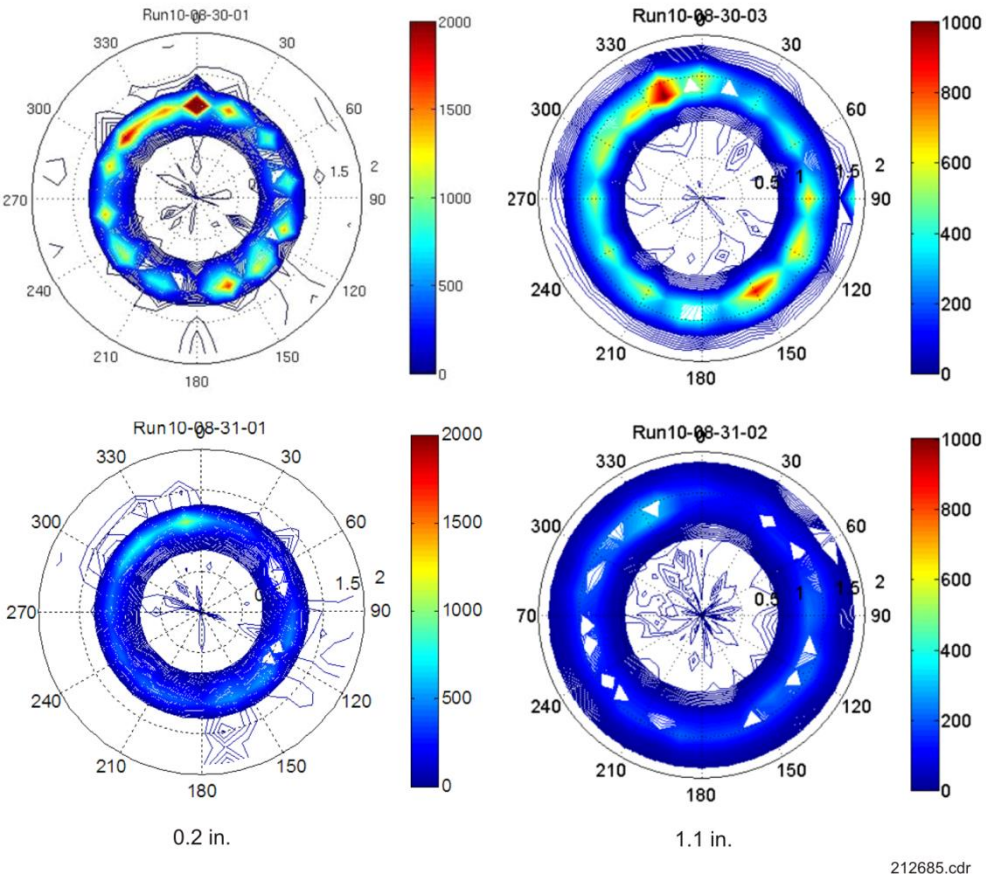

Figure 8-2. *PICS Main Patternation at Simulated 85 Percent LTO Condition and Half-Fuel Condition*

Figure 8-3 plots the normalized, circumferentially averaged volume flux versus radial distance for the 85 percent LTO (top) and the half-fuel flow conditions (bottom). As expected for a droplet-laden swirling jet, the peak of the volume flux moves radially outboard and the peak value decreases as the axial location goes from 0.2 in. to 1.1 in. However, there was no trendwise difference observed between the two fuel flowrates. Ninety-percent cone angles (the angle within which 90 percent of the liquid was collected, adjusted for the origin at the swirler radius) were approximately 70 degrees in both cases. The angle corresponding to the peak of the spray volume flux distribution was approximately 50 degrees in both cases.

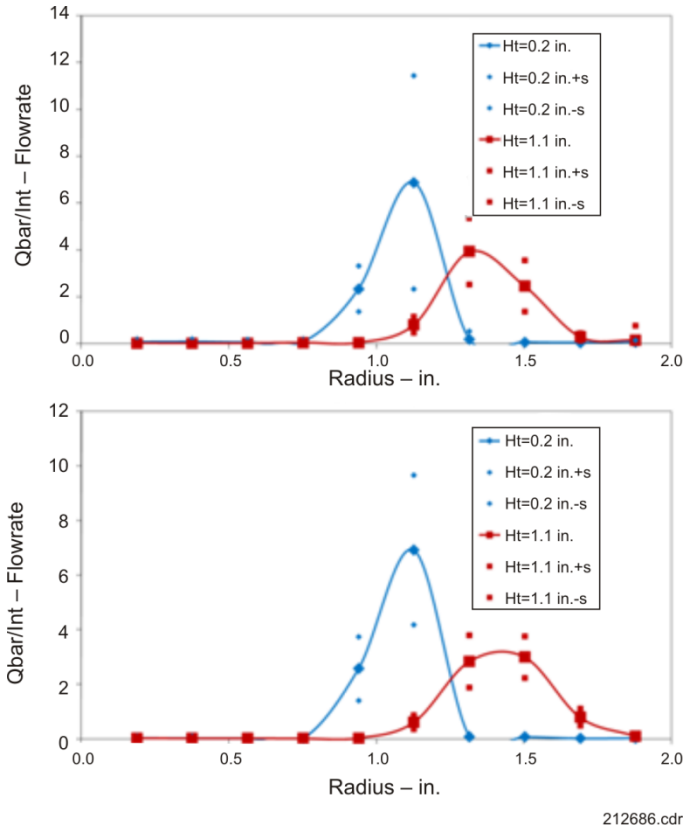

Figure 8-3. *PICS Main Normalized Circumferentially Averaged Volume Flux as a Function of Radial Location*

PDI measurements were made in a 76-degree sector at axial locations of 0.2 and 1.1 in. The mean droplet sizes in this sector at 0.2 in. downstream and 1.1 in. downstream were 40 µm and 38 µm, respectively, in the case of the 85 percent LTO flow condition. Slightly lower mean droplet sizes, 35 µm (0.2 in.) and 33 µm (1.1 in.), were observed in the half-fuel flow condition, as qualitatively seen in ***Figure 8-1***. For both heights, more uniform SMD distributions were observed in the half-fuel flow condition. This uniformity was primarily due to the presence of discrete fuel jets in the full-flow condition, as observed in the patternation plots and photographs.

The more uniform flowfield of the half-fuel flow condition can also be confirmed by the axial velocity profiles which were taken. While the values of spatially averaged axial velocity do not show a significant difference for either flowrate and for either height (50 to 55 m/s), the simulated 85 percent LTO flow condition data has a lower axial velocity region which corresponds to the high SMD region in the previous figure. As a result, a less uniform axial velocity profile exists for this condition than for the half-fuel flow condition.

Figure 8-4 shows a photograph of the pilot spray at the simulated 7 percent LTO condition (left) and corresponding patternation result (right) at 1.1 in. downstream of the swirler exit. The air pressure drop across the swirler and the fuel flowrate were 1.3 psid and 40 lbm/hr, respectively.

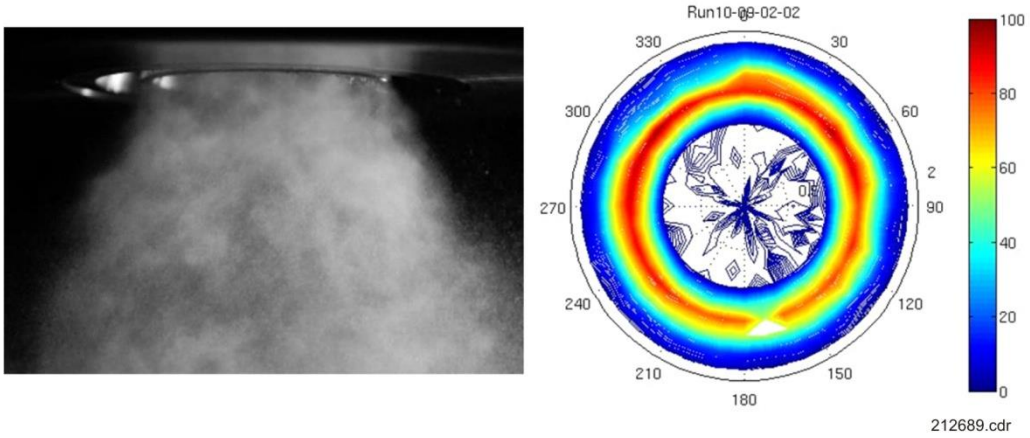

Figure 8-4. *PICS Pilot Spray Photograph and Fuel Distribution at Simulated 7 Percent LTO Condition*

The pilot spray was circumferentially very uniform at the simulated 7 percent LTO condition. The peak cone angle (approximately 50 degrees) and 90 percent cone angle (approximately 70 degrees) were similar to those measured for the PICS main stage.

8.2.2 Counterrotating External Staged Swirler Results

Two CRESS swirlers were tested. The ACd of the large CRESS) was designed to be 50 percent larger than that of the small CRESS since they were intended to be used in different stages of a combustor. A 4-in. and an approximately 20-in. ID air plenum were used for the Large and Small CRESS, respectively. Again, the simulated 85 percent LTO flow condition matched the air velocity and fuel jet momentum ratio for both geometries.

Figure 8-5 shows a photograph of the fuel spray emitted from the large CRESS for the simulated 85 percent LTO condition (49.5 in.-H2O air pressure drop and 23.4 pph fuel flow). Similar to the PICS, fuel streaks are observed in the ambient flow condition from the CRESS. These trace to the discrete injection locations within the device.

Figure 8-5. *CRESS Spray Photograph at Simulated 85 Percent Condition*

The measurement heights for Malvern (droplet size measurement), patternation, and PDI were 1.1 in. and 0.63 in. downstream from the swirler exit. Malvern results showed that there was no significant difference of SMD between the upstream (16.1 µm) and the downstream (16.6 µm) measurements.

Figure 8-6 gives the fuel distribution at both planes. As expected, the fuel distribution moved radially outward at the downstream location. The spray had slightly better circumferential uniformity ([max - min]/avg = 0.47) at the upstream location than at the downstream location ([max - min]/avg = 0.62). The peak and 90 percent cone angles for each height are approximately 10° and approximately 85° at z = 0.63 in. and approximately 20° and approximately 67° at z = 1.1 in. The change in cone angles is visible in the spray photograph in ***Figure 8-5*** as an inflection point in the spray cone.

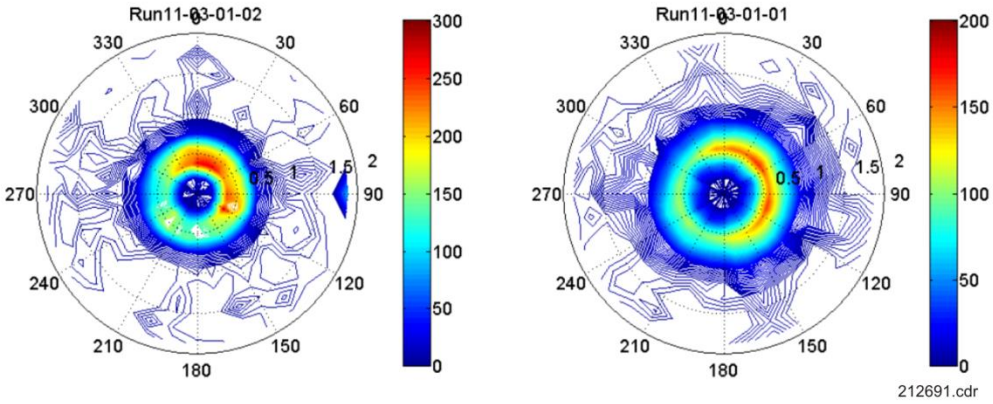

Figure 8-6. *Fuel Distribution of Large CRESS at 0.63 in. and 1.1 in. Downstream*

Figure 8-7 shows a normalized fuel distribution along the radial direction (circumferentially averaged) of both heights. As seen in ***Figure 8-6***, the peak of the volume flux moved radially outboard and the peak level decreased between z = 0.63 in. and z = 1.1 in.

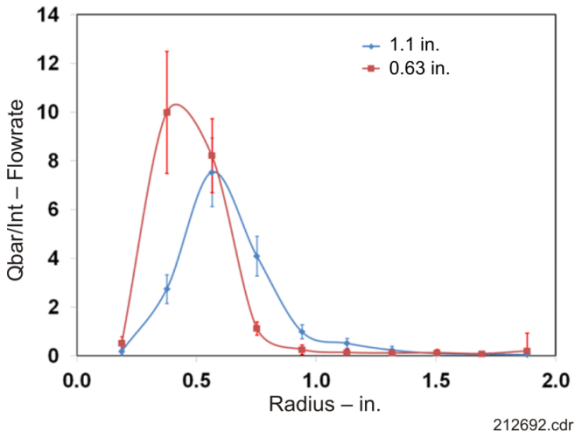

Figure 8-7. *Normalized, Circumferentially Averaged Fuel Volume Flux as a Function of Radial Location, Large CRESS*

The droplet SMD and axial velocity profiles measured by PDI are shown in ***Figure 8-8***. Unlike the PICS case, only two traverses (x, coordinate across the fuel injection orifice, and y, between adjacent two orifices) were performed. Both SMD and axial velocity were reasonably symmetric for the x- (+ mark) and y- (o marks) traverses and at the two axial planes, 0.63 in. (red) and 1.1 in. (blue) (the asymmetry of the right wing in the SMD plot is not that meaningful since fuel flow is minimal in that region). Regarding the axial velocity profiles, two observations are noteworthy: velocities in the upstream are slightly higher than those in the downstream at specific radial location; velocities across the entire region are positive, both of which imply that the size and strength of any recirculation zone from CRESS is small and weak.

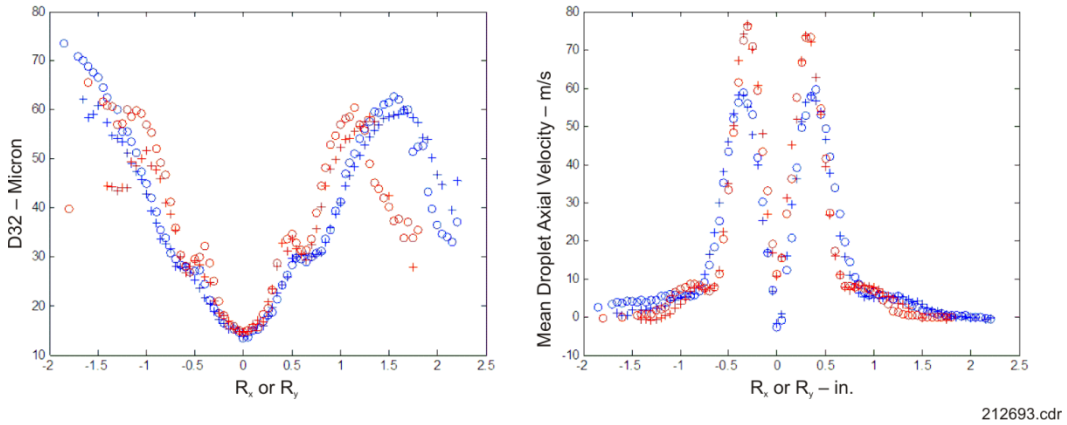

***Figure 8-8**. Radial Distributions of SMD and Droplet Axial Velocity of x and y Traverses, Large CRESS*

8.2.3 Small Counterrotating External Staged Swirler

The scale of fuel and airflow conditions for the small CRESS were 15.6 pph fuel flow and 49.5 in.-H_2O air pressure drop, respectively. The heights of patternation, Malvern, and PDI measurements were 0.5 in. and 1.1 in. downstream from the CRESS exit.

Figure 8-9 shows a representative photograph of the fuel spray injected from the small CRESS. In comparison with the large CRESS case, the current fuel spray cone diverges more significantly.

***Figure 8-9.** Small CRESS Spray Photograph at Simulated 85 Percent LTO Condition*

Figure 8-10 shows the fuel distribution acquired from the patternation test, from which the more radially outboard fuel distribution in the downstream is clear. The circumferential uniformities of both heights are slightly better than those of large CRESS. As shown, the width of fuel cones in the current geometry is not significantly larger than those in the large CRESS geometry. Peak and 90 percent cone angles were approximately 15 degrees and approximately 110 degrees, respectively, at z = 0.5 in., and approximately 15 degrees and approximately 70 degrees, respectively, at z = 1.1 in.

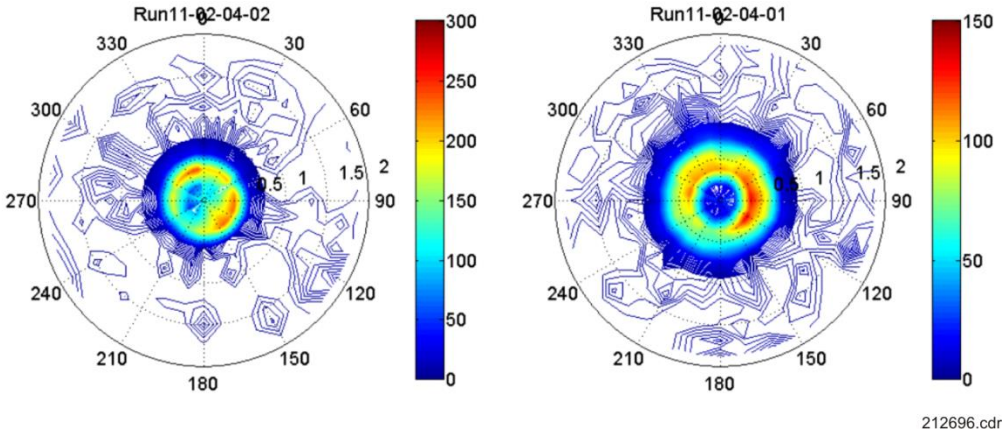

Figure 8-10. *Fuel Distribution of Small CRESS at 0.5 in. and 1.1. in. Downstream*

Figure 8-11 shows the normalized fuel distributions along radial direction of both heights. Unlike the large CRESS, the difference of fuel-peak radial locations of the two heights is not significant and the values of the peaks are both higher than those of the large CRESS.

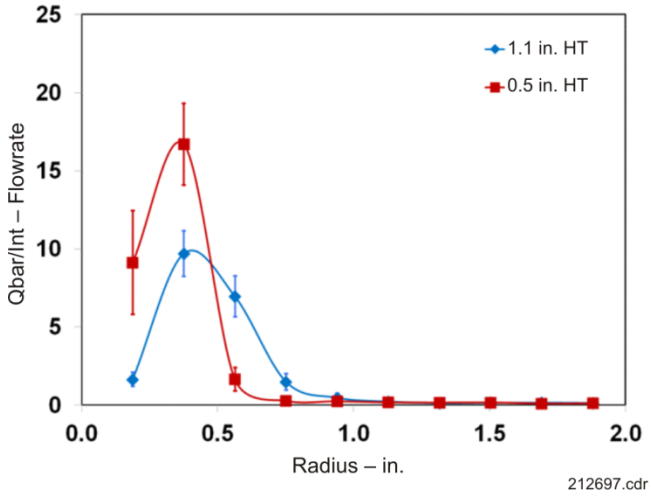

Figure 8-11. *Normalized, Circumferentially Averaged Fuel Volume Flux as a Function of Radial Location, Small CRESS*

Figure 8-12 shows the SMD and axial velocity of droplets along the radial coordinates. As observed in the large CRESS, the results of all traverses were symmetric. The center region of the SMD plots shows noticeable difference between the two heights. Meanwhile, the SMDs in the outer region are very similar for both heights. The axial velocity profiles confirm the two facts already observed in the large CRESS: higher peak velocity at the upstream plane and very weak recirculation zone (if any) at the center of the flowfield.

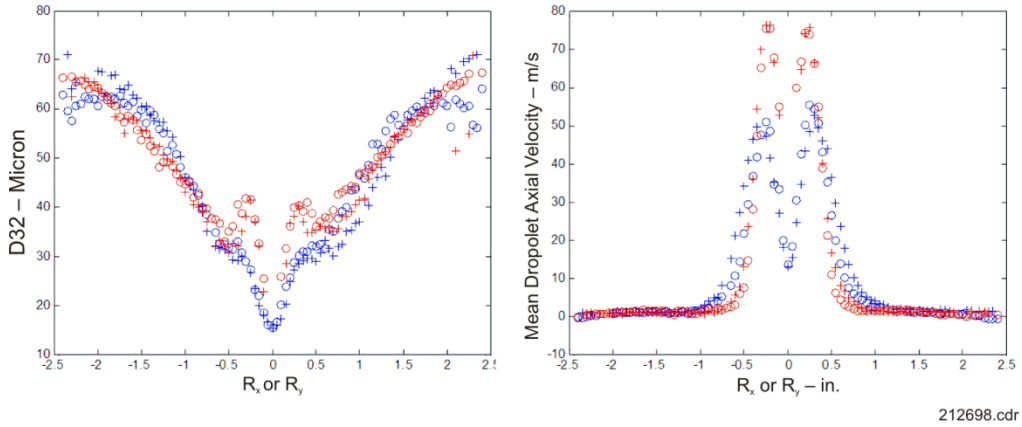

Figure 8-12. *Radial Distribution of SMD and Droplet Axial Velocity of x and y Traverses, Small CRESS*

The effective FAR for the small CRESS is shown in ***Figure 8-13***. Their peak values, approximately 0.65 at 0.5 inch and 0.35 at 1.1 inch, are both lower than those of large CRESS. The lower FARs imply that the air and fuel flux peaks were better aligned with the small CRESS than with the large CRESS, from which one can judge that the small CRESS is a better mixer than the large CRESS.

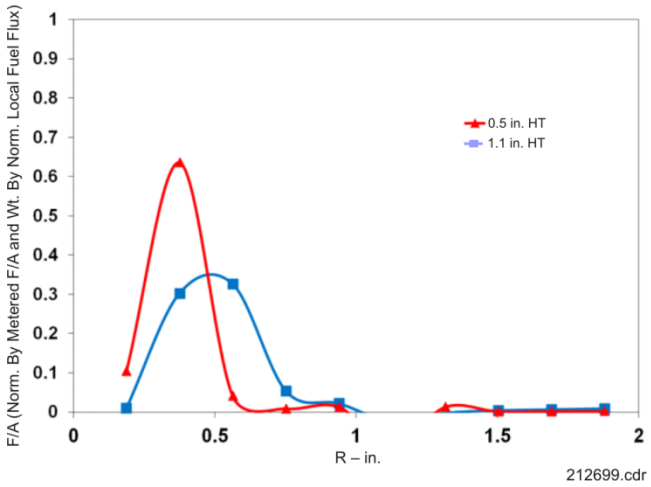

Figure 8-13. *Radial Distributions of Modified FAR at Two Different Heights*

8.3 TALON-XE FUEL SPRAY CHARACTERIZATION

8.3.1 Background

TALON X effort is achieved through improved front-end mixing and bulk stoichiometry. Under the NASA Advanced Small Turbine (AST)/Ultra-Efficient Engine Technology (UEET) program, combustor size and feature control were explored. Combustor size development was performed to discover the limit of the combustion residence to achieve minimal NOx emissions, while still achieving excellent combustion efficiency.

Feature control identified the proper hole pattern that produced the optimal mixing of quench jets with the approaching rich fuel-air mixture. Under the NASA N+2 program, the cost-share portion of the contract explores the front-end mixing quality through new and improved nozzle designs and bulk stoichiometry control, which involve detailed airflow distribution from the front end of the combustor. Uniformity of fuel-air mixture in the primary zone will minimize smoke and NOx emission. The effort in this task was spent on two categories. The first was to improve front-end mixing via nozzle type, front-end cooling, and swirl profile. Nozzle size and number are not explored due to application in existing core size. The second is bulk stoichiometry by changing cooling, front-end, and bulk lean FARs. Number of quench holes is not explored, since it was explored in feature control under the AST/UEET effort.

Improving fuel-air uniformity and enriching the front end will reduce NOx emissions. The NOx production rate tends to be higher at the rich and lean FAR. The excessive smoke limit also occurs at a lower FAR. The objective of the enhanced TALON-X is to achieve the mixing of least NOx production. At Point 1, the poorly mixed front end produces NOx emissions at a high rate and is at the smoke limit. By improving the fuel-air uniformity , the excessive smoke limit has increased and allows the primary zone to operate at a higher FAR to minimize NOx emissions contribution.

8.3.2 Swirler Concepts

There are three classes of swirler designs that had been designed to improve mixing. They are the airblast injectors, radial inflow swirlers called 3Px, and a hybrid of the two where the outer swirler is radial-inflow and the inner swirler is an axial helical vane swirler.

The new airblast injector has two outer swirlers that are counterswirled to generate turbulence; thus, they are called counterswirling airblast. The controlling parameters in the counterswirling airblast injectors are the outer airflow split and swirl strength. The outer swirling passage variant provides spray-angle control of the fuel injection. The atomization mechanism is the same as other airblast injectors, where slow moving liquid fuel is sheared between the outer and inner high velocity streams.

Six variations of the counterswirling airblast injectors were designed and assessed for spray performance. The inner swirler remained the same on all configurations. The changes are on the OD and OD2 passages where the parameters are flow direction (counterclockwise [CCW] or clockwise [CW]) and flow splits.

The 3Px swirlers are made of three radial streams of airflow. The fuel injector passes through the center of the swirler and injects fuel radially outward toward the swirl cup. The inner swirler is made of two counterswirling flowstreams. The counterswirler flowstream generates turbulence to enhance mixing. The radial fuel jets are first shattered by the oncoming airflow and followed by secondary atomization at the exit of the swirl cup, with airflow from the outer and inner swirlers. The design varied the magnitude of the counterswirl angle differences and the airflow split between the two inner passages. The design process also determines the mixing effectiveness of the swirl cup exit edge treatment with a fanglike shape. There are other one-off designs that were characterized. One of them is a swirler treated with chevrons to enhance mixing. Another one-off swirler is the 3P-2549. with a counterswirling passage is a ring of angled holes around the swirl cup. The intent is to have a direct air injection near the radial jets of fuel that will interact. The other 3Px swirlers have a lower counterswirl momentum interaction, since the airflow is introduced further upstream.

The last swirler design is a combination of the previous designs, called the hybrid airblast. The outer passages are that of the 3Px while the inner passage is that of the airblast injector. The variation is the center nozzle immersion and radial inflow swirler design. The were four variations of the radial inflow swirlers that were mated with the airblast filmer center. One of the swirlers is Swirler 1 from the 3Px matrix. The others were two-passage radial inflow swirlers, which do not have the counterswirling passage to generate turbulence.

8.3.3 Diagnostic Equipment

In order to characterize the fuel injection system design, three types of measurements are acquired to assess the spray performance. The first measurement is the ambient patternation test. ***Figure 8-14*** shows a diagram of the ambient spray patternation rig. It uses the fixed 60-point rake to measure the circumferential uniformity and angle of the liquid spray. It also provides the radial fuel flux distribution. The second measurement is PDI, shown in ***Figure 8-15***. The PDI equipment uses the atomized fuel as seed to measure the axial and tangential air velocity and droplet size distribution. With the radial air velocity distribution overlain onto the radial fuel flux distribution, a radial fuel-air uniformity can be determined. The third measurement is Malvern, which measures the average SMD through the center of the spray. The intent of this measurement is to assess the average SMD during starting condition.

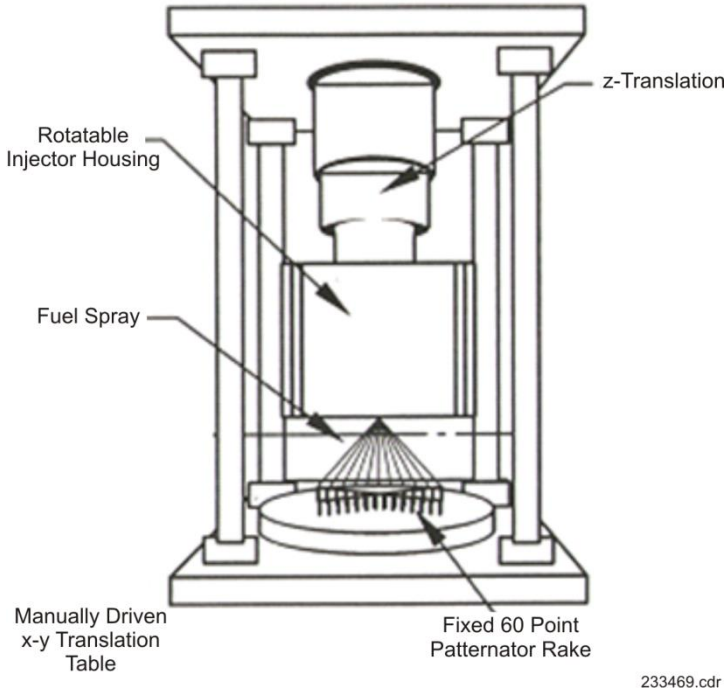

Figure 8-14. *Ambient Spray Patternation Rig*

Figure 8-15*. PDI Equipment*

The performance condition selected to simulate for this ambient spray testing is sea-level static takeoff. First, the air velocity is matched to the condition, followed by fuel to air momentum flux ratio. The typical percentage pressure drop across the fuel injector is about 4 percent of compressor discharge pressure. At takeoff inlet temperature, that translates to 0.24 Mach number. However at ambient temperature, the Mach number will have to increase to match the reference velocity. After the reference air velocity is set, the fuel flowrate is determined by the required momentum flux ratio of the fuel to air at the takeoff condition.

Examples of the fuel spray data taken by patternation and PDI are shown on ***Figures 8-16*** and ***8-18*** at 1.1 in. downstream of the swirler. ***Figure 8-16*** shows the overlay of the axial velocity and liquid fuel spray flux radial distribution. The overlay of profiles define the radial uniformity of FAR. The axial velocity and liquid spray flux profiles can be integrated and normalized to a fractional flowrate at each radial position. An example of the result

of the normalization is shown in ***Figure 8-17***. The integration of each curve should equal one. To differentiate which set of curves belongs to the better performer, a new parameter called the sum of weighed deviation (SWD) is introduced.

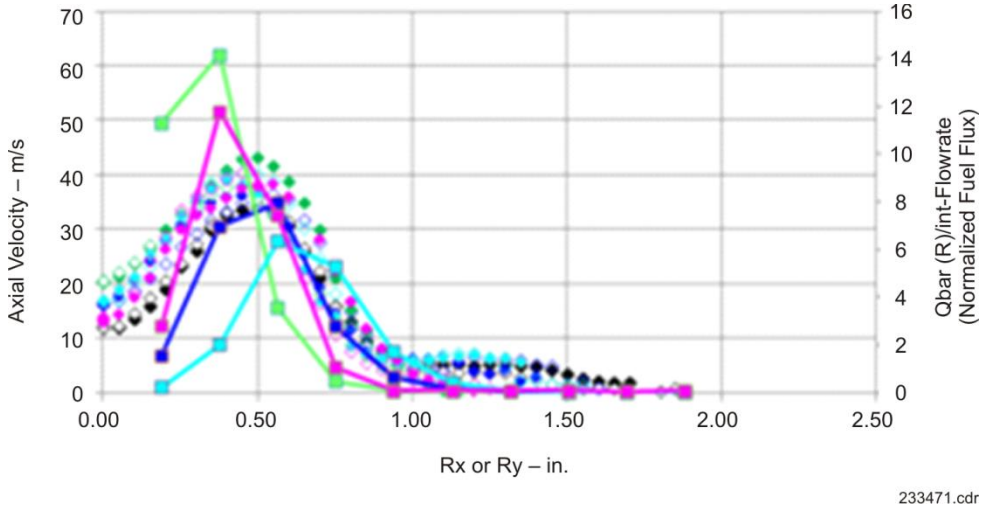

Figure 8-16. *Overlay of Radial Fuel Flux and Axial Air Velocity Distribution*

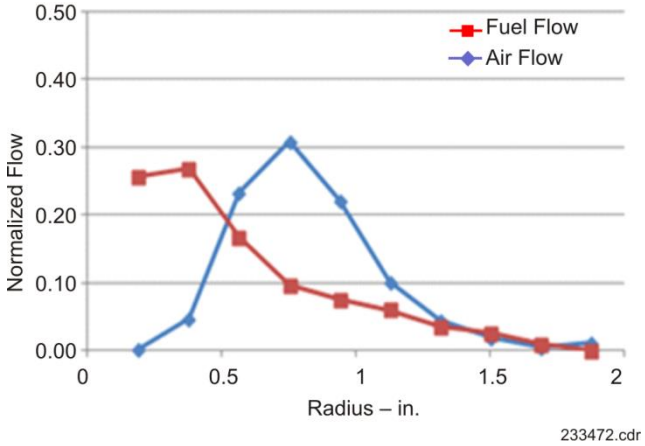

Figure 8-17. *Overlay of Normalized Fuel and Airflow Profile*

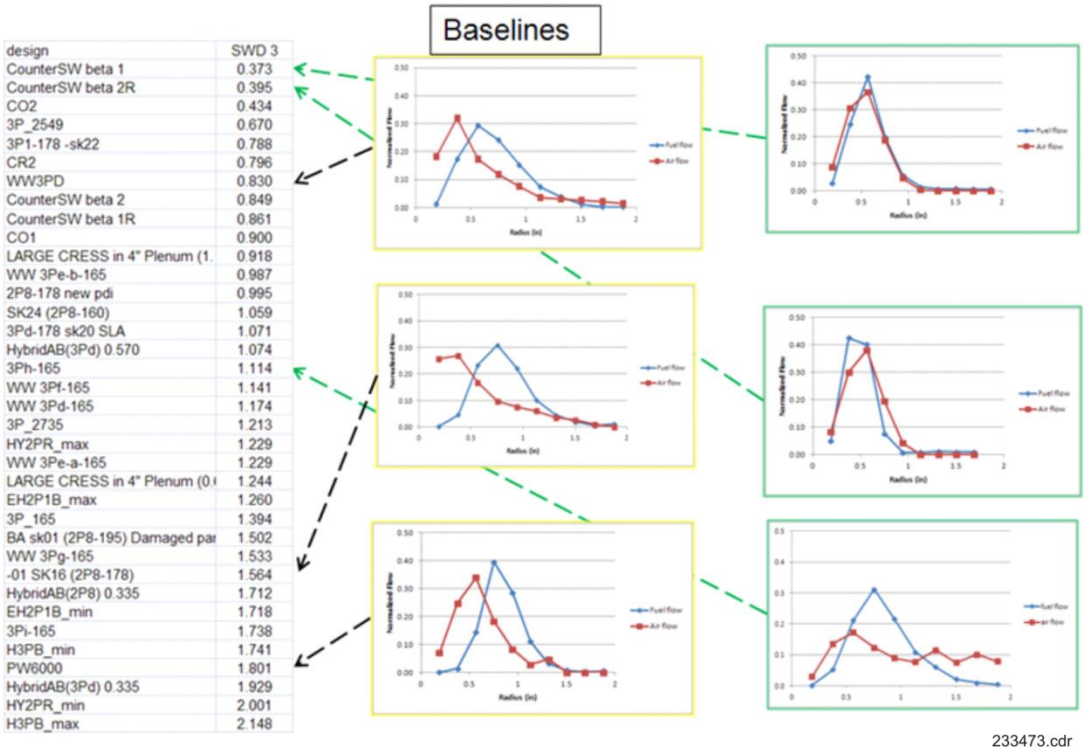

***Figure 8-18**. SWD Values of Various Designs*

The SWD parameter provides the quality of mixedness between the liquid fuel and airflow. A lower SWD for a given mixer implies better mixing.

Figure 8-18 summarizes the SWD values of various designs and shows how the set of normalized fuel and airflow profiles looks for good SWDs as well as bad. The best performers are the counterswirling airblast injectors. The worst are the hybrid airblast injectors. For hybrids, the majority of the fuel tends to be in the secondary breakup at the swirl cup, rather than in the primary breakup at the filmer. The best of the 3Px is the 3P2549, with the unique introduction of the counterswirling holes. The radial profiles for the 3P2549 is shown in ***Figure 8-19***. Though the profile is not an exact match, like the counterswirling airblast injector Beta 1, the distribution is an improvement over other 3Px, because the peak flow occurred at the same radial position.

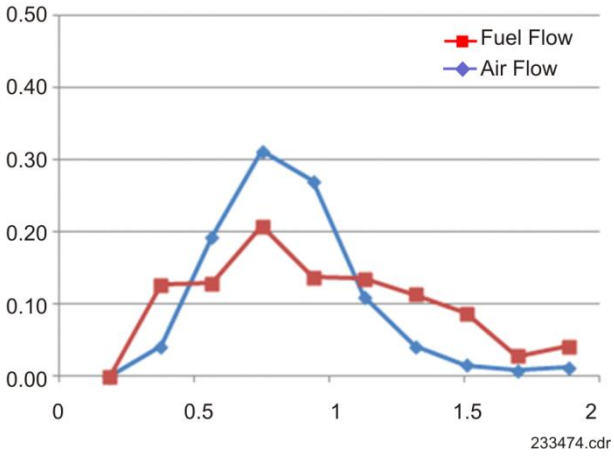

***Figure 8-19.** Normalized Fuel and Airflow for 3P2549*

The quality of the spray can be observed by the other result that patternation provides. ***Figure 8-20*** shows the overlay of SMD distribution versus fuel flux, which provides the SMD at the highest fuel flow position. The data in ***Figure 8-20*** applies to the counterswirling airblast fuel injector. Note that the different combination of the OD1 and OD2 swirlers controls the spray angle. ***Figure 8-21*** provides the circumferential uniformity quality.

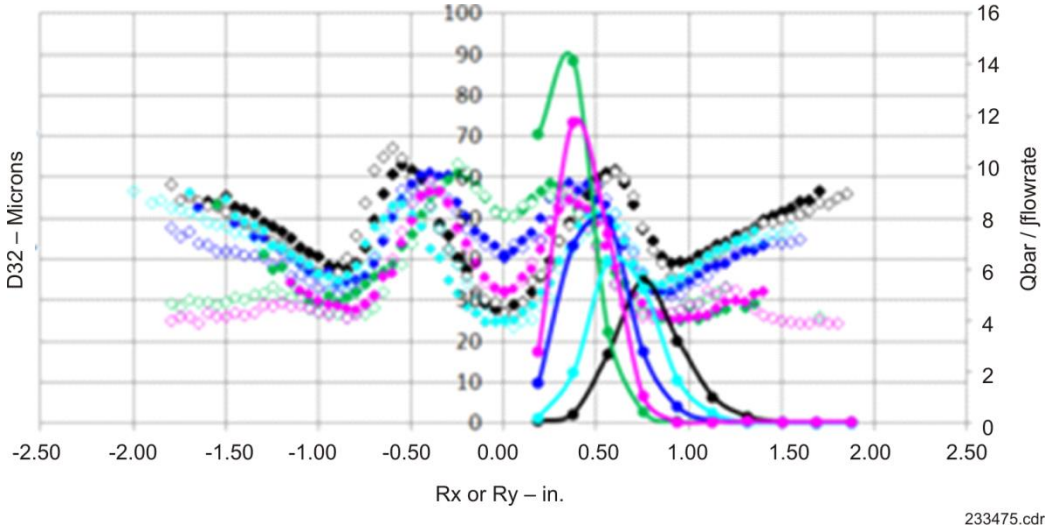

Figure 8-20. *Overlay of Radial Fuel Flux Distribution and SMD*

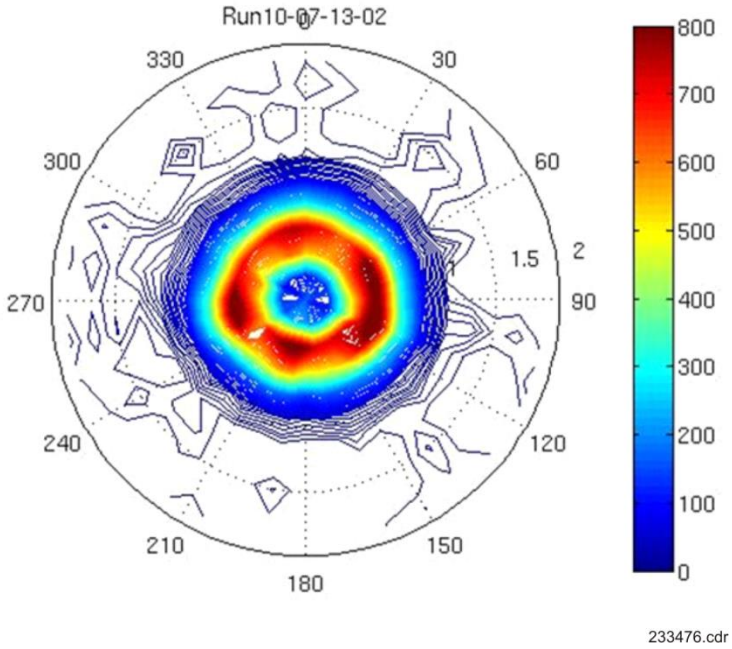

Figure 8-21*. Contour Plot of Liquid Spray*

A typical parameter that represents circumferential uniformity is circumferential uniformity = (max - min)/average.

In ***Figure 8-21***, one can discern eight bins overlaid on the spray contours. The contours are a processed data representation of fuel spray with the patternation rig. Each bin calculates the mass of collected fuel flow. The above equation takes the difference of the maximum fuel flow in one bin and minimum fuel in another and divides it by the average of the eight bins. A high value would represent high circumferential nonuniformity from the swirler and injector combination.

For starting condition, the air side pressure drop is set at 5 in. of water, and the fuel flow is set at 10 lb/hr. This is one of many typical starting conditions for a jet engine.

Based on the SWD and spray characteristics, five swirlers were selected to be tested in the NGPF five-sector arc rig of a TALON-X combustor (***Figure 8-22***). The aim of the selection is to validate the trend of the ambient test parameters against the emissions performance at high pressure.

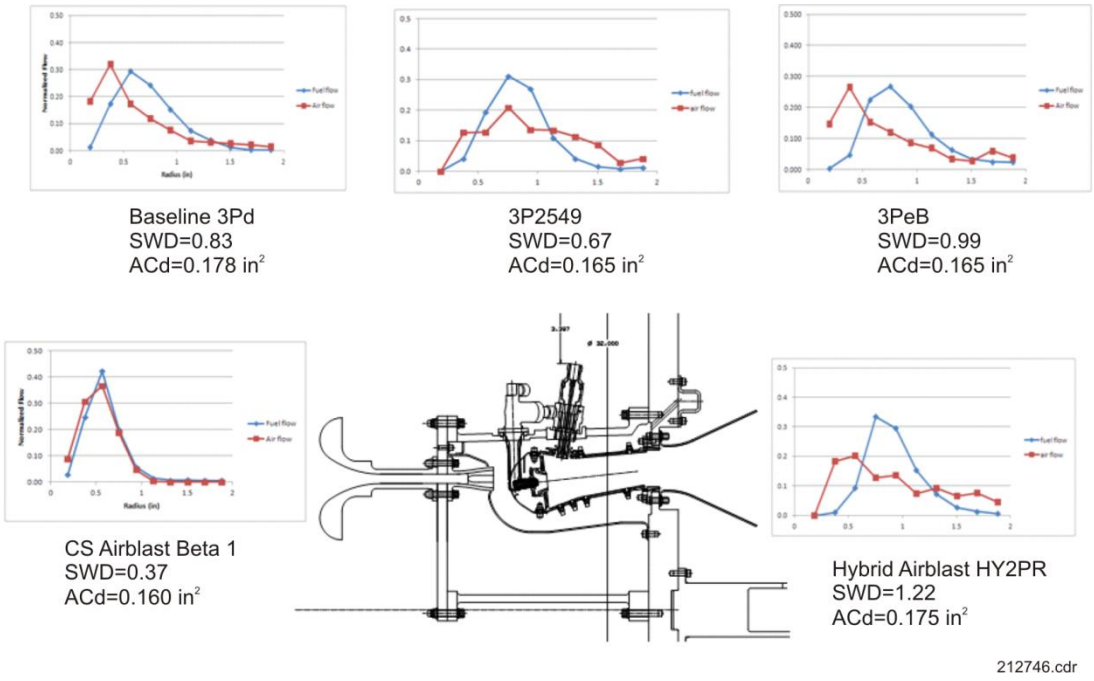

Figure 8-22. *Five Injectors Selected to Test*

9. TASK 3.3.2 — INTERNAL MIXER TESTING

An experimental effort was completed to investigate the impact of high levels of crossflow air turbulence on the atomization and mixing of a high-Weber number liquid jet. Main fuel injector/mixers for the axially controlled stoichiometry (ACS) combustor use high-Weber number liquid injected into a highly turbulent crossflow to enhance atomization and mixing. The effect of this very high-turbulence flow on a high-Weber number liquid jet has not been previously characterized.

Free stream turbulence in the crossflow air was generated by passing the flow over a grid formed by 1/8 in. diameter round or square bars). Turbulence intensities and length scales were characterized at various distances downstream of each grid configuration by using a hot film anemometer, with no liquid fuel injection. The desired turbulence level was then specified at the plane of the injection orifice by setting the proper distance between the grid and the orifice. Four configurations were used, providing different levels of turbulence intensity: approximately 3, 9, 15, and 25 percent.

Figure 9-1 shows turbulence intensity profiles downstream of round and square bar grids. Four points were chosen to evaluate liquid jet breakup: no bars, (3 percent turbulence, Point 1), round bars in 6 × 6 pattern (9 percent turbulence, Point 2), and square bars in 8 × 8 pattern (15 and 25 percent turbulence, Points 4 and 5 respectively).

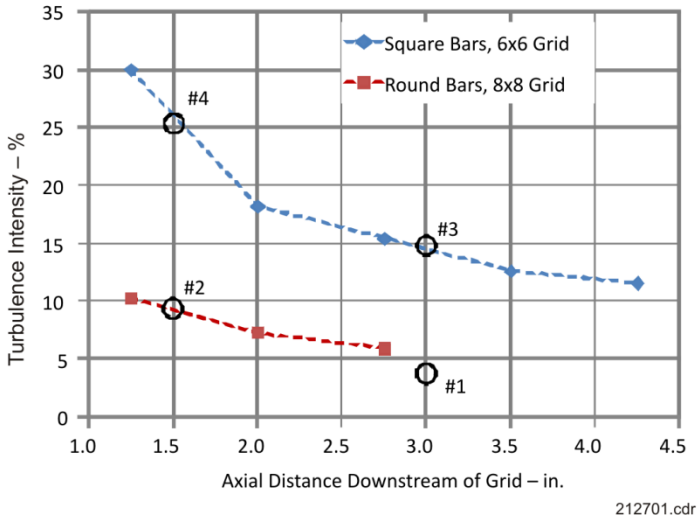

Figure 9-1. *Turbulence Intensity Profiles Downstream of Round and Square Bar Grids*

Liquid Jet-A was injected through a plane orifice. The target flow conditions are summarized in ***Table 9-1.*** PDI was used to measure droplet size and velocity distributions at two axial planes (0.75 in. and 1.75 in. downstream of the jet orifice). High speed shadowgraph movies were recorded with a Phantom v12 camera at 20,000 frames per second.

Table 9-1. *Target Flow Conditions*

Fluid	Jet A
Orifice Diameter (in.)	0.039
U_{Liquid} (ft/s)	70
Re_{Liquid}	12,000
U_{air} (ft/s)	400
Mom. Flux Ratio	20
We[1]	750
Oh	0.01
Air Turbulence	3 to 25%

Analysis of the data indicates an improvement in droplet dispersion for increased crossflow air turbulence. More spray remains downstream and behind the liquid column for the high-turbulence case. This is reflected in the PDI measurements of droplet size (***Figure 9-2***), which show a wider spray plume downstream of the liquid jet for the high turbulence case. Additionally, the high speed videos show larger-scale disturbances on the upwind-side of the liquid column, which may have an impact on the column breakup. This data set continues to be the subject of analysis, including the examination of velocity distributions for various droplet sizes, as well as the temporal fluctuations of the spray droplets interacting with the air turbulence.

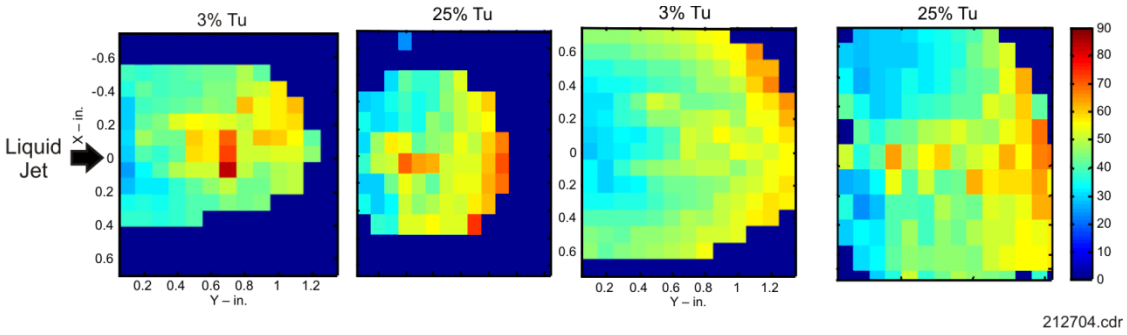

Figure 9-2. *Measured Droplet Size Distributions for Low and High Crossflow Air Turbulence*

Additional tests were conducted at various other Weber numbers spanning the various jet breakup regimes (We = 3, 10, 25, 50, 100, 250, and 750), both with low and high crossflow turbulence. A notable case was at We = 25, where a distinct difference in flow behavior was observed. Here, the air turbulence appears to promote an earlier onset of bag breakup and droplet stripping.

[1] We based on U_{air} and orifice diameter.

10. TASK 3.3.3 — SINGLE-SECTOR REACTING TESTING

10.1 ADVANCED AEROENGINE COMBUSTOR FACILITY

The AAC facility was established with UTC funding in 2009. This facility was used for this program. Up to 400 psig air can be supplied to this facility. The air is controlled and measured by sonic venturis upstream of the air heaters. Each air heater can deliver 3 pps air at temperatures up to 1,150°F. This heated air can be combined and delivered to the front end of the combustor or delivered separately to different combustor locations.

Liquid Jet A and vaporized C_3H_8 can be delivered to the combustor.

The test section options include an optically-accessible, single sector water-cooled combustor and another water-cooled combustor with no optical access. Other combustor geometries can be easily accommodated. The combustors are rated up to 300 psig.

The combustor pressure is set by a back pressure valve.

There is an inlet plenum/air preparation section followed by the test section. The test section is removable and can be replaced with various designs for different tests.

The test section used for this program can have optical access on all sides. The upstream optical access on the top and bottom of the rig was used for the air and fuel injection geometry for the axially controlled stoichiometry combustor concept.

A water-cooled gas-sampling emissions probe is available to acquire gaseous emission information. The sampling probe contains several gas-sampling orifices along its leading edge.

10.2 COUNTERROTATING EXTERNALLY STAGED SWIRLER

Designs for the liquid-fueled metal CRESS were completed that will be used in testing in the AAC. These designs were based on CFD calculations.

EINOx was found to scale as a function of P3 and T3. The CRESS EINOx data is significantly below the measurements taken in two previous programs, the 2008 NASA 9-injector rig and the General Electric High-Speed Civil Transport sector rig. Within the range tested, EICO is below 3 and the combustion efficiency above 0.9993.

10.3 PILOT-IN-CAN SWIRLER

The design was completed for the liquid-fueled metal PICS that was to be used in testing at the NASA CE-5 facility in March 2012. This design was based on CFD calculations.

High power testing with PICS was to be completed in the NASA CE-5 rig in March of 2012.

10.4 AXIALLY CONTROLLED STOICHIOMETRY COMBUSTOR

All emissions testing was done without windows, since air is added to the combustor flow to keep the windows cool.

10.5 PILOT ZONE CHARACTERIZATION

Previous UTC-funded CFD calculations generated the pilot premixer designs and determined the length of the pilot zone to ensure low NOx production and a uniform approach velocity to the main jets.

Testing was initiated by first characterizing the pilot region. The purpose of the pilot region in the AAC rig is to generate a uniform flow field with low NOx and CO levels.

The emissions as a function of the pilot equivalence ratio were also mapped. ***Figure 10-1*** plots the EINOx and the EICO as a function of pilot equivalence ratio. The same dependence on pilot equivalence ratio was observed for two different test days. ***Figure 10-2*** compares the pilot results with the Leonard and Steigmeir correlation. The pilot results are consistent with this correlation.

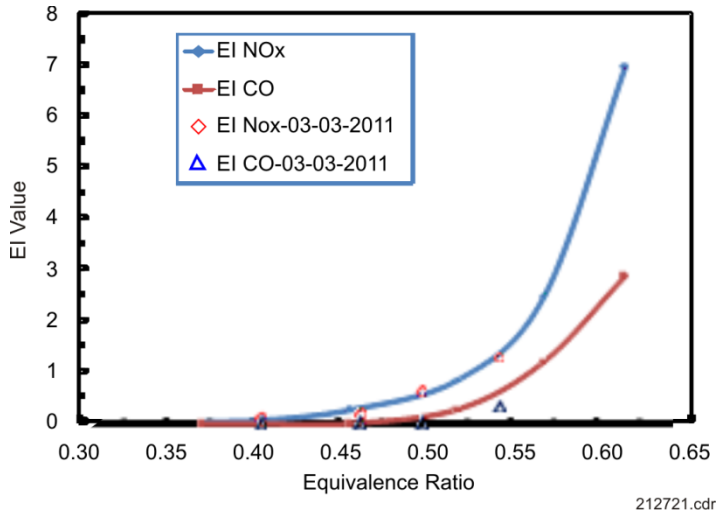

Figure 10-1. *CO and NOx Levels of Pilot Approach Flow*

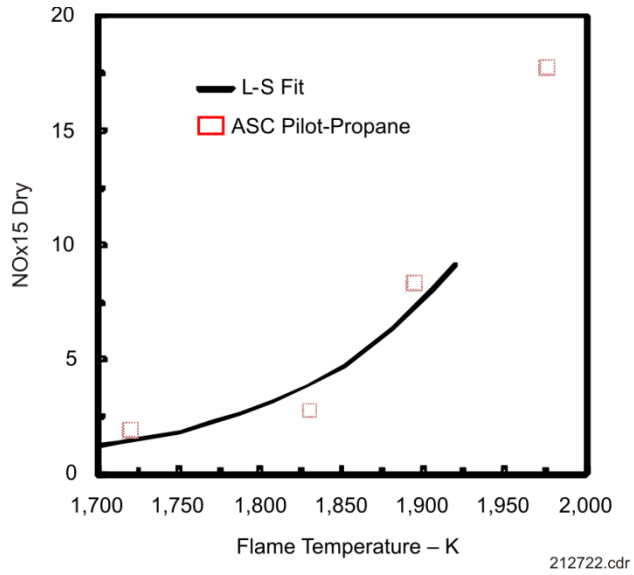

Figure 10-2. *NOx Levels of Pilot Approach Flow at Leonard and Steigmeir Levels*

10.6 AXIALLY CONTROLLED STOICHIOMETRY COMBUSTOR MAIN FUEL INJECTOR/MIXERS

For the initial results the approach air temperature/pressure were approximately 1,000°F/200 psia. This testing of concepts used gaseous propane for the pilot and main fuel injectors.

The impact of a change in pilot equivalence ratio and the main jet momentum flux ratio on the CO emissions for dual fueled main jets and OD-only fueled main jets is given in these figures. The EICO is higher for the OD-only fuel main jets. The EINOx was less than 1 for all conditions tested.

The conclusions of this testing are:

- Pilot Testing

  — Uniformity is achieved at the location of the secondary jets
  — Low dependency of CO and NOx on equivalence ratio below 0.55

- Fueled Main Jets

  — NOx emissions were less than 1 EI for all conditions tested
  — CO emissions decreased with increasing residence time
  — Richer pilot resulted in reduced CO emissions
  — Increased momentum flux ratio resulted in reduced CO emissions
  — Dual fueled jets had lower CO emissions than OD fueled jets

The tests then focused on inlet pressure, inlet temperature, and overall fuel air ratio variations. This condition represents the cruise condition of the N+2 cycle with 15 percent cooling air. This testing still used vaporized propane as the fuel for both the pilot and the main.

Figure 10-3 gives results as a function of equivalence ratio for an inlet pressure and inlet temperature of 200 psia and 1,000°F, respectively, and for two pilot equivalence ratios. The residence time from the center of the main jets to the sampling location varied as the equivalence ratio increased. At the highest equivalence ratio, the EINOx was 0.4 and the EICO was also less than 1.

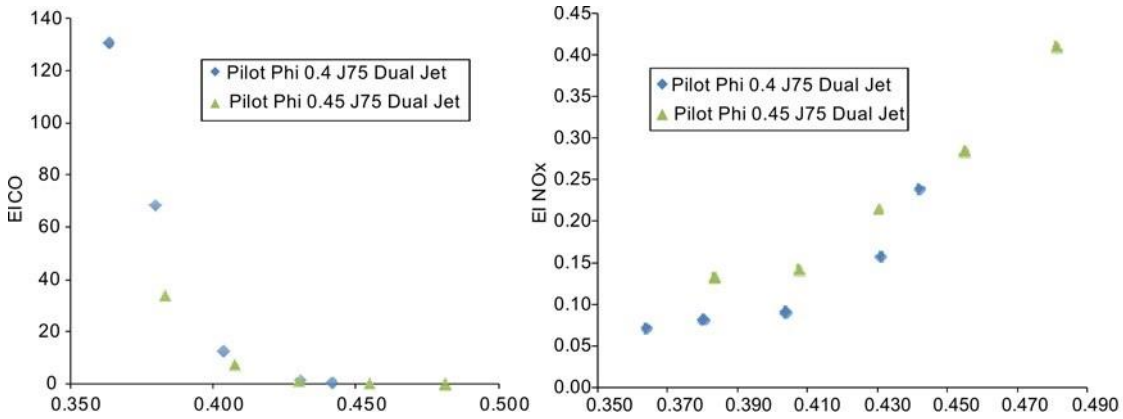

Figure 10-3. *Effect of FAR at Inlet Pressure and Temperature of 200 psia and 1,000°F*

Figure 10-4 gives results as a function of equivalence ratio for an inlet pressure and inlet temperature of 150 psia and 1,150°F, respectively, and for two pilot equivalence ratios. The residence time from the center of the main jets to the sampling location varied as the overall equivalence ratio increased. At the highest equivalence ratio the EINOx was 10 and the EICO was approximately 3.

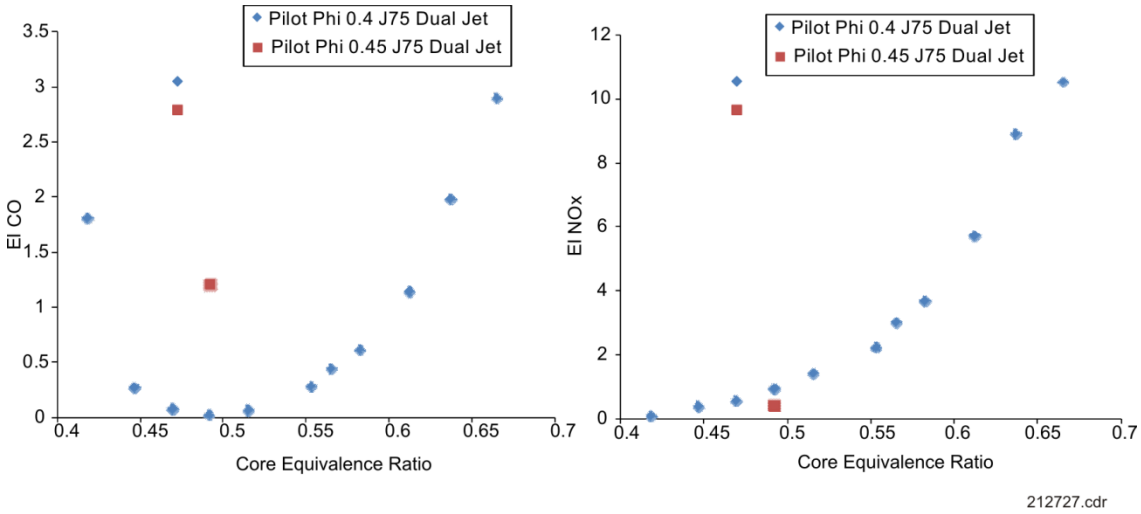

Figure 10-4. *Effect of FAR at Inlet Pressure and Temperature of 150 psia and 1,150°F*

Figure 10-5 gives results as a function of equivalence ratio for an inlet pressure and inlet temperature of 150 psia and 1,000°F for a pilot equivalence ratio of 0.4. The residence time from the center of the main jets to the sampling location varied as the equivalence ratio increased. At the highest equivalence ratio the EINOx was 8 and the EICO was approximately 3.

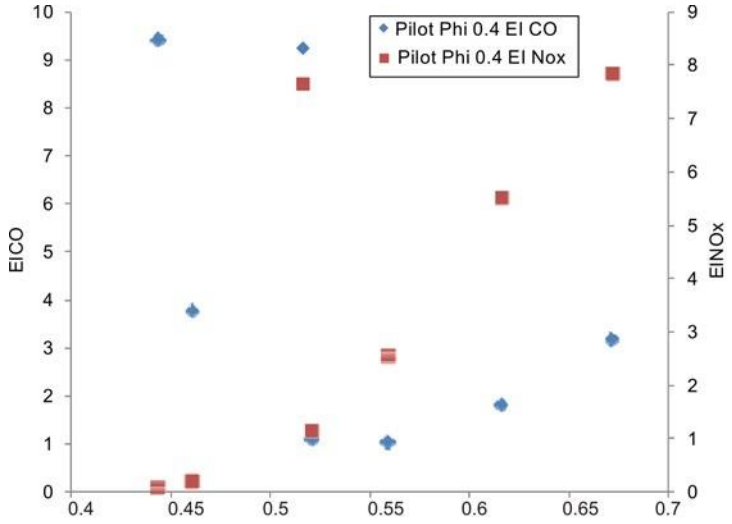

Figure 10-5. *Effect of FAR at Inlet Pressure and Temperature of 150 psia and 1,000°F*

An ACS main was designed that uses Jet A instead of vaporized C_3H_8. The first design was for vaporized Jet A to determine the effect of fuel composition on the ACS performance. The objective was to achieve the same level of mixing as with vaporized C_3H_8.

The vaporized jet A fuel nozzle has multiple orifices are on each main fuel injector/mixer fuel nozzle. The CFD results indicated similar mixing for this design and the vaporized C_3H_8 design.

The planar equivalence ratio distribution at downstream of the main fuel injector/mixer centerline is plotted in ***Figure 10-6***. The flow is observed to be fairly uniform. The average emissions-based equivalence ratio is approximately equal to the average of the ganged emissions-based equivalence ratio at each angular position and the average of the ganged emissions-based equivalence ratio at the +90-degree and -90-degree angular positions.

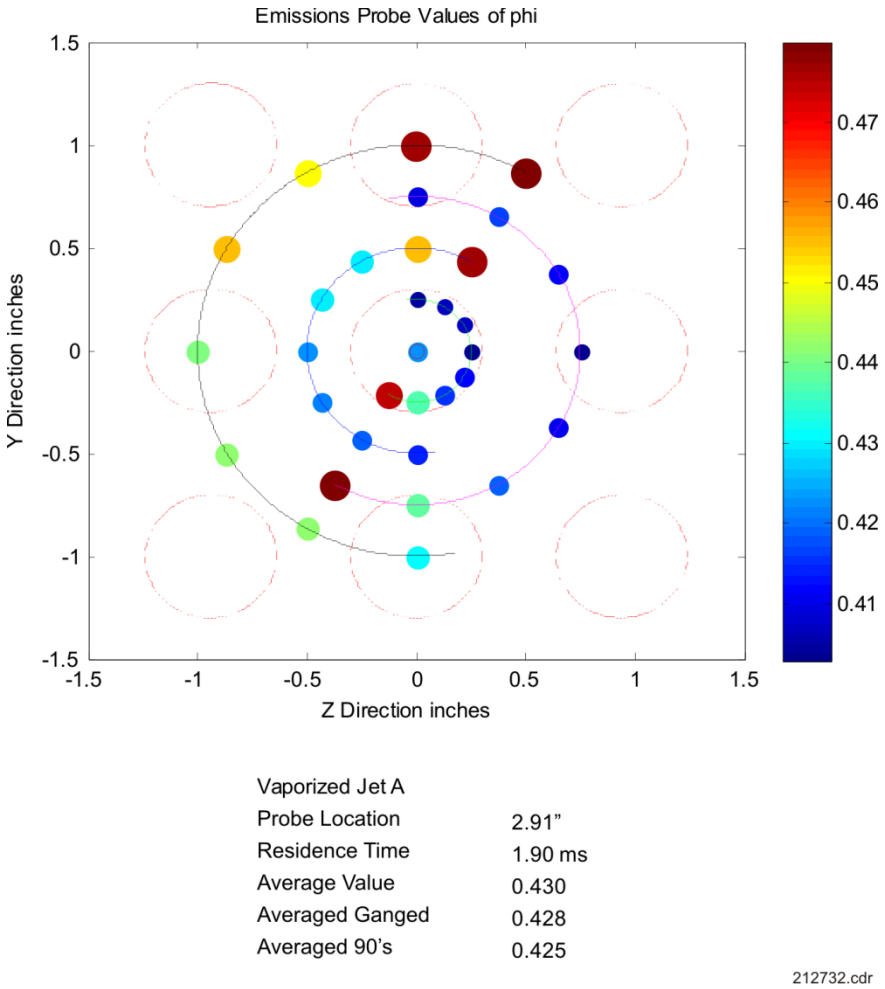

Figure 10-6. *Equivalence Ratio Distribution Downstream of Main Fuel and Airjets*

Figure 10-7 plots EICO versus hot core residence time for vaporized C3H8 and Jet A for four different operating conditions. The pilot fuel for both cases was vaporized Jet A. The EINOx was less than 5 for both main fuels. The CO levels with vaporized Jet A are 10 to 30 times lower than the levels with vaporized C_3H_8. The team is developing a path to confirm and to explain this difference.

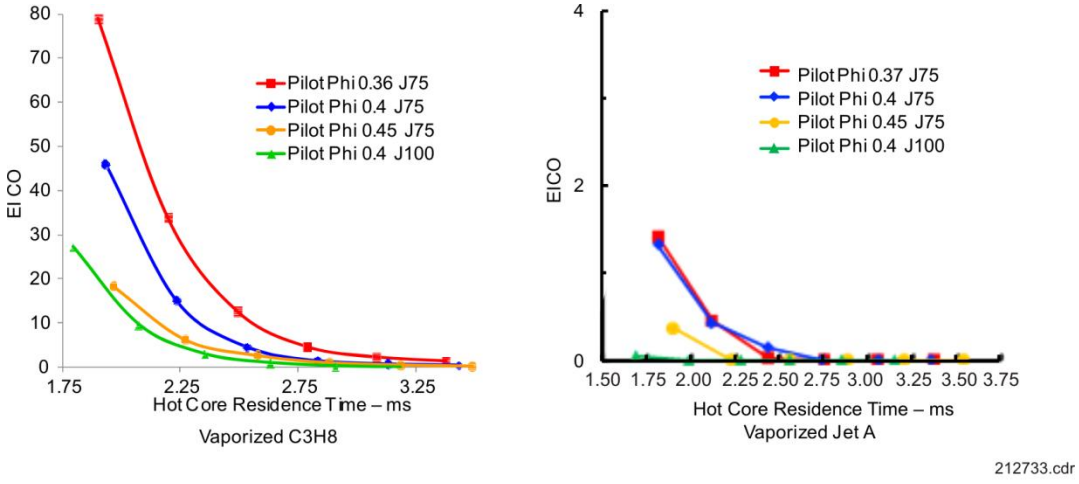

Figure 10-7. *CO Emissions Levels for Vaporized C_3H_8 and Jet A*

In April, ACS emission results were acquired for a vaporized C_3H_8 fueled pilot zone and a liquid Jet A fueled main zone.

The next focus was on a liquid fuel ACS main fuel injector design. The objective of this design was to assess the impact of amount of atomization, vaporization, and mixing time on the ACS performance A fuel nozzle is still being used inside the main air tube.

Figures 10-8 and ***10-9*** plot EICO versus hot core residence time for vaporized and liquid Jet A for four different operating conditions. The pilot fuel for both cases was vaporized C_3H_8. The CO levels with vaporized and liquid Jet A are very low and are approximately the same.

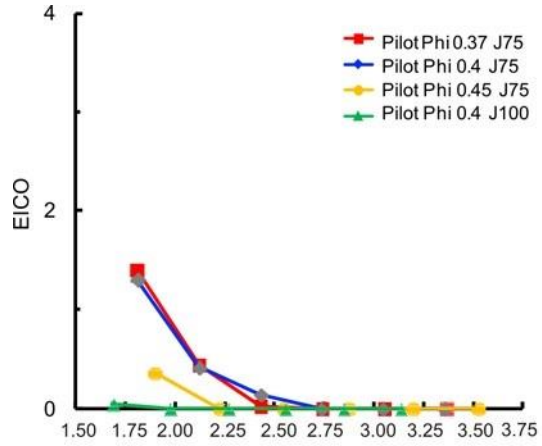

Figure 10-8. *CO Emissions Levels for Vaporized Jet A*

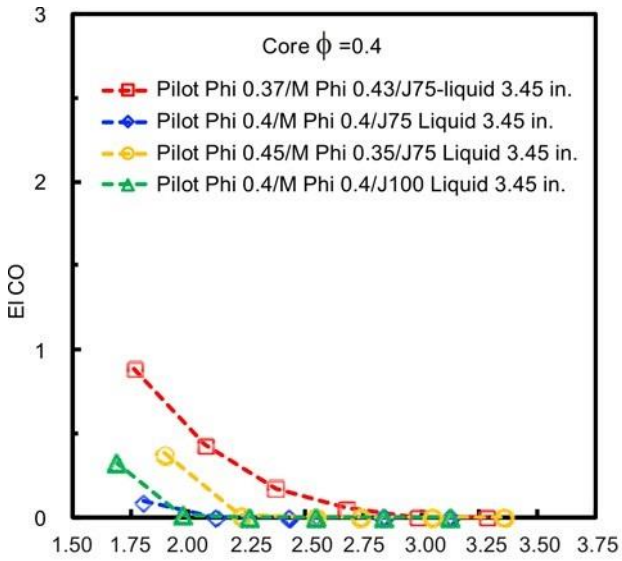

Figure 10-9. *CO Emissions for Liquid Jet A*

Consistent with the vaporized C_3H_8 and vaporized Jet A fueled main results, the measured NOx was extremely low for the liquid Jet A main results. ***Figure 10-10*** compares the vaporized C_3H_8 pilot-only results (open symbols) and the vaporized C_3H_8 pilot/liquid Jet A main results (closed symbols) with the Leonard and Steigmeir correlation (curve). The vaporized C_3H_8 pilot only results (open symbols) and the vaporized C_3H_8 pilot/liquid Jet A main results for two pilot equivalence ratios are consistent with this correlation. It is observed that very low NOx values have been achieved.

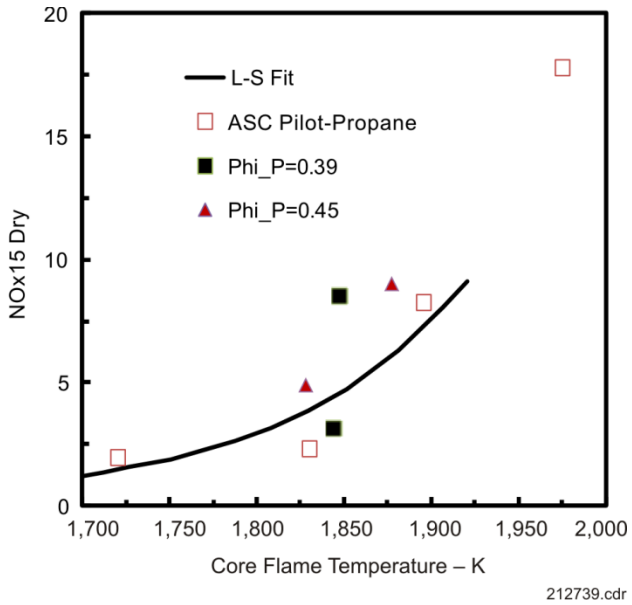

Figure 10-10. *NOx Levels of Pilot Approach Flow at Leonard and Steigmeir Levels*

Emission measurements were then acquired for the liquid Jet A location at 2.45 in. upstream of the mixer exit.

Figure 10-11 gives plots for EICO and NOx at 15 percent O_2 and dry versus hot core residence time and core flame temperature, respectively, for three different operating conditions. The pilot fuel for both cases was vaporized C_3H_8 and the main fuel is liquid Jet A. The flow conditions for these plots were combustor pressure of 200 psia, inlet temperature of 1,000°F, a pilot approach velocity of 70 ft/sec, and a Holdeman parameter of 2.54. The NOx data are at a probe location downstream.

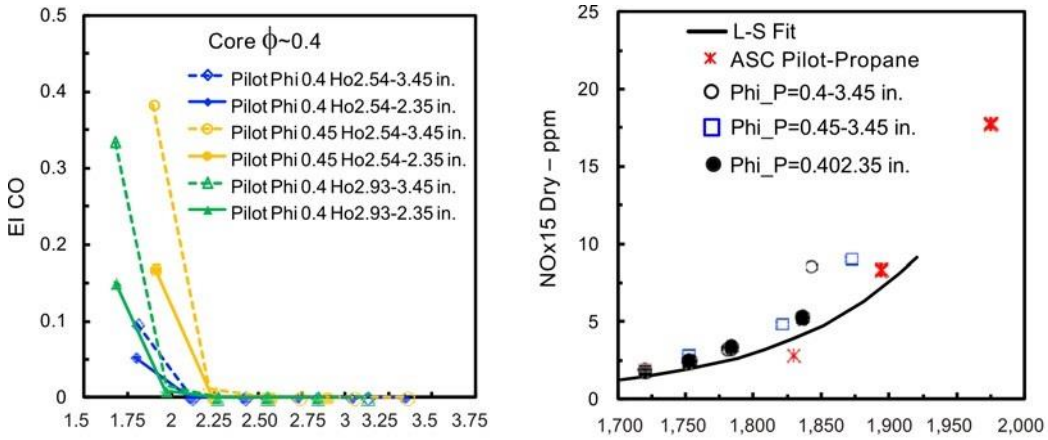

Figure 10-11*. CO and NOx Emissions for Liquid Jet A for Three Different Operating Conditions*

The CO levels with liquid Jet A for the two mixing locations are very low and approximately the same.

The NOx results are also not a function of the two mixing locations and the data follows with the Leonard and Steigmeir correlation.

Figure 10-36 gives plots for EICO and NOx at 15 percent O2 and dry versus hot core residence time and core flame temperature, respectively, for four different operating conditions. The pilot fuel for both cases was vaporized C3H8 and the main fuel is liquid Jet A. The flow conditions for these plots were combustor pressure of 200 psia, inlet temperature of 1,000°F, a pilot approach velocity of 45 ft/sec, and a Holdeman parameter of 5. The NOx data is at a probe location downstream.

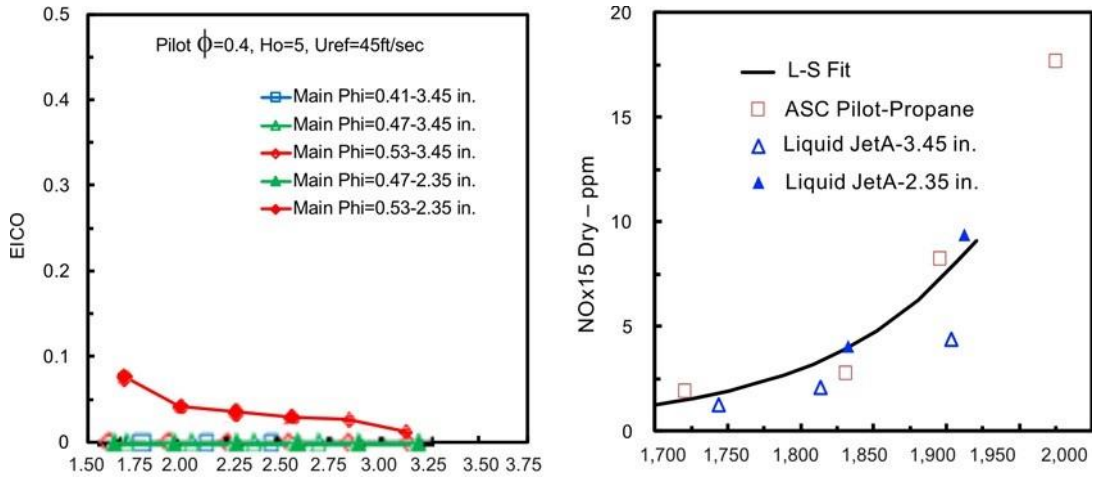

Figure 10-12. *EICO and NOx Emissions for Liquid Jet A for Four Different Operating Conditions*

The CO levels with liquid Jet A for both mixing locations are very low and approximately the same.

The NOx results are also not a function of the two mixing locations and the data follow with the Leonard and Steigmeir correlation.

Emission measurements were then acquired for the liquid Jet A location at 0.6 in. upstream of the mixer exit.

Figure 10-13 gives plots for EICO and EINOx versus FAR. The pilot fuel was vaporized C_3H_8, and the main fuel was liquid Jet A. The flow conditions for these plots were a combustor pressure of 200 psia, an inlet temperature of 1,000°F, a pilot approach velocity of 70 ft/ sec, and a Holdeman parameter of 2.54. The NOx data is at a probe location downstream from the center of the main fuel injector/mixer. At the cruise FAR the EINOx is approximately 5, with an EICO approximately 2.

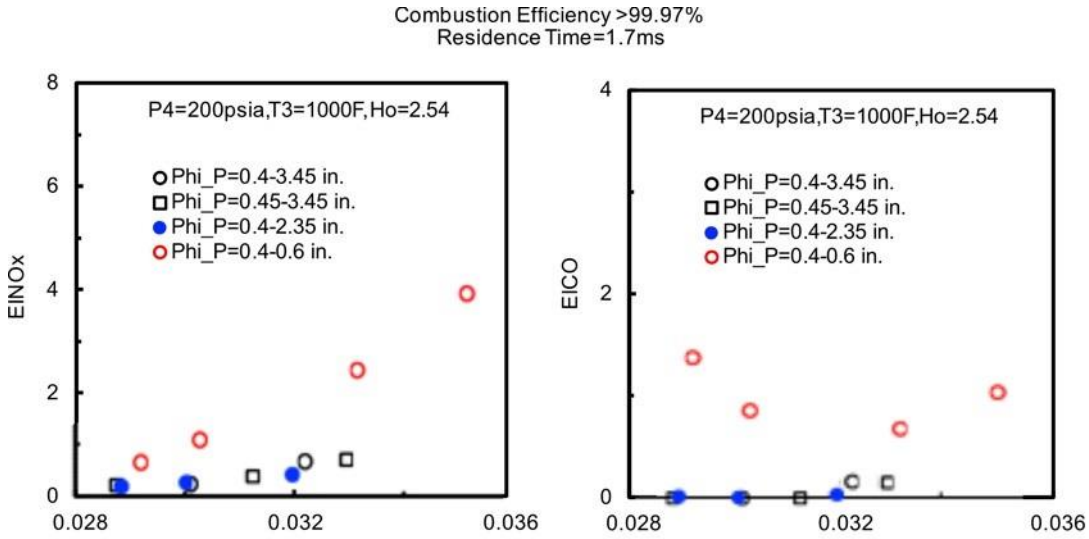

Figure 10-13. *Plots for EICO and EINOx Versus FAR*

Figure 10-38 gives plots for EICO and EINOx versus FAR. The pilot fuel was vaporized C_3H_8, and the main fuel was liquid Jet A. The flow conditions for these plots were a combustor pressure of 200 psia and an inlet temperature of 1,000°F. Data is given for two different pilot-approach velocities and two Holdeman parameters (2.54 and 5). The probe location is downstream from the center of the main fuel injector/mixer. The data indicates that there are no significant changes in the EICO or the EINOx due to a Holdeman parameter change.

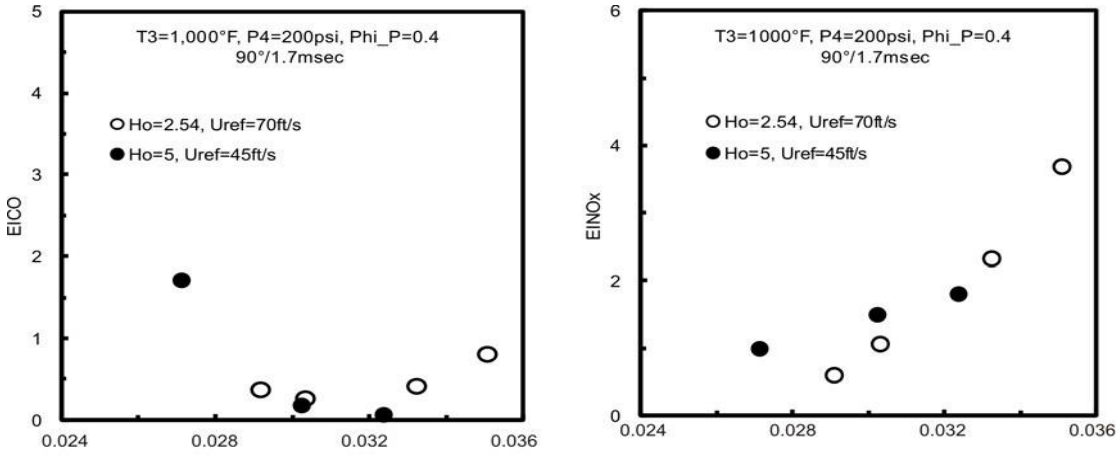

Figure 10-14. *Plots for EICO and EINOx Versus FAR, Two Holden Parameters and Pilot-Approach Velocities*

Figure 10-15 gives the results of generating the scaling parameters for P3 and T3. The plot on the left collapses the data at different temperatures at a P4 of 200 psia by the following expression:

EINOx/EINOx, ref = exp([T3 - Tref])/220) T3 – F

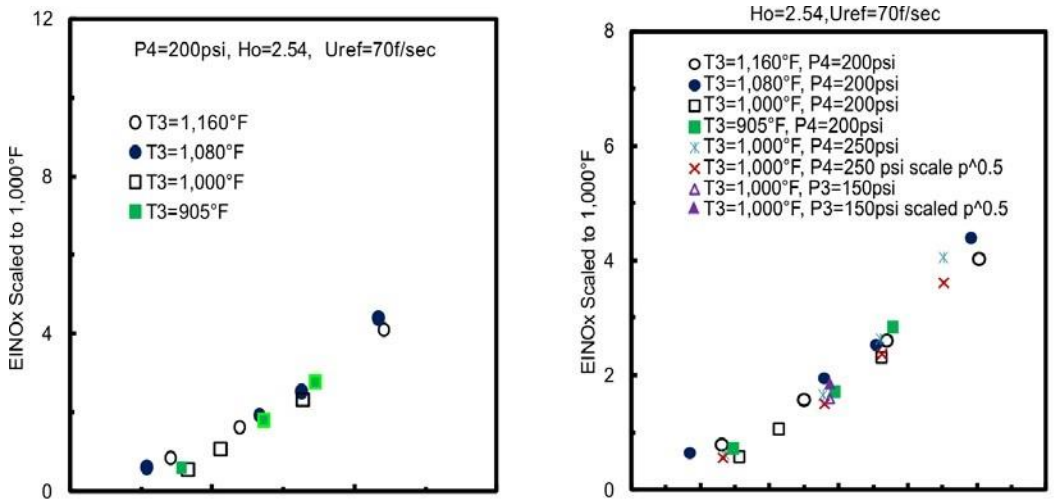

Figure 10-15. *Results of Generating Scaling Parameters for P3 and T3*

The plot on the right collapses all of the temperature scaled data at different pressures using a pressure exponent of 0.5. Both plots indicate that the data can be successfully collapsed with these scaling parameters.

As part of the ongoing effort to understand the impact on emissions of simplifying the design to make engine implementation simpler, additional testing with the simplified fuel injector/mixer was completed. Fuel and air injection only from the OD has a simplifying impact on engine implementation.

Therefore, a test was completed with no fuel and air injection from the bottom of the rig (ID side). The air and fuel removed were not replaced onto the OD. The results are shown in Figure 10-40, displaying the main NOx versus the main FAR. This data was corrected for the pilot NOx, and the change in the pilot to main mass ratio is plotted as well. As can be seen from ***Figure 10-16***, the main NOx is not dependent on jet-jet interactions.

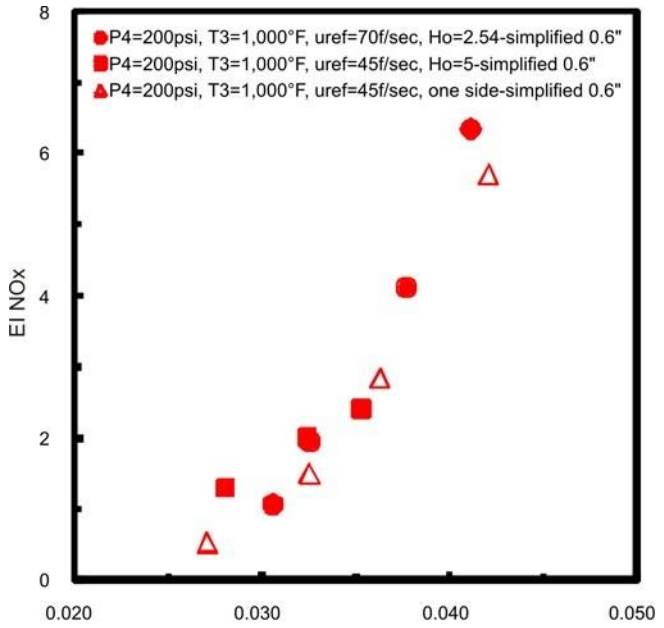

Figure 10-16. *Effect of One-Sided Fuel and Air Injection*

These results support the idea of fewer, larger main fuel injector/mixers or more, smaller fuel injector/mixers only located on the OD. This geometric configuration significantly simplifies engine implementation.

10.7 SUMMARY

- CRESS design exceeded the cruise EI goal of 5.
- Design of PICS completed. High-power testing was to be completed in the NASA CE-5 rig in March of 2012.
- Aerodynamic design, mechanical design, fabrication, and testing of different main fuel injector/mixers for an ACS have been completed during this program. The key accomplishments were:

  — Design approach resulted in three main simplified fuel injector/mixers that exceeded the cruise EI goal of 5

  — Low NOx generation (less than 5 EI at cruise conditions) by the main fuel injector/mixers can be achieved with peak equivalence ratios up to 1 at the exit of the main fuel injector/mixer.

11. TASK 3.3.4 — THREE-SECTOR NONREACTING MIXING TESTING

11.1 BACKGROUND

The flowfield and mixing characteristics in a combustor's front-end are critical to its performance, and are expected to differ between conventional RQL combustors and alternative lean-burn configurations that have higher front-end airflow. In addition, critical questions remain regarding details of the flowfield. Specific items of interest include:

- The front-end aerodynamics.
- The impact of cooling aerodynamics
- Validation of CFD tools used for combustor design.

To evaluate these aspects of the combustor flowfield, two 3-sector cold-flow rigs with optical access were fabricated. The first rig was fabricated from sintered nylon by an additive-manufacturing process (selective laser sintering [SLS]), and did not include cooling features in the combustor liner. The second rig comprised three sectors of an actual Talon-X combustor, with windows and air-feed plenums added, and included the capability to vary cooling flows. With these rigs, velocity measurements were obtained using a 1-D or 2-D LDV backscatter probe, viewing the combustor through a side-window or a downstream (exhaust) window to interrogate up to three velocity components. Mixing measurements were obtained using planar laser-induced fluorescence (PLIF) imaging of acetone seeded into the flow, through an intensified camera viewing the combustor through the side window while a laser sheet illuminated the combustor flow along an axial line. The results from the first, plastic rig were obtained under NASA contract funding, and are reported here. Measurements from an unconfined swirler rig were also obtained for comparison, and are reported here as well.

11.2 THREE-SECTOR RIG DESIGN AND SETUP

The plastic three-sector cold-flow rig used for the current study was designed with three main flow passages designated by Markers 1 to 3. The individual passages provide flow to the ID quench jets (1), swirlers (2), and OD quench jets (3) and allow the flowrates and pressure differentials of each passage to be controlled separately. The swirler flow passage (2) is further partitioned into three passages (one for each swirler) to permit particle seeding of the center swirler individually. This was done to conserve seed particles and to avoid excessive deposition of seed particles on the side-view windows. The internal combustor parts and partitions are fabricated using SLS. This process was selected over SLA because the SLS process uses a nylon material that exhibits better chemical resistance to ketones that are commonly used for tracer-based PLIF diagnostics. Aluminum side plates are used to seal the outer segments of the annular rig and provide additional rig stability. Windowholders are integrated into the side plate to provide side-view optical access in the combustor section.

The SLS combustor design is derived from the Talon X geometry. The rig was equipped with three SLS swirlers that are geometrically identical to metal swirlers previously used in full-annular engine. The combustor exit is open to the ambient lab atmosphere and the output is collected with a custom exhaust hood located approximately 3 in. downstream of the rig exit. TCA holes are included at the exit plane of the combustor.

11.3 UNCONFINED SINGLE-SWIRLER RIG

LDV measurements in an unconfined single-swirler rig were also performed to characterize the fundamental flow-field of a swirler in the absence of confined boundaries and adjacent swirlers. Such data can also be compared with concurrent ambient spray data performed for similar unconfined conditions but with a fuel spray.

In addition, these measurements provide data for CFD validation for simplified geometric conditions.

The unconfined rig consists of an upstream plenum that is supplied by a single air stream. The upstream flow control system is identical to that described above for the three-sector geometry. Flow from the single-swirler exhausts into the ambient room environment with no boundaries confining the flow. The output is collected with an exhaust hood that is located downstream of the swirler exit. Initial LDV measurements indicated that placements of the exhaust hood at this distance resulted in minimal impact on the measured profiles.

The unconfined rig was configured with either an SLS or a metal swirler, both having identical geometries. The SLS swirlers are identical to those used for the SLS three-sector testing, while the metal swirlers represent actual engine hardware that have been previously characterized in ambient spray experiments. Unconfined characterization of the metal swirlers has been included in the current study to provide a baseline for future metal three-sector tests using metal engine hardware.

11.4 LASER DOPPLER VELOCIMETRY SYSTEM

The LDV system consists of a probe head, pump laser, detectors and the associated signal processors. The fiber-coupled probe head (Dantec Dynamics) uses a back-scattering configuration (collects back-scattered light only) and contains transmitting and receiving optics. The back-scattering configuration is required for measurement in the complex three-sector confined geometry, as alignment and line-of-sight for a forward scatter system is overly complicated and prohibitive. The probe has a 60-mm diameter and is outfitted with a 400-mm lens. An Ar-Ion laser (Lexel) provided approximately 1 to 1.5 W of multi-line output energy. The 488- and 514-nm laser output wavelengths were fiber-coupled to the 2-D LDV probe using a distributor unit (Dantec Dynamics). An integrated Bragg cell operating at 40 MHz was used to eliminate velocity ambiguity. The collected laser scattering signal was coupled into a multimode fiber integrated into the probe head, and measured with a photomultiplier tube (PMT) (TSI Inc.). The resulting burst signal was finally processed with a burst spectrum analyzer (IFA 755, TSI Inc.) and converted to velocity. Time stamps and transit times were also recorded for each data point to allow for velocity bias correction in postprocessing.

The LDV probe was mounted to a four-axis translation system to permit measurements along a predefined traverse path. A primary challenge of performing measurements in the confined annular geometry of the three-sector rig is the complex geometry associated with optical access. Specifically, due to the curvature of the rig boundaries, the LDV probe head cannot simply be translated along orthogonal x- and y-coordinates. Instead the probe angle must be adjusted at each position to allow line of sight access to all the points of interest inside the rig. To simplify the process of generating a traverse file, a Matlab routine was generated to select the optimal probe head position and angle required to take measurements at any desired probe volume location.

Alignment of the LDV probe volume with the test rigs was performed using a custom alignment plate that is indexed with respect to the rigs using integrated locator pins. The plate contains a series of clearance holes that integrate with a movable pinhole jig that is used to locate and align the exact beam focus and probe volume location. Using this configuration, the spatial accuracy of the LDV probe alignment is expected to be better than 0.5 mm.

Polystyrene latex (PSL) microspheres with a 2-µm nominal diameter (Bangs Laboratories) were used as the LDV seed particles. The PSL particles were initially suspended in a methanol/water solution to avoid agglomeration and maintain a monodisperse size distribution. A custom particle seeder/mixer was used to generate a homogeneously seeded air stream required for the LDV measurements. The seeder consists of a long polyvinyl chloride (PVC) tube with an 8-in. diameter in a U-shaped configuration with a total flow length of 10 ft. The input air flow enters the seeder at one end, and the PSL solution is injected transversely using a siphon air atomizing nozzle (DeLavan). The flow length of the seeder was selected to provide sufficient residence time to vaporize all injected methanol. Methanol vaporization was also verified experimentally by seeding with a pure methanol solution and using the LDV system to detect any persistent droplets in the rig test section.

All measurements in the current study were completed with the 2-µm PSL spheres exclusively. The impact of particle size was initially investigated by comparing LDV results with either 1- or 2-µm PSL particles. These tests showed minimal difference in average and root mean squared (RMS) velocities, and thus both particle sizes are expected to accurately track the flow. The larger 2-µm particles were selected due to the higher resulting scattering signals and are used for all subsequent measurements.

Particle seeding density was adjusted to provide reasonable data acquisition rates while avoiding excessively high seed concentrations that can skew measurements with multiple particles passing through the measurement volume. Data rates as high as 500 Hz were observed in high velocity regions. Substantially lower data rates are

observed in low velocity recirculation zones and along the center swirler perimeter (only center swirler is seeded with particles resulting in increasing dilution at the swirler intersection boundaries).

Small amounts of particle accumulation are seen on internal rig and swirler surfaces. However, the PSL particles appear to produce relatively thin deposition layers, in comparison with ceramic particles, and are not expected to dramatically influence the flow characteristics. This has been verified experimentally through swirler ACd measurement performed before and after LDV measurement campaigns.

11.5 RIG SCALING AND OPERATING CONDITIONS

All experiments were performed under cold-flow conditions with a nominally room temperature air supply and ambient pressure at the combustor exit. To best match the flow physics of the combustor under hot-flow conditions the engine operating conditions were scaled. In addition, the size of the TCA holes at the exit plane of the rig was adjusted.

11.6 COMPUTATIONAL FLUID DYNAMICS SIMULATIONS

CFD simulations were performed for the three-sector and unconfined geometries. All CFD results presented in the figures below were generated using the Fluent-based detached eddy simulation (DES) code with an unstructured polyhedral grid. This was chosen over Allstar-based hybrid large eddy simulations (HLES) due to better overall accuracy and faster solution time. The CFD calculations were performed by P&W, simulating the exact geometry and aero conditions of the UTRC cold-flow experiments. Details of these simulations are reported elsewhere in this final report.

11.7 SELECTIVE LASER SINTERING THREE-SECTOR RESULTS

LDV measurements of axial velocity in the three-sector rig were performed along 31 line traverses. These planes were selected to provide a thorough survey of the front-end aerodynamics and also to coincide with standard CFD postprocessing output planes. Measurements were made in five facial planes, oriented parallel to the BH (perpendicular to the swirler centerline axis).

All measurements focused on the center sector of the three-sector configuration as this has the proper swirler boundaries. Also, the measured axial velocity is aligned parallel with the engine centerline (not the cant angle defined by the swirler BH).

Average LDV results for the axial traverse along the swirler centerline are presented in ***Figure 11-1***. This result is consistent with previous single-sector measurements, but differs from unconfined measurements described below. In general, the recirculation zone was found to extend further down stream in the confined geometry. ***Figure 11-1*** also includes Fluent DES CFD simulation results for comparison. Overall, the CFD results agree well with the three-sector rig data in the far-field, greater than 1 in. from the swirler exit. Agreement in the near-field is less favorable, with the CFD underpredicting the strength of the central recirculation zone. Additional CFD studies looking at near-field grid refinement did little to improve the agreement with rig data in this region.

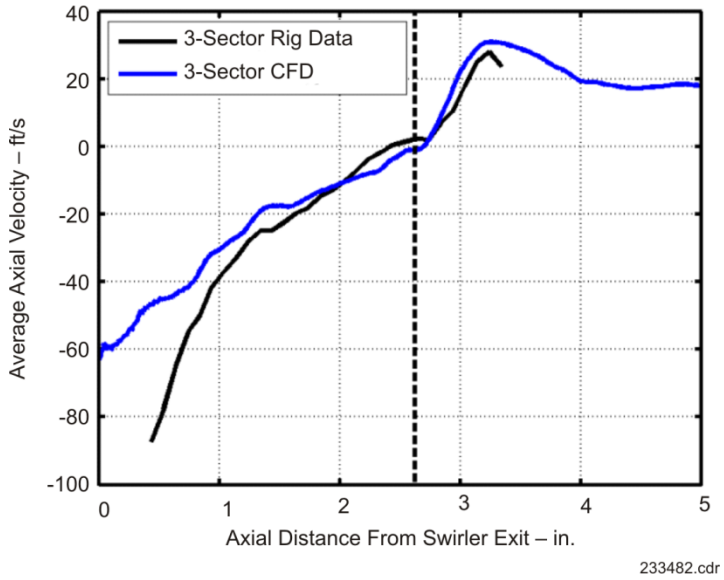

Figure 11-1. *Average LDV Results for the Axial Traverse Along the Swirler Centerline*

Overall, the CFD simulations do a better job of capturing the flow structures in the far-field. At these locations, the general velocity profiles and magnitudes are well captured. In the near-field, however, the CFD is less accurate at predicting the maximum and minimum velocities as well as the peak locations. These results are consistent with the observations made for the axial traverse data.

11.8 UNCONFINED SINGLE-SWIRLER RESULTS

LDV measurements in the unconfined single-swirler rig were acquired at the same five axial planes described above. Additional measurements were also acquired to allow direct comparison with ASR velocity data acquired with a phase Doppler particle analyzer (PDPA) system. At each axial location, x- and y-traverses were acquired using the 2-D LDV probe. Assuming the flow is axisymmetric, this provides data of all three velocity components without having to change the probe position (Y - trav = axial + radial, X - trav = axial + tangential). Unconfined measurements were performed using both an SLS swirler (identical to those used in the SLS three-sector work described above), as well as a metal swirler (intended for use in metal three-sector studies with cooling flows). These results provide baseline swirler aerodynamics data for SLS and metal rigs and can be used to assess the impact of confinement and swirler-swirler interactions.

11.9 UNCONFINED SLS SWIRLER RESULTS

LDV axial velocity measurements along the swirler centerline are presented in ***Figure 11-2*** for the unconfined SLS swirler experiments. The measured axial velocity profile from the SLS three-sector rig is also included for comparison. The unconfined results indicate a weaker recirculation zone than the three-sector results, as indicated by velocity region near the swirler exit. In addition, the axial extent of the recirculation zone is found to be shorter for the unconfined geometry and closes well upstream of the three-sector result. These differences are attributed to the influence of the confinement on the swirling flowfield.

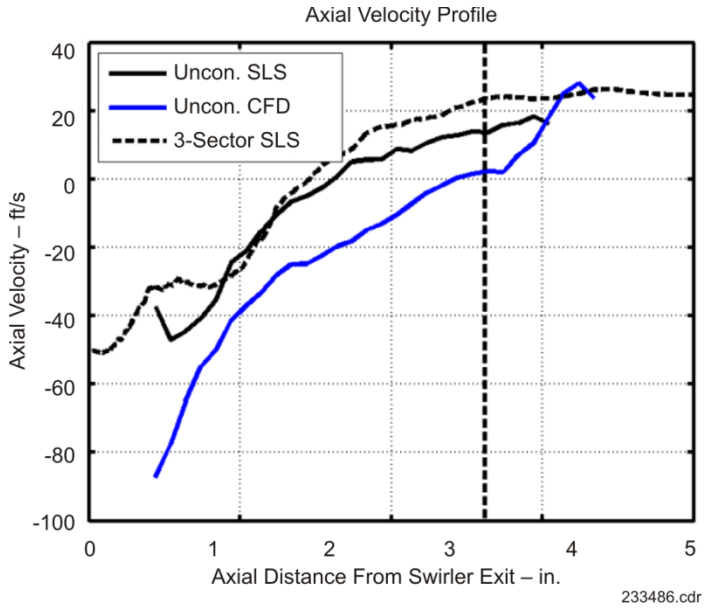

Figure 11-2. *LDV Axial Velocity Measurements Along Swirler Centerline, Unconfined SLS Swirler Experiments*

As expected, the peak velocity is attenuated and the peak velocity location widens as the flow propagates axially downstream. In comparison with the SLS three-sector measurements, the unconfined SLS results indicate a slower decay of the swirler exit velocity as well as more gradual widening of the peak velocity (smaller cone angle). Large differences in the magnitude and the extent of the recirculation are also observed between the unconfined and 3-sector rigs (consistent with results presented in ***Figure 11-2***).

11.10 UNCONFINED METAL SWIRLER RESULTS

LDV measurements in the unconfined rig configured with a metal swirler were completed to investigate the apparent asymmetry found in the SLS swirler flowfield. In addition, these measurements provide addition fundamental swirler aerodynamics data for comparison with future metal three-sector rig tests with cooling flows, and for additional CFD validation. Characterization of the unconfined metal swirler flowfield was carried out in the same manner as the SLS swirler described above. Specifically, measurements were performed in the same five axial planes for the x- and y-traverse orientations. Experiments were performed at pressure drop to match swirler, as well as at pressure drop to match swirler output velocity at engine hot-flow conditions. The latter measurements allow direct comparison with previously acquired ambient spray data for the same swirler geometry.

LDV measurements of axial velocity, taken along the swirler centerline, for the unconfined metal swirler configuration are presented in ***Figure 11-3***. Corresponding CFD results as well as unconfined SLS data are included for direct comparison. The metal axial profile generally follows the expected trends, but does exhibit a local maxima and minima in the recirculation. respectively. This trend is more evident in the metal data given that the axial traverse extends closer to the swirler exit. However, the SLS data does show evidence of this feature. This near-field profile is somewhat different that what is typically observed and requires further investigation. Comparing the SLS and metal rig data overall indicates similarities in the far field, and larger differences seen in the near field. The general velocity trend is very similar between SLS and metal, with only a slight offset in magnitude observed. The largest difference between SLS and metal swirlers are seen in the near-field in the recirculation zone, where the strength of the recirculation zone is considerably stronger for the SLS than the metal.

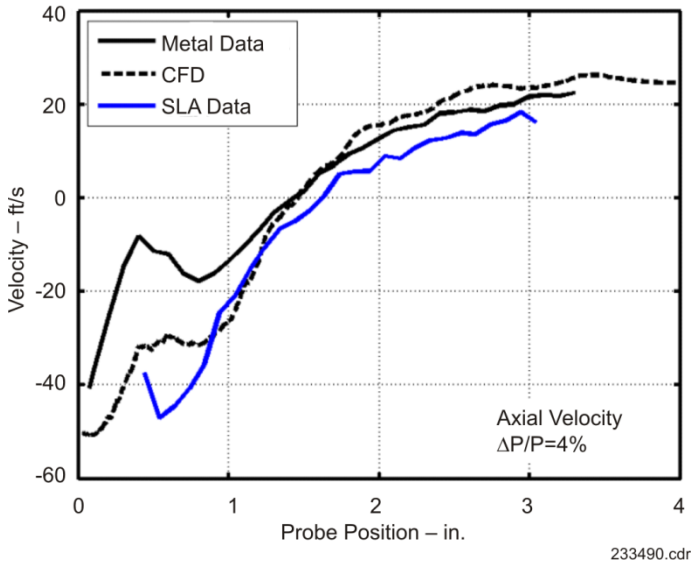

Figure 11-3. *Axial Velocity Profiles Along the Swirler Centerline for the Unconfined Geometry*

The metal rig axial profile also agrees well with the corresponding unconfined CFD results for distances downstream from the swirler exit. Differences in the near-field are somewhat large, and the CFD results lie between the SLS and the metal.

One important aspect of the previous unconfined SLS swirler studies was the presence of axial asymmetry in the velocity profiles moving downstream. Although not shown here, the unconfined metal swirler results showed excellent symmetry, with the x- and y-traverse data matching nearly exactly. This symmetry is expected for the

3PD swirlers given the axisymmetric passage design. Given that the metal 3PD swirler is actual engine hardware and that the flow is more symmetric, the metal results are considered to be most representative of actual swirler aerodynamics seen in engines.

11.11 SUMMARY AND CONCLUSIONS

- Comparison of unconfined and three-sector results with the SLS swirlers revealed that the central recirculation zone is stronger and extends further downstream for the confined three-sector geometry. Also, the axial decay of velocity was considerably faster for the three-sector. These differences are primarily attributed to the confined geometry.
- General conclusions were the same for the unconfined metal and SLS studies in comparison with the three-sector measurements. Specifically, the velocity decay and cone angle are always higher for the confined geometry. In addition, large differences in the strength of the central recirculation zone are observed.
- CFD simulations of the unconfined geometry were again able to best match the far-field profiles downstream of the swirler exit. Larger differences in the near-field profile, particularly in the recirculation zone, still remain.
- Comparison of unconfined measurements of air velocity and spray velocity measurements using the same swirler indicate relatively large differences in the flow structure with fuel present.
- Fluent-based DES simulations provide better agreement with unconfined air velocity profiles in comparison with the Allstar HLES simulations and the spray velocity data.

12. TASK 3.3.5 — THREE-SECTOR REACTING MIXING TESTING

12.1 EXECUTIVE SUMMARY

The three-sector ACS was tested at the UTRC Jet Burner Test Stand (JBTS) facility to verify that it could produce low NOx emissions with high combustion efficiency at relevant NASA N+2 engine conditions. Both Idle and Approach conditions were tested directly at the engine conditions. Test results showed high combustion efficiency. Before running the simulated conditions, pilot-only tests were run at the high pressure and temperature conditions to determine the optimum fuel flow splits between the pilot and main stage. The data showed that the pilot could be run efficiently down to an effective pilot zone equivalent ratio of 0.46. This optimum pilot equivalence ratio was then applied and the main stage equivalence ratio varied with FAR at simulated conditions. These tests demonstrated low NOx and high efficiency. This shows that, at the maximum temperature and pressure conditions of the facility, the enthalpy from the pilot zone is sufficient to maintain high combustion efficiency of the main stage, as long as the main stage equivalence ratio is above a certain lean threshold value. Pressure and temperature excursion tests were run to estimate the NOx pressure and temperature scaling coefficients. Using these scaling coefficients, the Environmental Protection Agency Parameter (EPAP) at this optimum pilot equivalence ratio was projected to have NOx emissions of 13 percent of Committee on Aviation Environmental Protection (CAEP) 6. Tests were also run with a pilot fuel flow split that was closer to stoichiometric to bound the emissions and ensure high combustion efficiency for the pressure and temperature excursion tests. For this pilot equivalence ratio closer to stoichiometric, which represents a more conservative estimate, the projected EPAP was 25 percent of CAEP 6.Therefore, it is expected that the NASA Advanced Subsonic Combustion Rig (ASCR) tests (which can reach the actual engine conditions) will meet the 25 percent of CAEP 6 goal set out as part of the NASA N+2 program.

12.2 INTRODUCTION

The three-sector ACS was designed and built during 2011. This arc sector combustor was then tested at UTRC at the JBTS from late November 2011 through January 2012. The results of that testing are shown in this report. The focus of the testing was on measuring the emissions (especially NOx emissions) produced by the burner.

12.3 ANALYSIS APPROACH

12.3.1 Geometry and Airflow Splits

There are three sectors in the current combustor. A relatively low amount of airflow is passed through the pilot swirler, with the majority passed through the main stage, and the rest applied to liner cooling. The low amount of pilot swirler airflow is designed so that it will pass sufficient at the select cycle conditions. A greater amount of NOx is expected from the pilot, as this must be self-stabilized through swirl, and therefore cannot be optimized solely for fuel-air mixing. Note that the main-stage injectors are positioned downstream so that the airflow passing through this stage will not impact the swirl-stabilized pilot zone. Since the pilot zone is designed to sustain not only itself, but also the main-stage, it is essential that stable reaction occurs in this zone. The main stage has been optimized for fuel-air mixing.

12.3.2 Test Plan

Because of the limits of the testing facility, some cycle conditions are scaled for the sector tests. Because of the lower pressure and temperature, this will result in a modified W_{ab}. Along with measuring the emissions the cycle conditions of interest, there are a few other objectives of the testing. The first is to estimate the optimum fuel-flow splits between the pilot and main-stage injectors. The second is to obtain pressure and temperature excursion data to scale the NOx emissions to actual engine conditions.

Because the combustor relies on fuel staging, it was not clear what the optimum fuel-flow splits would be between the pilot and main stages. This optimum fuel-flow split would be where the lowest NOx emissions are observed, with acceptable combustion efficiency. To find the optimum fuel flow splits, the test plan was run through a sweep of fuel distributions to the pilot and main stages at the cycle FAR.

The NOx emissions were expected to be highest around the stoichiometric condition, and to fall off for both rich and lean equivalence ratios. It was expected that the optimum point would be at a relatively low pilot equivalence ratio. As the pilot becomes excessively lean, the combustion efficiency may start to fall off to unacceptable levels. The fuel level that achieves both low NOx and acceptable combustion efficiency would be applied, with the rest of the fuel flow being directed through the main-stage injectors.

At the engine pressures and temperatures, the NOx emissions may be greater than what is directly measured in the JBTS rig. To estimate the true level of NOx at the high-power condition, pressure and temperature excursion tests were performed. Using this test data, the pressure and temperature scaling exponents can be estimated, and the NOx emissions at SLTO conditions can be projected to provide the EPAP value.

12.3.3 Instrumentation

Temperature, pressure, and emission measurements were made during the tests. The main reason for the thermocouple measurements is to provide a proof of life. Another objective is to notify us during the testing if the panels are becoming too hot. Thermocouples were also included on the sidewalls. An emissions probe is located at the exit of the combustor. The measurements of the probe can either be measured separately or ganged together to provide one averaged measurement. The probes were gained together for most of the current tests. For most of the emission points that are shown, only the emission data from the center sector is included, as the data from the side sectors is impacted by the sidewalls, and so is not representative of an annular combustor. The emissions data is able to measure parts per million of NOx, CO, unburned hydrocarbons, O_2, and CO_2. Exhaust smoke particulates are measured through a separate procedure, and were shown to be generally low.

12.4 ANALYSIS RESULTS

12.4.1 Continuity and Fuel-to-Air Ratio

Before the ACS was tested at JBTS, the combustor effective area (ACd) was measured separately. Initial cold-flow tests indicated that the predicted airflow as calculated from ACd was about 8 to 12 percent lower than the measured airflow. This suggests that the ACd of the combustor was slightly larger than previously measured. This is possible, as some of the panels were modified between the time of the cold-flow ACd tests and the JBTS tests. This cold-flow ACd difference remained fairly constant throughout the test, suggesting that additional combustor airflow leakage did not open up during the test.

12.4.2 Emission Results

Emission results are shown in ***Figures 12-1*** and ***12-2***. ***Figure 12-1*** shows EINOx and EICO as a function of the effective pilot zone equivalence ratio. ***Figure 12-2*** shows EINOx and combustion efficiency as a function of the effective pilot zone equivalence ratio. The combustor efficiency is very high at cycle conditions. The peak NOx emissions are shown at an effective pilot zone equivalence ratio of 1.016. Note that the NOx emissions fall off as the pilot is richer or leaner.

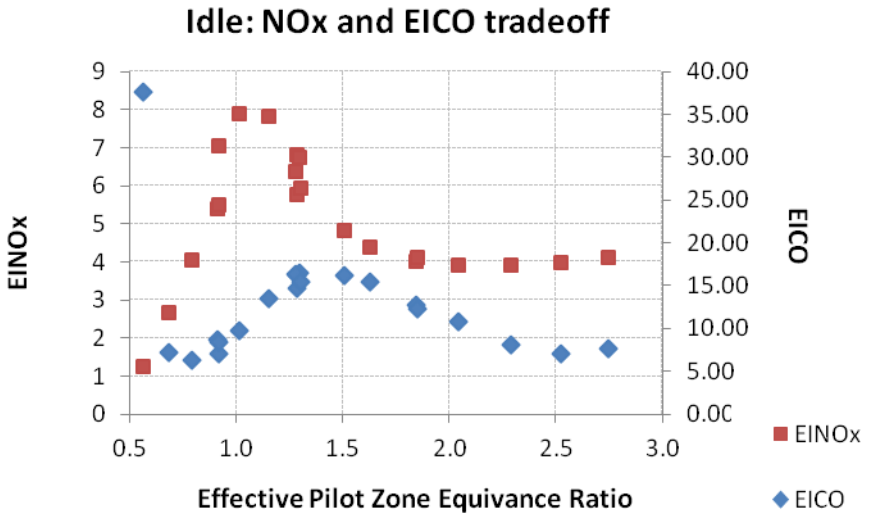

Figure 12-1. *Idle Emissions Results, Showing EINOx and EICO as a Function of Effective Pilot Zone Equivalence Ratio*

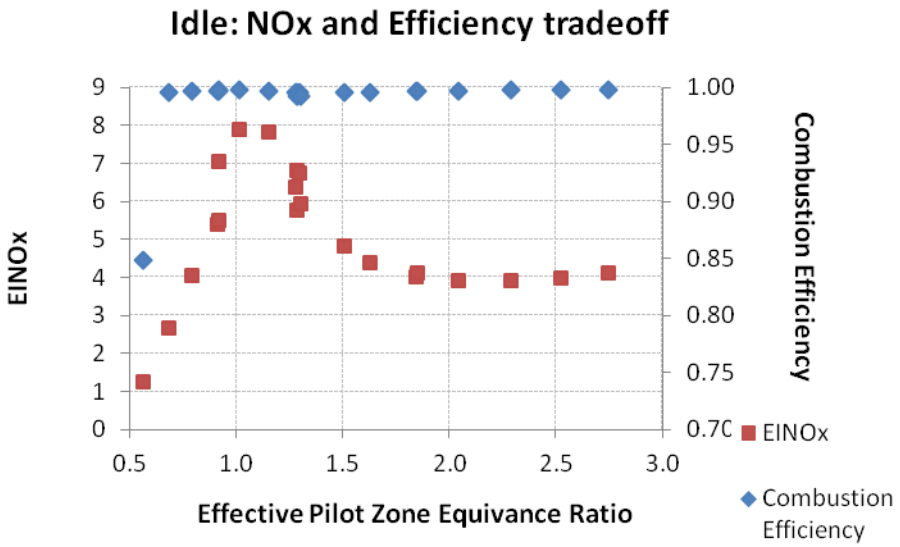

Figure 12-2. *Idle Emission Results, Showing EINOx and Combustion Efficiency as a Function of Pilot Equivalence Ratio*

Approach condition emission results are shown in ***Figures 12-3*** and ***12-4***. ***Figure 12-3*** shows NOx and CO as a function of the effective pilot zone equivalence ratio. ***Figure 12-4*** shows NOx and combustion efficiency as a function of the effective pilot zone equivalence ratio. Note that the lowest EICO (highest combustion efficiency) occurs at a rich effective pilot zone equivalence ratio. As long as the pilot equivalence ratio is fairly rich, the NOx is fairly constant at between 7 and 8 EINOx. As the percentage of fuel in the main stage increases, higher temperature and higher NOx emissions are produced. As the pilot zone equivalence ratio falls, the temperature decreases.

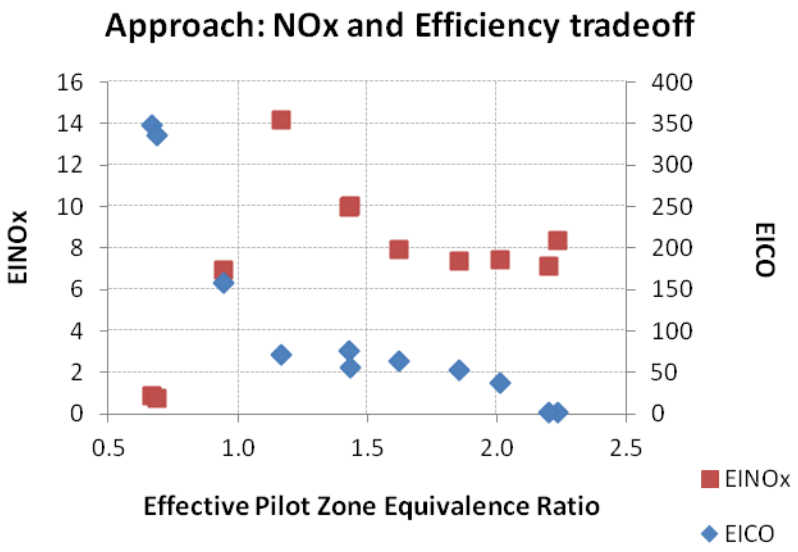

Figure 12-3. *Approach Emission Results, Showing EINOx and EICO as a Function of Pilot Equivalence Ratio*

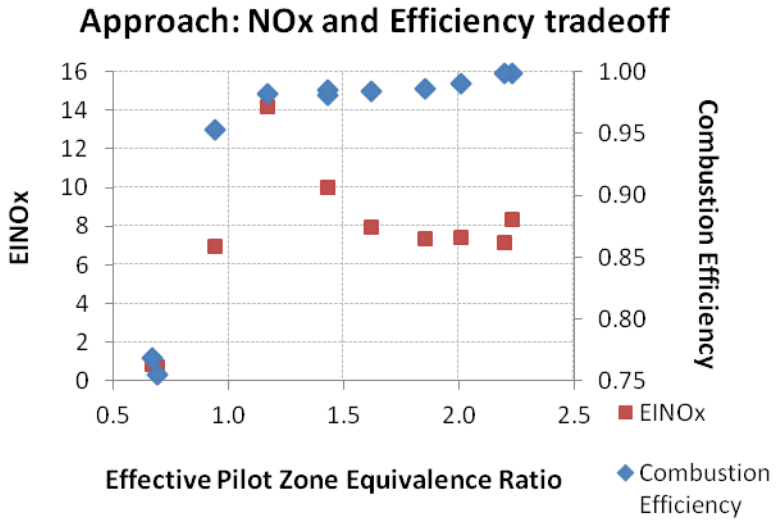

Figure 12-4. *Approach Emission Results, Showing EINOx and Efficiency as a Function of Pilot Equivalence Ratio*

To estimate the optimum fuel flow split between pilot and main at high power, the pilot was run at the highest conditions of the rig, without any fuel to the main stage. The optimum fuel flow through the pilot corresponds to the condition that produces both low NOx emissions and high combustion efficiency. ***Figure 12-5*** shows EINOx and EICO as a function of effective pilot zone equivalence ratio. ***Figure 12-6*** shows EINOx and combustion efficiency as a function of effective pilot zone equivalence ratio. The highest NOx is observed where the effective pilot zone equivalence ratio is near one. As the pilot zone becomes leaner, NOx decreases dramatically. Relatively high combustion efficiency (99.5 percent) is maintained up to an effective pilot zone equivalence ratio of 0.46. As the pilot becomes leaner beyond this point, the efficiency drops off rapidly. Therefore, for the low NOx SLTO simulated conditions, this equivalence ratio will be applied in the pilot. To bound the emission results and to ensure high combustion efficiency for temperature and pressure excursion points, tests with an effective pilot zone equivalence ratio of 0.8 were also run.

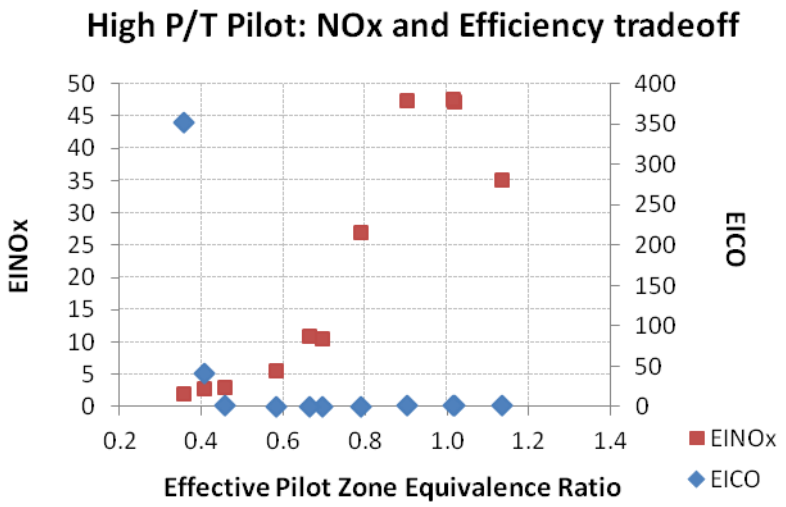

Figure 12-5. *High Pressure/Temperature, NOx and CO Tradeoff*

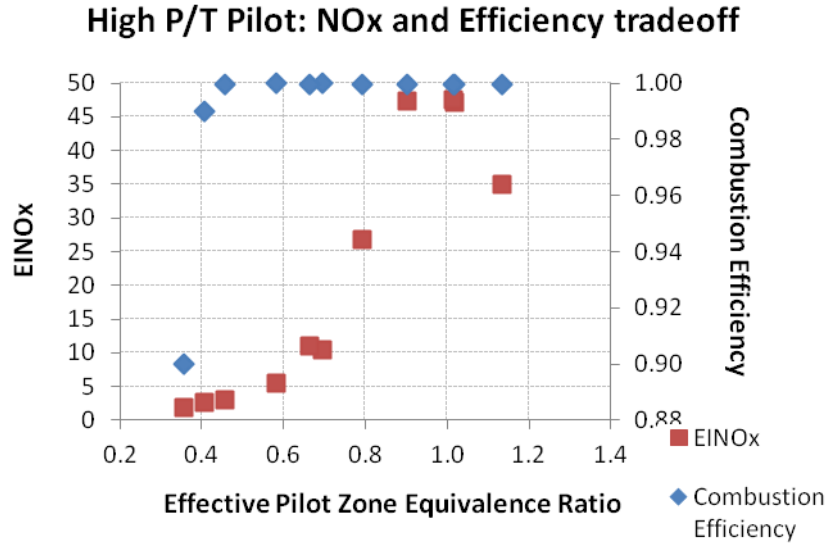

Figure 12-6. *High Pressure/Temperature, NOX and Efficiency Tradeoff*

Emission results for an effective pilot zone equivalence ratio of 0.46 are shown in ***Figures 12-7*** and ***12-8*** at the maximum pressure and temperature conditions of the facility. ***Figure 12-7*** shows EINOx and EICO data as a function of main stage equivalence ratio. ***Figure 12-8*** shows EINOx and combustion efficiency as a function of main stage equivalence ratio. Because the pilot equivalence ratio is held constant, the main stage equivalence ratio decreases as the FAR decreases. The NOx emissions decrease as the main stage equivalence ratio decreases. The combustion efficiency is maintained above 99 percent for main stage equivalence ratios as low as 0.56 at these conditions. As the main stage becomes leaner, the efficiency starts to drop off. Note that, because the main stage is dependent on the pilot zone to maintain efficient combustion, the emissions are dependent on the pilot equivalence ratio. As the pilot zone equivalence ratio increases, the temperature in the pilot zone increases, meaning that there will be more enthalpy available to maintain efficient combustion in the main stage. The main stage should then be able to maintain high combustion efficiency at lower main stage equivalence ratios. It is found that this is the case.

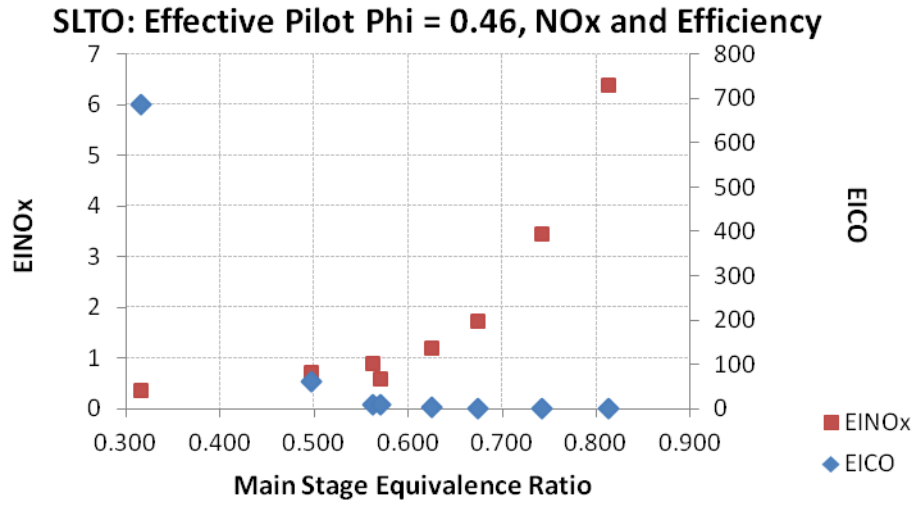

Figure 12-7. *SLTO — Effective Pilot Phi = 0.46, NOx and CO*

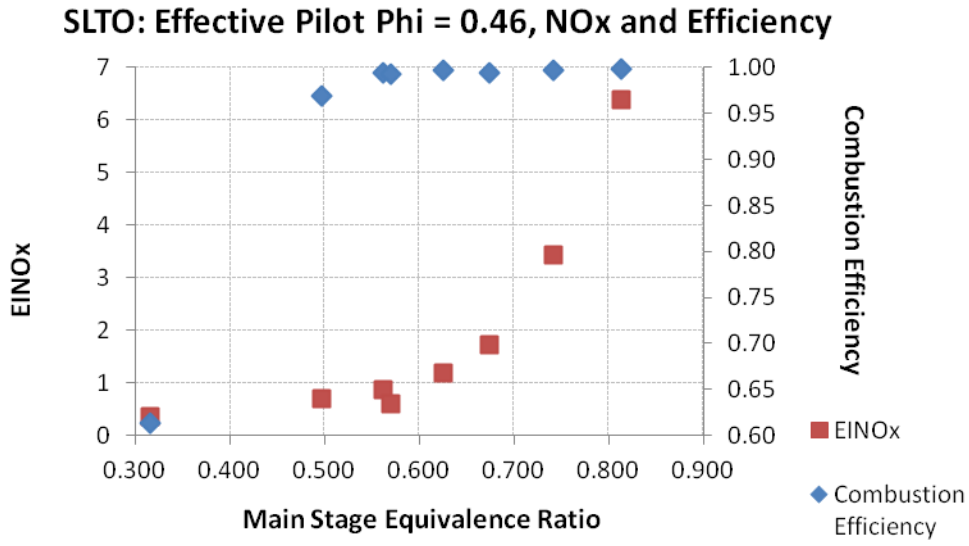

Figure 12-8. *SLTO — Effective Pilot Phi = 0.46, NOx and Efficiency*

Emission results for an effective pilot zone equivalence ratio of 0.8 are shown in ***Figures 12-9*** and ***12-10***. ***Figure 12-9*** shows EINOx and EICO data as a function of FAR. ***Figure 12-10*** shows EINOx and combustion efficiency as a function of main stage equivalence ratio. Again, the NOx emissions decrease as the main stage equivalence ratio decreases. Note that because more fuel is directed through the pilot, the main stage equivalence ratio is lower, even for the same FAR as before. For these conditions, the combustion efficiency is maintained above 99 percent for main stage equivalence ratios as low as 0.49. Below this point, the efficiency starts to drop off. Because of the higher pilot zone equivalence ratio and temperature, the NOx produced in the pilot zone is higher. This is evident by comparing the NOx results in ***Figure 12-8*** and ***Figure 12-10***. Although the main stage NOx may be lower due to the leaner main stage equivalence ratio, the NOx contribution from the pilot more than offsets this. Note that a few repeat points were taken later on in the test cycle (on later days), near the cycle FAR. These repeat points showed slightly lower EINOx than the previous test points (about 4.5 EINOx versus the 6.4 EINOx of the earlier tests), all with a high combustion efficiency. It is unclear why this slight drop in EINOx was observed.

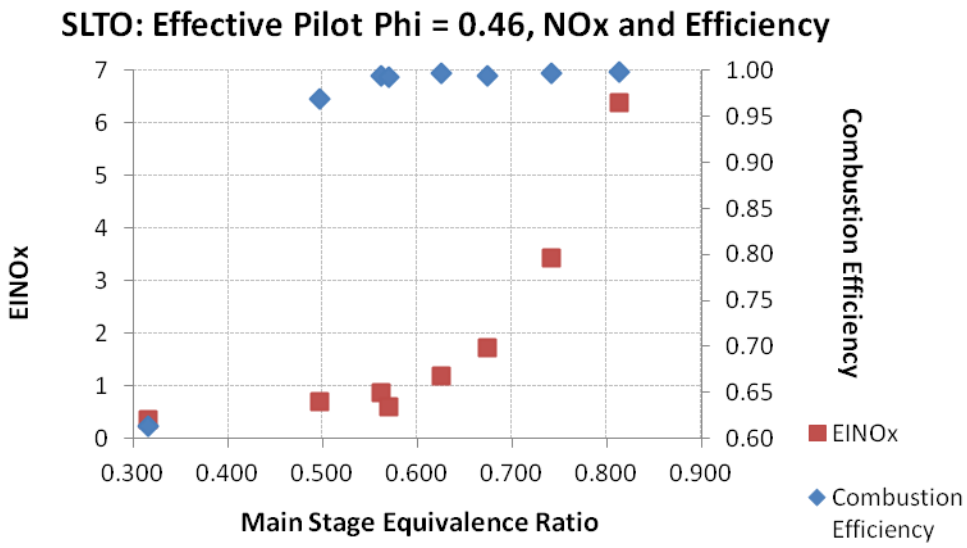

Figure 12-9. *SLTO — Effective Pilot Phi = 0.8, NOx and CO*

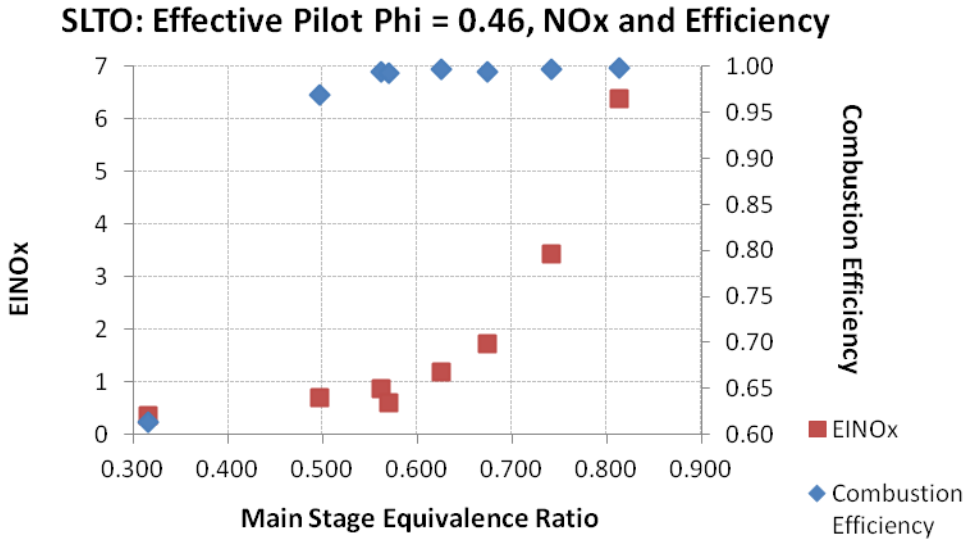

Figure 12-10. *SLTO — Effective Pilot Phi = 0.8, NOx and Efficiency*

Pressure and temperature excursion data was also obtained. The NOx pressure and temperature scaling coefficients were then estimated from the previous simulated SLTO data. The emissions contributions from the pilot and main were estimated separately for the emissions engine conditions, as these were expected to have different pressure and temperature scaling coefficients. The total emissions were then combined for both to give a projection of the EPAP. The EPAP was calculated for effective pilot zone equivalence ratios of both 0.8 and 0.46, as shown in ***Table 12-1***. For an effective pilot zone equivalence ratio of 0.8, the NOx was projected to be 25 percent of CAEP 6. Note that this is a more conservative estimate, as the data showed that the pilot can operate reliably at lower equivalence ratios. For an effective pilot zone equivalence ratio of 0.46, the NOx was projected to be 13 percent of CAEP 6.

Table 12-1. *EPAP Projections Using Pressure and Temperature Excursion Data*

	Condition	***EPAP Coef***	***EINOx***	***EICO***	***EIHC***
Effective Pilot Zone Equiv. Ratio = 0.8	Takeoff	0.2423	24.5	0.8	0.6
	Climb	0.6197	16.3	4.1	1.4
	Approach	0.3614	7.4	37.9	0.8
	Idle	0.6377	6.3	15.8	1.4
		ACS	22.74	26.57	2.19
		CAEP/6	90.11	118	19.6
		% CAEP/6	25%	23%	11%

	Condition	***EPAP Coef***	***EINOx***	***EICO***	***EIHC***
Effective Pilot Zone Equiv. Ratio = 0.46	Takeoff	0.2423	10.0	0.1	0.1
	Climb	0.6197	4.4	0.6	0.2
	Approach	0.3614	7.4	37.9	0.8
	Idle	0.6377	6.3	15.8	1.4
		ACS	11.88	24.22	1.31
		CAEP/6	90.11	118	19.6
		% CAEP/6	13%	21%	7%

12.5 CONCLUSIONS/RECOMMENDATIONS

The three-sector ACS combustor was tested at the UTRC JBTS facility to verify that it could produce low NOx emissions with high combustion efficiency at relevant NASA N+2 engine conditions. Both Idle and Approach conditions were tested directly at the engine conditions. Idle test results, which employed only the pilot, showed high combustion efficiency, even at relatively low FARs. At Approach conditions, combustion efficiency above 99 percent was observed for fuel flow splits where the majority of the fuel was flowed throught the pilot. SLTO conditions were simulated by applying the same flow parameter as SLTO and scaling the air/fuel flow consistent with the maximum pressure and temperature capabilities of the facility. Before running the simulated SLTO conditions, pilot-only tests were run at the facility pressure and temperature limits to determine the optimum fuel flow splits between the pilot and main stage. The data showed that the pilot could be run efficiently down to an effective pilot zone equivalent ratio of 0.46. This optimum pilot equivalence ratio was then applied and the main stage equivalence ratio varied with FAR at simulated SLTO conditions. These tests demonstrated low NOx and high efficiency. At the temperature and pressure limits of the facility, the enthalpy from the pilot zone is sufficient to maintain high combustion efficiency of the main stage, as long as the main stage equivalence ratio is above a certain lean threshold value. Pressure and temperature excursion tests were run to estimate the NOx pressure and temperature scaling coefficients. Using these scaling coefficients, the EPAP at this optimum pilot equivalence ratio was projected to have NOx emissions of 13 percent of CAEP 6. Tests were also run with a pilot fuel flow split that was closer to stoichiometric to bound the emissions and ensure high combustion efficiency for the pressure and temperature excursion tests. For this pilot equivalence ratio closer to stoichiometric, which represents a more conservative estimate, the projected EPAP was 25 percent of CAEP 6. Therefore, it is expected that the NASA ASCR tests (which can reach the actual engine conditions) will meet the 25 percent of the CAEP 6 goal set out as part of the NASA N+2 program.

13. TASK 3.3.6 — FIVE-SECTOR PERFORMANCE TESTING

13.1 FIVE-SECTOR PERFORMANCE RIG AND FACILITY

A key asset for development of low-NOx combustors is the arc sector performance rig facility installed at the UTRC JBTS. There were two activities executed: the facility itself and the combustor test articles. UTRC executed the design, procurement, and installation of the facility features, and P&W executed the design, procurement, and builds of the test articles.

Arc-sector rig combustion tests were performed in UTRC's JBTS. The JBTS is a self-contained combustion facility having five combustion test cells. In each cell, steady state high-pressure air is supplied. The air is heated by a non-vitiated gas-fired heater. Hydrocarbon fuels are supplied. Hydrogen, oxygen, and nitrogen gas systems are also provided. The JBTS is supplied with cooling water from a 6-in. city-water main. Exhaust flow cooling is provided by water-spray from a closed-loop cooling system (CLCS). Emissions analysis equipment provides measurement of smoke, unburned hydrocarbons, CO, CO_2, O_2, and nitrogen oxides.

Arc-sector tests are performed in Cell 3 of the JBTS. The arc-sector facility is shown in a cutaway drawing in ***Figure 13-1***. The includes a traversing emissions probe for obtaining exhaust-gas samples. The arc sector rig facility was a clean-sheet-of-paper design.

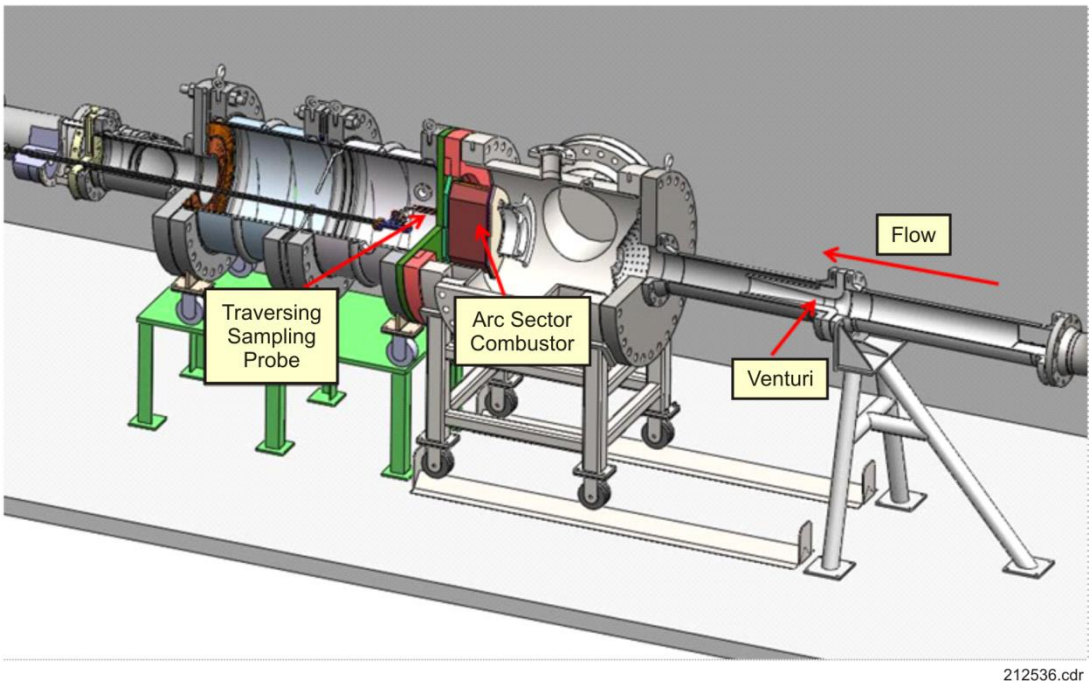

Figure 13-1. *Conceptual Layout of UTRC Rig Facility*

The schematic shows the primary pressure vessel and two downstream spool pieces adapted from a previous program. All were existing parts. Flow is from right to left in this view. Upstream and downstream piping was new. An arc sector test article is shown in the pressure vessel in ***Figure 13-1***.

The baseline test article was a high-integrity simulation of the P&W Geared Turbofan combustor/diffuser section.. This is an engine with a Talon X combustor. The basic test article was a five-sector arc cut from an engine program development combustor. The diffuser case faithfully mimicked the development design, and development fuel injectors were used. The purpose of the baseline test was to confirm the five-sector rig as a valid development tool through comparison of results to annular and engine results.

Figure 13-2 shows the arc sector rig facility.

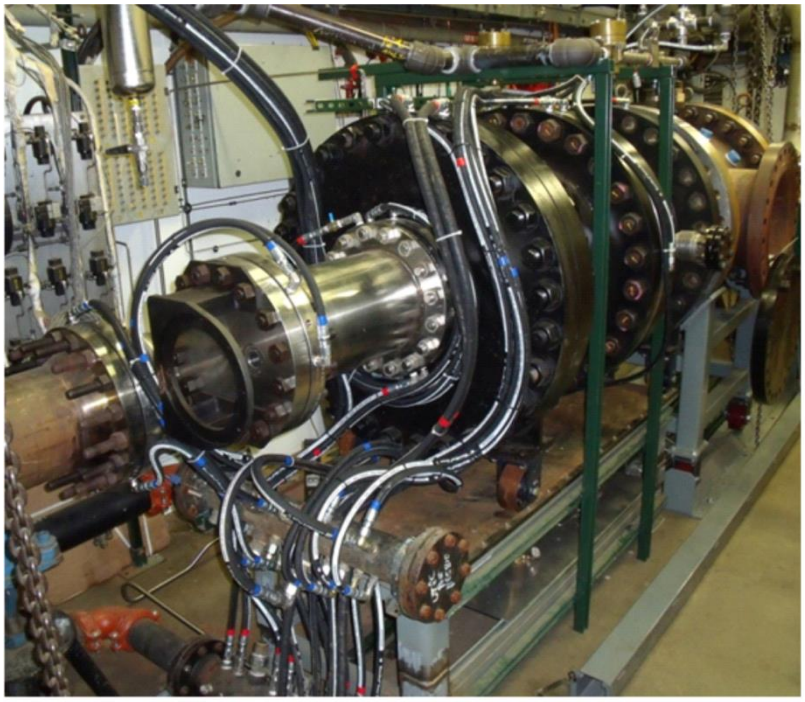

Figure 13-2. *Arc Sector Rig Facility*

13.2 MULTISECTOR TESTING OF THE TALON XE

13.2.1 Test Objective

The five-sector injector arc rig is designed as a workhorse to be a cost-effective tool to evaluate the performance of a combustion system.

13.2.2 Rig Description

The five-sector arc rig simulates the TALON-X combustor. The combustor is actually a cutout section of an actual annular combustor with added cooled sidewall. The shell uses the liner panels if possible. A minor change is the addition of a second ignitor near the side wall for an infinite tube probe for facility safety. The diffuser system made of a cover and sheet metal follows the same surface contour as that of the engine. ***Figure 13-3*** shows a cross-section of the test facility, and ***Figure 13-4*** shows the test facility with the arc rig installed. The TCA is simulated with metered extraction at the aft end of the diffuser case.

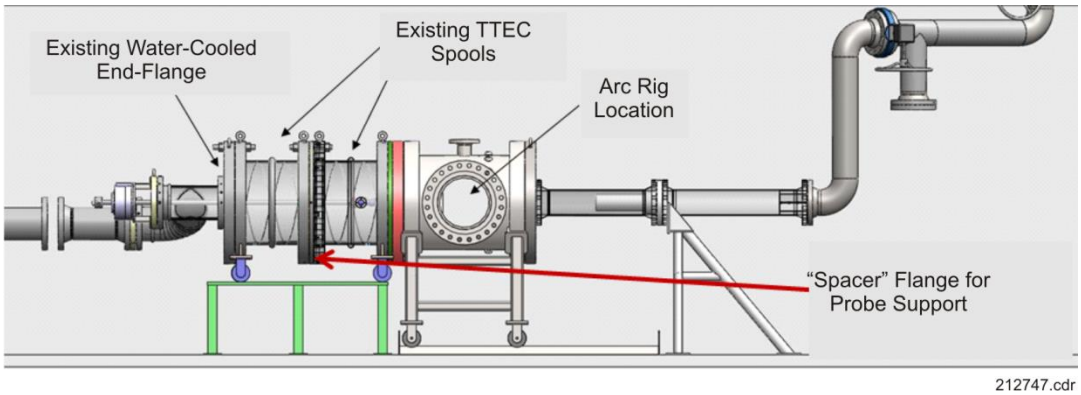

Figure 13-3. *Cross-Section of Test Facility at UTRC*

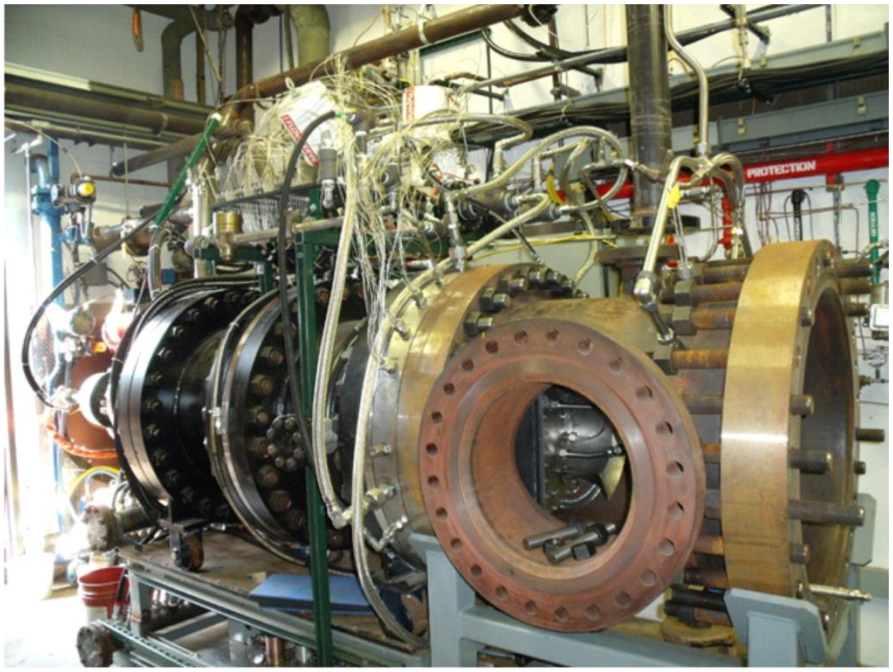

Figure 13-4. *Test Facility With Arc-Rig Installed*

13.2.3 Test Plan

The primary objective of the test plan is to assess the emissions performance. It also had points to obtain temperature and pressure scaling to make projection at higher pressures and temperatures.

13.2.4 Instrumentation

In conjunction with the pressure instrumentation, there are five inner diameter and three outer diameter liner thermocouples in line with the fuel injectors as proof of light. There are also thermocouples on the sidewall to ensure it is adequately cooled. For facility structural safety, an infinite-tube probe is placed at the spare ignitor boss to monitor the acoustics. At the combustor exit there is a five-probe rake that traverses to take gaseous and smoke emissions samples.

13.2.5 Results

The NOx emissions from the arc-sector rig matched quite well with that of the annular rig counterpart.

Figure 13-5 shows the comparison of NOx emissions corrected to cycle conditions. The baseline sector rig simulated the annular rig well in NOx emissions. However, the Build 2 burner did not show any significant NOx emissions reduction. A root-cause analysis was conducted and the finding indicated three possible reasons for the poor performance.

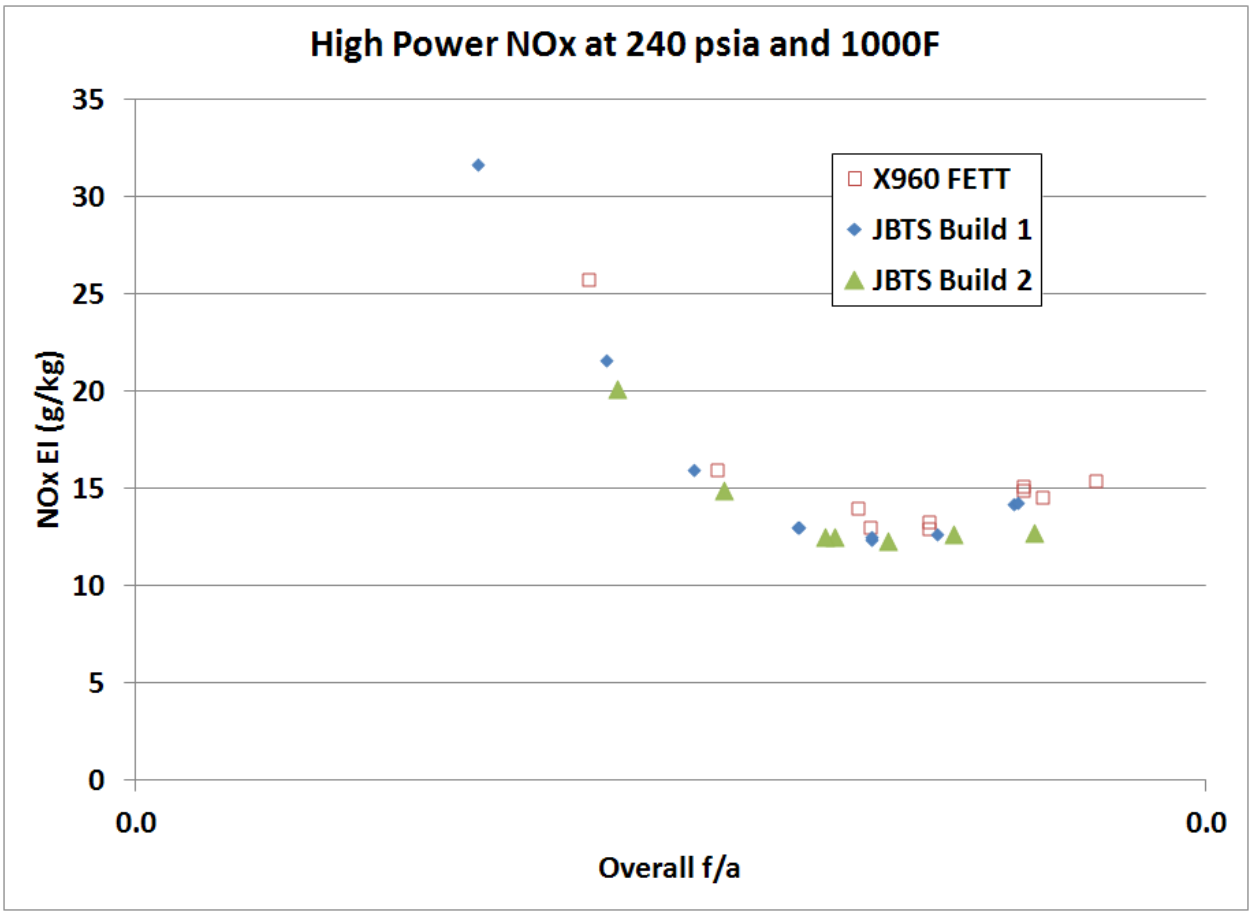

Figure 13-5. *NOx Emissions Corrected to Common Inlet Pressure and Temperature*

Simulated takeoff power smoke emissions in a sector rig that is limited to scaled pressure and temperature does not simulate well. With the inlet temperature being lower than the true inlet temperature, the local chemistry and temperature that produces and destroys smoke would be significantly changed. ***Figure 13-6*** shows the comparison of smoke emissions for the annular Rig 2 temperature conditions. The higher temperature has significantly lower smoke numbers.

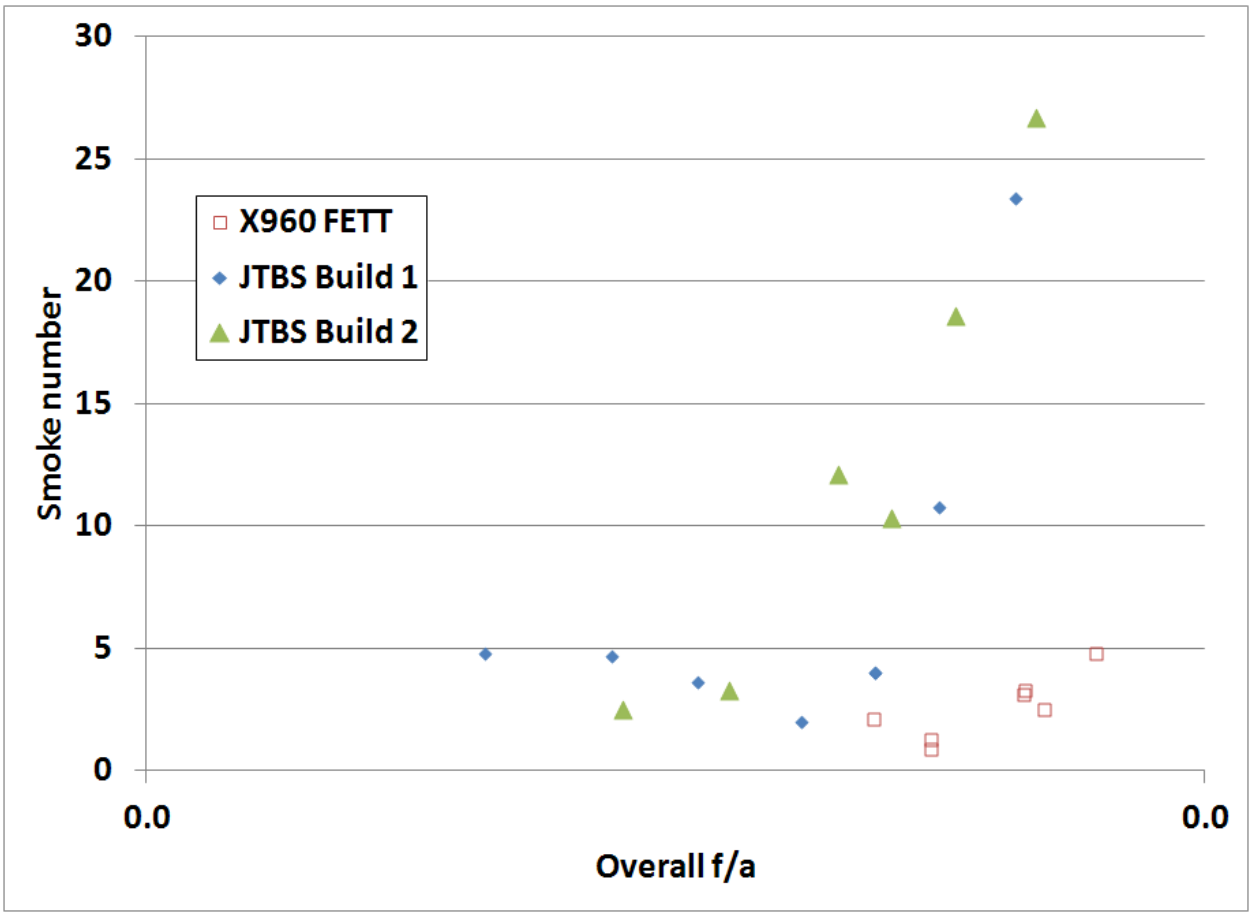

Figure 13-6. *Comparison of Smoke Numbers*

The data for Approach NOx emissions tells the same story as that of the takeoff simulation. ***Figure 13-7*** shows the comparison of NOx emissions at approach for the two builds.

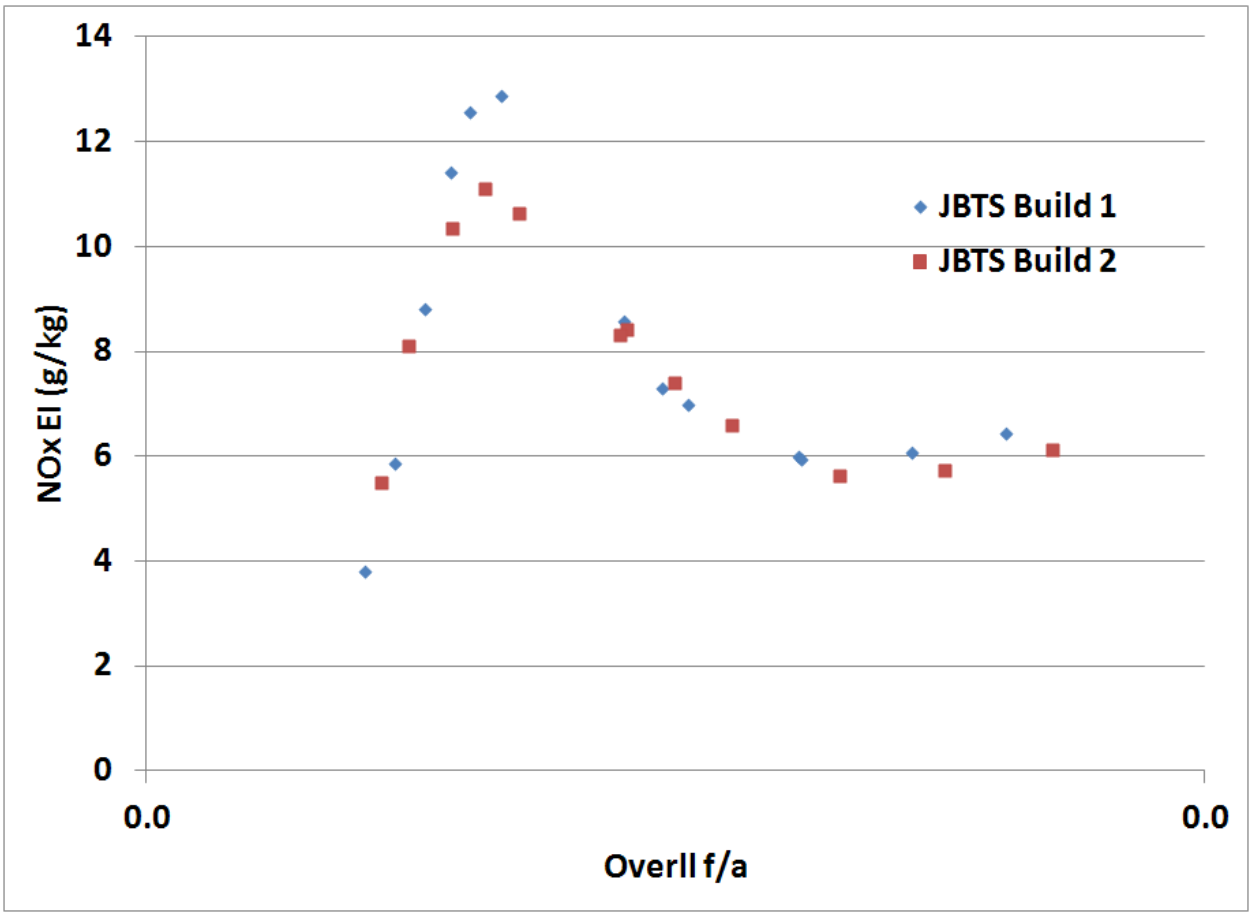

Figure 13-7. *Approach NOx Emissions*

The sector rig did a good job simulating the idle condition. The inlet temperature and pressure are within the rig facility capacity. ***Figure 13-8*** shows the NOx emissions comparison. Build 1 NOx emissions compares well with the annular rig. While Build 2 NOx emissions does show a reduction at the higher FAR, that did not occur at higher temperature and pressure.

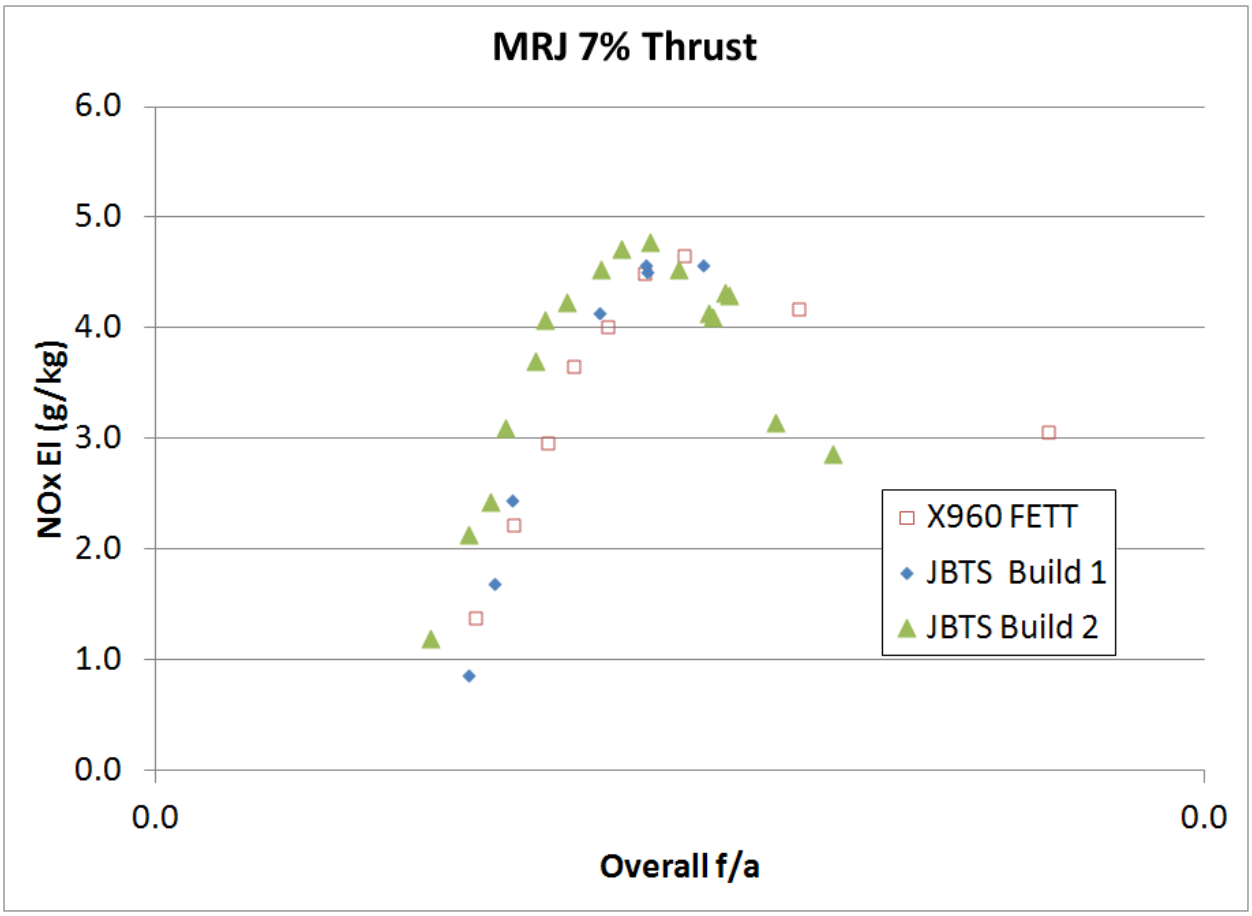

Figure 13-8. *Idle NOx Emissions*

The idle CO emissions trend appears to behave as expected. ***Figure 13-9*** shows the comparison of the CO emissions. Although the arc sector rig has lower emissions than the annular rig, the lowest CO emissions seem to occur at the same overall FAR. The reason for differences may be due to the two types of fuel nozzles that the annular rig uses. Of the two types, one may have lower local front-end FAR that may have caused higher CO emissions. The sector rig only uses one nozzle type, thus the difference.

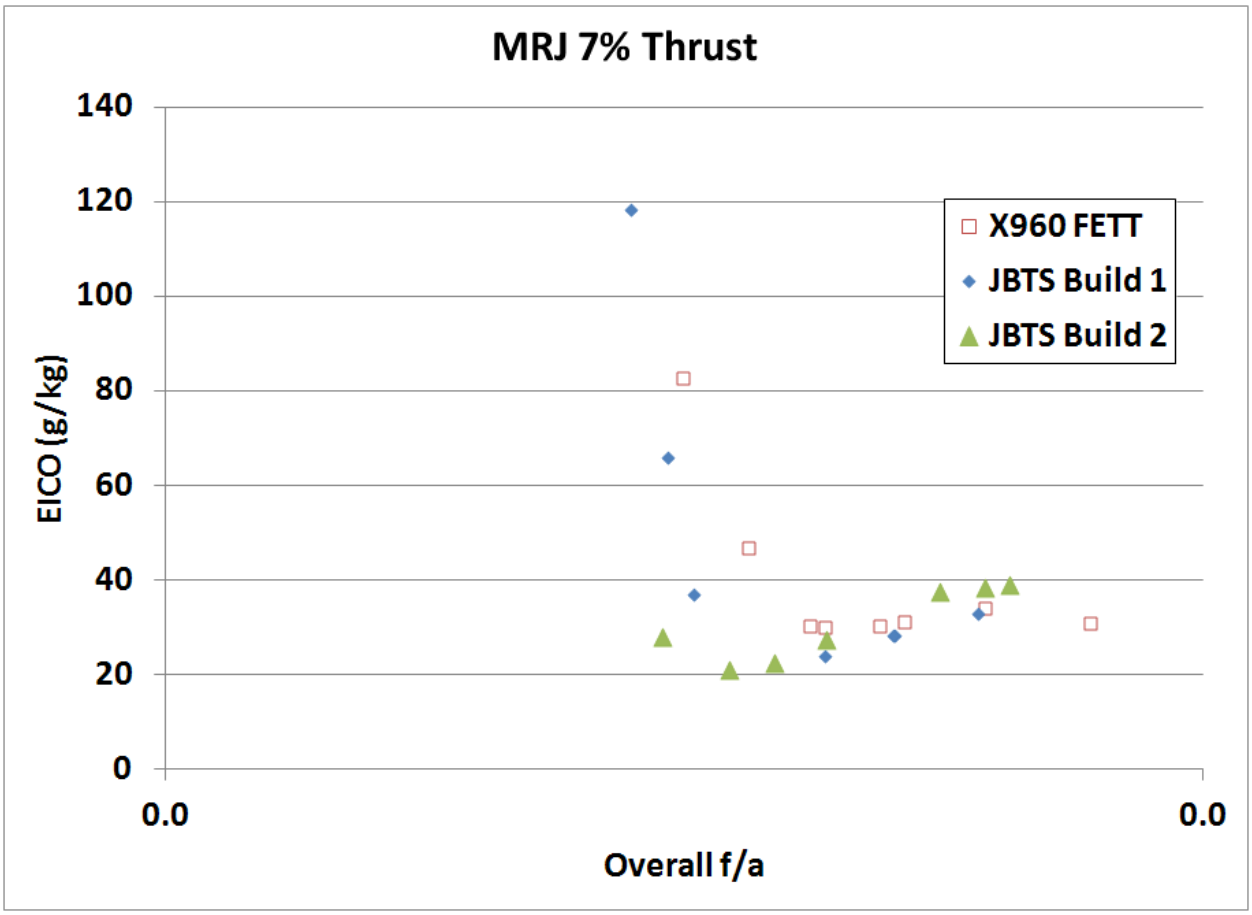

Figure 13-9. *Idle CO Emissions*

The idle hydrocarbon (HC) emissions also behave as expected. ***Figure 13-10*** shows the comparison of the HC emissions. The difference between Build 1 and the annular rig is due to the same reason as the CO emissions above. Build 2 has lower HC emissions than build 1 is due to the lower swirler airflow. Lower swirler airflow produces a higher FAR front-end. Thus, as expected, Build 2 has a lower LBO.

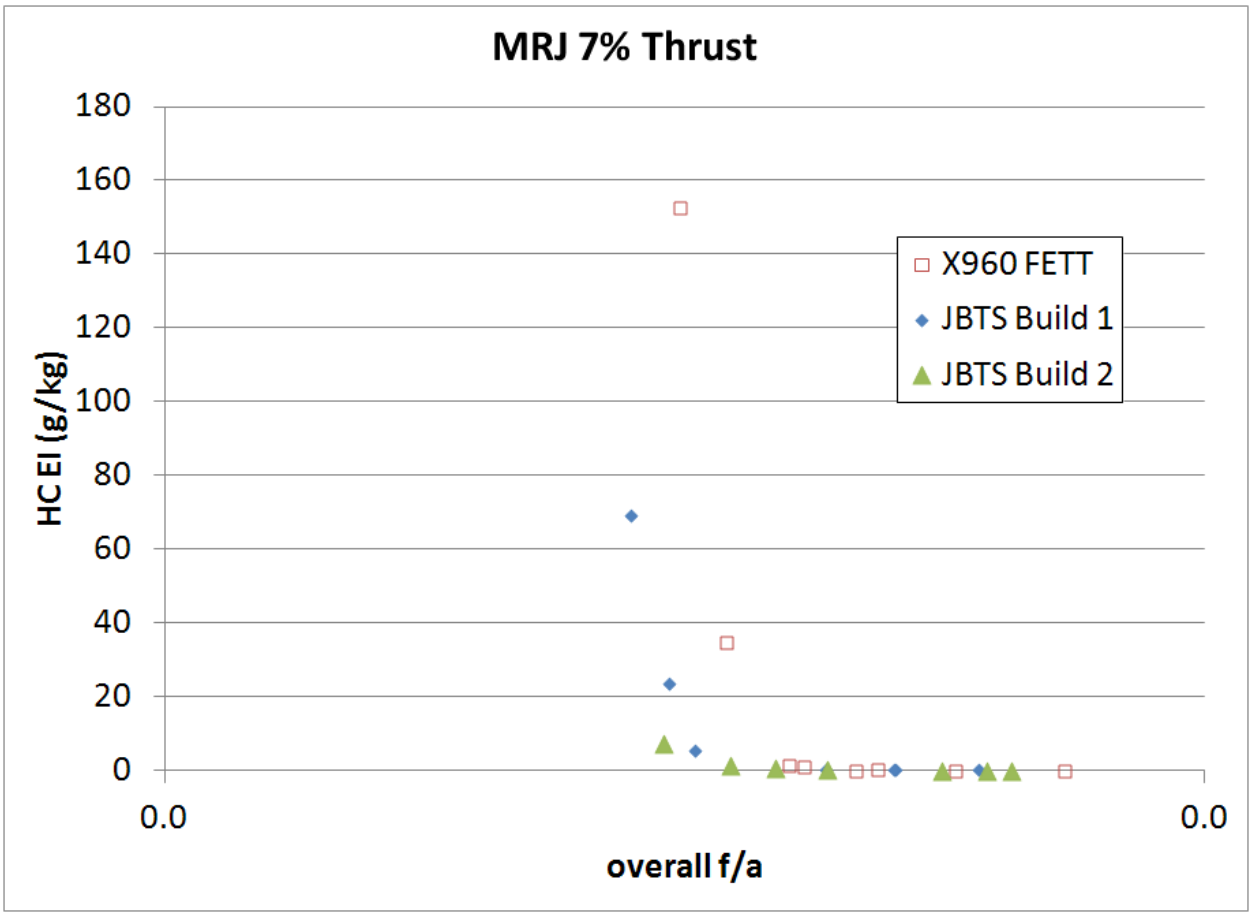

Figure 13-10. *Idle HC Emissions*

13.2.6 Recommendation

The five-build planned sector rig should be completed to validate the cold flow characterization of the fuel injection system for fuel-air uniformity trending with emissions performance.

Investigation needs to be made to identify the proper characterization that trends with emissions performance, if correlation is poor. This will save future development cost. All the characterizations were taken downstream of the swirlers.

14. TASK 3.4.1 — DOWNSELECT AND DESIGN/FABRICATION OF ASCR

14.1 EMISSIONS PROBE

In preparation for combustion tests in NASA's ASCR rig, UTRC has designed and fabricated a piccolo-probe assembly for obtaining gas-samples for emissions measurement. The probe assembly can be fit to either the CRESS or the ACS test articles. The assembly comprises nine fixed but removable water-cooled probes, with multiple holes in each probe for gas-sample extraction from the combustor exit plane. The individual probes are held by small flange mounts along the OD of their support-flange (housing), and allowed to accommodate thermal growth (move freely) on their opposite ends. The assembly is shown from the FLA view in ***Figure 14-1***. All sample lines and cooling-water lines will be routed through the ASCR rig's inlet plenum for egress from the ASCR rig.

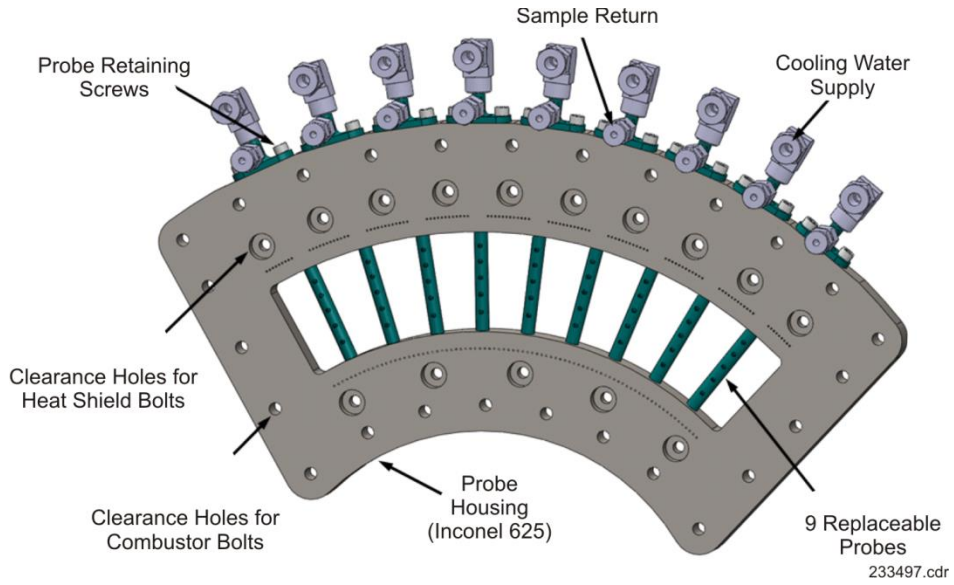

Figure 14-1. *Forward-Looking-Aft (FLA) View of Piccolo-Probe Assembly*

Design requirements for this piccolo-probe included the following:

- Common (universal) design that fits both the CRESS and ACS combustor rigs
- No change to the combustor hardware for testing at UTRC versus NASA — this requires the piccolo-probe housing (support flange) to be compatible with the combustor rig mounting bolt pattern used in the UTRC rig
- Maintenance of (incorporate) the combustor exit throat cooling scheme used in the UTRC rig
- Provision for mounting the exhaust heat shield surrounding the combustor exit
- Routing of the cooling-water and emissions-sample lines through the rig's inlet plenum, without interference with required rig hardware and plumbing
- Minimal air leakage through the probe mounting holes
- Cooling with open-loop water for the probes, with water spray into the exhaust
- Ability to operate and sample combustion gases at combustor exit conditions up to 900 psia pressure and4,000°F temperature
- Ability to remove individual probes, for repair or replacement
- Accommodation of differential thermal growth (avoid thermal stresses).

The piccolo-probe design shown in ***Figure 14-1*** satisfies the above requirements. As shown, the assembly's *housing* (i.e., small flange supporting the individual probes — see label in ***Figure 14-1***) is sandwiched between the combustor and the large combustor mounting flange. The exhaust heat-shield then mounts to the aft face of the piccolo-probe *housing*.

The piccolo-probe assembly fits into a pocketed section of the combustor mounting flange, thus preserving the axial position of the combustor, plumbing, and support structure (with respect to the mounting flange's upstream face) when the combustor is moved from UTRC to the NASA facility. Because the assembly is mounted within this pocket, the assembly must be removed from the combustor mounting flange if individual probes need to be removed for repair or replacement, so the probes can slide out free of obstructions.

The UTRC exit throat will be replaced by the thicker piccolo-probe housing at NASA (with the extra thickness being accommodated by the deeper pocket in the combustor mounting flange for NASA). The exit throat and probe housing are both air-cooled as shown in the figure, by cooling-air that passes through holes in the throat or housing material. For the piccolo-probe housing at NASA, as compared to the exit throat at UTRC, these cooling holes were repositioned along the OD to avoid interference with the individual probes. The holes adjacent to the probes were angled to provide cooling air in the probes' wakes.

In the NASA installation, the UTRC exit throat is replaced by the piccolo-probe assembly. The air-cooling arrangement in the piccolo-probe housing is equivalent to the UTRC exit throat, except for some displacement of the holes to avoid the individual probes, and the total number of cooling holes is the same.

Nine emissions sample lines will egress the NASA rig through sample lines FES1 through FES9, and the high-pressure cooling water will enter through lines IHP2/W2, as shown in the figure. There will be no water return line, since the probe cooling water will spray directly into the combustion exhaust stream.

Various views of an individual probe are shown in ***Figure 14-2***, showing the cooling-water flow passages and the sample-gas flow passages. Gas samples are obtained from the forward-facing portion of each probe, and high-pressure cooling water sprays into the exhaust stream from the aft-facing portion of each probe. For gas sampling from each probe, five holes are spaced on centers of equal area. These five holes feed a common gas-sample flow passage which leads to the 1/8-in. swagelock fitting, and a single sample line then exits the rig for each probe. Thus, nine sample lines exit the rig altogether.

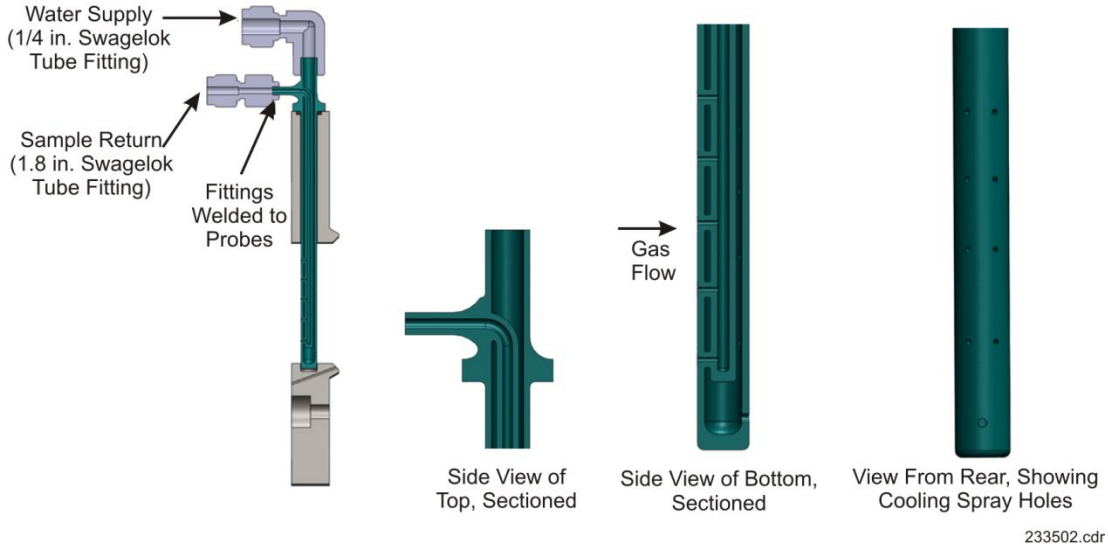

Figure 14-2. *Views of Individual Probe*

Each probe is fixed at its top by a small flange and two retaining screws. The bottom of each probe is slip-fit into a recess in the probe-assembly housing, to accommodate differential thermal growth between the probes and the housing (***Figure 14-3***).

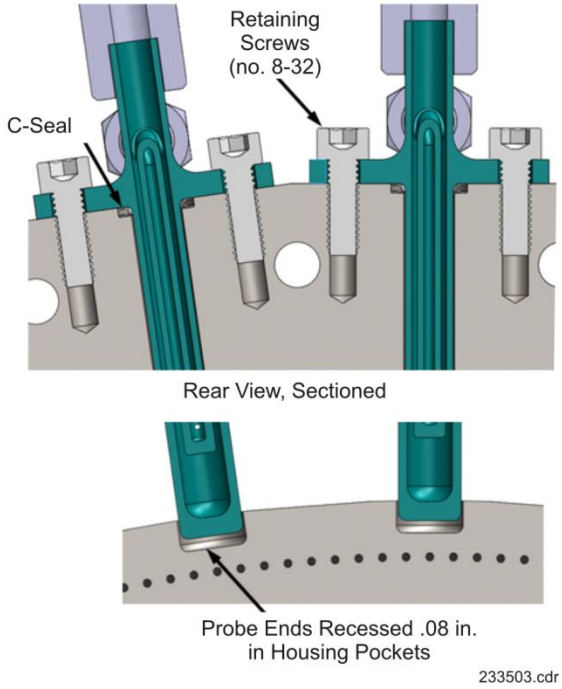

Figure 14-3. *Sectioned View, Showing Fit and Mounting of Individual Piccolo-Probes in Their Housing*

ATTACHMENT A — STATEMENT OF WORK

NASA N+2 CONTRACT STATEMENT OF WORK — FUEL SYSTEM ARCHITECTURE

28 JULY 2010

1.0 SCOPE

This Statement of Work (SOW) is a request for the supplier to provide information in support of NASA's N+2 Contract. Pratt and Whitney (P&W) is seeking industry engagement to develop innovative ways to design / fabricate a fuel system for the N+2 program. P&W is considering making multiple awards and may share the results of these studies with NASA. From a system level perspective, the goal of this SOW is to find the optimal procurement approach. The optimal approach can be based on currently available technology, or it can be based on new technologies that require development. The supplier can also propose a solution that uses a mixture available technologies / products and new technologies.

Responders to this SOW are requested to provide a description of the technical approach and business approach for the N+2 fuel system. In the case where the proposal requires new technologies, the supplier should indicate the scope of development needed to mature these new technologies for incorporation into the proposed fuel system. The supplier is asked to provide any validation requirements needed for those products and technologies that are not mature for use in a fuel system application.

1.1 NASA N+2 OVERVIEW

In response to the NASA Research Announcement NNH09ZEA0001N-SSFW1, Amendment No. 2, Pratt & Whitney (P&W) has proposed a comprehensive program for combustor development. This program will culminate in the delivery of a three-nozzle arc sector rig to NASA-Glenn with the goal of demonstrating a 75 percent reduction of Landing Take-off (LTO) NOx in an N+2 gas turbine engine and airframe. The reduction of LTO NOx is based upon a review of combustor requirements of P&W N+2 engines using the Geared Turbo Fan architecture and suitable airframes. Combustor concepts will be considered based on previous NASA-funded work as part of the High Speed Civil Transport (HSCT) Program, Ultra Efficient Engine Technology (UEET) Program, and the Supersonic Low Emissions Combustor Program, as well as extensions to P&W world class, low emissions TALON combustors and novel concepts being worked at P&W and the United Technologies Research Center (UTRC) under internal funding. Detailed computational fluid dynamics (CFD) calculations with P&W advanced Large Eddy Simulation (LES)-based codes will be used to develop and screen the various combustor concepts. Concepts will be evaluated as sub-components, simplified configurations, and full combustor geometry.

In parallel to these efforts, work shall be performed on the key enabling technologies of cooling, fuel system staging and control, and acoustics analysis and prevention. The cooling effort will focus on approaches and materials to improve the industry-leading capabilities of P&W's impingement film floatwall (IFF). Proposed fuel staging and control efforts plan to take advantage of advances in miniaturization and distributed control to develop simplified, robust fuel system controls and valves. P&W is considering approaches for the N+2 combustor that include such concepts as fuel staging internal and external to the fuel nozzles, active combustion control, individual control of each fuel nozzle, potential multiple manifolds, operation with alternative fuels, heated fuels, and other options. The acoustics efforts will be based on P&W/UTRC proprietary models and control approaches. The proposed program of combustor concept evaluation using CFD and test rigs, will culminate in the design and fabrication of a combustor test rig suitable for testing at NASA intended to demonstrate achievement of NASA N+2 emissions goals, accompanied by data as to how the cooling approach, fuel system design, and acoustics will enable achievement of those goals.

1.2 SOW OVERVIEW

The goal of this SOW is to focus on key enabling technologies in the areas of fuel system staging and control. P&W wishes to determine what options are available in these areas by surveying the industry for various fuel system architectures. The fuel system for the N+2 combustor should be capable of smoothly controlling and

measuring fuel flow in four independent circuits within a single sector, with the flexibility of controlling anywhere between 2 and 6 circuits total. The definition of circuit has been kept broad to encourage suppliers to propose new methods of fuel delivery. This includes controlling the fuel flow smoothly and independently within the fuel nozzle.

When proposing a fuel system architecture, the supplier is requested to keep the other factors, including cost, weight, durability, and operability, on par with current systems. Although the supplier should strive to keep these factors within the current range of products, trades among these factors shall be explicitly stated and high-lighted in the proposals.

1.3 SOW KEY CONSIDERATIONS

The following is provided as a guide to the format and information expected in response to the SOW.

A. Responses shall provide a description of the architecture with the following information:

   1. Schematic or system block diagram and description of operation.
   2. Existing system or 3-D graphic models, if available.
   3. Description of changes between existing and proposed systems
   4. An assessment of the following technical performance measures:
      a) Ability to meet functional requirements
      b) Safety, reliability and maintainability requirements
      c) Life
      d) Physical envelope
      e) Recurring and non-recurring costs
      f) Dry weight
      g) Environmental assessment
      h) Others - any factors that would impact the overall reliability and performance, but is not explicitly listed or mentioned in the SOW.

B. Responses shall address the benefits of the proposed system architecture, why the proposed architecture is recommended, and a discussion of any system/component limitations.

C. Responses shall include an assessment of Technology Readiness Level (TRL) and Manufacturing Readiness Level (MRL). The assessment shall include a plan demonstrating how all system/component elements that are currently not TRL-6 will achieve the desired maturity level prior to 2020. The TRL and MRL assessment should also include:

   1. The required technology development roadmap.
   2. Test program plan to validate TRL/MRL technical goals and air worthiness.

This SOW combines many related technologies into a single proposal. As such, respondents to this SOW are instructed to address only those areas where they have expertise. While specific details on subsystems should be included where possible, suppliers should not take these as inviolate design requirements. Alternatives that could better achieve key considerations are encouraged to be suggested. P&W envisions this study effort would be the basis for future collaborative efforts between the supplier and PW to develop the technologies identified in the study.

Suppliers are encouraged to meet as many of the requirements as possible, but all trade-offs shall be explicitly documented. The focus of this SOW is on the fuel staging and control aspects of the fuel system. The entire fuel

system architecture has been included to allow for as many design considerations as possible. Suppliers are encouraged to be as innovative / novel in their proposals as possible.

1.4 PROPOSAL PROCESS AND TIMELINE

Proposals for this SOW will follow a three step process. First, suppliers are to respond to the initial request for quote (RFQ). The response to the RFQ should include a high level summary of what the proposal is, the timeline required to complete the study, and a detailed cost break-down to complete the study. Responses should include enough detail so that an evaluation can be made of what the proposal will encompass, i.e. a whole fuel system solution or a focused change to a subsystem. The cost breakdown should delineate the cost of resources, additional studies, and testing required to complete the study. Responses to the RFQ are expected within 30 days of receipt of this SOW. Submissions shall be submitted in paper and electronic forms (Adobe Acrobat or MS Office) per the terms of the accompanying P&W RFQ.

The responses to the RFQs shall be evaluated by a P&W engineering team, and the chosen responses will receive a Purchase Order (PO) to complete the study. For each chosen proposal, the supplier shall provide an in-person debriefing on its technical and business approach. This debriefing shall be made 4 weeks after receipt of the PO. The debriefing is expected to highlight any issues that may arise from the chosen approach and highlight the benefits of the proposal over current systems. The debriefing shall provide as much detail as possible, but a completed study is not expected. A Power-Point presentation is expected with the debriefing, and an electronic copy (Adobe Acrobat, MS Office formats) shall be provided.

90 days after receipt of the PO, suppliers are expected to submit their final reports for each chosen proposal. All reports are due no later than 31 December 2010. The final reports shall provide the information requested in sections 1 through 3 of this SOW. The final report shall be submitted in paper and electronic (Adobe Acrobat, MS Office formats) forms per the terms of the accompanying PO.

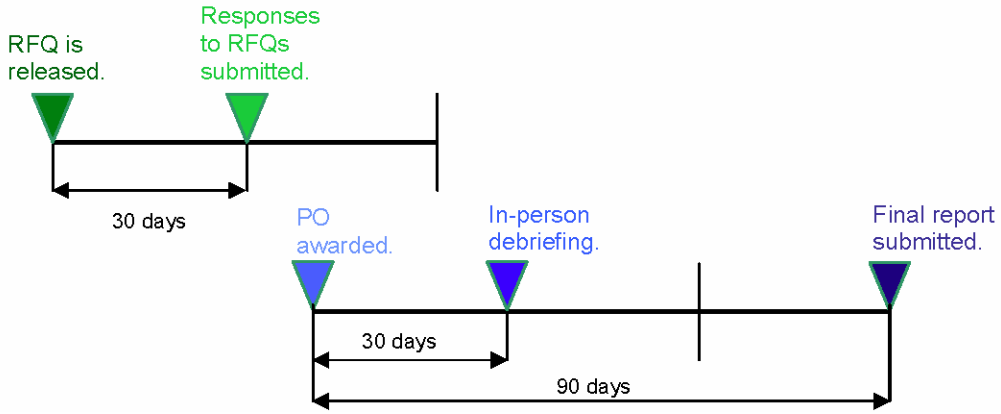

Figure 1: Time-line for Proposals to this Statement of Work

2.0 FUEL SYSTEM ARCHITECTURE REQUIREMENTS

The following section describes the fuel system requirements that are needed to meet the needs of the N+2 combustor. The fuel system under consideration for this trade study will include everything from the fuel inlet in the aircraft through fuel delivery to the individual fuel nozzles. The supplier may propose to make architectural changes to a portion of the fuel system only, but should identify that portion on a schematic of the full system and discuss the relationship between the portion and full system including potential system level impacts. Trades among requirements can be made if the overall system has a gain in performance. When trades are made where a requirement is not met, the supplier should highlight this and then note the overall system gain. The following requirements of the fuel system need to be considered in the proposed architecture.

2.1 FUNCTIONAL REQUIREMENTS

The Fuel System shall modulate fuel supply to the engine based on command. The system shall provide those features necessary to allow the engine to be started on the ground and in the air within the typical commercial starting envelope. The system, under electronic engine control command, shall provide those features needed to control engine power, engine acceleration, deceleration and stability. The system shall permit fuel flow modulation from the minimum start flow up to the declared maximum flow limit. Fuel flow stability at steady state shall be less than ± 0.15% of point. This stability requirement shall include but shall not be limited to any self-induced limit cycling within the item. For the fuel flow loop (WFENG/WFREQ) the goal for the minimum bandwidth (frequency at which the amplitude response attenuates by 3 db) shall be at least 50 rad/sec and the phase lag at 50 rad/sec shall not exceed 90°.

The fuel flow increase from min to max flow shall be at least 100% FS/sec to a max of 400% FS/sec. The fuel metering valve shall fail-safe closed. Accuracy goal for engine start will be better than current systems, with a goal of 1% accuracy above the start region. The system shall have built in test capability and shall be able to accommodate all of today's commercial fuel types, currently densities of 775-840 kg/m3, with considerations for future fuels types in the density range of 750-840 kg/m3.

The Fuel System shall provide fuel shut-off for normally commanded and overspeed conditions. Minimum pressurization for fuel actuation may be an optional capability.

Minimum HP pump pressure rise during engine starting will be sufficient to satisfy actuation requirements. The system shall provide adequate fuel pressure to hold the actuator (s) in position during windmill relight and high power shutdown with actuation flow provided for the actuator(s). The fuel system may have the optional capability to provide fuel pressurization for fuel metering and actuator flow and pressure supply.

The Fuel System shall have low pressure boost pumping capability and meet typical commercial fuel inlet pressurization requirements under normal and emergency operating conditions. The system shall be designed such that the normal airframe boost pressure can prime the fuel system during start-up.

The Fuel System shall provide high pressure relief capabilities.

The Fuel System will provide flow distribution and equalization for combustion and delivery of fuel to each fuel stage and nozzle. The fuel system for the N+2 combustor shall be capable of smoothly controlling and measuring fuel flow in four independent circuits within a single sector with the flexibility of controlling anywhere between 2 and 6 circuits total. The fuel system's goal is to control fuel flow to 0.1% accuracy at each fuel nozzle with a minimal dynamic response of 10 Hz at Idle in order to minimize combustion dynamics

The Fuel Metering Unit shall provide an ecology system to drain manifold fuel. The Ecology Drain shall purge the required volumes during spool-down from speeds at or above idle condition. The ecology drain system shall not affect the engine operation during start. The capability of not affecting the motive flow pressuring during normal engine operation should also be considered.

The IFPC (FSM) Service Life goal will be 50,000 operating cycles or 60,000 engine hours whichever occurs first.

The capability to provide a supply of motive flow to the aircraft shall be considered in the proposed fuel system.

The proposed fuel system architecture will have a way to protect downstream components within the system. The system shall meet the specified requirements when operated long-term (i.e. 2-3 months) with fuels (including low lubricity fuels) contaminated to a 'long-term' contamination level, which is considered equivalent to that permitted by ATA Specification 103, (2g/1000 US gal). The contamination composition shall be assumed equivalent to that specified in Table 1 below:

Table 1: Fuel Contamination Schedule (9.3 grams)

Contaminant	Particle Size	Quantity
Ferroso-Ferric Iron Oxide [Fe_3O_4 (Black Color), Magnetite] Ferric Iron Oxide [Fe_2O_3, Hematite]	0 - 5 microns 0 - 5 microns 5 - 10 microns	1.0 g / 1,000 US gal. 4.7g / 1,000 US gal 0.3g / 1,000 US gal.
Sharp Silica Sand	150-300 microns 300-420 microns 420-1000 microns 1000-1500 microns	0.25 g / 1,000 US gal. 0.25 g / 1,000 US gal. 0.45 g / 1,000 US gal. 0.25 g / 1,000 US gal.
Prepared dirt conform to ISO 12103-1 Arizona test Dust A2 Fine Grade	Mixture as follows (cumulative distribution) 1 micron (2.5 - 3.5%) 2 microns (10.5 - 12.5%) 3 microns (18.5 - 22.0%) 4 microns (25.5 - 29.5%) 5 microns (31.0 - 36.0%) 7 microns (41.0 - 46.0%) 10 microns (50.0 - 54.0%) 20 microns (70.0 - 74.0%) 40 microns (88.0 - 91.0%) 80 microns (99.0 - 100.0%)	2.0 g / 1,000 US gal.
Cotton linters	Below 7 Staple (U.S. Department of Agriculture Grading Standards SRA-AMS 180 and 251)	0.1 g / 1,000 US gal.
Crude naphthenic acid		0.03 percent by volume
Salt water prepared by dissolving salt in distilled water or other water containing not more than 200 parts per million of total solids	4 parts by weight of Na Cl 96 parts by weight of H_2O	0.01 percent by volume entrained

2.2 PHYSICAL REQUIREMENTS

Physical envelope, interfaces and installation process will be similar to current systems unless a substantial gain in system level metrics occurs. However, the combustor considered for the NASA N+2 project may require multiple and different diffuser case penetration options than traditional systems.

2.3 ENVIRONMENTAL REQUIREMENTS

Trade studies shall consider maximum fuel temperatures to not exceed 250°F initially in the next 5 years with a goal of up to 350 Deg F in the 2015 to 2025 timeframe. The proposed fuel system should also consider applications where the fuel temperatures may reach 700°F past the 2025 timeframe. The minimum engine fuel inlet temperature shall be -40°F (-40°C) or the minimum temperature resulting in fuel viscosity of 12 centistokes.

Maximum ambient temperature environments within the nacelle shall be assessed at typical commercial environments while considering environments 50 -100°F hotter. Typical commercial engine vibration/loading should be assessed.

The fuel system shall not leak from any part / component except at drains specifically provided for this purpose. The fuel system will meet the same EMI / lightning/ EMP requirements as current systems.

2.4 RELIABILITY, MAINTAINABILITY, AND SYSTEM SAFETY REQUIREMENTS

When proposing the fuel system architecture, the supplier shall identify all know reliability, maintainability, and system safety (RMSS) deficiencies and hazards. When possible the supplier will provide RMSS- related analysis such as:

- reliability allocations.
- preliminary failure modes and effect analysis.
- system safety analysis.
- preliminary hazard analysis.

The proposed fuel system will address these reliability and maintainability requirements:

- Mean Time Between Overhaul (MTBO): comparable to current systems.
- Line replaceable unit (LRU) removal time: comparable to current systems.
- Mean time between failures: same or better than current systems.

The following characteristics are needed to meet the safety requirements of the N+2 Combustor. For this subset of characteristics, the minimum requirement must be met. The overall system proposal must meet all these requirements in order to meet the goals of the SOW:

- Fire safety: the item shall meet the requirements of CPW125 chapter 3.19.2 during and after exposure to a 2000 deg F flame for 5 minutes. CPW125 paragraph 3.18 d) shall be replaced by "The ability to shutdown the engine shall not be impaired or it is permissible for the engine to shut down in a non-hazardous manner within the test period."
- Explosion proofness: with the exception of devices intended to ignite fuel-air mixtures, all electrical components shall not ignite any explosive mixture surrounding that component.
- Blade out safety: comparable to current systems.
- Redundancy: any control feature must fail is a "safe" position.
- Safety criticality: must be higher than current technology. Since these nozzle are novel, they will received increased scrutiny.
- Failsafe position and rate of failsafe: individual fuel nozzles and fuel stages are to fail in a predetermined nominal position that allows for the safe operation of the engine without unbalancing the other fuel nozzles.

2.5 MATERIALS OF CONCERN

All hardware installed on the engine shall comply with PWA-328A, "Design Requirements for Product Materials of Concern".

Pratt & Whitney Materials of Concern:

1. ARSENIC & COMPOUNDS
2. ASBESTOS FIBERS
3. BENZENE (EXCEPT IN FUEL)
4. BERYLLIUM
5. BISPHENOL A
6. CADMIUM & COMPOUNDS
7. CHLORINATED SOLVENTS — 1,1,1 — TRICHLOROETHANE (METHYL CHLOROFORM)

8. CHLORINATED SOLVENTS — CARBON TETRACHLORIDE
9. CHLORINATED SOLVENTS — METHYLENE CHLORIDE (DICHLOROMETHANE)
10. CHLORINATED SOLVENTS — PERCHLOROETHYLENE (TETRACHLOROETHYLENE)
11. CHLORINATED SOLVENTS — TRICHLOROETHYLENE
12. CHLORINATED SOLVENTS — OTHERS
13. CHROMIUM, HEXAVALENT (CrVI) AND ITS COMPOUNDS EXAMPLES: SODIUM DICHROMATE,
14. STRONTIUM CHROMATE
15. COBALT DICHLORIDE
16. CYANIDE COMPOUNDS
17. DIMETHYL-FORMAMIDE
18. ETHYLENE GLYCOL ETHER COMPOUNDS
19. FORMALDEHYDE
20. HEXABROMOCYCLODODECANE (HBCDD)
21. HYDRAZINE
22. HYDROFLUORIC ACID
23. LEAD & COMPOUNDS
24. MDA (4',4'—METHYLENE-DIANILINE)
25. MERCURY & COMPOUNDS
26. METHYL BROMIDE (BROMOMETHANE)
27. METHYL ETHYL KETONE (2-BUTANONE/ MEK)
28. METHYL ISOBUTYL KETONE (MIBK)
29. N-METHYL-2-PYRROLIDONE (NMP)
30. N-PROPYL BROMIDE (1 -BROMOPROPANE / NPB)
31. OZONE DEPLETING SUBSTANCES — CFCS AND HALONS (CLASS I) & HCFCS (CLASS II)
32. PBDES — DECA-BROMODIPHENYL ETHER (DBDE)
33. PBDES — HEXA-BROMODIPHENYL ETHER (HBDE)
34. PBDES — OCTA-BROMODIPHENYL ETHER (OBDE)
35. PBDES — PENTA-BROMODIPHENYL ETHER (PBDE)
36. PERFLUOROCARBON SOLVENT
37. PERFLUOROOCTANOIC ACID (PFOA)
38. PERFLUOROOCTAN E SULFONATES (PFOS)
39. PHTHALATE — BENZYL BUTYL PHTHALATE
40. PHTHALATE — BIS(2-ETHYLH EXYL) PHTHALATE (DEH P)

41. PHTHALATE — DIBUTYL PHTHALATE
42. POLYBROMINATED BIPHENYLS (PBBS)
43. POLYCHLORINATED BIPHENYLS (PCBS)
44. SHORT CHAIN CHLORINATED PARAFFINS (SCCPS)
45. STYRENE
46. THALLIUM
47. THORIUM, ALLOYS CONTAINING
48. TOLUENE
49. TOLUENE DI-ISOCYANATE
50. XYLENE

3.0 VALIDATION REQUIREMENTS

Component and/or system validation and certification efforts are expected to follow current US NASA and FAA practices. These specifics of which requirement or TRL will be imposed are not yet defined but may follow both civil and military practices.